Dynamics of Surface Catalytic Reactions on TiO_2

Dissertation
zur Erlangung des Doktorgrades
an der Fakultät für Mathematik, Informatik und Naturwissenschaften
Fachbereich Physik
der Universität Hamburg

vorgelegt von
Helena Gleißner

Hamburg
2025

Gutachter der Dissertation:	Prof. Dr. Andreas Stierle PD Dr. Michael Martins
Zusammensetzung der Prüfungskommission:	Prof. Dr. Andreas Stierle PD Dr. Michael Martins Dr. Heshmat Noei Prof. Dr. Alf Mews Prof. Dr. Daniela Pfannkuche
Vorsitzende der Prüfungskommission:	Prof. Dr. Daniela Pfannkuche
Datum der Disputation:	10.07.2025
Vorsitzender des Fach-Promotionsausschusses PHYSIK:	Prof. Dr. Wolfgang J. Parak
Leiter des Fachbereichs PHYSIK:	Prof. Dr. Markus Drescher
Dekan der Fakulät MIN:	Prof. Dr.-Ing. Norbert Ritter

Eidesstattliche Versicherung

Hiermit versichere ich an Eides statt, die vorliegende Dissertationsschrift selbst verfasst und keine anderen als die angegebenen Hilfsmittel und Quellen benutzt zu haben.
Sofern im Zuge der Erstellung der vorliegenden Dissertationsschrift generative Künstliche Intelligenz (gKI) basierte elektronische Hilfsmittel verwendet wurden, versichere ich, dass meine eigene Leistung im Vordergrund stand und dass eine vollständige Dokumentation aller verwendeten Hilfsmittel gemäß der Guten wissenschaftlichen Praxis vorliegt. Ich trage die Verantwortung für eventuell durch die gKI generierte fehlerhafte oder verzerrte Inhalte, fehlerhafte Referenzen, Verstöße gegen das Datenschutz- und Urheberrecht oder Plagiate.

Hamburg, den Unterschrift

Abstract

This thesis addresses the findings of two projects in the field of photocatalysis on TiO_2 single crystal-based model catalysts under ultra-high vacuum (UHV) conditions.
The first concerned the dynamics of the CO photo-oxidation to CO_2 on rutile TiO_2(110) measured by time-resolved photoelectron spectroscopy at the free-electron laser (FEL) FLASH in Hamburg. For this pump-probe experiment, a laser of 770 nm served as an optical pump to initiate the reaction, and the third harmonic of the FEL with a photon energy of 643 eV probed the O 1s, Ti 2p, and C 1s core levels. The formation of CO_2 by CO oxidation was observed within the first 800 ± 250 fs after the reaction was initiated. Calculations using density functional theory propose that the oxygen activation pathway for CO oxidation via an O_2-TiO_2 charge transfer complex can be directly excited by a 770 nm pump laser. During the reaction, residual traces of water in the UHV environment occupy CO adsorption sites, hindering further CO_2 formation. Compared to the anatase-TiO_2(101) surface, oxygen is activated via the same mechanism. Interestingly, CO_2 is formed more quickly on rutile (110) and remains on the surface for a shorter time, which indicates a shorter lifetime of the charge carriers that initiate the reaction. These findings are important for the design of photocatalysts.
The second project addresses the influence of the localized surface plasmon resonance of TiO_2(110) supported Au nanoparticles (NPs) on the oxidation of CO. Gold NPs with diameters between 2 to 12 nm were grown via molecular beam epitaxy under UHV conditions on stoichiometric rutile TiO_2(110) single crystal substrates. The samples were characterized via scanning tunneling microscopy (STM), low-energy electron diffraction (LEED), and X-ray reflectivity (XRR). The oxidation of (preadsorbed) CO at 95 K under O_2 atmosphere was monitored by X-ray photoelectron spectroscopy (XPS). The oxidation was found to be fast and efficient on small 3 nm Au nanoparticles grown at room temperature, as 90 % of the CO molecules were converted into CO_2 within 40 minutes. On larger nanoparticles grown at 500 °C with median diameters between 4.5 to 6 nm, the amount of pre-adsorbed CO was significantly lower due to the decrease in surface area in large particles. Further experiments under UV and 530 nm light illumination were carried out to excite the local surface plasmon resonance (LSPR), resulting in higher and faster CO to CO_2 conversion rates compared to dark conditions. To increase the

amount of preadsorbed CO, the TiO_2 supported Au nanoparticles were overgrown with Pt. Nominal coverages above one monolayer Pt were found to enable room temperature CO adsorption. Room temperature CO oxidation on Pt-Au/TiO_2 was then measured in a $1{\cdot}10^{-6}$ mbar O_2 atmosphere with 0.5 and 1 L preadsorbed CO. Under 530 nm and in dark conditions, CO oxidation was observed for 0.5 L, but not for 1 L CO. Coverages resulting from 1 L CO exposure block all adsorption sites, leading to the self-poisoning of the catalyst. When the Pt-Au/TiO_2 sample is heated, Pt segregates into the subsurface due to its higher surface free energy compared to Au.
The findings provide insight into the influence of preparation parameters on the (photo-) catalytic CO oxidation on Au/TiO_2 and Pt-Au/TiO_2 as preparation temperature and size. This project is followed up by a time-resolved CO oxidation experiment at the FEL FLASH, for which the insight into the influence of preparation parameters on the light-induced catalysis is of importance.

Zusammenfassung

Für diese Dissertation wurden zwei Projekte im Bereich der Photokatalyse an TiO_2-Einkristall-Modellkatalysatoren durchgeführt.
In dem ersten Projekt wurde die Dynamik der CO-Photooxidation zu CO_2 auf Rutil-TiO_2(110) mittels zeitaufgelöster Photoelektronenspektroskopie am Freie-Elektronen-Laser (FEL) FLASH in Hamburg untersucht. In diesem Pump-Probe-Experiment wurde die Reaktion mit einem 770-nm-Laser initiiert, während die dritte Harmonische des Freie-Elektronen-Lasers (FEL) mit einer Photonenenergie von 643 eV zur Anregung der O 1s-, Ti 2p- und C 1s-Kernniveaus diente. Die Bildung von CO_2 durch CO-Oxidation wurde innerhalb der ersten 800 ±250 fs nach Reaktionsbeginn beobachtet. Berechnungen auf Basis der Dichtefunktionaltheorie legen nahe, dass der Sauerstoffaktivierungsweg für die CO-Oxidation über einen O_2-TiO_2-Ladungstransferkomplex direkt durch den 770-nm-Pumplaser angeregt wird. Während der Reaktion blockiert Wasser, das in Spuren in der UHV-Umgebung vorkommt, die CO-Adsorptionsstellen, was die weitere CO_2-Bildung behindert. Genau wie bei der Anatas-TiO_2(101) Oberfläche wird Sauerstoff durch den gleichen Mechanismus aktiviert. Interessant ist, dass CO_2 auf Rutil (110) schneller gebildet wird und kürzer auf der Oberfläche verbleibt, was auf eine geringere Lebensdauer der Ladungsträger, die die Reaktion initiieren, hinweist.
Das zweite Projekt untersucht den Einfluss der lokalisierten Oberflächenplasmonresonanz von TiO_2(110)-geträgerten Au-Nanopartikeln auf die lichtinduzierte CO-Oxidation. Goldnanopartikel mit Durchmessern zwischen 2 und 12 nm wurden mittels Molekularstrahlepitaxie unter UHV-Bedingungen auf stöchiometrischen Rutil-TiO_2(110) Einkristallsubstraten aufgewachsen. Die Proben wurden mittels Rastertunnelmikroskopie (STM), niederenergetischer Elektronenbeugung (LEED) und Röntgenreflektivität (XRR) charakterisiert. Die Oxidation von voradsorbiertem CO bei 95 K unter O_2-Atmosphäre wurde mittels Röntgenphotoelektronenspektroskopie (XPS) verfolgt. Es zeigte sich, dass die Reaktion auf 3 nm großen Au-Nanopartikeln, die bei Raumtemperatur gewachsen wurden, besonders schnell und effizient verlief. Innerhalb von 40 Minuten wurden 90 % des CO in CO_2 umgewandelt. Auf größeren Nanopartikeln mit mittleren Durchmessern von 4.5 bis 6 nm, die bei 500 °C gewachsen wurden, war die Menge des voradsorbierten CO aufgrund zunehmend bulk-ähnlicher Eigenschaften signifikant geringer. Experimente unter 530-nm-Licht

zur Anregung der lokalen Oberflächenplasmonresonanz (LSPR) und unter UV-Licht zeigten eine schnellere Umwandlung von CO zu CO_2 im Vergleich zu dunklen Bedingungen. Um die Menge des voradsorbierten CO zu erhöhen, wurden die auf TiO_2-geträgerten Au-Nanopartikel mit Pt überwachsen. Eine nominale Bedeckung von mehr als einer Monolage Pt ermöglichte die CO-Adsorption bei Raumtemperatur. Die CO-Oxidation auf Pt-Au-TiO_2 wurde bei Raumtemperatur unter O_2-Atmosphäre mit 0.5 L und 1 L voradsorbiertem CO untersucht. Unter 530-nm-Bestrahlung sowie unter dunklen Bedingungen wurde eine CO-Oxidation für 0.5 L, jedoch nicht für 1 L CO beobachtet. Eine Bedeckung durch 1 L CO blockiert alle Adsorptionsstellen, was zu einer Inaktivierung des Katalysators führt. Beim Erhitzen der Pt-Au-TiO_2-Probe segregieren Pt-Atome aufgrund der höheren freien Oberflächenenergie im Vergleich zu Au in die Nanopartikel und Au-Atome an die Oberfläche. Dieses Projekt wird durch ein zeitaufgelöstes CO-Oxidationsexperiment am Freie-Elektronen-Laser FLASH fortgeführt, bei dem das Verständnis des Einflusses von Präparationsparametern auf die lichtinduzierte Katalyse von entscheidender Bedeutung ist.

Contents

Chapter 1

Introduction

Titanium dioxide (TiO_2) is a widely used material across various industries due to its high refractive index, chemical and biological stability, non-toxicity, affordability, and abundance in nature [1]. Its use as a white pigment dates back to the 13th century BCE when it was applied to Egyptian papyri [2], and it remains a key ingredient in modern paints. Beyond paints, TiO_2 is found in printing inks, synthetic fibers, and cosmetics.
However, the most interesting properties of TiO_2 are its photocatalytic properties. Photocatalysis has emerged as an essential technology for tackling modern challenges and offers promising solutions for reducing greenhouse gas emissions, improving air quality, and advancing clean energy systems [3–5].
A breakthrough in this field occurred in 1972 when Fujishima and Honda [6] demonstrated the photoelectrochemical splitting of water on TiO_2 electrodes. They showed that an n-type TiO_2 electrode connected to a platinum electrode generated a photocurrent under UV light, which catalyzed water splitting into O_2 and H_2. In TiO_2, electron-hole pairs are generated in the conduction and valence band under light with a photon energy greater than the bandgap. Fujishima and Honda's research established TiO_2 as a key photocatalyst, spurring extensive research into its photoreaction mechanisms, efficiency improvements, and practical applications.
The reaction studied by Fujishima and Honda is one potential area of application. Photodriven water splitting and hydrogen production offer a sustainable pathway to clean energy [7]. It is also used in wastewater treatment, where TiO_2 has demonstrated remarkable capabilities in breaking down pollutants and organic contaminants, contributing to cleaner water sources [8]. In construction, TiO_2 can enhance self-cleaning surfaces and help combat urban pollution as an additive in concrete [9]. Additionally, it can be used for air purification by efficiently breaking down volatile organic compounds (VOCs) and improving indoor and outdoor air quality [10]. The renewable energy sector is also exploring TiO_2 for photovoltaic applications, particularly in dye-sensitized solar cells (DSSCs), which have the potential to drive innovation in cost-effective and efficient solar energy

conversion [11–13]. Beyond energy and environmental applications, TiO_2 is applied in green chemistry as a catalyst for sustainable chemical reactions, reducing the need for harmful reagents and minimizing ecological impact [14].

The first commercial exploitation of the photocatalytic properties of TiO_2 was applied in Japan to combat the darkening of light covers in tunnels caused by exhaust compounds. The TiO_2-coated glass covers for tunnel lamps are self-cleaning due to the UV radiation emitted by sodium lamps, which is strong enough to break down exhaust pollutants [15]. The superhydrophilicity of TiO_2 enhances its self-cleaning properties, which makes it especially effective for outdoor applications such as coatings for roads and buildings [4]. One notable example is the Centre Pompidou in Metz, France, designed by architect Shigeru Ban [16]. Its white roof consists of PTFE-coated fiberglass with a TiO_2 coating by TAIYO Europe GmbH. This patented HYDROTECT coating allows self-cleaning through photocatalytic degradation of pollutants under UV light, preserving the building's white appearance.

As TiO_2 has a band gap in the UV region of 3-3.2 eV, only around 5 % of the solar spectrum can be harvested for the photoinduced applications mentioned [17]. One approach to also harvest visible light is using metal nanoparticles with a localized plasmonic resonance in the visible light region. One material for this purpose is gold, a non-toxic metal. Using gold as a catalyst has led to valuable commercial applications in various industrial processes. For instance, Au-doped Pd catalysts are employed to synthesize vinyl acetate [18]. Adding gold to palladium catalysts enhances the reaction rate and selectivity while preventing self-poisoning [19]. Moreover, introducing Au-Pd catalysts enabled a cost-effective shift from acetylene to the cheaper ethylene as a reactant, further reducing production costs [20]. A gold catalyst, developed by the catalyst manufacturer Johnson Matthey, has the potential to replace mercury-based $HgCl_2$ catalysts in the commercial hydrochlorination of acetylene to vinyl chloride monomers, the precursor for polyvinyl chloride (PVC) [21]. The hydrochlorination of acetylene was first studied by Hutchings [22] in 1985 and was one of the first reports on the catalytic efficiency of gold nanoparticles. Due to mercury's high toxicity, the Minamata Convention of 2013 mandated a reduction in its use [23]. Since 2008, an Au-NiO_x core-shell catalyst has been commercially used for the oxidative esterification of methacrolein to methyl methacrylate, which is the monomer for poly(methyl methacrylate) (PMMA), also known as acrylic glass [24]. The Au-NiO_x core-shell catalyst replaces the original Pd_3Pb catalyst by reducing the by-product formation and cost while working under similar reaction conditions and lifespan.

In the context of Au on TiO_2, Haruta [25] demonstrated that nanoscale gold particles on reducible supports, e.g., TiO_2, are exceptionally effective catalysts for CO oxidation. The CO oxidation on Au-TiO_2 is widely studied with the highest efficiency at a nanoparticles size of 2-3 nm. Au nanoparticles on TiO_2 are commercially available as AUROlite from

AuTEK or NanAucat from 3M for oxidizing CO [26].

Photocatalytic reactions on gold nanoparticles are potentially driven by hot electrons generated by the localized surface plasmon resonance (LSPR) excitation [27]. LSPR refers to the collective oscillation of conduction band electrons in metal nanoparticles when exposed to light, particularly at specific wavelengths. This phenomenon occurs in the visible region of the electromagnetic spectrum for gold nanoparticles [28]. When the gold nanoparticles are illuminated, hot electrons with energies greater than the Fermi level of the metal are generated. These hot electrons can transfer to adsorbed molecules on the nanoparticles' surface, activating them for subsequent chemical reactions. The energy provided by these hot electrons can lower the activation energy required for catalytic processes, making them more efficient and selective. By coupling gold nanoparticles with semiconductors such as TiO_2, hot electrons generated by the gold nanoparticles can be injected into the conduction band of TiO_2, thereby facilitating charge separation and improving overall catalytic efficiency [29].

The LSPR of gold nanoparticles is already used for the technique of surface-enhanced Raman Scattering (SERS) [30]. The plasmonic oscillations, which are induced by lasers, generate highly localized electromagnetic fields, amplifying the Raman scattering signal of nearby molecules by several orders of magnitude.

CO oxidation is chosen as a probe reaction to study the properties of plasmonic gold nanoparticles. Catalytic oxidation reactions are pivotal in industrial and environmental processes, with carbon monoxide (CO) oxidation serving as a benchmark reaction to evaluate catalyst performance [31]. The reaction is widely studied on different materials and various pressures. Still, studies on the time-resolved dynamics are rare on photocatalysts. In this context, the development of free-electron lasers (FEL) [32] brought new possibilities to study ultrafast processes by using elaborate surface science techniques, e.g., X-ray Photoelectron Spectroscopy with the short FEL pulses for pump-probe experiments. In heterogeneous catalysis, reactions occur through short-lived intermediates and transition states, which are difficult to capture with steady-state techniques. Most experimental methods only provide information about stable reactants and products, leaving reaction mechanisms largely inferred from theory. FELs provide intense, ultrashort X-ray pulses that enable femtosecond time-resolved spectroscopy, revealing real-time electronic and structural dynamics [33]. This is crucial for studying energy transfer, bond breaking and formation, and charge redistribution during reactions. The ability to trigger reactions with femtosecond optical lasers and probe them with X-ray absorption or emission spectroscopy allows researchers to map out reaction pathways and identify key intermediates [32].

Motivation and Structure of the Thesis

The thesis consists of two research projects.

1. Ultrafast Photocatalysis on Rutile (110): Previous studies [34] have revealed the dynamics of CO oxidation on anatase (101), providing critical insights into surface reaction mechanisms and giving insight into the oxygen activation within 1.2 ps probed by time-resolved X-ray Photoelectron Spectroscopy (XPS) at the FEL FLASH in Hamburg. However, a knowledge gap remains regarding similar ultrafast processes on rutile (110). This study aims to investigate and compare the reaction dynamics of CO oxidation on rutile (110) under ultrafast conditions, providing a deeper understanding of the surface-specific catalytic behavior. The project was written in a manuscript format and is attached as Chapter 5.

2. Plasmonic Photocatalysis with Au and Pt-Au Nanoparticles on TiO_2: Epitaxially grown gold nanoparticles on rutile TiO_2(110), followed by platinum overgrowth, serve as model catalysts to explore the role of plasmonic enhancement in visible-light-driven photocatalysis. The aim is to examine the plasmonic enhancement of the CO oxidation using gold nanoparticles and Pt-Au nanoparticles on TiO_2 under visible and UV light irradiation. The results are discussed in Chapter 6.

Chapter 2 presents a state-of-the-art literature review on TiO_2-based photocatalysis, ultrafast catalytic dynamics, the growth of noble metal nanoparticles, and CO oxidation mechanisms. Chapter 3 describes the basics of the applied surface science techniques. The experimental setups at the DESY Nanolab and the FLASH beamline PG2 are documented in Chapter 4.

Chapter 2

State of the Art

This chapter gives an overview of the literature on titanium dioxide (TiO_2) for photocatalysis, focusing on the reaction dynamics of CO oxidation and the growth of Au nanoparticles (NPs) to enhance its catalytic activity.

2.1 Titanium Dioxide

Titanium dioxide is one of the most studied metal oxides [1]. The naturally occurring polymorphs are rutile, anatase, and brookite. The thermodynamically most stable polymorph is rutile, while anatase transforms to rutile at ∼900 K. The transformation temperature varies with pressure, heating rate, sample, and particle morphology [35]. It commonly serves as a model metal oxide surface due to its stability and high abundance. The lattice of TiO_2 is built of repeating unit cells that include one titanium (Ti) ion and two oxygen (O) atoms. In the context of ionic bonding, titanium is assigned a charge of 4+ and oxygen a charge of 2−. However, the Ti-O bond exhibits both covalent and ionic characteristics. Titanium has a coordination number of six, and oxygen has a coordination number of three, meaning that each titanium ion in the bulk material bonds with six oxygen ions. The unit cells of rutile and anatase as a ball-stick model are depicted in Fig. 2.1. Rutile has a denser structure and greater thermodynamic stability, yet anatase is frequently formed in the synthesis of TiO_2 due to its lower surface energy compared to rutile. The structural characteristics of rutile and anatase are detailed in Table 2.1 [35].

2.1.1 From Atoms to Solids

Based on their electronic structure, solid-state materials are fundamentally divided into metals, semiconductors, and insulators. The molecular orbital theory describes the electronic structure of solids. The orbitals of an isolated atom possess discrete energies. To form the electronic structure of a molecule, these atomic orbitals ϕ must combine to form

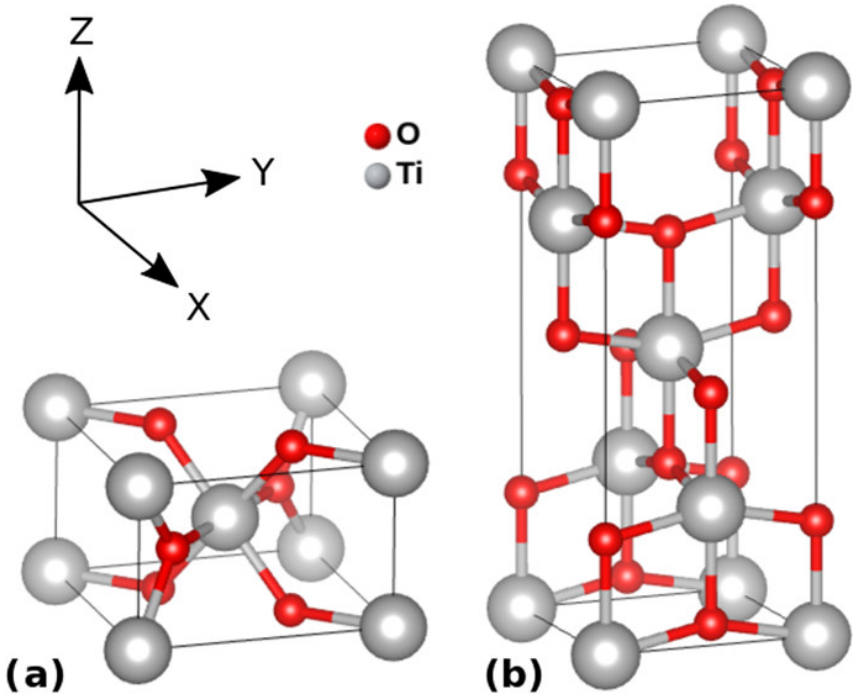

Figure 2.1: Unit cell of a) rutile and b) anatase TiO_2. Image taken from [36].

Table 2.1: Structural properties of anatase and rutile taken from [35].

Property	Anatase	Rutile
Crystal structure	Tetragonal	Tetragonal
Atoms per unit cell (Z)	4	2
Space group	$l\frac{4}{a}$md	$l\frac{4_2}{m}$md
Lattice parameters (nm)	a = 0.3785	a = 0.4594
	c = 0.9514	c = 0.29589
Unit cell volume (nm^3)	0.1363	0.0624
Density (kg m^{-3})	3894	4250
Calculated indirect band gap		
(eV)	3.23-3.59	3.02-3.24
(nm)	345.4-383.9	382.7-410.1
Experimental band gap		
(eV)	∼3.2	∼3.0
(nm)	∼387	∼413

molecular orbitals

$$\Psi = \sum_{i=1}^{N} c_i \phi_i \tag{2.1}$$

weighted with the coefficient c. The combinations form discrete energy levels that are either bonding, antibonding, or non-bonding, depending on the constructive or destructive interference of wavefunctions. This approach is known as the method of linear combination of atomic orbitals (LCAO) [37]. The quantity of initial atomic orbitals is equivalent to the total number of combined molecular orbitals. Bonding orbitals result from the constructive interference of the atomic orbitals, leading to an increased electron density between the nuclei. Antibonding orbitals result from the destructive interference of atomic orbitals with reduced overlap. Bonding orbitals lower and antibonding increase the system's energy. Non-bonding orbitals result from non-interacting atomic orbitals, which preserve their atomic character. The bond is stable when the system's overall energy decreases through electrons in bonding molecular orbitals.
As the number of atoms increases to nearly infinite when forming a bulk-like solid, the discrete energy levels merge into continuous energy bands, as shown in Fig. 2.2.

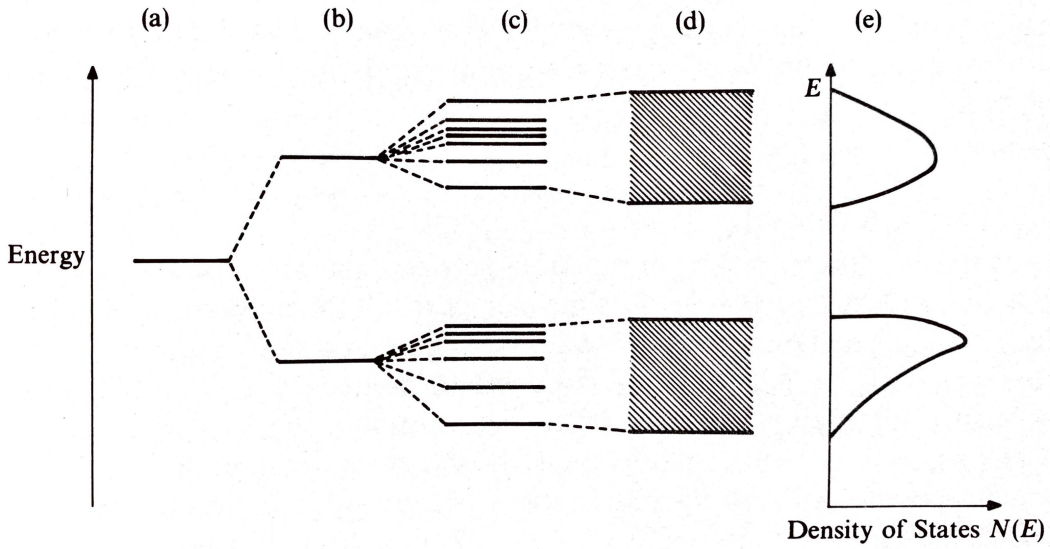

Figure 2.2: Schematic representation of orbital energies for: a) an atom, b) a diatomic molecule, c) a multi-atomic molecule with discrete orbital energy levels, d) a solid with an infinite number of energy states forming energy bands, and e) a density of states with a band gap [38].

All energy levels up to the Fermi energy are fully occupied at absolute zero, while those above it remain empty. At temperatures above 0 K, the probability for a state with the energy E being occupied at temperature T is given by the Fermi-Dirac distribution

$$F(E) = \frac{1}{1 + exp[(E - \mu)/k_B T]}, \tag{2.2}$$

with the the Boltzmann constant k_B and the electrochemical potential μ [39].
The width of the bandgap between the valence band (highest filled energy band) and conduction band (lowest unfilled energy band) determines whether a solid is conductive, semiconductive, or insulating [38]. In metals, the Fermi energy is located in a partially filled-band. Semiconductors exhibit moderate band gaps of a few eVs, enabling conductivity under heat or light. Insulators possess wide band gaps (>5 eV), making electron excitation from the valence to the conduction band unlikely under normal conditions. The electronic structure is sketched in Fig. 2.3 [39].

The excitation of charge carriers follows specific selection rules. For atoms, during elec-

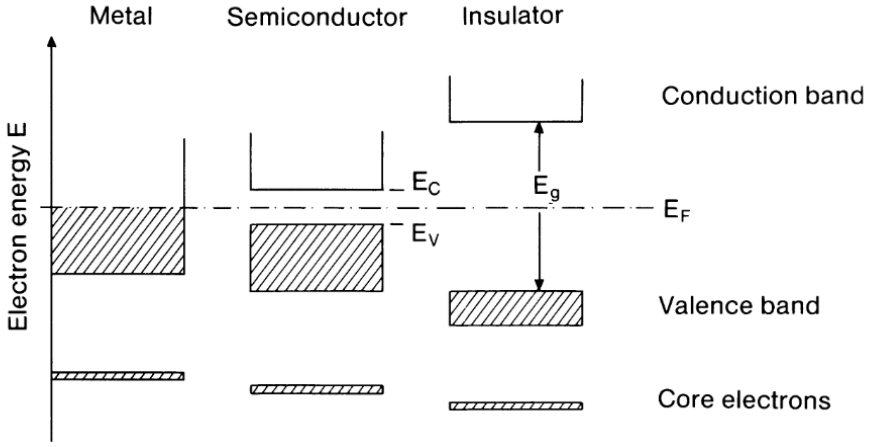

Figure 2.3: Band gap of metals, semiconductors, and insulators [39].

tron excitation, the angular momentum quantum number l has to change by $\Delta l = \pm 1$, and therefore, transitions such as s-s, p-p, and d-d are forbidden. In solids, electrons can be described by Bloch wavefunctions characterized by a wavevector k (the crystal momentum) based on the periodicity of the lattice. For optical transitions (induced by photons), the wave vector has to remain unchanged with the selection rule $\Delta k = 0$ to follow the conservation of momentum, as the photon's momentum is negligible compared to the electron's. This rule prohibits transitions involving indirect band gaps, where the valence band maximum and the conduction band minimum are at different k-values. While such transitions can occur due to interaction with phonons, plasmonic excitations, or multi-photon absorption, they are less likely compared to direct bandgap transitions with $\Delta k = 0$ [38]. This concept is used to explain the difference in catalytic activity on anatase and rutile TiO_2 in Sec. 2.2.1.

2.1.2 Rutile (110) Surface

Rutile is the thermodynamically most stable and dense polymorph of TiO_2, with the (110) facet being its most stable surface. On the bulk-terminated (110)-(1 × 1) surface

(depicted in Fig. 2.4 (a)) the topmost atoms are bridging oxygen (O_b) bound to two Ti atoms (instead of three in bulk) and pentacoordinated in-plane titanium atoms (Ti_{5c}). Oxygen vacancies can form either in-plane or at the bridging oxygen sites. Highly oxygen-reduced rutile surfaces exhibit a (1×2) reconstruction.

The thermodynamic Wulff construction describes the equilibrium shape of a single crystal by relating the normal distance of a facet from the crystal center to its surface free energy. Mathematically, this is expressed as

$$\gamma_i = \frac{h_i}{\lambda} \tag{2.3}$$

with the orientation-dependent surface free energy γ_i of facet i, its normal distance from the Wulff point h_i, and a constant accounting for volume λ. The resulting crystal shape minimizes the total surface free energy [40]. The Wulff construction for rutile is shown in Fig. 2.4 (b), where the (110) facet has the lowest calculated surface area and constitutes 56 % of the total Wulff construction [41, 42]. In experiments under UHV conditions, the rutile (110) surface needs to be cleaned by Ar^+ ion sputtering to remove contaminants from the surface. Since oxygen is more likely to be removed by sputtering, a reduced, oxygen-deficient, and disrupted surface is left after sputtering. The excess charge from the oxygen reduced Ti^{4+} to Ti^{3+}. To obtain a smooth surface, annealing is required. During annealing in UHV above 700 K, excess surface Ti^{3+} diffuses into the bulk, leading to a less reduced surface [43]. During annealing above 470 K in O_2, Ti^{3+} diffuses towards the surface and builds with the gaseous O_2 new layers of TiO_2 in the form of rosettes [44], leading to a stoichiometric surface.

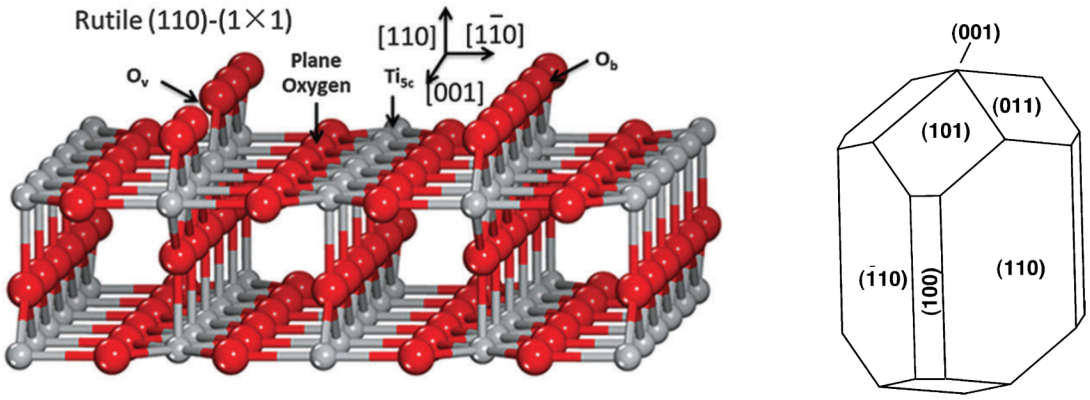

Figure 2.4: Ball-stick representation of the rutile (110)(1×1) surface (left) from [45] and Wulff construction of rutile (right) from [1]; first appearance in [41].

2.1.3 Defect States

Titanium dioxide is a reducible metal oxide with an affinity to form defects in the form of oxygen vacancies V_O or titanium interstitials Ti_{int}. Defects can be induced by either ion sputtering or heating in UHV, which removes oxygen atoms. This process leads to the formation of various phases in the Ti-O system, depending on the temperature and Ti-O ratio. Oxygen vacancies serve as adsorption and reaction sites on metal oxide surfaces [46]. An oxygen vacancy leaves behind two unpaired electrons, forming two Ti^{3+} ions and introducing a donor level within the bandgap, located 0.75–1.18 eV below the conduction band minimum [47]. One kind of defects, oxygen vacancies, behave differently in rutile and anatase as several calculations [48, 49] found the lowest formation energy of oxygen vacancies at subsurface positions in anatase (110) and on the surface in rutile (110). These results are in alignment with experimental observations [50] Oxygen vacancies influence the catalytic activity of each polymorph differently. Generally, surface defects enhance, and bulk defects decrease the photocatalytic activity on TiO_2 [51]. Surface vacancies might promote charge carrier separation while being available for the photocatalytic reaction. Bulk defects as charge traps promote recombination since the charge carriers are not available for the photocatalytic reaction at the surface [51].
Defects on rutile (110) are required for the chemisorption of O_2 by providing electrons to stabilize the adsorption [52]. On defect-free rutile (110) O_2 only physisorbs [53]. In rutile, defects within the TiO_2 bulk structure can be visually identified, as the transparent stoichiometric crystal darkens to a deep blue color due to the presence of color centers. These defects lead to n-type doping and reduce the material's resistivity [54].

2.2 Photocatalysis

Photocatalysis on titanium dioxide is widely studied due to its efficiency in enabling chemical reactions under UV light. TiO_2 has applications in water and air purification [3], hydrogen production [55], and self-cleaning surfaces due to its antiviral and antibacterial properties [4,5,15]. When TiO_2 absorbs photons with an energy equal to or greater than its bandgap ($\sim$3 eV for rutile), electrons are excited from the valence band to the conduction band. These charge carriers can participate in redox reactions: electrons in the conduction band reduce oxygen to form reactive oxygen species (ROS) [15], while holes in the valence band oxidize water (to form hydroxyl radicals) or organic molecules [56]. These ROS drive the degradation of pollutants and water splitting for hydrogen production. The redox reaction competes with electron-hole pair recombination. Recombination can be lowered by introducing trap states, leading to a separation of the charge carriers [51]. Due to the wide band gap of 3 eV in rutile and 3.2 eV in anatase, the exploitation of the solar range is limited to UV-light and below in wavelength, which amounts to $\sim$5%

of the solar spectrum [57]. Thus, modifications to increase the yield are a promising approach to enhance the catalytic activity. Possible modifications to access the visible region and enable visible light absorption with TiO_2 are doping, self-doping, and introducing heterojunctions or metal nanoparticles [58]. For the modification by doping, non-metal elements like nitrogen [59], sulfur [60], or carbon [61], or metal elements like iron [62] or vanadium [63], are incorporated into the TiO_2 lattice. This creates mid-gap states in the bandgap, accessible with visible light absorption [61]. The incorporation might also induce recombination centers, reducing charge carrier lifetime. For self-doping, oxygen vacancies and Ti^{3+} are generated in the lattice, leading to states in the bandgap [64]. Another approach is to form a heterojunction by coupling TiO_2 with a narrow-bandgap semiconductor, such as CdS [65], to facilitate charge carrier separation and extend the absorption energy range. The method that is addressed in this thesis is the deposition of metal particles (e.g., Au, Ag) onto the TiO_2 surface to enhance visible-light absorption via localized surface plasmon resonance (LSPR) [66–69]. These nanoparticles also act as electron sinks, reducing the recombination probability of photogenerated charge carriers [3].

2.2.1 Photocatalytic CO Oxidation on TiO_2

Carbon monoxide oxidation ($CO + \frac{1}{2} O_2 \longrightarrow CO_2$) has long served as a prototypical reaction for heterogeneous catalysis due to its fundamental importance in environmental catalysis, such as automotive exhaust treatment, and its applicability in industrial processes [31].

CO Adsorption on Rutile (110)

The adsorption of CO on reduced and stoichiometric TiO_2 surfaces was studied by various authors and several techniques [53, 70–79]. On rutile (110) as well as anatase (101), CO adsorbs with the C atom bound to the Ti_{5c} site with a C-Ti σ-bond [76–78]. In presence of defects (Ti^{3+}) the additional charge promotes electron transfer to CO. This enhanced interaction is also observed in temperature-programmed desorption (TPD) which gives a desorption temperature of CO from stoichiometric rutile (110) at ∼170-135 K and from the reduced surface at ∼350 K [70]. Below 70 K, a full monolayer of CO adsorbs in a zig-zag 2×2 superstructure due to intermolecular repulsion [73]. Above 70 K, rutile (110) is saturated by half a monolayer of CO. While on stoichiometric rutile (110), a single adsorption band at 2088 cm^{-1} for CO bound to Ti_{5c} sites is observed in reflection–absorption IR spectroscopy (RAIRS), on the reduced rutile (110) surface an additional second-band at 2178 cm^{-1} is assigned to CO bound to a Ti_{5c} located second nearest to an oxygen vacancy [74].

O_2 Adsorption on Rutile (110)

Molecular oxygen only physisorbs on the stoichiometric surface below 85 K [53]. On reduced rutile (110), oxygen vacancies provide chemisorption sites for two O_2 per vacancy [72]. Chemisorption requires charge transfer to the adsorbed O_2 molecule, which can result in the superoxide radical anion ($^{\bullet}O_2^-$), peroxide ion (O_2^{2-}) or the dissociated oxide ion (O^{2-}) [76].

CO_2 Adsorption on Rutile (110)

The product of the CO oxidation is CO_2. CO_2 adsorbs similarly to CO on the Ti_{5c} sites [80, 81] and desorbs at 150-200 K. On reduced rutile (110), the oxygen vacancy sites provide further adsorption sites for CO_2, from which the desorption is observed at ∼200 K. Based on DFT calculation and STM measurements, the adsorption of CO_2 on rutile (110) is stabilized in the presence of water or hydroxyl groups [82].

CO Photooxidation on Rutile (110)

The photooxidation of CO to CO_2 on rutile and anatase TiO_2 was studied by RAIRS [83, 84] and X-ray photoelectron spectroscopy (XPS) [85]. Consistent with findings from powdered sample studies [70], stoichiometric anatase (101) shows faster CO_2 formation rates under UV illumination compared to reduced anatase (101) as well as both reduced and stoichiometric rutile (110). On both TiO_2 polymorphs, CO is only oxidized in the presence of O_2 and simultaneous UV illumination [85]. The UV illumination initiates the photocatalytic reaction by generating electron-hole pairs in the conduction and valence bands [58]. The gas-phase O_2 dissociates by capturing the generated electron, leading to the formation of adsorbed oxygen. This chemisorbed oxygen ion subsequently reacts with the adsorbed CO to produce CO_2 [83]. Adsorbed oxygen is required for CO oxidation, as lattice oxygen does not contribute as a source for this photoreaction [86]. The adsorption and photoactivation of oxygen are critical steps that initiate CO oxidation as an electron-mediated reaction, thereby competing with charge carrier recombination [87]. The effectiveness of this process significantly influences the overall catalyst efficiency. Increased charge carrier lifetimes enhance the likelihood of interaction with gas-phase oxygen molecules. Multiple studies [84,88] have reported shorter charge carrier lifetimes in rutile compared to anatase. One explanation is that anatase possesses an indirect band gap that reduces electron-hole pair recombination, allowing a greater proportion of generated charge carriers to promote this reaction pathway. In contrast, the direct band gap of rutile results in shorter charge carrier lifetimes, thereby decreasing catalytic efficiency [84].

2.2.2 Dynamics of Photoreactions

The study of photocatalytic dynamics has evolved significantly since the pioneering work of Norrish and Porter [89] in 1949 on flash photolysis, which laid the groundwork for ultrafast reaction dynamics. Ahmed Zewail, often called the "Father of Femtochemistry," was awarded the Nobel Prize in 1999 for observing chemical reactions in real-time at the femtosecond scale [90]. A key tool in femtochemistry are pump-probe experiments [91]. An ultrashort pump pulse excites the system, which is then probed/measured after a specific time delay by another ultrashort pulse. These advancements enabled the study of ultrafast processes such as charge generation, transfer, and recombination in photocatalytic materials like TiO_2 [34, 92]. The insight into the lifetime of charge carriers in rutile and anatase TiO_2 is considered responsible for the higher photocatalytic activity of anatase compared to rutile. Femtosecond transient absorption spectroscopy [88] revealed that the recombination time of charge carriers in anatase is two orders of magnitude slower compared to rutile (110) due to a higher bulk defect density in rutile. Another study [84] also found shorter lifetimes of charge carriers in rutile compared to anatase by transient photoconductance measurements, but assigned their findings to the difference in the band structure. A direct band gap causes a shorter lifetime in rutile, while the indirect band gap of anatase hinders recombination and prolongs charge carrier lifetimes.

The dynamics of photoinitiated reactions on rutile were studied with ethanol [93] and acetone [94]. Ethanol photodissociation studied by time-resolved two-photon photoemission revealed a lifetime of 24 fs for the excited transition state associated. This time is found to be similar to other alcohols on TiO_2, which indicates that alcohols on TiO_2 share a similar photochemistry [93].

A pump-probe experiment on the acetone photooxidation on TiO_2 (110) observed the fragmentation of acetone after 300-700 fs via multiphoton ionization of methyl radical, as the product of the acetone fragmentation [94]. The mechanism is assigned to the interaction of acetone with "hot" holes induced by the laser pulse. These studies also serve as an opportunity to test theoretical models for charge carrier transfer dynamics.

At free-electron lasers, X-ray absorption spectroscopy with femtosecond resolution is available. With this technique, the hole transport dynamics in anatase were studied, identifying the energy level and lifetime of holes in nano-crystals of anatase. Trapped holes are formed in the bandgap region within 0.3 ps and decay within 8.0 ps [95]. Combined with DFT calculations, X-ray adsorption spectroscopy simulations give insight into the energy levels of trapped states and their lifetimes. The hole transfer from single crystal anatase (101) to water was observed by time-resolved X-ray photoelectron spectroscopy in an optical pump FEL probe experiment [92]. The hole transfer to water is observed within 285 fs after excitation by the pump laser, and hydrogen bonds were identified as a potential charge-transfer pathway during photocatalysis.

2.2.3 Ultrafast CO Oxidation

Observing the dynamics of photocatalysis on an ultrafast timescale, i.e. for reaction times in the femto- to picosecond range, is crucial to understanding the reaction mechanisms in heterogeneous catalysis. In the following, several studies are briefly outlined to highlight the relevance of ultrafast probing techniques and introduce key reaction mechanisms for CO oxidation in relation to the scientific question of this dissertation.

A study on anatase TiO_2 as a metal oxide photocatalyst by Wagstaffe *et al.* [34] revealed the dynamics of the CO oxidation by optical pump soft x-ray probe photoemission spectroscopy at the FEL FLASH. The CO_2 formation was observed after 1.2 ps after initiation of the reaction and for 1.6 ps. The offset was assigned to the activation of physisorbed molecular oxygen.

Previous studies focused on the ultrafast dynamics of the CO oxidation were primarily studied on metals such as Ru(0001) [96,97], Pt(111) [98] and Pd(111) [99], due to their relevance in car catalysts. In 1999, Bonn *et al.* [96] used two-pulse correlation measurements to trace the CO oxidation on Ru(0001). They utilized a setup with two laser pulses of the same energy (800 nm), duration (110 fs), and intensity. They determined the conversion yield via time-of-flight spectroscopy, i.e., as a function of the delay in the time of arrival of the laser pulses. The clean Ru(0001) surface was first covered with 0.5 monolayers of atomic oxygen by exposing the surface to 5 L O_2, then exposed to 1.8 L CO. Within the first picosecond, the femtosecond laser pulse excited the electrons in the metal substrate, resulting in a very high transient electronic temperature. The energy of phonons and electrons equilibrate after $\sim$1 ps, as the electrons dissipate their excess energy via electron-phonon coupling. The signal of CO_2, the product of CO oxidation, and the CO signal from CO desorption are observed relative to the delay of the two femtosecond laser pulses. They show that the signal of CO desorption with an FWHM of 20 ps results from phonon coupling and the increase in temperature of the substrate surface. As the energy for the CO desorption (E = 0.83 eV) is significantly lower than for CO_2 formation (E = 1.8 eV) [100], the reaction cannot be activated thermally since CO would desorb before reacting with the activated O. Hence, the CO oxidation is only accessible via the laser excitation pathway. A CO_2 signal with an FWHM of 3 ps was observed, resulting from hot electrons induced by the two laser pulses with a temporal separation of less than the electron-phonon equilibrium time. In 2015, Öström *et al.* [97] used optical pump X-ray probe spectroscopy to study the transient states during the CO oxidation on Ru (0001). The clean Ru (0001) surface was first exposed to O_2 at 800 K, then to CO at 300 K, resulting in CO and atomic O adsorption. The optical laser (400 nm) excited electrons in the substrate and subsequently increased adsorbate-substrate vibrations. The X-ray FEL probes the electronic states of the O K-edge via X-ray absorption spectroscopy. They show that oxygen is activated in 280 $\pm$ 100 fs, and after 800 $\pm$ 250 fs, a new state ap-

pears that is assigned to CO_2 formation. The CO_2 formation in less than one ps is in line with the findings from Bonn *et al.* [96] that CO_2 formation is driven by hot electrons. This proposition was made possible by the advancements in pump-probe x-ray spectroscopy, which allowed the observation of transition states that were not accessible by other techniques before.

2.3 Gold Nanoparticles on Titanium Dioxide

It is commonly known that bulk gold is chemically inert and the least active metal [101], yet gold nanoclusters can mediate catalytic reactions [102]. The first studies of gold as a catalyst date back to 1925 [103]. The studies by Hutchings [22] in 1985 on supported gold catalysts for hydrochlorination of acetylene as well as the investigations of Haruta and co-workers [25,104] in 1987 and 1989 on the low-temperature CO oxidation on metal oxide supported gold raised this field of research to the attention of a broader scientific community. Since then, gold nanoparticles have been widely studied on different metal oxides, including reducible metal oxides, e.g., TiO_2, Fe_2O_3, Co_3O_4, as well as non-reducible metal oxides, e.g., Al_2O_3 [105]. These gold/metal oxide systems were shown to catalyze a variety of chemical reactions, such as CO oxidation [25], H_2 oxidation [106], the water-gas shift reaction ($CO + H_2O \rightleftharpoons CO_2 + H_2$) [107], selective oxidation of ethene and propane [108], dehydrogenation of alcohols and carboxylic acids [109–111] as well as the oxidation of volatile organic compounds (VOC) [28, 112]. Panayotov and Morris have reviewed the Au/TiO_2 system [28]. The present thesis focuses on CO oxidation on Au/TiO_2.

2.3.1 From Bulk to Supported Nanoparticles

The chemical inactivity of bulk Au is favored by two factors: the filled d-band (from the Fermi level located above the d-band) and the s-d coupling matrix element [101]. For attractive adsorption, the metal and the adsorbate hybridization has to gain energy by only filling the bonding and not the anti-bonding states. This energy gain has to counteract the orthogonalization energy resulting from quantum mechanics. The orthogonalization energy is proportional to the coupling matrix element. The d-band of gold is filled, therefore, the antibonding state located below the Fermi level would be filled upon adsorption and no energy is gained by binding adsorbates to Au. The size of the coupling matrix element for transition metals increases with each period. It decreases with higher atomic number, as d-states are bound more tightly with increasing nuclear charge. For example, the coupling matrix element for Au is larger than for Cu, an element two rows above Au with similarly filled d-states, which results in an increased coupling matrix element in

comparison [101].
In contrast, undercoordinated Au atoms, such as those located at the corners and edges of nanoclusters, differ significantly in electronic structure, impacting adsorption behavior. Taking CO as an example of an adsorbate, no adsorption on smooth Au(111) is observed even at 25 K [113]. But on a rough Au(111) film, CO adsorbs even at 170 K [113], as CO adsorbs more strongly on e.g. Au(211)-like step sites than on Au(111) terrace sites [114]. According to the d-band model, molecules bind more strongly at steps than at terrace sites because the center of the d-band shifts with decreasing coordination of an atom closer to the Fermi level [115].
In a theoretical study [116], the adsorption of CO and O_2 on Au was studied to examine possible CO oxidation pathways. On Au(111) terraces, CO and O_2 both do not adsorb, and on Au(110), CO chemisorbs while no O_2 activation was calculated. Interestingly, the study suggests that on Au(310) surfaces, CO + O_2 adsorption is energetically feasible, yet the CO oxidation competes with the desorption of O_2. On an Au_{38} cluster, O_2 dissociates and oxidizes adsorbed CO to CO_2.
For practical purposes, nanoparticles require a support structure to be utilized as catalysts as this enables lower costs, even dispersion of Au NPs, and inhibition of sintering. The support also provides adsorption sites for reagents and reaction products [28]. Metal oxides are viewed as the most suitable support materials for Au nanoparticles, as the particles, as well as the interface between support and Au nanoparticles, play an active role in influencing the catalytic performance [117]. Especially Au nanoparticles on reducible oxides like TiO_2 and Fe_2O_3 show higher catalytic activity than Au on non-reducible oxides like SiO_2 and Al_2O_3 [118–120]. The lower energy metal-oxide bond and smaller bandgap of reducible oxides may influence the electron density of the gold nanoparticles and the position of the Au d-band relative to the Fermi level [121]. The size of the gold nanoparticles highly influences the catalytic efficiency as it decreases for particles larger than 4 nm in diameter for various supporting materials [122]. This trend is observed on "model" film and "real" powder Au/TiO_2 catalysts, as seen in Fig. 2.5. The nature of the active sites on Au/TiO_2 is still under debate, as calculation and UHV studies propose that anionic $Au^{\delta-}$ sites [123–126] are responsible for the increased activity. In contrast, steady-state experiments proposed oxidized or cationic $Au^{\delta+}$ sites [127–129] as the origin of catalytic enhancement. One potential explanation for this controversy suggests that anionic $Au^{\delta-}$ sites form under UHV conditions with a low O_2 partial pressure. In contrast, under higher oxygen pressure, the interaction between Au/TiO_2 and oxygen leads to oxidation and $Au^{\delta+}$ formation [130]. The most crucial factors influencing the catalytic activity are quantum size effects, electronic effects, availability of low coordination sites, and the perimeter site between metal particles and support. To properly address these factors, the experimental variables that influence the Au/TiO_2 sample preparation and

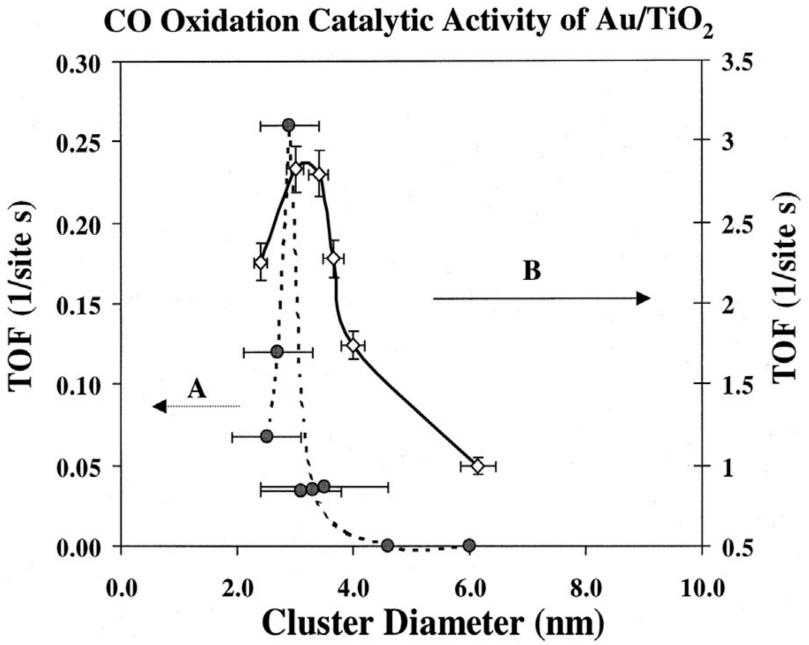

Figure 2.5: Turn-over-frequency of CO oxidation depending on the size of A) "real" high surface Au/TiO_2 catalysts (data from [131]) and B) "model" Au/TiO_2 catalysts (data and figure from [132]).

the resulting nanoparticle growth behavior need to be assessed.

2.3.2 Growth of Au on TiO_2

For a systematic and controlled study of the Au/TiO_2 system, planar model catalysts are prepared in UHV by vapor deposition of Au on a $TiO_2(110)$ single crystal. Gold grows in 2D islands for small amounts of evaporated metal and only builds 3D structures after reaching a critical coverage [133]. The transition coverage from 2D to 3D depends on the defect density and temperature and is ∼0.09 ML Au on a stoichiometric TiO_2 (110) surface, 0.19 ML on the stoichiometric surface at 160 K, and ∼0.22 ML Au on the non-stoichiometric surface at 300 K after roughening by Ar ion sputtering [134]. Oxygen vacancies act as nucleation centers and increase the number density of Au nanoparticles while reducing the mean particle size [135]. Compared to other metals like Pt, Ni, or Co, the nucleation and growth of Au on TiO_2 are characterized by forming relatively large, three-dimensional clusters with low cluster densities. Gold atoms exhibit high diffusion rates on stoichiometric and reduced TiO_2, leading to larger cluster sizes with preferential nucleation at step edges. This behavior is attributed to the weak Au-Ti binding energy, confirmed by density functional theory (DFT) calculations. If oxygen adatoms are present on TiO_2, the diffusion of gold decreases due to stronger bonding with surface oxygen, resulting in smaller clusters and a significantly higher cluster density compared to growth

on reduced TiO_2 [136].
For a metal particle with isotropic surface energy, a (hemi-)spherical shape is assumed, and the contact angle is given by the Young-Dupre relationship

$$\cos(\theta) = \frac{\gamma_o - \gamma_{mo}}{\gamma_m} \tag{2.4}$$

with $\theta, \gamma_o, \gamma_m, \gamma_{mo}$ being the contact angle, oxide surface energy, metal surface energy, and the metal-oxide interfacial energy [137]. For metal clusters with anisotropic surface energy, the nanoparticles form facets described by the Wulff construction [138,139], which is described in Sec. 2.1.2.
If the nanoparticles are facetted, the facet of the Wulff shape at the interface gives the angle between the particle and support. The nanoparticle is truncated by Δh given by

$$\frac{\Delta h}{h} = \frac{E_{\text{ad}}}{\gamma_m} \tag{2.5}$$

with the adhesion energy $E_{\text{ad}} = \gamma_o + \gamma_m - \gamma_{mo}$ [137].

Sintering

Annealing Au/TiO_2 under UHV to a temperature of 700-775 K leads to dewetting and island growth by Ostwald ripening [140]. This process is thermodynamically driven and possible due to the mobility of Au atoms and small clusters over the surface [141]. As larger particles are more stable and stay relatively localized on the TiO_2 surface, they accumulate material at the expense of the size and number of other particles that are smaller in relation to them. Overall, Ostwald ripening leads to larger nanoparticles [142–144]. During this process, no encapsulation by TiO_x was reported [144], which is observed for other metal nanoparticles as Pt [145]. Furthermore, exposure to $CO+O_2$ leads to the sintering of Au nanoparticles, especially of smaller particles [146, 147].

2.3.3 Catalytic Reaction on Au/TiO_2

Au on TiO_2 is the most studied gold model catalyst, experimentally and theoretically [148]. The properties of Au/TiO_2 are controllable by pretreatment of the substrate, e.g., via influencing surface structure and stoichiometry and via tuning the parameters of gold deposition, such as the amount of deposited material and temperature during or after deposition. Catalytic systems intended for industrial usage, i.e., Au/TiO_2 powder catalysts, are efficient for numerous catalytic reactions such as CO oxidation [104], aniline oxidation [149], benzylamine oxidation [150], and selective nitroaromatics hydrogenation [151]. The catalytic activity is influenced by various parameters, such as the total surface area, the number of surface atoms, defects, low-coordination atoms, the perimeter, the surface

structure and composition, nanoparticle-support interactions, quantum size effects, impurity atoms, and the charge of the nanoparticle [152].

Quantum size effects or a metal-to-insulator transition are observed for gold particle sizes below 3.5 nm in diameter and 1.0 nm in height, consisting of approximately 300 gold atoms [153]. One-atom-layer-thick 2D clusters showed a bandgap of 0.6-1.5 eV, whereas 3D clusters with three atomic layers have metal-like properties with no bandgap.

Electronic effects and low coordination sites result from the particle size. It influences the electronic structure and, therefore, the position of the d-band. Experiments of Au clusters on amorphous carbon showed that with decreasing size of Au clusters up to a critical diameter of 2.6 nm (or about 150 atoms), the d-band narrows and shifts closer to the Fermi level, resulting in more active nanoparticles. The d-band shifts away from the Fermi level for a further decrease in the nanoparticle size [154]. Low coordination sites are generally more reactive due to energetically higher-lying d-states. These states are more suitable for interaction with valence states of adsorbates [101, 115, 155, 156]. The increased catalytic activity of small Au particles might be due to the low-coordinated gold atoms in corner-like positions [115, 155].

Perimeter sites between the Au nanoparticles and the TiO_2 support are considered to be the catalytically active sites and the origin of the enhanced catalytic activity. Several studies determined that the adsorption of O_2 at the perimeter site on Au/TiO_2 is the crucial step of the CO oxidation [102, 125, 157, 158]. The support itself, the contact between Au and support, and the size of Au nanoparticles influence the activity and allow tuning the energy barriers for reaction intermediates to facilitate specific reaction pathways [120]. One group proposed dual-catalytic sites involving Au and Ti to activate oxygen [159].

Adsorption of Carbon Monoxide

CO on Au/TiO_2 is not only interesting as a reagent for the CO oxidation but is also used to probe the electronic structure of the gold nanoparticle. The signal position in the infrared spectra of adsorbed CO gives insight into the electronic structure [160] as the stretching frequency for CO on Au correlates with the electronic state of the Au nanoparticle and decreases with an increase in negative charge. The excess charge on the Au atom weakens the CO-Au bond [161]. Au-CO on reduced TiO_2 is only stable up to 150 K, but on oxidized TiO_2, Au-CO is stable above 350 K due to the stronger bond and less excess charge compared to the reduced surface.

Another factor in the bond strength is the size of the Au particles. Thermal desorption measurements on an $Au/TiO_2/Ru(0001)$ model catalyst showed that the activation energy of adsorption decreases from 65 kJ mol^{-1} for $\sim$2 nm particles to 51 kJ mol^{-1} for $\sim$4 nm particles [162], which is in agreement with other studies [163]. It is essential to highlight that the key factor is not the size but the thickness of the nanoparticles, as CO binds

more strongly to mono- or bilayer Au nanoislands than to multilayer particles. Multilayer particles exhibit a more Au bulk-like adsorption behavior [162]. The influence of the thickness thus extends to the catalytic activity in general [160].

Adsorption of Oxygen

The adsorption and activation of oxygen is a key step in the catalytic activity of gold clusters. O_2 does not adsorb molecularly or dissociatively on bulk gold, yet it is energetically possible on gold clusters. The exact mechanism is still under debate [157].
As for CO, 2D islands presumably bind atomic oxygen more strongly than thicker 3D particles [164], which is an assumed reason for the increased catalytic activity of small nanoparticles. Under an O_2 pressure of 1 mbar, Au nanoparticles on TiO_2 can be oxidized. While the binding energy of prepared nanoparticles in XPS spectra is close to bulk gold, under 1 bar O_2, an oxidized Au species was observed in the XP Au 4f core level spectrum 2.4 to 2.6 eV higher in binding energy than the bulk value. The oxidation was most efficient for 2 nm particles compared to 3.3 nm particles, in line with measurements on the catalytic activity. Under lower pressures of 0.1 mbar O_2, no oxidized Au was observed [165]. Important to note for XPS measurements is that O_2 exposure of Au/TiO_2 can induce reversible band bending, which results in shifts to lower binding energies of the lattice peaks in Ti 2p and O 1s core level. The peak shift depends on the O_2 partial pressure and is reversible [166].

Adsorption of Water

Water can influence the stability of gold clusters and can promote or inhibit certain reactions on the gold-support interface. Water may dissociate at vacancy sites on TiO_2, forming surface hydroxyl groups. Oxygen vacancy sites are also nucleation centers for gold atoms. As water occupies these vacancy sites, it promotes the agglomeration of gold due to fewer available nucleation centers [167]. Water has two roles during catalysis: the activation of O_2 and the decomposition of carbonate species [168]. It can serve as an oxygen source for the CO oxidation, which was confirmed by a study [169] using isotopic labeling. Isotopically labeled oxygen ^{18}O has two more neutrons than the commonly occurring ^{16}O and can be detected by mass spectroscopy. Under UHV conditions a Au/TiO_2 surface covered with $^{16}O_a$ adatoms was exposed to CO and $H_2^{18}O$ at 300 K and the formation of $C^{16}O^{16}O$ and $C^{16}O^{18}O$ was observed. The latter CO_2 species indicates that the oxygen in $H_2{}^{18}O$ activated the CO oxidation. With increasing water pressure, more $C^{16}O^{18}O$ was detected but the overall produced CO_2 decreased [169]. Another study [170] found that at 300 K, the CO oxidation to CO_2 increased with the water pressure up to 0.1 Torr but decreased at a water pressure of 0.5 Torr. At 400 K, water does not influence the CO_2

formation rate.

CO oxidation

For CO oxidation, the turnover frequency of gold supported on reducible oxides increases with a decrease in size up to a size of ∼2 nm, while it decreases with a further size reduction [146, 171].
Several mechanisms of CO oxidation on Au/TiO_2 are found for different temperature ranges and pressures [172]. The mechanism above 80 °C (350 K) is most likely the Mars-van-Krevelen mechanism [173], where the lattice oxygen at the perimeter site of the Au nanoparticle is the active oxygen species. CO at the perimeter site reacts with lattice oxygen to CO_2, leaving an oxygen vacancy behind. This vacancy is healed in the second step of the reaction by gas phase oxygen.
The low-temperature CO oxidation at 120 K was studied by Green *et al.* [159, 174, 175] with transmission IR spectroscopy. CO adsorption sites on Au and TiO_2 were identified by the CO stretching frequency. It was observed that only CO adsorbed on TiO_2 was oxidized to CO_2. By heating and recooling, CO was exclusively present on Au and showed no CO_2 formation when exposed to oxygen at 120 K. This indicates that CO oxidation occurs at dual catalytic sites at the perimeter of the Au/TiO_2 interface. For that to take effect, the first step is the adsorption of molecular oxygen at the perimeter site. DFT calculations found an O_2 bond in a di-σ configuration binding to five-fold coordinated surface Ti_{5c} and Au at the interface (Fig. 2.6B). This bond is stabilized by charge transfer from the Au atom to the Ti_{5c} site. CO adsorbed on TiO_2 diffuses to the perimeter site and forms a CO-O_2 intermediate (C), stabilized by interaction with the adjacent Au site. The O-O bond of the molecular oxygen weakens, and the intermediate CO_2-Ti and O-Ti are formed (D). The latter species is trapped due to a high diffusion barrier and reacts directly with another CO at the Au/TiO_2 perimeter site (E). The diffusion barrier of CO on TiO_2 is ∼0.3 eV and on Au 0.5-0.7 eV. At 120 K, CO on Au is kinetically trapped and does not diffuse toward the catalytic sites. At higher temperatures, CO on Au is more mobile and may diffuse to the reaction site. Simultaneously, the desorption rate of CO on TiO_2 also increases, which shifts the oxidation to CO-Au [159].

Towards Light-Induced Catalysis

The section above described the catalytic activity of small Au nanoparticles on TiO_2 independent of light. By moving to light-induced catalysis, the following mechanisms are essential to understanding the influence of light on the Au/TiO_2 system.
As a wide band-gap semiconductor, photocatalysis on TiO_2 is activated by photons in the UV region with an energy above 3 eV, exciting electrons from the valence band to the

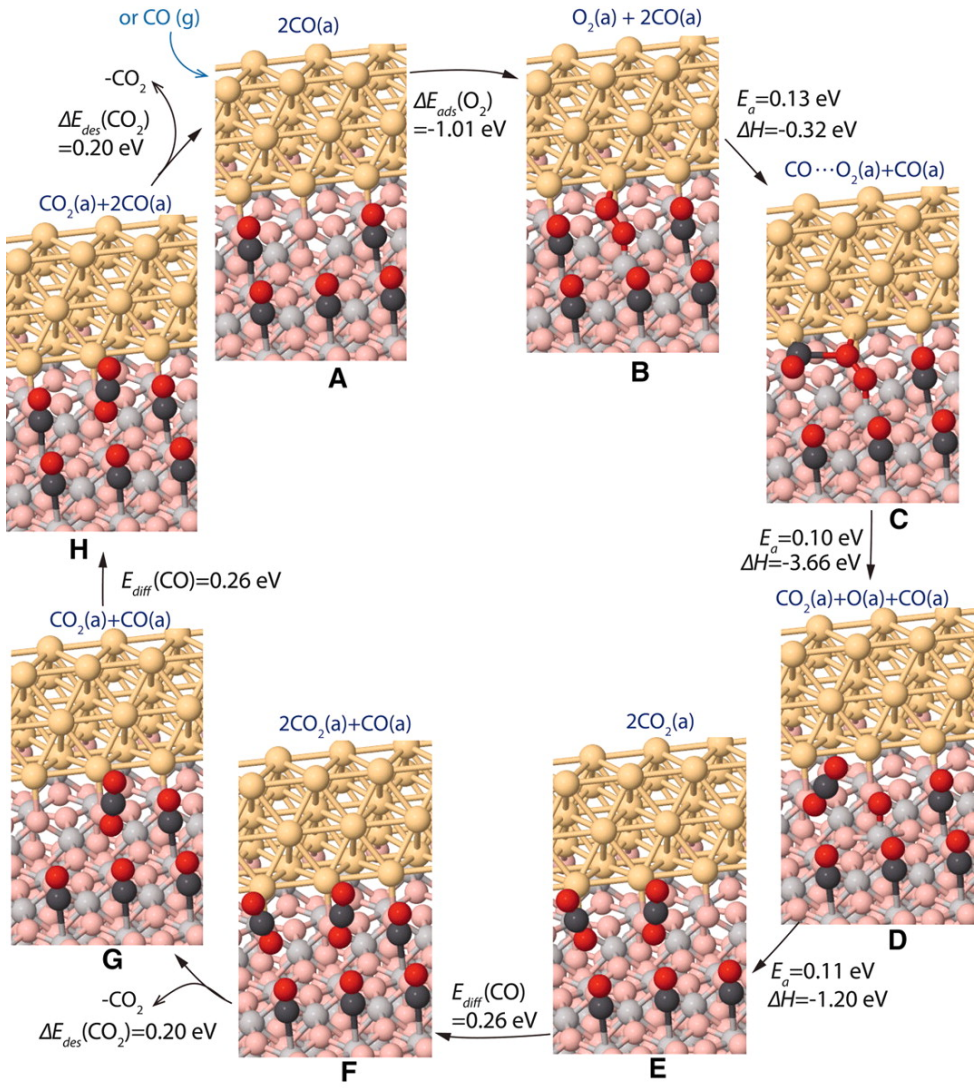

Figure 2.6: CO oxidation mechanism based on DFT calculations on Au/TiO_2. The Au atoms are depicted in yellow, Ti in grey, CO in black-red, and lattice O in pink. The illustrated steps are: adsorption of O_2 (A $\rightarrow$ B), interaction between O_2 and CO (B $\rightarrow$ C), reaction of O_2 with CO (C $\rightarrow$ D), reaction of adsorbed atomic oxygen with CO (D $\rightarrow$ E), diffusion of CO (E $\rightarrow$ F and G $\rightarrow$ H), and desorption of CO_2 (F $\rightarrow$ G and H $\rightarrow$ A). Image taken from [159].

conduction band. Only 3-5 % of the solar spectrum matches the minimal required energy. Hence, one aim is to modify TiO_2 for visible light absorption. Metal NPs are not only able to achieve visible light activity for the Au/TiO_2 system but also enhance the charge carrier separation for UV-induced catalysis. Charge separation reduces the recombination rate and, therefore, increases photocatalytic efficiency under UV light [28].
When the metal and semiconductor are connected, electrons are transferred from the semiconductor to the metal until the Fermi level of the metal and semiconductor align [176]. Due to the alignment, a surface space charge region forms. At the metal-semiconductor interface, the difference of work functions of the metal ϕ_M and semiconductor ϕ_{SC} lead

to an upward or downward-band bending to align the Fermi level of the metal and the semiconductor [87]. The degree of band bending compared to the bulk value is

$$V_{BB} = \phi_M - \phi_{SC}. \tag{2.6}$$

For an n-type semiconductor such as TiO_2 with $\phi_M > \phi_{SC}$, the Fermi level of the metal and the semiconductor align by a transfer of electrons from the semiconductor to the metal. The so-called Schottky-barrier

$$\phi_{SB} = \phi_M - \chi_{SC} \tag{2.7}$$

forms, with χ_{SC} being the electron affinity of the semiconductor. In the case of $\phi_M < \phi_{SC}$, the contact is ohmic and without a barrier [87]. The Schottky barrier height strongly depends on the atomic structure of the metal-semiconductor interface, the defect density, the history of the substrate, and the size of the metal nanoparticles. Measurement of the local barrier height (LBH) [177] gave insight into the dependence on defects and gold particle size. For Au nanoparticles with a particle height < 0.4 nm, the LBH of the Au nanoparticles was between -0.4 and 0 eV smaller than the substrate, which indicates that electrons might transfer from Au to TiO_2, resulting in a partially positive charge of Au. For Au particles with a height above 0.4 nm, the LBH of Au exceeds TiO_2 by 0 - 0.8 eV, indicating that larger Au particles accept negative charge from the TiO_2 substrate. This transition also falls into the metal-to-insulator transition mentioned in Section 2.3.3.
Under UV light, electrons are excited to the conduction band, and the Fermi level of TiO_2 rises. To achieve equilibrium of the Fermi level of Au and TiO_2, electrons flow from TiO_2 to Au and shift the Fermi level of Au up, re-equilibrating the Fermi levels [28]. The shift of the Fermi level after photoexcitation seems to depend on the size of Au nanoparticles. In a study of Subramanian *et al.* [68], the Fermi level shift of TiO_2 and Au/TiO_2 was probed with a C_{60}/C_{60}^- redox couple. Smaller 3 nm Au nanoparticles on TiO_2 induce a greater shift of -60 meV of the flat band potential than larger 8 nm particles with a -20 meV shift compared to the shift after photoexcitation for pure TiO_2. The negative shift indicates an enhanced charge separation and more efficient reducing properties related to the size difference. Charge separation decreases recombination and improves photocatalytic efficiency.

2.3.4 Localized Surface Plasmon Resonance

Gold improves UV-induced photocatalysis on TiO_2 and opens the possibility to visible light-induced photocatalysis based on surface plasmon resonance excitation. This phenomenon is based on the collective oscillations of the metal conduction electrons.

Metal nanoparticles can be modeled as a lattice of ionic cores and freely moving electrons, the Fermi sea [178]. An external oscillating electromagnetic field can induce coherent oscillations of the electron gas at defined frequencies, called plasmons. The energy of the plasmons is specific to the material and given by

$$E_\mathrm{p} = \hbar\sqrt{\frac{ne^2}{m_\mathrm{e}\epsilon_0}} = \hbar\omega_\mathrm{p}, \tag{2.8}$$

with the permittivity of free space ϵ_0, electron density n, electron charge e, the electron mass m_e and the plasma frquency ω_p [179]. At surfaces, plasmons occur as surface plasmon polaritons (SPP) and are coupled to surface plasmon modes as propagating or standing waves. If the particle is smaller than the incident wavelength, the surface plasmons are localized to the nanoparticle, resulting in a dipole over the whole particle. The field created by this dipole forces the electrons to return to the initial position. The oscillation amplitude maximizes at the localized surface plasmon resonance (LSPR) frequency. For metal nanoparticles, the LSPR is in the UV-Vis region [179].
For small nanoparticles (<10 nm) with $d << \lambda$, the quasi-static approximation applies, as the field inside the nanoparticle is constant and the particle resembles an electric dipole [179]. In the dipolar approximation, the extinction and scattering cross-section can be written as

$$\sigma_\mathrm{ext} = \frac{18\pi\epsilon_\mathrm{m}^{3/2}V}{\lambda} \cdot \frac{\epsilon_2}{(\epsilon_1 + 2\epsilon_\mathrm{m})^2 + \epsilon_2^2} \tag{2.9}$$

and

$$\sigma_\mathrm{sca} = \frac{32\pi^4\epsilon_\mathrm{m}^2V^2}{\lambda^4} \cdot \frac{(\epsilon_1 - \epsilon_\mathrm{m})^2 + \epsilon_2^2}{(\epsilon_1 + 2\epsilon_\mathrm{m})^2 + \epsilon_2^2} \tag{2.10}$$

with the particle volume V the dielectric function of the surrounding medium ϵ_m and the complex dielectric function of the metal $\epsilon_1 + i\epsilon_2$ [28]. The dielectric function defines the plasmonic properties. The extinction cross-section (Equ. 2.9) is maximized when the denominator is minimized under the so-called Fröhlich condition [28]:

$$\epsilon_1 = -2\epsilon_m. \tag{2.11}$$

The simplest model for the dielectric function is derived from the Drude or free electron model. In this model, electrons move freely as an electron gas around the ionic lattice, and the dielectric function ϵ depending on the frequency ω is

$$\epsilon(\omega) = 1 - \frac{\omega_\mathrm{p}^2}{\omega(\omega + i\gamma_\mathrm{b})}, \tag{2.12}$$

with the plasma frequency ω_p and the bulk damping constant γ_b [179]. Bulk damping describes the damping of moving electrons by scattering them with the ionic lattice. It

is inversely proportional to the mean free electron path l of the electrons with $\gamma_b = v_F/l$. Here, v_F is the Fermi velocity or the velocity of the conduction band electrons [28]. For the visible light region $\gamma_b << \omega_p$, the dielectric function simplifies to [179]

$$\epsilon_1 = 1 - \frac{\omega_p^2}{\omega^2} \tag{2.13}$$

For the resonance condition $\epsilon_1 = -2\epsilon_m$, the LSPR frequency is given by

$$\omega_{max} = \frac{\omega_p}{\sqrt{2\epsilon_m + 1}} \tag{2.14}$$

and depends on the dielectric function of the surrounding medium ϵ_m and the plasma frequency of the bulk material. This is only valid for small spherical nanoparticles with diameters below 10 nm [179]. The dipole approximation does not apply for larger particles, and the particle excitation becomes quadrupole or higher multipole in nature. For other shapes, such as rods, discs, or stars, multiple resonance frequencies for each axis of the particle are visible in the absorption spectrum.

The dependence of the LSPR wavelength on the surrounding medium can be observed in, e.g., Au nanoparticles on Al_2O_3 and TiO_2 [180]. Furthermore, the LSPR frequency also changes with the size of the nanoparticles, redshifting with increasing nanoparticle size. In Fig. 2.7, the Surface Differential Reflectivity Spectrum in the UV-Vis region shows the enhanced scattering due to the LSPR of gold nanoparticles on TiO_2 [180]. The effects of the medium and size can be seen in Fig. 2.8, where the plasmonic peak positions of Au/TiO_2 and Au/Al_2O_3 are plotted for different sizes of Au nanoparticles. With increasing size, the peak positions shift to larger wavelengths. This trend is observed for both supports. For the same size of Au nanoparticles, the LSPR on Al_2O_3 is 80 nm blue-shifted compared to TiO_2. The redshift increases with increasing metal nanoparticle size in the range of up to 10 nm [180].

The decay of LSPR excitation occurs through radiative damping, where plasmons re-emit photons, and non-radiative damping, which involves electron-hole excitations that can drive catalytic reactions [182].

Plasmon-mediated photocatalysis can be categorized into two primary mechanisms: direct and indirect photocatalysis [28]. In direct photocatalysis, the plasmonic metal nanoparticle is the light absorber and catalytic site. The energy generated from LSPR excitation directly interacts with adsorbed reactant molecules, promoting their activation and transformation. In indirect photocatalysis, the energy from LSPR excitation is transferred from the metal nanoparticle to an adjacent semiconductor. This process enhances charge separation within the semiconductor, leading to increased catalytic efficiency. Two examples with different proposed mechanisms on Au/TiO_2 are water splitting [183] for the former

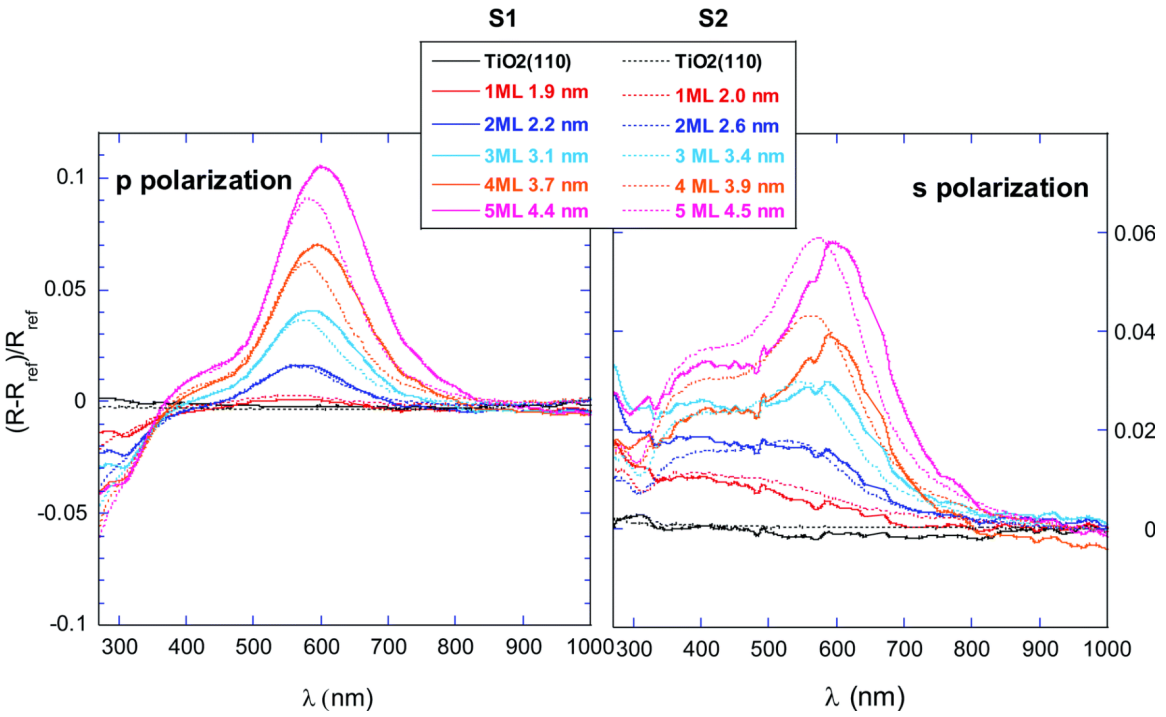

Figure 2.7: Surface Differential Reflectivity Spectroscopy of two Au/TiO_2 samples, S1 and S2, during gold deposition at room temperature. The legend gives the nominal thickness in ML and the diameter in nm. Image taken from [180].

and H_2 dissociation [184] for the latter mechanism.

The study by Liu *et al.* [183] demonstrated that incorporating plasmonic Au nanoparticles with TiO_2 significantly improves photocatalytic water splitting under visible light, increasing efficiency by 66-fold. In contrast, ultraviolet illumination reduces activity four-fold. Electromagnetic simulations suggest that enhancement stems from local electric field amplification near TiO_2, boosting electron-hole pair generation rather than direct charge transfer.

Mukherjee *et al.* [184] investigated the visible-light-driven dissociation of H_2 on gold nanoparticles on TiO_2 at room temperature. Au/TiO_2 catalysts were exposed to H_2 and D_2 gases and illuminated with a laser. The formation of HD molecules confirmed plasmon-induced dissociation. The proposed mechanism is the "hot electron" generation by LSPR excitation. The hot electrons transfer into the antibonding molecular orbitals of adsorbed H_2, creating a transient negative ion, destabilizing the H-H bond and triggering dissociation, which would otherwise be a thermally impossible reaction at room temperature.

Other proposed mechanisms responsible for the visible light activity are resonant energy transfer [185], where the relaxation of the localized surface plasmon dipole generates electron-hole pairs in the semiconductor, and light-to-heat conversion [186], where the LSPR-induced heating drives the reaction.

The photophysical mechanism is still under debate. In situ, time-resolved studies on

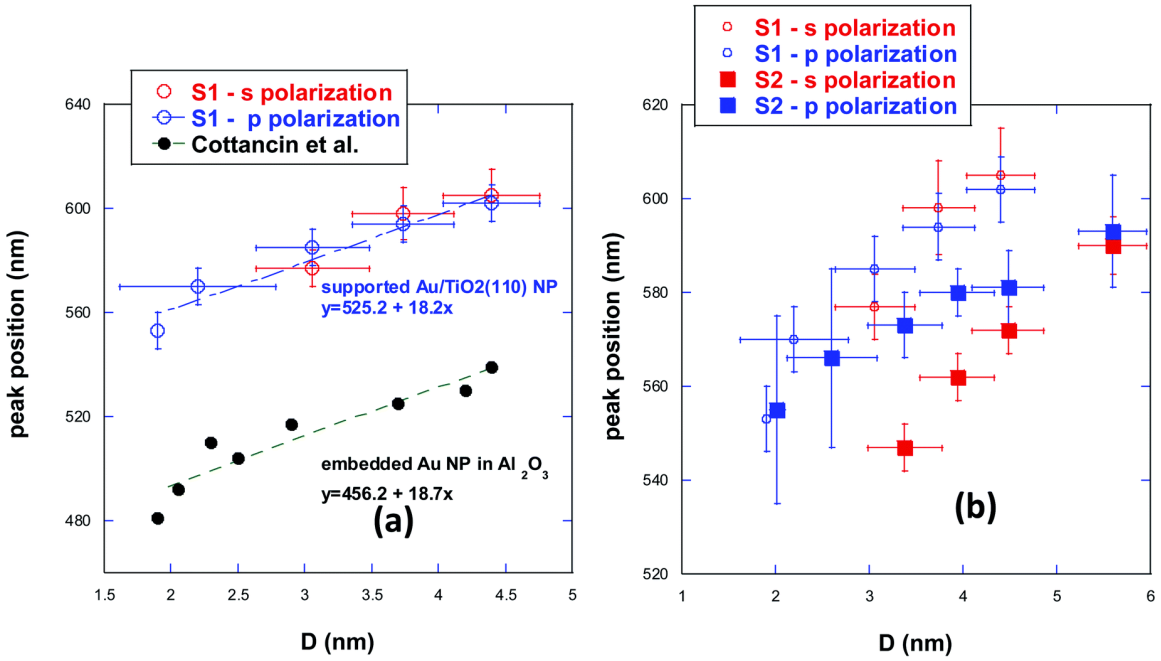

Figure 2.8: Plasmonic peak position for Au NPs on TiO_2 (110) NPs in s (red) and p (blue) polarization and for Au/Al_2O_3 (data from [181]). Image taken from [180].

model photocatalytic systems could clarify the mechanism at play.

For "real" Au/TiO_2 catalysts (e.g., powders or 3D mesoporous structures), gold nanoparticles increase light scattering and, therefore, increase the probability of photoexcitation of TiO_2. Although the exploitation of the localized surface plasmon resonance has been studied by different approaches that try to tailor Au/TiO_2 catalysts, studies of the LSPR-induced photocatalysis on model Au/TiO_2 catalysts are rare. The extensive research on small catalytic Au nanoparticles (∼3 nm) enabled a deep understanding of the underlying mechanism of those small nanoparticles. The results on the catalytic activity of the model and real Au/TiO_2 catalysts are in good agreement [28], so studies of the photocatalytic mechanisms of larger, plasmonic Au/TiO_2 are needed to gain a deeper understanding of the catalytic mechanism at play. Such investigations aim toward highly controlled femtosecond time-resolved studies at free-electron lasers. Hot electrons occur and dissipate on a time scale of femto- to picoseconds, which are measurable at pump-probe experiments at free-electron lasers. This thesis is a surface science approach to studying the influence of light on gold nanoparticles on model catalysts.

2.4 Platinum-Gold Nanoparticles on Titanium Dioxide

In the context of this thesis, the aim of overgrowing Au nanoparticles on TiO_2 with Pt was to increase the model catalyst's capability for CO adsorption compared to pure Au due to the higher binding affinity of Pt.

2.4.1 Growth of Pt on Au/TiO_2

The growth behavior of Pt on TiO_2 differs from Au in terms of diffusion and cluster formation, reflecting the stronger metal-titania interactions of Pt [136]. Platinum forms smaller clusters with higher densities than gold, as its diffusion rate on the TiO_2 surface is slower. While Pt clusters tend to form on both terraces and step edges, gold preferentially nucleates at step edges due to its higher mobility and the lower binding energy of Au to the TiO_2 surface than Pt. On oxidized TiO_2, the diffusion of Pt slows due to enhanced bonding with surface oxygen. This leads to higher densities of smaller clusters, mirroring trends observed for gold, yet to a lesser extent [136]. The growth of Pt-Au on TiO_2 for low coverages of 0.1 ML was studied by Park *et al.* [187]. When evaporated separately, pure Pt forms smaller clusters with higher cluster densities than pure Au under similar deposition conditions due to the greater mobility of Au on the TiO_2 surface. When Pt is deposited first, followed by Au, bimetallic clusters form, as Au nucleates at existing Pt clusters. The bimetallic Pt-Au clusters exhibit less sintering than pure Au, as the Pt-Pt and Au-Pt bonds ar stronger than Au-Au, resulting in smaller cluster sizes with increasing Pt fraction. Furthermore, annealing induces encapsulation by reduced titania, which is mitigated by the presence of Au at the cluster surface compared to pure Pt clusters [187]. For higher coverages of a few monolayers of Pt and Au, bimetallic Au-Pt clusters form regardless of the order of deposition [188]. Au stays at the cluster surface when Au is deposited on Pt. This is expected due to the lower surface free energy of Au, which drives its migration to the surface. Conversely, when Pt is deposited on Au clusters, a significant fraction of Pt remains on the surface, indicating limited atomic diffusion within the clusters at room temperature [188].

2.4.2 CO Adsorption and Oxidation on Pt

CO binds strongly to Pt on both terrace and defect sites, leading to poisoning under high CO concentrations and reducing its catalytic efficiency [189].
In TPD measurements, CO desorption from Pt surfaces exhibits characteristic peaks at different temperatures depending on the coordination environment of the adsorption sites. CO desorption from terrace sites is observed at approximately 400–420 K and from step and defect sites at around 500 K, implying a stronger binding of CO at undercoordinated Pt sites [190]. The CO adsorption behavior on Pt clusters deviates from single-crystal surfaces, since Pt clusters provide a higher proportion of low-coordinated sites, resulting in stronger bonds to CO and, thus, higher desorption temperatures. The desorption peak for CO on 0.25 ML Pt clusters appears at 500 K, attributed to step-like binding sites [190]. CO adsorption on Pt surfaces can also induce structural changes. CO on Pt(100) induces a change of the surface structure from the "hex" reconstruction to a (1×1) surface at 300-

340 K [191] and on Pt(110), a lifting of the (1×2) reconstruction to the unreconstructed (1×1) surface at room temperature [192].
The CO oxidation on Pt occurs via the Langmuir-Hinshelwood mechanism. Adsorbed CO and atomic O form CO_2, which directly desorbs [193]. Molecular oxygen O_2 dissociates at 140 K on Pt and the dissociation requires more than one surface site [194–196]. The CO oxidation rate depends on the mobility of CO, which diffuses on the surface to the less mobile O atoms [197]. A lower CO oxidation rate is found on Pt nanoparticles than on bulk Pt surfaces. Since nanoparticles have more step edges and defects, the CO-Pt bond is stronger, and the diffusion of CO is limited [198].

2.4.3 CO on Pt-Au/TiO_2

The CO adsorption and oxidation on Pt-Au/TiO_2 were studied by Tenney *et al.* [198]. Temperature-programmed desorption (TPD) measurements demonstrate that CO binds strongly to Pt sites, with desorption occurring at approximately 500 K. This temperature aligns with the desorption from undercoordinated Pt sites, such as steps or kinks, which are abundant on nanoscale clusters [190]. As Au content in the clusters increases, the amount of CO adsorbed at room temperature decreases, reflecting a reduction in available Pt sites on the surface. CO adsorbs on Au nanoparticles only below 175 K. For bimetallic Au-Pt nanoparticles, a mixed Pt-Au adsorption site for CO is observed, with CO desorption occurring at ∼230 K. CO adsorption can induce the diffusion of Pt to the cluster surface, even if the surface mainly consists of Au atoms. Based on DFT calculations, CO-induced Pt migration to the surface is thermodynamically favorable due to the CO-Pt bond strength. CO oxidation is facilitated only on clusters with exposed Pt surface sites, as O_2 dissociation, the first step in the reaction, requires neighboring Pt atoms. CO oxidation does not occur on clusters with Au-dominated surfaces because O_2 cannot dissociate on Au at RT. Although CO exposure leads to surface migration of Pt, it is unlikely for two neighboring Pt atoms to appear at the surface. Additionally, the adsorption energy of O_2 is lower than for CO, and O_2 adsorption might not trap Pt at the surface [198].
This thesis approaches Pt overgrowth to locate Pt at the surface of the Au nanoparticle for the CO oxidation, which is performed with preadsorbed CO under an O_2 atmosphere. The growth order of Au and Pt in this thesis is reversed (first Au, then Pt) compared to the above-mentioned study [198], where Au was deposited on top of Pt clusters to test the CO oxidation.

Chapter 3

Physical Principles of Surface Science Techniques

This chapter explains the relevant surface science techniques and underlying theory of each method. X-ray Photoelectron Spectroscopy (XPS) was used to study the CO (photo-) oxidation on rutile-TiO_2(110) in a time-resolved experiment at the FEL FLASH and on (Pt-)Au/TiO_2 with a lab-based source. All sample surfaces were characterized using Low Energy Electron Diffraction (LEED), Scanning Tunneling Microscopy (STM), and X-ray Reflectivity (XRR). Additionally, UV-Vis Surface Differential Reflectance Spectroscopy (SDRS) or Grazing Incidence X-ray Diffraction (GIXRD) was performed for specific investigations related to the localized surface plasmon resonance and growth orientation of Au nanoparticles, respectively.

3.1 Ultra High Vacuum

Ultrahigh vacuum conditions in the 10^{-10} mbar range are required for the sample preparation and most surface-sensitive techniques (XPS, LEED, and STM). In UHV, the average distance between collisions of two gas molecules/atoms is 12 orders of magnitude larger than under ambient pressure. The average distance between collisions for two molecules in the gas phase is given by the mean free path

$$\lambda = \frac{k_\mathrm{B}T}{\sqrt{2}\pi d^2 p} \tag{3.1}$$

with Boltzmann constant k_B, temperature T in kelvin, diameter of gas molecules d, and pressure p [199]. The mean free path for a nitrogen molecule at room temperature is approximately 600 km at UHV conditions of $1{\cdot}10^{-10}$ mbar, but 60 nm at ambient pressure of 1 bar.

When working with single-crystal surfaces, the rate of collisions between atoms/molecules

and a surface is important to determine when a surface will be covered by contaminants or dosed gases. The impinging rate $\dot{z}$ on a surface of 1 cm^2 per second depends on the partial pressure p, the molecular weight m, the average thermal velocity of atoms $\langle v \rangle$, Boltzmann constant k and temperature T via $p = 2m\langle v \rangle \dot{z} \simeq 6kT\dot{z}/\langle v \rangle$. At a pressure of 10^{-6} mbar, it takes one second for the necessary amount of N_2 molecules ($m = 28$) to hit the surface to form a monolayer [200]. On this basis, the unit Langmuir (L) is defined as one Langmuir equal to an exposure of $1 \cdot 10^{-6}$ Torr or $1.33 \cdot 10^{-8}$ mbar for one second. Assuming a sticking coefficient of 1, one L covers the surface with one monolayer.

3.2 X-ray Photoelectron Spectroscopy

X-ray Photoelectron Spectroscopy (XPS), also known as Electron Spectroscopy for Chemical Analysis, is a widely used, non-destructive method for surface characterization. Photoelectron spectroscopy is based on the photoelectric effect, which was first observed by Heinrich Hertz in 1887 [201] and subsequently elucidated by Albert Einstein in 1905 [202]. The photoelectric effect describes the emission of electrons from a material after exposure to photons with an energy greater than the binding energy of the electrons. For cases of elastic photoemission, where the photoelectron exits the material without scattering and therefore without losing energy, the binding energy E_B^F relative to the Fermi level E_F can be calculated using the kinetic energy E_{kin}, the work function ϕ and the photon energy $h\nu$ (with the Planck constant h and the wavelength ν) through the following equation

$$E_B^F = h\nu - E_{kin}^{SA} - \phi_{SA} = h\nu - E_{kin}^{SP} - \phi_{SP}. \tag{3.2}$$

The work function is the energy difference between the Fermi level E_F and the vacuum level E_{VL} [203]. The work function differs relative to the sample (SA) or the spectrometer (SP), as depicted in Fig. 3.1a.

3.2.1 The Photoelectron Spectrum

In the XP survey spectrum (Fig. 3.1c), not only photoelectron peaks of the elemental core levels but several other features such as Auger peaks, energy loss feature (satellites), and the background due to inelastically scattered electrons are visible. The binding energy of a photoelectron is specific to the atomic core level and its chemical surroundings, reflecting the electron structure. The background of the photoelectron peaks appears step-like, as inelastically scattered photoelectrons contribute to the background on the higher binding energy side of the peak [204].

The **intensity** of a specific photoelectron line depends on several factors: the cross-section σ for photoemission from the particular level of element A at photon energy $h\nu$, the

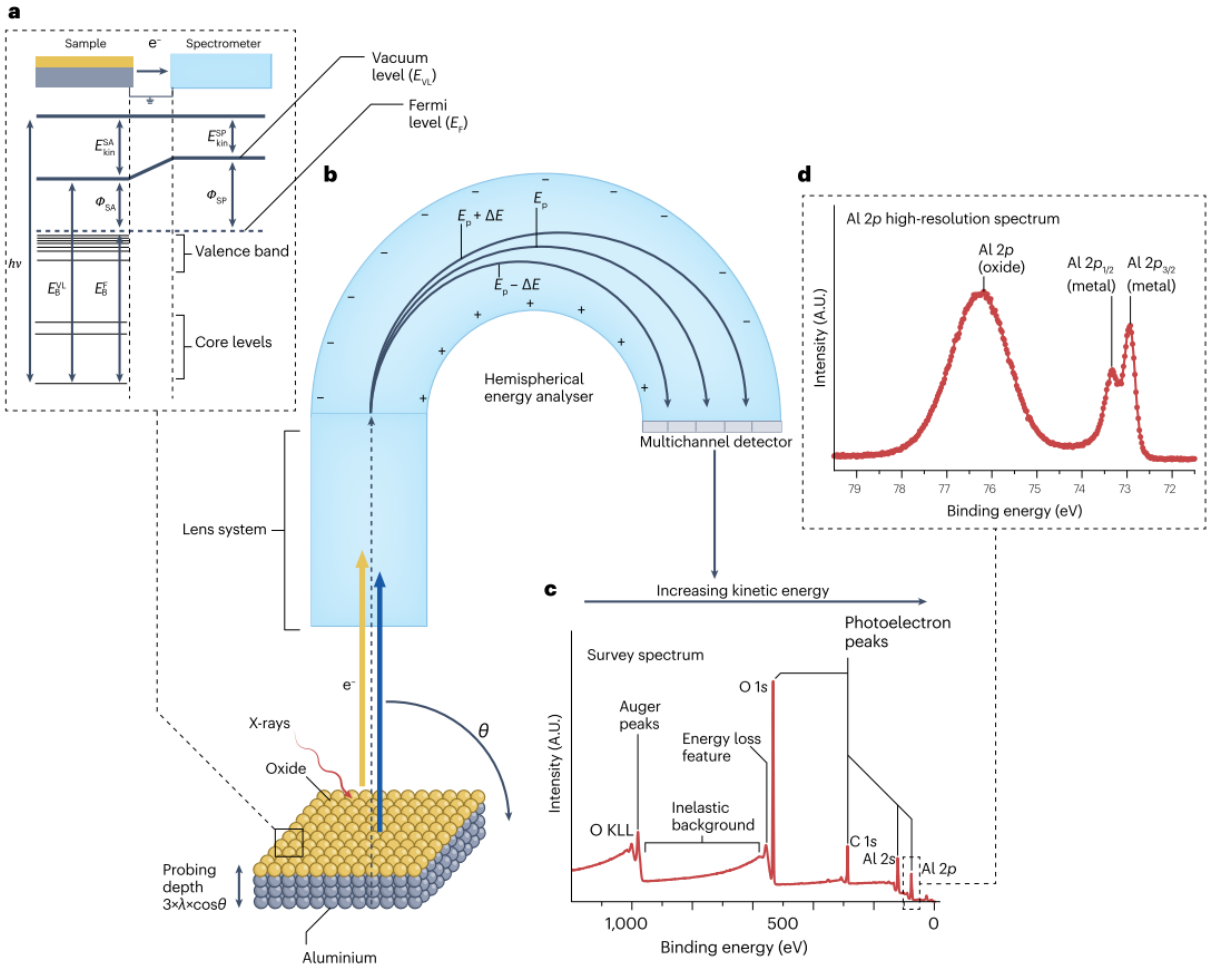

Figure 3.1: A general overview of XPS. a) Energy level diagram of the sample in electric contact with the spectrometer. b) XPS experimental set-up. c) Survey spectrum and d) detailed core-level spectrum. Image taken from [203]

constant X-ray flux J_0, the angular asymmetry parameter $L_A(\gamma)$ of the level A involved and the angle γ between the incident photons and the emitted photons, the spectrometer transfer function $Q(E_A)$, the number density of atoms N^0_A contributing to the line, the attenuation length $\lambda_A(E_A)$ of photoelectrons with kinetic energy E_A, and the angle θ between the emitted photoelectrons and the sample normal [205]. The intensity

$$I^0_A = N^0_A \, \sigma_A(h\nu) \, J_0 \, L_A(\gamma) \, Q(E_A) \, \lambda_A(E_A) \, \cos\theta = N^0_A \, S \tag{3.3}$$

can be simplified by using the atomic sensitivity factor S. The atomic fraction C of an atom j in the sample is determined by

$$C_j = \frac{I_j/S_j}{\sum_i I_i/S_i}. \tag{3.4}$$

The **Full Width Half Maximum** of a photoelectron peak depends on the natural line width of the energy level E_n, the natural width of the X-ray source E_p, and the instrumental resolution of the hemispherical analyzer E_inst [204]. The total FWHM amounts to

$$\Delta E = \sqrt{\Delta E_\mathrm{n}^2 + \Delta E_\mathrm{p}^2 + \Delta E_\mathrm{inst}^2}. \tag{3.5}$$

The natural line width E_n is expanded due to the lifetime τ of the core hole state, as described by the uncertainty principle

$$\Delta E_\mathrm{n} = \frac{\mathrm{h}}{\tau}. \tag{3.6}$$

The lifetime τ of a core hole is determined by competing decay processes such as fluorescence, Auger emission, and the Coster-Kronig process. Fluorescence occurs when a core hole is filled by an electron from a higher energy level, releasing excess energy as X-ray photons. The probability of fluorescence increases with increasing atomic number. In contrast, for Auger emission, the energy from filling a core hole is transferred to eject another electron from a higher shell [204].
The Coster-Kronig process is a rapid variant of Auger emission, occurring when energy from a core hole is transferred within subshells of the same principal quantum number. This transition occurs due to strong electronic wave function overlap, resulting in short core-hole lifetimes in the order of femtoseconds. These short lifetimes lead to spectral broadening, often spanning several electron volts, as dictated by the uncertainty principle [204].
Furthermore, the broadening of the photoelectron peak can also be influenced by alterations in the number of chemical bonds contributing to the peak, the order of the electronic environment, and factors such as X-ray damage or surface charging [206].

Spin-Orbit Splitting

The electronic levels of atoms are described using the notation nl_j, where n is the principal quantum number, representing the energy level of the electron ($n = 1, 2, 3, \ldots$). The orbital angular momentum quantum number l defines the shape of the electron orbital and is denoted as s, p, d, etc., corresponding to $l = 0, 1, 2, \ldots$. The total angular momentum quantum number j is determined by the vector sum of the orbital angular momentum (l) and the spin angular momentum (s), with $j = l + s$. Here, s represents the spin quantum number, which can take values of $+\frac{1}{2}$ or $-\frac{1}{2}$, indicating the two possible spin orientations of the electron [204].
For most levels, except for s-levels ($l = 0$), the spin angular momentum vector of an unpaired electron can align either parallel or antiparallel to the orbital angular momentum

vector. This alignment creates two distinct states, which are referred to as doublet states. These states have slightly different energies due to spin-orbit coupling, which results from the interaction between the electron spin and its orbital motion around the nucleus. Spin-orbit coupling splits the energy levels into two components, leading to two closely spaced lines in the photoelectron spectrum. The p-levels ($l = 1$) split into $p_{3/2}$ and $p_{1/2}$, d-level ($l = 2$) into $d_{5/2}$ and $d_{3/2}$ and f-levels ($l = 3$) into $f_{7/2}$ and $f_{5/2}$ with the relative peak ratios of 2:1, 3:2 and 4:3, respectively. The ratio results from the number of electrons that occupy each state, which is given by $2l + 1$. The energy difference between these lines depends on the strength of the spin-orbit interaction, which varies with the atomic number and the specific electronic configuration of the atom [204]. In Fig. 3.1d) the splitting of the metallic Al 2p into Al $2p_{3/2}$ and Al $2p_{1/2}$ is shown.

Chemical Shifts

The binding energy of an electron varies with the chemical environment. These chemical shifts in binding energy enable a more detailed analysis of a sample beyond just elemental composition. A higher positive charge on an atom causes a shift to higher binding energies, while a more negative charge results in a shift to lower binding energies. Similarly, neighboring atoms with higher electronegativity increase the positive charge on the initial atom, leading to a shift to higher binding energies, and the opposite effect occurs with less electronegative neighbors. Chemical shifts are typically small in the order of a few electron volts, so curve fitting is necessary for a precise chemical composition analysis [204].

3.2.2 Line Shapes and Curve Fitting

Data fitting is required to extract information about chemical states, atomic concentrations, and electronic environments from the XP Spectrum. The FWHM, the peak area, and the exact position are obtained by fitting. The quantitative analysis starts with an approximation of the background. The most used backgrounds are linear and Shirley backgrounds. The linear background is often chosen for fitting surface components with no contribution to the background scattering [203]. The Shirley background [207], developed by Shirley in 1972 for the valance spectrum of gold, works well for spectra where the inelastic scattering creates a drop in the background that decreases from high to low binding energies. After background adjustment, peaks can be fitted into the XP Spectrum. The mathematical representation of XPS peaks is primarily based on Lorentzian

$$l(x) = \frac{1}{1 + 4x^2} \tag{3.7}$$

and Gaussian

$$g(x) = \exp\bigl(-4\ln(2)x^2\bigr) \tag{3.8}$$

functions. The Lorentzian function reflects the natural line shape of photoemission and the X-ray, while the Gaussian function accounts for phonon broadening and scattering within the sample and the analyzer transmission function [203]. For simplicity, not the convolution of a Gaussian and a Lorentzian is used but the Gaussian-Lorentzian product (GL) pseudo-Voigt function:

$$\mathrm{GL}(x,m) = \left[\frac{1}{1+4\frac{m}{100}x^2}\right] \cdot \exp\left(-(1-\frac{m}{100})(4\ln 2)x^2,\right) \tag{3.9}$$

where m is the mixing parameter controlling the Gaussian and Lorentzian contributions [208]. GL(x,0) corresponds to a pure Gaussian.
The core level of metal often required an asymmetric peak shape for an accurate approximation by fitting. The generalized Lorentzian asymmetric (LA) peak shape introduces asymmetry into XPS peaks to better represent experimental data.

$$\mathrm{LA}(x;\alpha,\beta) = \begin{cases} [l(x)]^{\alpha}, & x \leq 0, \\ [l(x)]^{\beta}, & x > 0, \end{cases} \tag{3.10}$$

α and β control the asymmetry of the Lorentzian function $l(x)$ on the low- and high-energy sides of the peak, respectively. To model experimental peaks with asymmetry, the convolution of the LA function and a Gaussian function to produce a Voigt-like asymmetric shape is used:

$$\mathrm{LA}(x:\alpha,\beta,n) = N\int_{-\infty}^{\infty} \mathrm{LA}(\tau:\alpha,\beta)g(x-\tau:n)d\tau,$$

with the normalization factor N, and the full width at half maximum (FWHM) n of the Gaussian function [208].

Auger Peaks

Auger peaks arise from the process of filling core vacancies generated by photoemission. The energy of an Auger line is determined by the binding energy of the photoionized core level (A), the binding energy of the electron filling the vacancy (B), and the energy of the emitted Auger electron from the ionic state (C), which is given by the following equation:

$$E_{\mathrm{ABC}} = E_{\mathrm{A}} - E_{\mathrm{B}} - E_{\mathrm{C}} \tag{3.11}$$

Since the energy of an Auger electron is defined by the energy difference between the involved core levels and the filling electron's level, it is independent of the exciting photon energy. Auger lines always appear at the same kinetic energy but vary in binding energies

depending on the X-ray source energy. In contrast, core photoelectrons are characterized by their binding energy and exhibit different kinetic energies when the excitation energy changes. In Auger spectroscopy, the notation for core levels are the principal quantum numbers K, L, and M ($n = 1, 2, 3, \ldots$), with subshells indicated by indices, e.g., L_2 for $2p_{1/2}$ [204].

Satellites

In XPS, satellites are additional peaks near the main photoelectron peaks. Two processes that give rise to satellites are shake-up and shake-off. When the core electron leaves the atom, it can excite an additional electron from a higher shell to a higher discrete energy level (shake-up) or into the vacuum (shake-off). The outgoing photoelectron loses the kinetic energy required for the excitation of the other electron. The shake-up contributes an additional peak appearing on the higher binding energy side of the main photoelectron line, while the shake-off excitation contributes to the background of inelastically-scattered electrons [204].

3.2.3 Surface Sensitivity

The surface sensitivity of electron-based techniques such as XPS and LEED is determined by the inelastic mean free path (IMFP) λ of electrons in a material. It quantifies the average path length electrons move through a material before losing kinetic energy due to inelastic scattering and depends on the initial energy E of the electron. The intensity I of electrons escaping from a material follows an exponential attenuation described by the Lambert-Beer law

$$I = I_0 \exp\left(-\frac{d}{\lambda(E)\cos\theta}\right) \tag{3.12}$$

with the initial intensity I_0, the sampling depth d and the electron emission angle relative to the surface normal θ [203]. Only photoelectrons that retain their initial kinetic energy in XPS contribute to the core-level spectra. Inelastic scattered photoelectrons appear as a background signal at higher binding energies. For normal emission ($\theta = 0°$), approximately 63% of the detected signal originates from a depth $d = \lambda$, 86% from $d = 2\lambda$, and 95% from $d = 3\lambda$. As a result, the probing depth of XPS is typically defined as 3λ [203]. The IMPF λ is similar for most solids and mainly depends on the kinetic energy, and is referred to as a universal curve (Figure 3.2). Typical kinetic energies of photoelectrons using XPS are 500-1400 eV with Al Kα source and correspond to an inelastic mean free path of 1-3 nm. For LEED, electrons with energies of 50-150 eV are used, with an IMFP of less than 1 nm [209].

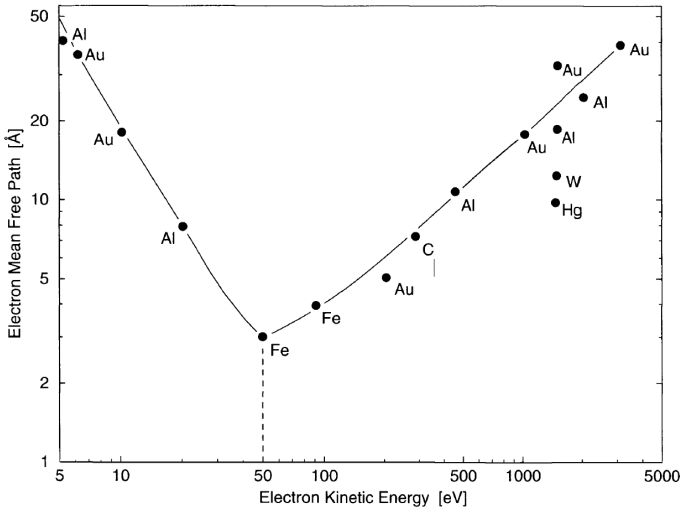

Figure 3.2: Universal curve of the inelastic mean free path taken from [210]. Originally from [211].

3.2.4 Lab-based X-ray Generation and Detection

Typical laboratory X-ray sources for XPS operate on the following principle: a metallic target (anode) is bombarded with high-energy electrons, creating a vacancy in the inner electron shells. Electrons from higher energy levels then fill the vacancy, emitting the excess energy as X-rays. For an aluminum target, the primary transitions involved in X-ray generation are from L_3 ($2p_{3/2}$) and L_2 ($2p_{1/2}$) to K (1s), referred to as Kα_1 and Kα_2, respectively. The transition from L_1 (2s) to K (1s) is forbidden by quantum selection rules [204].
Aluminum, commonly used as an anode in laboratory X-ray sources due to its narrow line width, produces X-rays with an energy of 1486.6 eV for Kα and a natural line width of approximately 0.85 eV. In addition to these main lines, other features, such as satellite lines, additional transitions, and Bremsstrahlung, contribute to the continuous background [204].

Monochromator

Monochromation of the X-ray source radiation is necessary to enhance the energy resolution of the XP spectrum and filter out Bremsstrahlung and other transitions such as Kβ radiation. The monochromator is usually a crystal made out of quartz (SiO_2) and only reflected wavelengths that fulfill Bragg's law ($n\lambda = 2d\sin\theta$) interfere constructively. By arranging the X-ray source and monochromator along a Rowland circle, X-rays focus at a specific point [204]. The energy resolution of Al Kα radiation can be narrowed from 0.85 eV to 0.167 eV after diffraction by $(10\bar{1}0)$ planes of quartz (SiO_2) monochromator with a Bragg angle θ of 77.5° [212].

Detection Principle

Hemispherical analyzers are the most commonly used detectors for measuring the kinetic energy of photoelectrons. The operation of the hemispherical analyzer is analogous to that of a spherical capacitor. A voltage is applied between two hemispherical electrodes, creating a radial electrostatic field. Electrons with a kinetic energy equal to the pass energy E_{P} entering this field are focused to a single point at the exit slit. Before entering the hemispherical analyzer, the photoelectrons are retarded to a selected pass energy E_{P} [204]. The path of an incoming electron with a kinetic energy of E_{P} is defined by the radius $R_0 = (R_{\mathrm{in}} + R_{\mathrm{out}})/2$. To focus the pass energy at the exit slit, a potential of

$$V_{\mathrm{out}} = \mathrm{e}E_{\mathrm{P}}\,(3 - 2\frac{R_0}{R_{\mathrm{out}}}) \tag{3.13}$$

has to be applied to the outer hemisphere, and a potential of

$$V_{\mathrm{in}} = \mathrm{e}E_{\mathrm{P}}\,(3 - 2\frac{R_0}{R_{\mathrm{in}}}) \tag{3.14}$$

to the inner hemisphere [210]. The potential difference is [204]

$$V_{\mathrm{out}} - V_{\mathrm{in}} = \mathrm{e}E_{\mathrm{P}}\,(\frac{R_{\mathrm{out}}}{R_{\mathrm{in}}} - \frac{R_{\mathrm{in}}}{R_{\mathrm{out}}}). \tag{3.15}$$

Photoelectrons entering with an angular spread α are focused by a distance of $2R_0\alpha$ closer to the center of the analyzer. The energy dispersion, given by $2R_0\Delta E/E_0$, can be fine-tuned by adjusting the slit width w. The overall relative energy resolution of the hemispherical analyzer is

$$\frac{\Delta E}{E_{\mathrm{P}}} = \frac{w + R_0\alpha^2}{2R_0}. \tag{3.16}$$

Electrons exiting the hemispherical analyzer with specific energies are amplified by a Chevron (v-shaped) multichannel plate (MCP) stack and then detected by delay line anodes [213].

3.3 Scanning Tunneling Microscopy

The scanning tunneling microscopy (STM) technique was introduced by Binnig and Rohrer [214] in 1981, earning them the Nobel Prize in Physics in 1986. In STM, a metallic tip scans the sample surface in a raster pattern, maintaining a distance of just a few nanometers. This distance is controlled by a feedback loop that adjusts to keep a steady tunneling current between the tip and the sample. Since there is no direct contact between the tip and the sample, measurements can be performed rapidly with minimal

disturbance to sensitive surfaces. However, this method is limited to conductive samples and necessitates ultra-high vacuum (UHV) conditions [215]. Standard measurements typically take several minutes to complete, covering areas ranging from several tens to hundreds of square nanometers. Under ideal conditions, atomic resolution can be obtained. STM is based on quantum tunneling, which occurs when electrons pass through a potential energy barrier that would be forbidden according to classical physics. A small bias voltage separating the Fermi levels of the sample and tip, ranging from 0.01 to 10 V, causes electrons to tunnel through the vacuum gap, creating a tunneling current extremely sensitive to changes in distance to the sample surface. The vacuum barrier is influenced by the sample's work function and the separation distance z between the tip and the sample [216]. In a 1D model, the influence of these parameters on the tunneling current I_T can be described for low temperatures and voltages by:

$$I_\mathrm{T} \propto \exp\left(-\frac{z\sqrt{2m_\mathrm{e}\phi}}{\hbar}\right), \tag{3.17}$$

with the electron mass m_e and the sample work function ϕ. This expression indicates that the tunneling current between the tip and the sample decreases exponentially with increasing tip-sample distance z and is a function of the local density of states of the sample at the Fermi energy level [217]. The measurement mechanism and alignment of energy levels between the sample and the tip are displayed in Fig. 3.3. In an STM setup, piezoelectric rods position the tip accurately along the x, y, and z axes. The z-direction controls the tip's vertical position, which is managed using a feedback loop. This feedback mechanism either maintains a constant tunneling current by adjusting the distance to the sample surface or holds the tip at a constant height while the tunneling current is varied. Meanwhile, the x and y directions are specifically used to adjust the tip's position on the sample plane and enable raster scanning. Artifacts in STM images often stem from

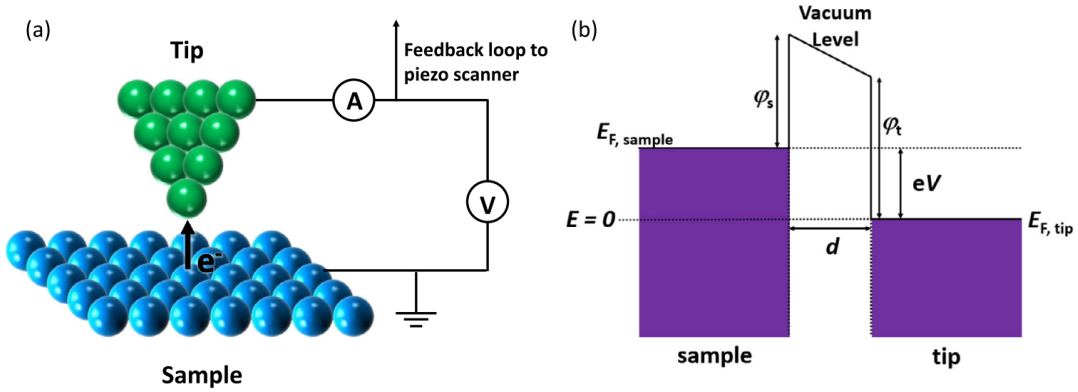

Figure 3.3: a) Schematic illustration of an STM setup b) energy level diagram of sample and tip during STM measurement. Image taken from [217].

the measurement process, such as tip shape, non-linear piezoelectric response, thermal drift, and external vibrations. To minimize these artifacts, STM systems are typically installed on stable platforms, and various measures are taken to isolate the measurement equipment from vibrations and temperature fluctuations [218].

3.4 X-Ray Reflectivity

With X-ray reflectivity (XRR) the thickness, density, and interface roughness of thin films and multilayer structures can be investigated. It relies on the specular reflection of X-rays. Light with the incident wave vector $\mathbf{k}_i$ under the incident angle α either reflected with a wave vector $\mathbf{k}_r$ under the angle α or transmitted with the wave vector $\mathbf{k}_t$ under the angle α' (Fig. 3.4). **Snell's law** relates the incident angle α to the refracted angle α' via

$$n_1 \cos\alpha = n_2 \cos\alpha' \tag{3.18}$$

with the refractive index n of the media [219]. In the case of X-rays, the refractive index n depends on the dispersion δ and absorption β, and is given by

$$n = 1 - \delta + i\beta = 1 - \frac{2\pi r_e \rho_\mathrm{e}}{k^2} + i\frac{\mu}{2k} \tag{3.19}$$

with the incident wave vector $k = 2\pi/\lambda$, the electron density ρ_e , the classical electron radius $r_e = e^2/(4\pi\eta_0 m_\mathrm{e} c^2) = 2.8179 \cdot 10^{-15}$ m, and the absorption coefficient μ. For X-rays, the diffractive index is smaller than unity. By setting $\alpha' = 0$, the critical angle for total external reflection α_c is simplified under small angles to:

$$\alpha_c = \sqrt{2\delta} = \lambda\sqrt{\frac{r_\mathrm{e}\rho_\mathrm{e}}{\pi}}. \tag{3.20}$$

The intensity of the reflected and transmitted wave is given by the absolute square of the coefficients r and t, which are described by the **Fresnel equations** [219]. Under small angles ($\alpha \ll 1$) and for elastic scattering ($|\mathbf{k}_i| = |\mathbf{k}_r| = |\mathbf{k}_t|/\mathrm{n}_2$) the Fresnel coefficients are

$$r = \frac{\alpha - \alpha'}{\alpha_i + \alpha'} \quad \text{and} \quad t = \frac{2\alpha}{\alpha + \alpha'}. \tag{3.21}$$

The **Parratt formalism** [220] extends the Fresnel equations to multilayer systems and gives an exact method to determine the intensity of light reflected from a multilayered system. For a system with N layers at each interface $(m-1, m)$ the incident wave $\mathbf{k}_{\mathrm{t,m-1}}$ is partially reflected ($\mathbf{k}_{\mathrm{r,m-1}}$) or transmitted to the next layer ($\mathbf{k}_{\mathrm{t,m}}$). The reflectivity at

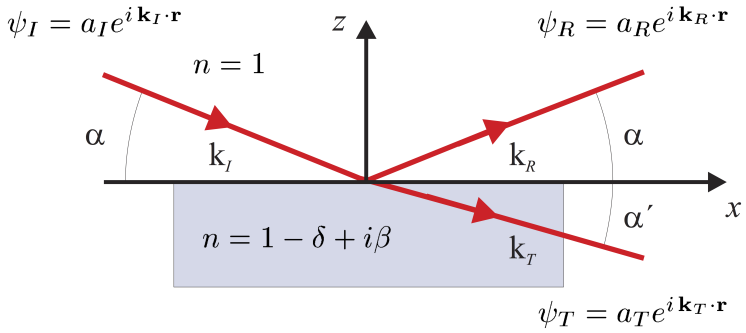

Figure 3.4: Reflection and transmission of X-rays at an interface. Taken from [219].

the interface after Parrat is

$$R_{\mathrm{m,m\text{-}1}} = \frac{r_{\mathrm{m\text{-}1,m}} + R_{\mathrm{m+1,m}} e^{-ik_{\mathrm{m}} d_{\mathrm{m}}/2}}{1 + r_{\mathrm{m\text{-}1,m}} R_{\mathrm{m+1,m}} e^{-ik_{\mathrm{m}} d_{\mathrm{m}}/2}}, \tag{3.22}$$

with the thickness d_{m} of layer m and the Fresnel coefficient

$$r_{\mathrm{m\text{-}1,m}} = \frac{k_{\perp,\mathrm{m\text{-}1}} - k_{\perp,\mathrm{m}}}{k_{\perp,\mathrm{m\text{-}1}} + k_{\perp,\mathrm{m}}} \tag{3.23}$$

with the wave vector normal to the surface $k_{\perp,\mathrm{m}} = k_{\mathrm{m}} \sin\alpha_{\mathrm{m}}$. The total reflectivity of the multilayered system is calculated recursively by applying the formula to each layer up to the substrate. The substrate is considered infinite in thickness with no multiple reflections. The reflected intensity of the surface is the interference of all reflected waves at the different interfaces. Due to the phase difference $e^{-ik_{\mathrm{m}} d_{\mathrm{m}}/2}$, constructive and destructive interference occur, resulting in oscillations, so-called Kiessig fringes, related to the layer thickness d_m with the difference of two maxima $\Delta\theta \approx \frac{\lambda}{2d_{\mathrm{m}}}$.
The vertical **roughness** of a layer is approximated by Gaussian-distributed height fluctuations

$$g(z) = \frac{1}{\sqrt{2\pi}\sigma_{\mathrm{m}}} \exp\left\{-\frac{1}{2}(z - d_{\mathrm{m}})^2 \sigma_{\mathrm{m}}^2\right\}, \tag{3.24}$$

with the standard deviation $\sigma_{\mathrm{m}} = \sqrt{\langle z^2 \rangle}$ as roughness [221]. The data was fitted using the software Fewlay based on the Parrat formalism [222].

3.5 Electron and X-ray Diffraction

3.5.1 Bragg's Law

Bragg's law describes the condition that must be fulfilled for constructive interference when electrons or photons are diffracted by a lattice:

$$2d \sin\theta = n\lambda, \tag{3.25}$$

where d is the interplanar spacing, θ the incident angle, λ the wavelength, and n the diffraction order. Constructive interference, and thus a detectable diffracted beam, occurs only when the path difference between rays scattered from adjacent lattice planes is an integer multiple of the wavelength, resulting in matching phases. If the condition is not fulfilled, the reflected photons or electrons interfere destructively.

3.5.2 Reciprocal Lattice

The signal detected by diffraction techniques corresponds to the reciprocal lattice. The reciprocal lattice is a mathematical construct describing the periodicity of a crystal lattice in reciprocal space. The 3D crystal lattice can be described in real space by

$$\mathbf{R}_n = n_1\mathbf{a}_1 + n_2\mathbf{a}_2 + n_3\mathbf{a}_3 \tag{3.26}$$

with the primitive lattice vectors $\mathbf{a}_1$, $\mathbf{a}_2$ and $\mathbf{a}_3$ and integers n. The reciprocal lattice vectors $\mathbf{a}_1^*, \mathbf{a}_2^*, \mathbf{a}_3^*$ are related to the real-space lattice vectors $\mathbf{a}_1, \mathbf{a}_2, \mathbf{a}_3$ by:

$$\mathbf{a}_1^* = \frac{2\pi}{V}(\mathbf{a}_2 \times \mathbf{a}_3), \quad \mathbf{a}_2^* = \frac{2\pi}{V}(\mathbf{a}_3 \times \mathbf{a}_1), \quad \mathbf{a}_3^* = \frac{2\pi}{V}(\mathbf{a}_1 \times \mathbf{a}_2) \tag{3.27}$$

with the unit cell volume $V = \mathbf{a}_1 \cdot (\mathbf{a}_2 \times \mathbf{a}_3)$ [219]. Any point of the reciprocal lattice is given by

$$\mathbf{G} = h\mathbf{a}_1^* + k\mathbf{a}_2^* + l\mathbf{a}_3^* \tag{3.28}$$

with the three integers (h, k, l), called Miller indices. Miller indices specify the planes in a crystal lattice and are orthogonal to the vector $\mathbf{G}_{hkl}$, as depicted in Fig. 3.5. The Miller indices (h, k, l) for a plane can also be determined by the intercept of the plane closest to the origin (a_1/h, a_2/k, a_3/l) on the axes $\mathbf{a}_1$, $\mathbf{a}_2$ and $\mathbf{a}_3$. If a plane is parallel to an axis, the intercept along that axis is considered infinite, and its reciprocal is zero. Negative intercepts are indicated with a bar over the corresponding index (e.g., $\bar{h}$). For gold with a cubic lattice with $a = b = c$, the interplanar distance is

$$d_{hkl} = \frac{a}{\sqrt{h^2 + k^2 + l^2}}. \tag{3.29}$$

Rutile has a tetragonal lattice with $a = b \neq c$, and the interplanar distance is

$$d_{hkl} = \frac{1}{\sqrt{\frac{h^2 + k^2}{a^2} + \frac{l^2}{c^2}}}. \tag{3.30}$$

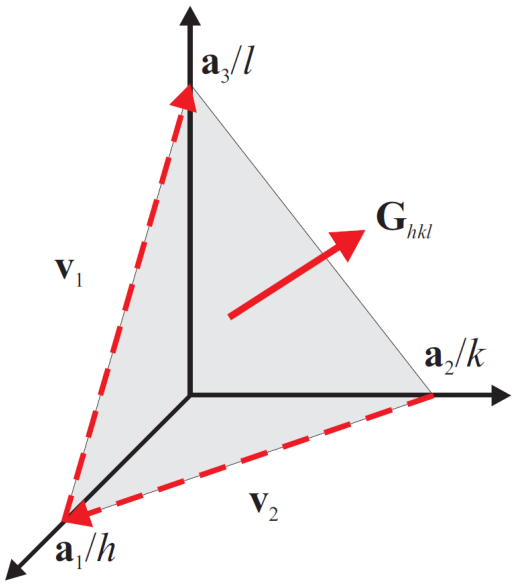

Figure 3.5: Visualization of the reciprocal lattice vector $\mathbf{G}_{hkl}$ with the Miller indices h, k, l. Image taken from [219].

3.5.3 Laue Condition and Ewald Sphere

The Ewald sphere is a useful construction for visualizing diffraction events. First the scattering vector $\mathbf{Q}$, that describes the momentum transfer during scattering, is

$$\mathbf{Q} = \mathbf{k} - \mathbf{k}' \tag{3.31}$$

with the incoming $\mathbf{k}$ and scattered $\mathbf{k}'$ wavevectors. When the Laue condition ($\mathbf{Q} = \mathbf{G}$), which is equivalent to the Bragg condition, is fulfilled, the scattering signal from a crystal lattice is observed [219]. The Ewald sphere can visualize this condition, as seen in Fig. 3.6. The incident wavevector $\mathbf{k}$ ends at the origin O and starts at A, which serves as the center of the Ewald sphere. A sphere (a circle in 2D) with the radius $|\mathbf{G}|$ is drawn from there. The Laue condition is fulfilled for any reciprocal lattice point on the circle/sphere, and a scattering signal can be measured in the direction of the scattering vector $\mathbf{k}'$.

3.5.4 Low Energy Electron Diffraction

Low-energy electron diffraction (LEED) is a technique used to map the periodic lattice structure of surfaces. In 1924, de Broglie proposed the wave-like nature of electrons [223],

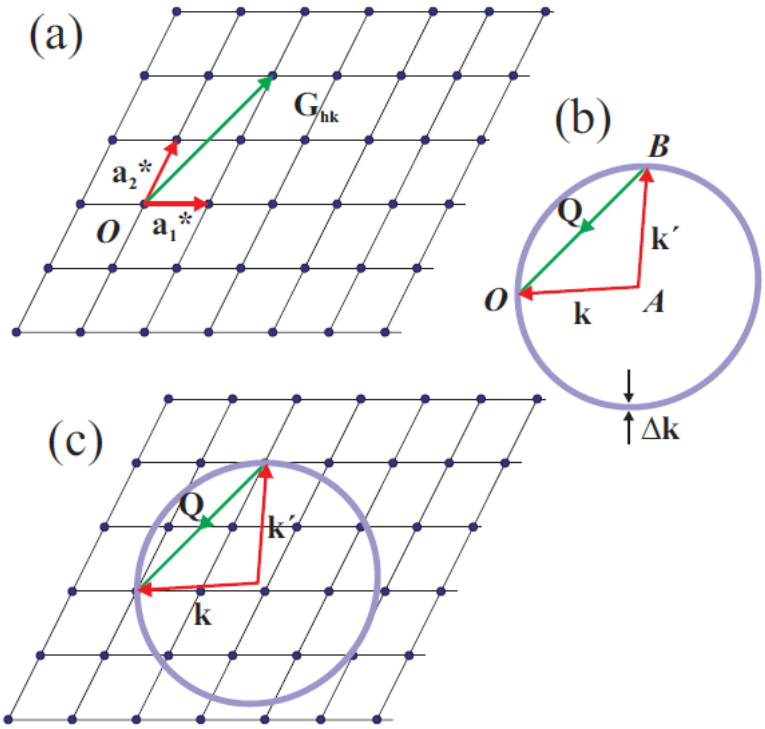

Figure 3.6: Construction of the Ewald sphere (circle in 2D) in reciprocal space. Taken from [219].

a concept later confirmed by Davisson and Germer through interference experiments conducted on a nickel single crystal [224]. The de Broglie wavelength of an electron is determined by its kinetic energy E_{kin}, the electron mass m_{e}, and the Planck constant h.

$$\lambda_{\mathrm{dB}} = \frac{h}{\sqrt{2m_{\mathrm{e}} \cdot E_{\mathrm{kin}}}} = \frac{h}{\sqrt{2m_{\mathrm{e}} \cdot \mathrm{e}U}}, \tag{3.32}$$

with the electron accelerated by the electric field U. Acceleration energies of 100 eV correspond to a wavelength of ∼1 Å, which is in the range of interatomic distances. In this energy range, electrons interact only with the first few atomic layers of a material due to their short escape depth or inelastic mean free path, as shown in Fig. 3.2. Therefore, the lattice is effectively treated as two-dimensional (2D). This reduces the 3D reciprocal lattice vector $\mathbf{G}_{\mathrm{hkl}}$ to $\mathbf{G}_{\mathrm{hk}}$. When Bragg's law ($2\,d \sin\theta = n\lambda$) is fulfilled, the constructive interference at specific angles results in a pattern of spots on the detector screen. Since the periodicity orthogonal to the surface is no longer given, the reciprocal lattice is constructed by lattice rods [218]. The diffraction pattern is defined by the size of the diffraction vector $\left|\vec{k_0}\right| = 2\pi/\lambda_{\mathrm{dB}}$, defining the size of the Ewald sphere, as visualized by Fig. 3.7.

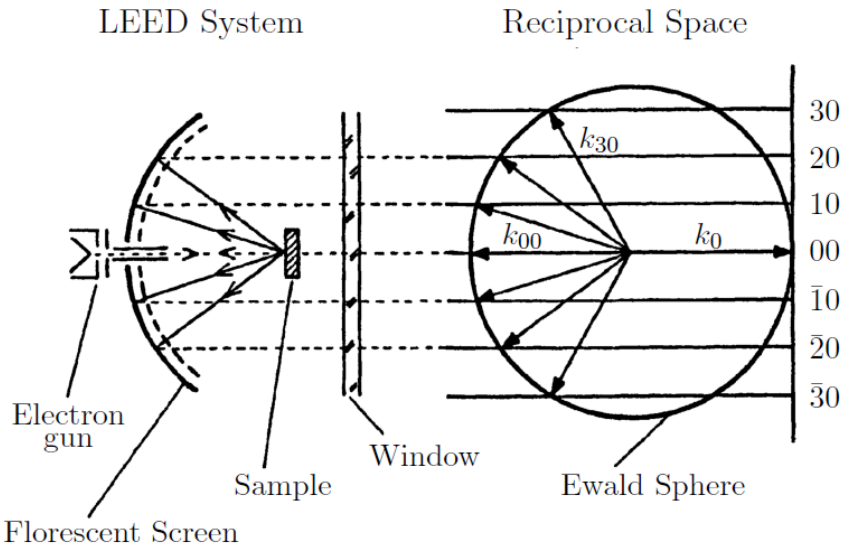

Figure 3.7: Scheme of a LEED setup [218].

3.5.5 X-Ray Diffraction

X-ray diffraction is based on scattering of X-rays by periodic atomic planes within a crystal [219]. Constructive interference is observed if Bragg's law is fulfilled. The momentum transfer during scattering is described by scattering vector

$$\mathbf{Q} = \mathbf{k}_f - \mathbf{k}_i \tag{3.33}$$

with the wavevector $\mathbf{k}$ if the incoming (i) and outgoing (f) photon. For elastic scattering, no energy is transferred ($|\mathbf{k}_\mathrm{i}|=|\mathbf{k}_\mathrm{f}|$). The magnitude of the scattering vector is

$$|\mathbf{Q}| = 2k \sin\theta = \frac{4\pi}{\lambda} \sin\theta. \tag{3.34}$$

and if Bragg's law is fulfilled (Eq. 3.25),

$$Q = \frac{2\pi}{d}. \tag{3.35}$$

XRD, especially GIXRD, is a sophisticated method to characterize the structural properties of nanoparticles, thin films, surfaces, and interfaces with high surface sensitivity. For the scope of the thesis, these basic principles are sufficient for the relevant discussions, with further details on the methods being available in [225].

3.6 Free-Electron Lasers for Studying Ultrafast Processes

Free-electron Lasers generate intense, tunable, coherent electromagnetic radiation pulses from microwaves to X-rays. The first free-electron laser (FEL) was designed by John Madey at Stanford University and started operation in 1976 [226]. The ultrashort pulses of FELS allow the study of ultrafast processes and reaction dynamics with various techniques, e.g., time-resolved XPS.

Operation principle of FELs

In FELs, first electrons are accelerated to near-light speeds using a superconducting linear accelerator (linac) or a synchrotron. At near light speed, electrons exhibit relativistic properties, significantly increasing their mass energy. The ratio between the total energy E and rest energy with the rest mass m_0 is given by the Lorentz factor

$$\gamma = \frac{E}{m_0 c^2}. \tag{3.36}$$

with the speed of light c [227]. The high-energy electron beam is directed through a wiggler or undulator, consisting of a series of alternating magnetic fields. The alternating magnetic fields cause the electrons to oscillate in a sinusoidal path. This oscillatory motion induces the emission of synchrotron radiation. The wavelength λ of the emitted radiation is given by:

$$\lambda = \frac{\lambda_u}{2\gamma^2}\left(1 + \frac{K^2}{2}\right) \tag{3.37}$$

In this formula λ_u is the undulator wavelength, and K the dimensionless undulator strength parameter, defined as

$$K = \frac{eB\lambda_u}{2\pi m_e c} \tag{3.38}$$

with the magnetic field B. The factor $1/2\gamma^2$ from Eq. 3.37 originates from two relativistic effects. The factor $1/\gamma$ is due to the relativistic Lorentz contraction, and $1/2\gamma$ due to the relativistic Doppler effect causing a blue shift of the radiation moving towards an observer [228]. The initially emitted photons are randomly distributed in phase and direction, and the light is incoherent. Some emitted photons interact with the electron beam, initiating the emission of further photons. This process is called self-amplified spontaneous emission (SASE). Due to the interaction, the electrons lose energy to emitted photons, which leads to modulation or microbunching of the electrons (Fig. 3.8). Electrons of one microbunch emit coherent radiation, which interferes constructively due to the matching phase, leading to an exponentially increased intensity of the radiation and also further

microbunching [229]. Microbunching causes the electrons to radiate coherently, so instead of the beam intensity scaling linearly with the number of electrons N_e, it is proportional to N_e^2 [227].
The electron bunch is dumped at the end of the undulator, and the coherent light is passed to the beamline. The spectrum of the FEL beam consists of the fundamental wavelength and odd higher harmonics with shorter wavelengths. [230]
The data in this work were taken at the FEL FLASH in Hamburg, which uses SASE to obtain wavelengths in the soft X-ray regime. FLASH operates with a 10 Hz macrobunch repetition rate, with each 400 pulses with a frequency of 1 MHz. In contrast to SASE, FELs can also be seeded by a laser tuned to the resonance of the FEL. The FEL FERMI at the Elettra-Sincrotrone in Trieste [231] operates a seed laser with a wavelength of 240-260 nm.

The short pulse length of a few hundred femtoseconds of FELs is ideal for time-resolved pump-probe experiments. An optical laser, which is synchronized with the FEL, can be used as a pump pulse to excite the sample into a state that is then probed by the FEL. The laser system at FLASH used in this work is the Burst-mode Optical Parametric Amplification (OPCPA) laser system and is described in [233]. The laser pulses are provided by a Ti:sapphire oscillator synchronized to the FEL.

Time-resolved Detection

For pulsed light sources, e.g., FELs, time-of-flight (TOF) spectrometers are employed to resolve the kinetic photoelectron energy for time-resolved photoelectron spectroscopy. In time-of-flight spectrometers, the kinetic energy is measured through the flight time t_{TOF} needed to pass the distance s through an electrostatic lens system to the detector and is given by the time between the trigger at time-zero t_0 and the measured time. The kinetic energy is

$$E_{\mathrm{kin}} = \frac{m v_e^2}{2} = \frac{m s^2}{2 t_{\mathrm{TOF}}^2} \tag{3.39}$$

with the electron velocity v_e [234]. Since electrons do not only eject perpendicular to the sample surface, this calculation is only valid for small acceptance angles. With complex back conversion algorithms, larger acceptance angles with a high kinetic energy resolution can be measured since the position of the electron arriving at a 2D detector differs depending on the ejection angle, which, on the other hand, influences the path through the lens system. The time-of-flight spectrometer was used at the FLASH beamline, and the back-conversion was provided by the beamline scientists [235].

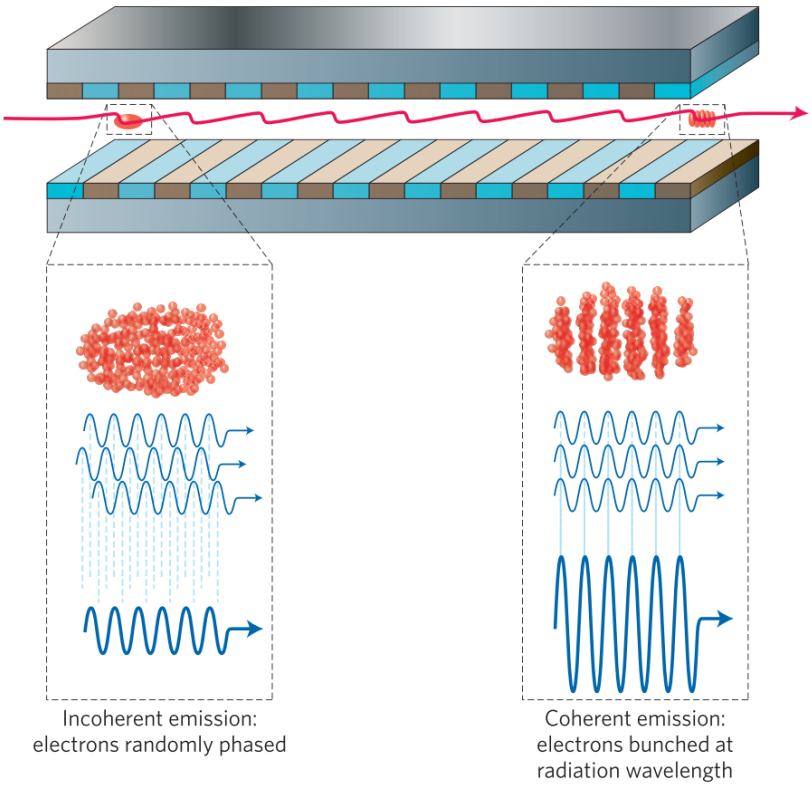

Figure 3.8: Process off microbunching of the electron beam in the undulator. Image taken from [232].

Chapter 4

Experimental Realization

This chapter describes the experimental setups used to obtain the data for this thesis. The ultrafast CO oxidation was studied at the free-electron laser FLASH [230]. The preparation, characterization, and CO oxidation on (Pt-)Au/TiO_2 was carried out in the DESY Nanolab [236].

4.1 DESY NanoLab

The DESY Nanolab has several ultra-high vacuum (UHV) chambers for X-ray Photoelectron Spectroscopy (XPS), Scanning Tunneling Microscopy (STM), Reflection-Absorption Infrared Spectroscopy (RAIRS), two preparation chambers with molecular beam epitaxy (MBE), and a zinc growth chamber. All UHV chambers are connected via a UHV tunnel system, in which samples can be introduced through a load lock chamber [236]. Within the tunnel system, the samples can be transferred on sample holders. The samples are mounted with tantalum clips on Mo sample plates.

Achieving Ultra High Vacuum

All experiments were performed under UHV conditions with a base pressure in the 10^{-10} mbar range. These conditions are achieved in stainless steel chambers equipped with different pumps. A pre-vacuum of up to 10^{-3} mbar is reached with membrane or rotary vane pumps. An ultra-high vacuum is reached with turbomolecular pumps. To maintain the ultra-high vacuum of 10^{-10} mbar, ion-getter-pumps, which continuously use a high-voltage electric field to ionize gas molecules, and titanium sublimation pumps, which trap molecules by reacting with the periodically sublimated titanium.

4.1.1 Sample Preparation Chambers (MBE)

The sample preparation chambers MBE I and MBE II (Fig. 4.1) are equipped with sputter guns, a heating stage, an oxygen cracker, and an ErLEED 150 LEED/Auger system. In MBE I, a triple electron beam evaporator (EFM 3T by FOCUS) equipped with a Pt rod is mounted. In MBE II, the gold evaporator (e-beam evaporator EFM 3 by FOCUS), used for this thesis, is mounted. Metals are evaporated in the UHV evaporator (EFM 3) via e-beam heating. The electron beam heats the crucible or rod, causing the evaporant to reach the evaporation temperature. At constant electron emission current (I_{EM}) and beam energy, the measured ion flux is directly proportional to the atomic flux. The heating power (high voltage) can be adjusted to maintain a constant evaporation rate [237]. The calibration is explained in the appendix in Section B.1.

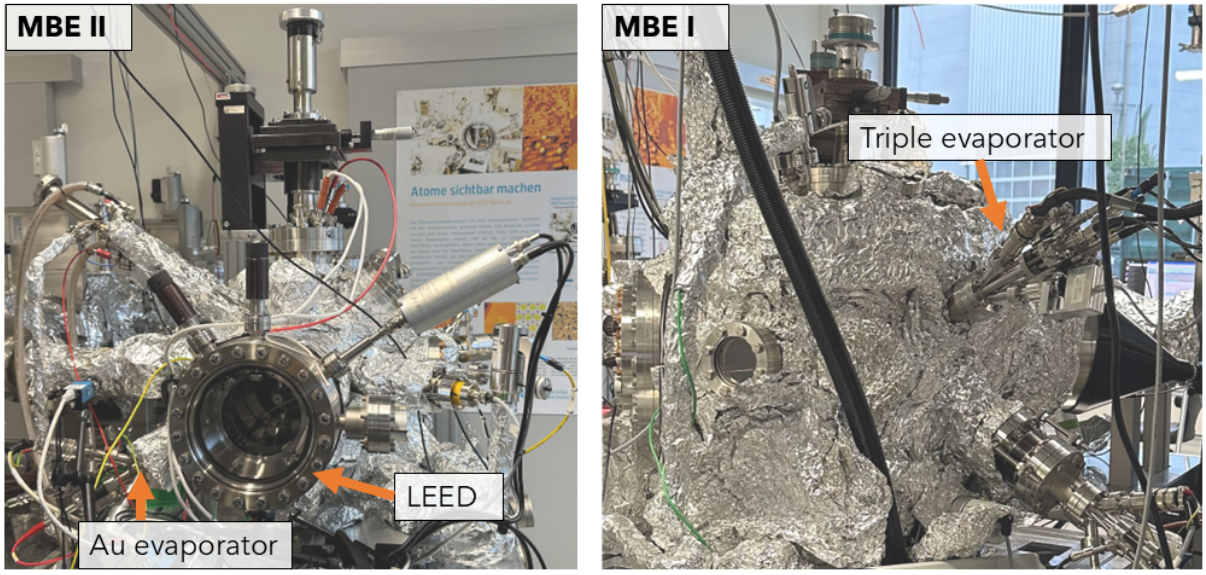

Figure 4.1: MBE II and I chamber from the DESY NanoLab used for Au and Pt evaporation.

4.1.2 XPS

The XPS setup from SPECS (Figure 4.2) includes the X-ray source XR50M, a UV source UVS 300, the monochromator Focus 500, the hemispherical energy analyzer Phiobos 100/150, and the delay line detector 3DDLD4040-150. The manipulator of the XPS chamber is equipped with a cryostat for liquid nitrogen cooling to 95 K and the e-beam heating station EBH 150 for heating up to 1000 °C. The chamber is additionally equipped with a sputter gun. Sample characterization and catalysis experiments were performed in this chamber with a base pressure of $5 \cdot 10^{-10}$ - $1 \cdot 10^{-9}$ mbar. All XPS spectra were fitted in CasaXPS [238].

4.1.3 STM

The Scanning Tunneling Microscope (Figure 4.2) is a UHV AFM XA system from Omicron and reaches a base pressure better than $5 \cdot 10^{-10}$ mbar. The chamber also has an e-beam heating station, a sputter gun, and leak valves. The system uses a decoupled baseplate and air-damped legs to reduce perturbing vibrations. An etched tungsten tip in a constant tunneling current mode was used for the measurements with a bias voltage of +1.5-1.7 eV. The images were measured with the software MATRIX and analyzed with Gwyddion [239].

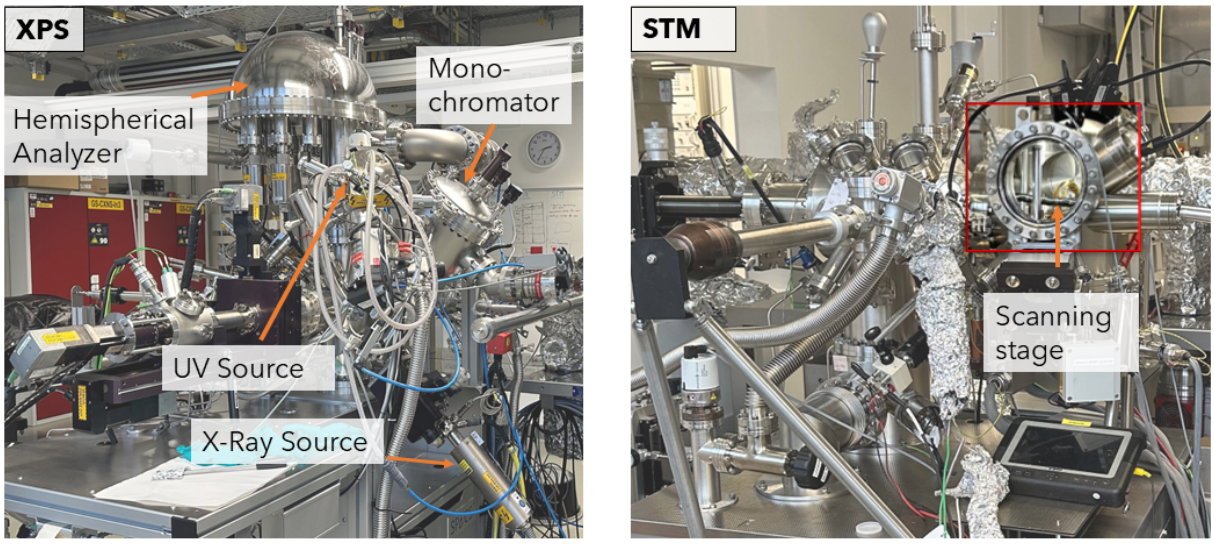

Figure 4.2: XPS and STM setup from the DESY NanoLab.

4.1.4 X-ray lab

The X-ray Reflectivity measurements were done at one of two diffractometer setups, each equipped with a Cu Kα X-ray source and either a 2D or point detector. The measurements were performed in air under an incident angle θ from 0-4°. The data were fitted in the software Fewlay [222].

4.1.5 Sample Preparation and Growth of Au Nanoparticles

To prepare the surface, the rutile TiO_2(110) single crystal was cleaned by repeated argon ion sputtering and annealing cycles in UHV. The samples are mounted on Mo sample plates with Ta clips, as depicted in Fig. 4.3, after washing the clips, sample plates, and substrate in ethanol and isopropanol using an ultrasonic bath. The preparation is illustrated in Fig. 4.4.

First, for degassing, the sample is slowly heated to the annealing temperature of 800-850 °C to minimize contamination of the UHV chamber. Then, argon ions are accelerated

with a sputter gun to the surface to remove residual contamination. As Ar sputtering roughens the surface, annealing is done to heal the surface from imperfections. As oxygen is more likely to be removed by sputtering than titanium, the resulting surface is reduced, with oxygen vacancies forming in the lattice. To obtain a stoichiometric rutile (110) surface, a partial pressure of $1 \cdot 10^{-6}$ mbar O_2 was chosen during the annealing step to 800-850 °C and during cooling down. Annealing in UHV leads to diffusion of Ti^{3+} into the bulk, which is visible by a blue coloring of the otherwise transparent crystal [240]. This was observed at the edges of the crystal, which were in contact with the Ta clips holding the substrate on the sample holder. The exact preparation parameters are listed in the appendix in Tab. B.1. The preparation was finished after a sharp 1x1 LEED pattern was obtained, which indicates a smooth, stoichiometric surface. The annealing temperature was monitored by a pyrometer measuring the temperature of the Mo sample plate next to the TiO_2 single crystal.

The nanoparticles were grown by MBE using an e-beam evaporator EFM 3 from Focus equipped with a Mo crucible filled with Gold from Goodfellow (99.999 % purity). The amount of Au for each sample can be estimated via a flux monitor and cross-referencing to a sample for which XRR layer thickness observations were carried out. Some samples were overgrown with Pt using the triple evaporator EFM 3T from Focus, equipped with a Pt rod. The techniques XPS and XRR were applied to determine the amount of gold. Using fitted XPS data, the fitted peak areas (A) of the core level spectra of O 1s, Ti 2p, and Au 4f (and Pt 4f) were compared. The relative sensitivity factor (RSF) normalizes the measured XPS signal. As described in Sec. 3.2, the Au amount is determined by

$$C_{\mathrm{Au}}(\%) = \frac{A_{\mathrm{Au4f}}/\mathrm{RSF}_{\mathrm{Au4f}}}{A_{\mathrm{Au4f}}/\mathrm{RSF}_{\mathrm{Au4f}} + A_{\mathrm{O1s}}/\mathrm{RSF}_{\mathrm{O1s}} + A_{\mathrm{Ti2p}}/\mathrm{RSF}_{\mathrm{Ti2p}}(+A_{\mathrm{Pt4f}}/\mathrm{RSF}_{\mathrm{Pt4f}})}. \quad (4.1)$$

For the adsoprtion studies, the Au(111) and Pt(111) single crsystals surfaces were cleaned by Ar^+ sputtering with a pressure of $1 \cdot 10^{-6}$ mbar Ar for 10-20 min. Au(111) was subsequently annealed to 800 °C for 20 min. Pt(111) was annealed to 700 °C in $5 \cdot 10^{-7}$ mbar O_2 for 20 min and then flash-annealed in UHV to 900 °C.

4.1.6 Low Temperature CO Oxidation

For experiments with liquid nitrogen cooling, the sample stage of the XPS was cooled to 95 K in 1 hour. To ensure a water-free sample surface, the sample was flash-annealed to 600 K and cooled to 95 K within 15 min. For the CO oxidation, CO is dosed via a leak valve. The amount of dosed CO is given in Langmuir (1 L = $1 \cdot 10^{-6}$ Torr or $1.33 \cdot 10^{-8}$ mbar for one second). First, 2-5 L CO was dosed, and the C 1s, O 1s, and Ti 2p core level scans were measured. Then, the samples were exposed to $1 \cdot 10^{-6}$ mbar molecular O_2 in steps of 10, 15, or 20 minutes under light (365 nm or 530 nm) or dark conditions. After each step,

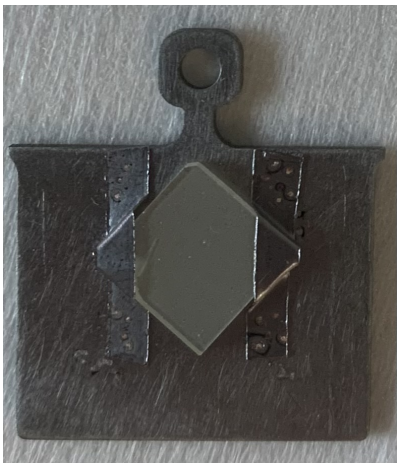

Figure 4.3: Rutile $TiO_2(110)$ single crystal mounted with Ta clips on a Mo sample holder.

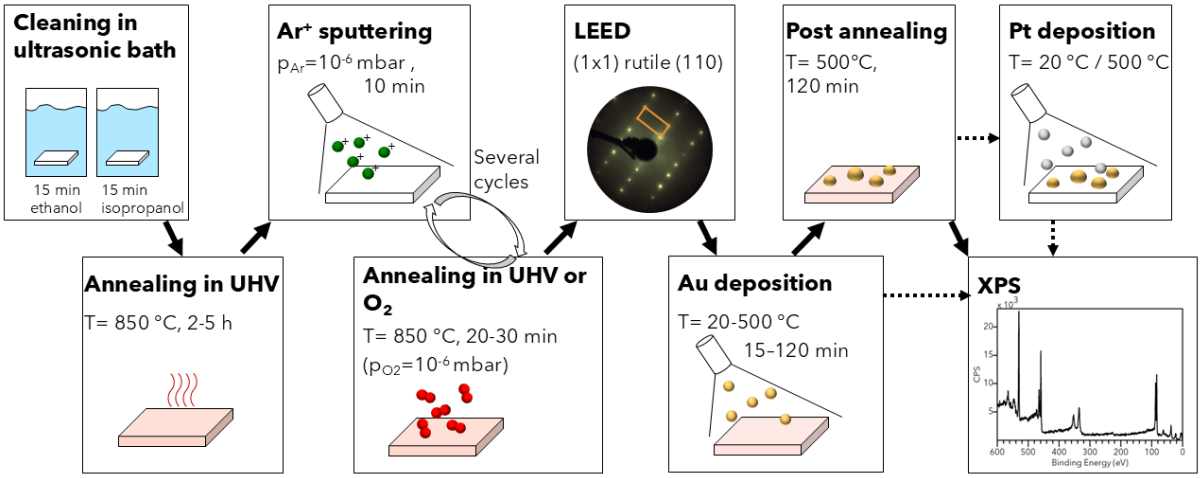

Figure 4.4: Preparation of the (Pt-)Au/$TiO_2(110)$ samples.

the scans of the C 1s, O 1s, and Ti 2p core levels were repeated to monitor the changes and production of CO_2 until no further changes were detected. Some samples were measured *in situ*, meaning that the XP spectra were taken under the oxidation condition. For UV light-induced catalysis, a Herolab UV-L lamp with a wavelength of 365 nm, and for visible light catalysis, a collimated LED from Thorlabs with a wavelength of 530 nm was used.

4.2 UV-Vis Surface Differential Reflectance Spectroscopy

The UV-Vis Spectroscopy setup is part of the sputter deposition chamber at the PETRA III beamline P03. The measurements were conducted in reflection under an incidence angle of 55°. The light source is a 75 W xenon lamp (LOT-Oriel, Germany) with a wavelength of 280 to 800 nm. The light was focused with lenses (Thorlabs) to a spot size on the sample of approximately 0.5×0.5 mm^2. The reflected light was recorded with a GlacierX spectrometer (B&W TEK). The spectra were taken with an acquisition time of 75 ms and averaged over 100 spectra. The relative change in reflectance ΔR_λ was

determined by

$$\Delta R_\lambda = \frac{R_{\mathrm{Au/TiO2}} - R_{\mathrm{TiO2}}}{R_{\mathrm{TiO2}}}, \tag{4.2}$$

with reflectance of the Au/TiO_2 samples $R_{\mathrm{Au/TiO2}}$ and the reference signal R_{TiO2} of the TiO_2 substrate.

4.3 Grazing Incidence X-Ray Diffraction at PETRA P07

At the beamline P07 [241], Au/TiO_2 samples were measured under grazing incidence with an angle of 0.03° and an energy of 73.7 keV. The detector is a 2D detector by Varex with 2880 x 2880 pixels and a pixel size of 150 x 150 µm. 2481 scans over a sample rotation of 126° with a speed of 0.1°/s were acquired.

4.4 FLASH Beamline PG2

This section is partially taken from the experimental section of the manuscript "Dynamics of the CO Photooxidation to CO_2 on Rutile (110)", which is part of this thesis and attached in chapter 5. The time-resolved photoemission data were taken at the plane grating monochromator beamline PG2 [242, 243] of the free-electron laser FLASH [230, 244] located at Deutsches Elektronen-Synchrotron (DESY) in Hamburg, Germany. The fundamental wavelength of FLASH was 5.79 nm (214 eV) with a pulse energy of 25-40 µJ. To probe the core level of oxygen O 1s, the monochromator was tuned to the third harmonic of 1.93 nm (643 eV). The FEL pulses were delivered with a macrobunch repetition rate of 10 Hz, with each macrobunch consisting of 400 bunches with a 1 MHz repetition rate. The temporal FWHM of each FEL pulse was <100 fs, though stretched in the monochromator to 150 fs. The optical pump laser with a wavelength of 770 nm (1.6 eV) matches the pulse pattern of the FEL. The maximum single pulse energy of the optical laser was 5-10 µJ with a spot size of approx. 300 µm under normal incidence. The fluence could be calculated to be 7-14 $mJ{\cdot}cm^{-2}$ under the measurement geometry of 55° sample tilt with respect to the incoming laser beam. To prevent CO desorption the laser fluence was attenuated to 2.2 mJ cm^{-2}. The temporal FWHM of the optical laser pulse was ∼120 fs. A mechanical delay stage set the temporal delay of the optical laser with respect to the FEL beam. The experimental setup used at the beamline was the wide-angle electron spectrometer (WESPE) [234] chamber (Fig. 4.5. WESPE consists of a sample preparation chamber with an ion gun, heating station, and low-energy electron diffraction (LEED). The main experimental chamber is equipped with a Themis 1000 high-resolution time-of-flight spectrometer with a three-dimensional delay line detec-

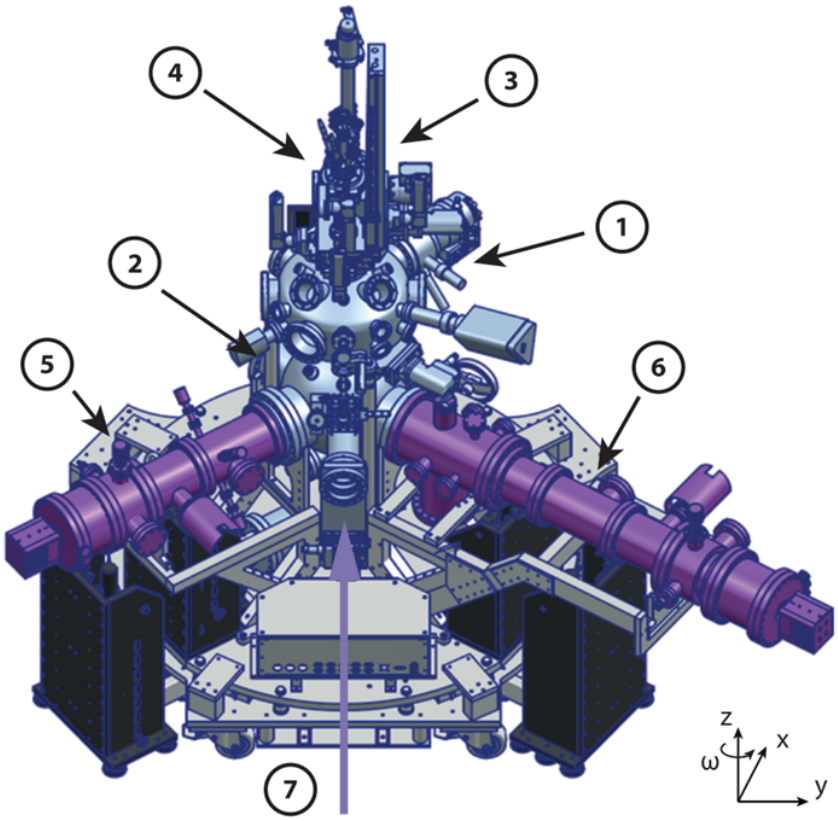

Figure 4.5: End-station WESPE used at FLASH PG2 with (1) Preparation chamber, (2) measurement chamber, (3) manipulator, (4) load lock, (5) Themis 1000, (6) Themis 1000 WAL, (7) beamline connection. Image taken from [234]

tor (3D-DLD4040-4Q, Surface Concept), beamline connection, and leak valves for dosing gases. The spectra were recorded with a pass energy of 20 eV. The used gases were Ar (purity 99.999%) for sample preparation and CO (purity 99.97%) and O_2 (purity 99.999%). The cryostat in the manipulator, which holds the sample under investigation, allowed cooling with liquid He. The rutile TiO_2(110) single crystal (7 mm x 7 mm x 1 mm) was cleaned under UHV conditions with a base pressure of $3 \cdot 10^{-10}$ mbar by repeated cycles of 1 keV Ar^+ ion sputtering and annealing to 650 °C and cooled in $1 \cdot 10^{-6}$ mbar O_2 until a (1×1) LEED pattern was obtained During the CO oxidation, the sample was cooled by liquid He to 80 K and was held in an atmosphere of CO and O_2 with partial pressures of both $3 \cdot 10^{-8}$ mbar. The incident pulses were scanned across the sample surface to avoid potential laser-induced damage.

Via an algorithm provided by the research team at the PG2 beamline [234], the data is reconstructed into data files containing information for each individually detected photoelectron. To obtain time-resolved data, first, for each run time zero, the value of the delay stage, for which the FEL and optical laser overlap, is determined. For the extrac-

tion of time-resolved spectra, time zero was always placed in the center of the binning window. The averaged photoelectron spectra for each complete run were calibrated on the O^{2-} lattice peak of TiO_2 to 530.4 eV [1]. Each lattice peak was fitted in MATLAB with a Gaussian function, and the difference to 530.4 eV was defined as energy offset E_{corr}. The binding energy was calculated by

$$E_{\mathrm{bin}} = E_{\mathrm{mono}} - E_{\mathrm{kin}} - E_{\mathrm{corr}} \tag{4.3}$$

The O 1s time-resolved photoelectron spectra were extracted in 200 fs windows and fitted in CasaXPS [238] with a GL(30), a Gaussian Lorentzian function with 30 % Lorentzian.

Determination of Time-Zero

When the FEL beam and the optical laser are spatially and temporally aligned, sidebands appear below and above the main peak in the photoelectron spectrum. These sidebands appear through laser-assisted photoemission and are replicas of the main peak shifted by the photon energy of the laser. The signal of the main lattice peak (± 0.4 eV) and of the first-order sidebands appearing 1.6 eV below and above the main peak are plotted versus the delay time. The signal of the lattice peaks and the sidebands can be fitted with a Gaussian function in the time domain by

$$f(x) = a \cdot \exp\left(-\frac{(x-b)^2}{c^2}\right) \tag{4.4}$$

with the

$$FWHM = 2\sqrt{\ln 2} \cdot c. \tag{4.5}$$

The center b of the Gaussian is time zero, and the FWHM describes the temporal resolution. The fits of the sidebands in the Ti 2p and O 1s spectra give a temporal resolution of 250 fs.

Chapter 5

Dynamics of the CO Photooxidation to CO_2 on Rutile (110)

This chapter is a manuscript that was submitted to Communications Chemistry in February 2025.

Abstract

Free-electron lasers (FELs) enable the study of the ultrafast dynamics of photocatalytic reactions by time-resolved X-ray photoelectron spectroscopy (tr-XPS) with femtosecond time resolution. In an optical pump-soft X-ray probe photoemission experiment conducted at the free-electron laser in Hamburg (FLASH), we observed the ultrafast oxidation of CO to CO_2 on rutile TiO_2(110) in the O 1s core level region. Within 800± 250 fs after laser excitation, CO_2 as a product of the photooxidation of CO is detected. Based on density functional theory calculations, we propose that the oxygen activation pathway for the CO oxidation is initiated via an O_2-TiO_2 charge transfer complex directly excited by the 770 nm pump laser. Residual water in ultra-high vacuum occupies adsorption sites for CO and inhibits further CO_2 formation.

5.1 Introduction to Reaction Dynamics on TiO_2

Photocatalysts are promising materials to harvest solar energy [245] or purify polluted air and water [3]. Recent pandemics showcased the significance of the antibacterial and antiviral properties of photocatalytic surfaces [246, 247]. One promising material is TiO_2, a widely applied photocatalyst with strong oxidizing properties. TiO_2 is low-cost, non-toxic [248], chemically and biologically stable, and shows antiviral and antibacterial properties [4, 5, 15]. The interest in TiO_2 as a photocatalyst increased in 1972 when Fujishima

and Honda used a TiO_2 semiconductor photoanode for water splitting under UV light [6], and since then, this oxide was considered a component for solar cells [245]. Today, the photocatalytic properties of TiO_2 were studied for a range of reactions, such as water splitting [249] for hydrogen generation [55], and were tested in field studies for the degradation of pollutants in air and water [5, 15], e.g., as an additive for concrete [17]. Rutile is the most stable polymorph of TiO_2 and is a widely studied model system for science on metal oxide surfaces [1]. Therefore, research on rutile contributes to a deeper understanding of the nature of photocatalysts.

One well-studied heterogeneous catalytic model reaction is CO oxidation due to its simplicity and its character as a benchmark system [31]. CO oxidation has a single product, CO_2.CO photooxidation on rutile and anatase TiO_2 was studied using Infrared Reflection Absorption Spectroscopy (IRRAS) as well as X-ray Photoelectron Spectroscopy (XPS) [83–85]. As expected from studies on powdered samples [70], stoichiometric anatase (101) is the most photocatalytically active surface under UV-illumination, exhibiting faster reaction kinetics compared to reduced anatase (101) as well as reduced and stoichiometric rutile (110) in converting CO to CO_2. CO oxidation on both TiO_2 polymorphs was only observed in an O_2 atmosphere under concurrent UV illumination.

The UV-illumination initiates a photocatalytic reaction, as an electron-hole pair is generated in the conduction and valence band [58]. Gas-phase O_2 dissociates by trapping the generated electron, resulting in adsorbed oxygen. The chemisorbed oxygen ion reacts with adsorbed CO to form CO_2 [83]. The adsorption of oxygen is necessary for the reaction, as studies show that lattice oxygen is not an oxygen source for this photoreaction [86]. The adsorption and photoactivation of oxygen is the crucial step, initiating the CO oxidation as an electron-mediated reaction, and thus competing with charge carrier recombination [87]. The efficiency of this process directly impacts the efficiency of the catalyst. A longer lifetime of charge carriers increases the probability of interacting with a gas-phase oxygen molecule. Different studies [84, 88] found a shorter lifetime of charge carriers in rutile compared to anatase. The reason is that anatase has an indirect band gap that inhibits electron-hole pair recombination and therefore enables a higher percentage of generated charge carriers to initiate this reaction pathway. The direct band gap of rutile results in a shorter lifetime of charge carriers, thus lowering the catalytic efficiency [84].

The studies on the lifetimes of charge carriers focus on the bulk properties of the materials, leaving a knowledge gap of catalytic reactions that occur at the surface. The general observation of longer lifetimes of electron-hole pairs in anatase is in alignment with the higher photocatalytic efficiency. Still, it ignores the influence of adsorbates on the catalytic surface under reaction conditions. In addition, the lifetimes of surface charge carriers may differ from bulk charge carriers and are influenced by band bending, defects, surface traps, and adsorbates [250]. It is therefore important to study the reaction

dynamics in a catalytic environment to elucidate the reaction mechanism [87].

The ultrafast real-time dynamics during the CO oxidation on anatase TiO_2 was previously studied by Wagstaffe *et al.* [34] in a pump-probe experiment at FLASH. On anatase (101) CO photooxidation to CO_2 induced by a 770 nm laser was observed with a delayed onset between 1.2 and 2.8 ($\pm$0.2) ps after illumination. Based on Density Functional Theory (DFT) calculations, an O_2-TiO_2 charge transfer (CT) complex was proposed, that enabled a direct charge transfer from the anatase-TiO_2 valence band to the O_2 molecular states in the bandgap. It was proposed that the directly excited adsorbed oxygen dissociates and provides the oxygen adatoms for the CO oxidation. This indicated that charge transfer can occur on a faster timescale than previously reported [251, 252]. In liquid media, such as water and methanol, charge transfer of surface trapped electrons to molecular oxygen was observed within 100 ns by transient absorption spectroscopy [251]. Similarly, electron transfer from TiO_2 to gas-phase oxygen was reported to occur within 10-100 µs and in water vapor within 2 µs [252].

Here, we present an ultrafast optical pump-X-ray probe photoemission study on the dynamics of CO photooxidation on rutile (110) at the FEL FLASH at the Deutsches Elektronen-Synchrotron (DESY) in Hamburg. Free-electron Lasers with pulses in the femtosecond timescale allow the study of ultrafast surface dynamics and possible reaction intermediates that are observable on picosecond timescales [253, 254]. Using superconducting RF accelerator technology, FLASH provides high-repetition rate photon pulses to observe chemical dynamics with sub-picosecond temporal resolution [230, 244]. The dynamics of the photoinduced CO oxidation to CO_2 was monitored on rutile (110) with a temporal resolution of 250 fs. The formation of CO_2 is observed within 200 to 800 fs after illumination with an optical laser with a wavelength of 770 nm. Time-Dependent Density Functional Tight-Binding (TD-DFTB) calculations, *performed by a collaborating group from the Bremen Center for Computational Materials Science* showed the formation of an O_2-TiO_2 charge transfer complex as a possible pathway for ultrafast oxygen activation.

5.2 Results of CO Oxidation Dynamics on Rutile

In this experiment, we studied the ultrafast dynamics of the CO oxidation to CO_2 on rutile (110) in a controlled gas atmosphere of CO and O_2 each with a partial pressure of $3 \cdot 10^{-8}$ mbar at a sample temperature of 80 K. An optical pump laser (770 nm/1.6 eV) and the third harmonic of the FEL (hv = 643 eV) as a probe beam were spatially and temporally overlapped. The relative timing between the pump and probe pulses was controlled by a mechanical delay stage as part of the optical laser setup. The rutile TiO_2(110) sample surface was prepared as described in the experimental section. With the FEL, the O 1s, Ti 2p, and C 1s core levels were probed. As a prerequisite for the

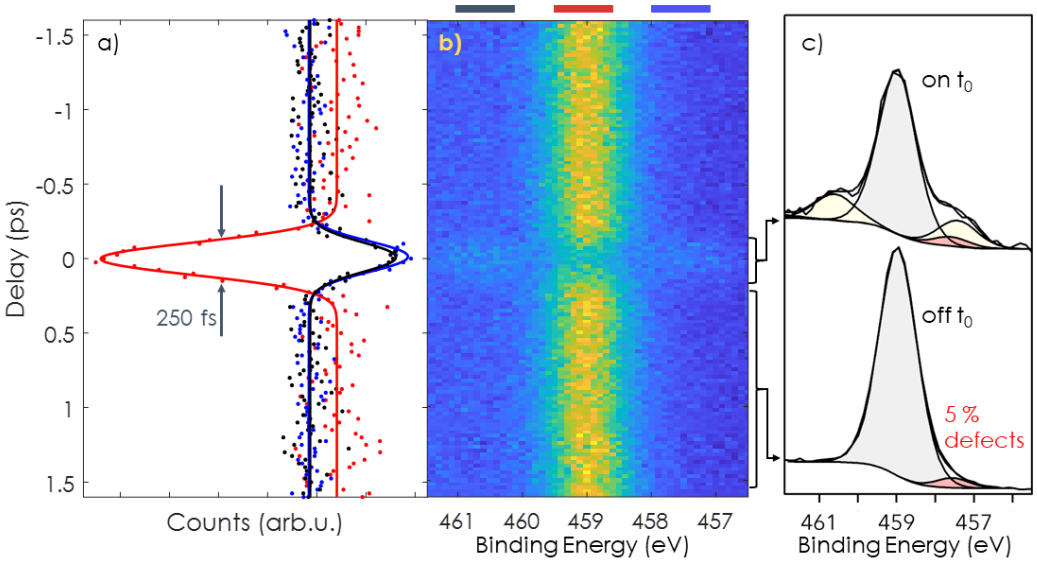

Figure 5.1: Intensity profile (a) of the lattice peak and corresponding sidebands taken from distinct energy regions of the XP map (b) of the Ti 2p core level. The black, red, and blue bars indicate the binned energy region for the line profile. c) XP spectra during (top) and off time-zero (bottom).

pump-probe experiments, the temporal resolution could be determined to be 250 fs. For this, the Full Width Half Maximum (FWHM) of the sidebands at zero delay in the Ti 2p (Figure 5.1) and O 1s (Figure A.1) core level spectra have been evaluated. Sidebands appear when the optical laser and the FEL are temporally and spatially overlapped, and are represented as a replica of the original photoemission line shifted by the energy of the optical laser through absorption or stimulated emission [235, 255]. The Ti 2p spectra (Figure 5.1 c) exhibit a small shoulder on the lower binding energy side of the Ti^{4+} $2p_{3/2}$ lattice peak, assigned to Ti^{3+} surface defects. The area of the Ti^{3+} $2p_{3/2}$ peak amounts to 5 ± 1 % compared to the Ti^{4+} contribution. As one single oxygen vacancy contributes to two Ti^{3+}, the estimated amount of oxygen vacancies at the surface is 2.5 ± 0.5 % [256]. Defects can also occur in the form of Ti^{3+} interstitials.

In prior XPS experiments, the kinetics of CO oxidation to CO_2 on rutile TiO_2 (110) under UV light (365 nm) was studied with an X-ray laboratory source (hv = 1486.6 eV) at the DESY Nanolab [236]. In the O 1s core level region, adsorbed CO gives rise to a component at a binding energy of 536.1 eV and CO_2 at 535.0 eV on rutile (110) with a difference of 1.1 eV between the two components (Figure A.2). The assignment of the binding energies of the O 1s core level of CO and CO_2 in this study is in agreement with previous results [85]. Slight differences in the binding energy are expected due to coverage-dependent shifts [78]. Here we monitored the ultrafast dynamics of the conversion of CO

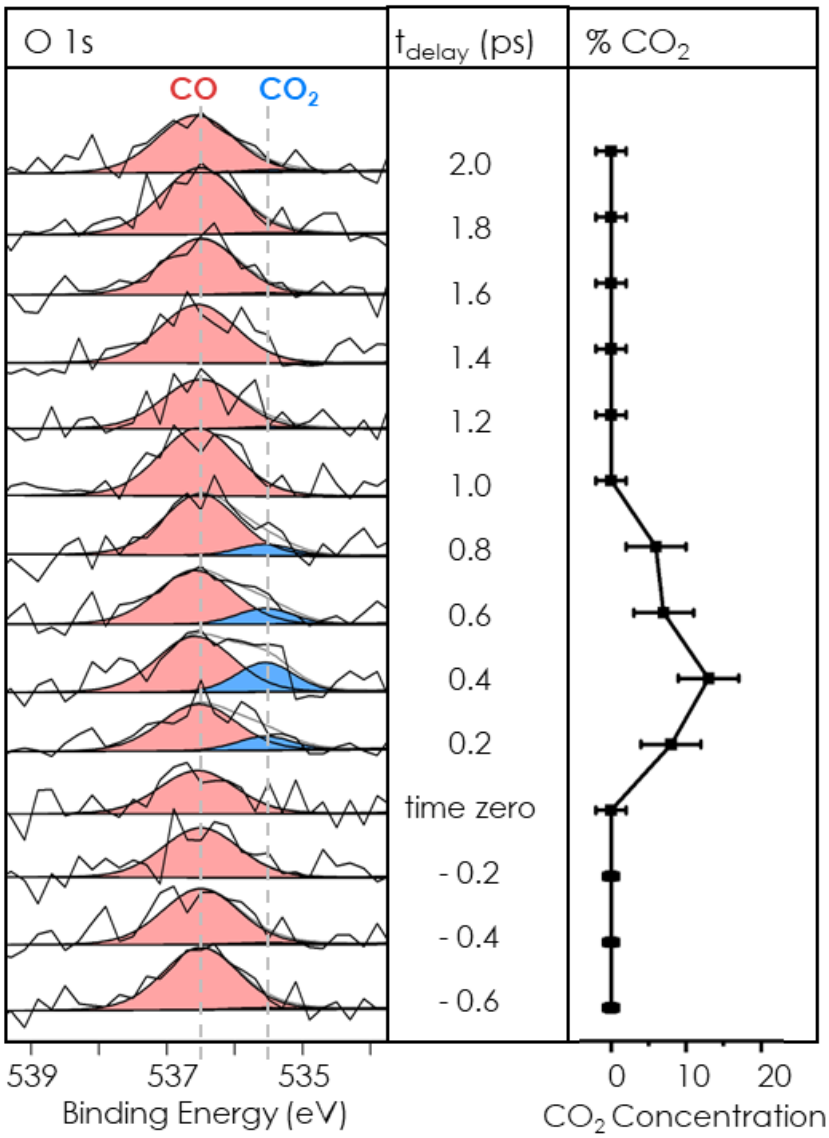

Figure 5.2: Deconvoluted time-resolved O 1s core level spectra binned by 200 fs steps reveals the ultrafast CO (red) oxidation to CO_2 (blue) on rutile (110) at 80 K at FLASH. The data were taken within the first 15 min after flash-annealing the surface.

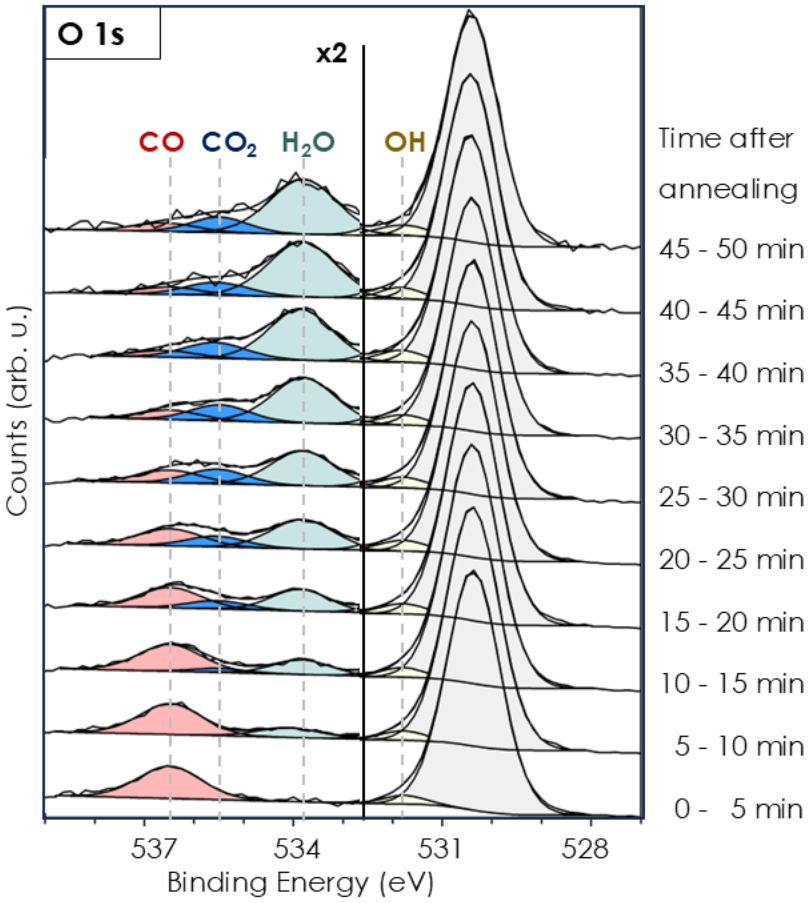

Figure 5.3: Deconvoluted O 1s core level average spectra during CO oxidation at FLASH binned in 5 min steps after heating and cooling the sample to 80 K. Adsorbed CO (red), produced CO_2 (blue) and adsorbed water (light blue).

to CO_2 in the oxygen O 1s core level. The O 1s core level was chosen to monitor the time-resolved CO oxidation, as the favorable stoichiometry of the reaction product CO_2, consisting of two oxygen atoms, results in higher absolute count rates. Additionally, the cross-section for photoionization at 643 eV is higher for the O 1s region than the C 1s region [257]. To obtain enough statistics to extract the time-resolved data shown in Figure 5.2, the data were binned by steps of 200 fs. The detected photoelectrons of the O 1s and Ti 2p core level region have a kinetic energy of 100 eV and 175 eV, respectively, and the inelastic mean free path (λ) of TiO_2 for electrons at those energies is calculated to be 5.6 Å and 6.8 Å [209]. The XPS probing depth, from which 95 % of the measured photoelectron originates, corresponds to 3λ [203]. In TiO_2, which has a layer spacing of 3.25 Å in the [110]-direction [258], the photoelectrons measured for the Ti 2p region originate from the first 6.3 atomic layers and for O 1s from the first 5.2 atomic layers. This emphasizes the high surface sensitivity of this technique.

XP spectra of the O 1s core level were recorded within a delay range of -2 ps before to 12 ps after optical excitation. The results presented and discussed in detail in this work were only recorded within the pump-probe delay range from -0.6 to 2.0 ps in which the CO_2 formation was observed. After the sample preparation, data were collected for 50 min. Because of the increasing amount of water on the surface during the experiment, data were analyzed by integration over the first 15 min to observe the intrinsic behavior of the system, as displayed in Figure 5.2. The CO peak arises at 536.5 eV on rutile (110) at 80 K in $3 \cdot 10^{-8}$ mbar CO atmosphere. At this temperature, it was reported that half a monolayer of CO adsorbs on rutile (110) [73]. In the range of the first 800 fs after the pump laser initiates the reaction, a peak shoulder located at 535.5 eV appears, which is assigned to the formation of CO_2 [85]. The maximum amount of CO_2 is detected at 400 fs with 13 $\pm$ 4 % normalized to the CO signal. The complete binding energy and delay range from -2 to 12 ps is shown in Figure A.3 as spectra and in Figure A.4 as a XP color map. No other CO_2 signal was resolved in that delay range up to 12 ps within the sensitivity of our experiment.

The data averaged over the whole delay window in 5 min bins after the flash-annealing is shown in Figure 5.3. During data acquisition at 80 K in a CO/O_2 atmosphere with a partial pressure of $3 \cdot 10^{-8}$ mbar for CO and O_2 each, residual water in the UHV system of the experimental chamber accumulates on the surface. The peak at 534 eV is assigned to water [92] and increases with time. Water partially dissociates to hydroxyls (OH) on the rutile surface and appears as a shoulder of the lattice O^{2-} peak at 531.8 eV [259]. This shoulder is already visible within the first 5 min and before the H_2O peak at 534 eV appears. The OH signal increases with the water coverage. Water impedes the adsorption of CO and promotes the stabilization of adsorbed CO_2 [82]. As H_2O binds more strongly to the rutile (110) surface than CO, the CO peak decreases over time as H_2O

blocks adsorption sites and inhibits readsorption of CO from the gas-phase as seen in the time-averaged data (Figure 5.3). The data collected in the first 5 minutes in the absence of adsorbed water does not offer sufficient statistics for time-resolved binning. In the first 15 min, used for the time-resolved analysis in Figure 5.2, a low amount of water and a negligible amount of CO_2 is adsorbed on the surface. This is in contrast to the spectra from 15-50 min, which show a clear CO_2 signal as a broad shoulder and a further increasing water signal, indicating that the surface is covered with a non-negligible amount of CO_2 and H_2O. After 40 min the CO_2 signal does not increase anymore, indicating that no further CO is oxidized. Water accumulates further on the surface, blocking the adsorption sites for CO and O_2. The CO_2 formation was observed using the time-resolved spectra within the first 800 fs with a binning of 200 fs recorded in the first 0-15 min after flash-annealing. For comparison, the data for 0-15 min and 15-30 min after heating were binned in 500 fs time windows and CO_2 formation at 535.5 eV was observed for both data sets in the spectra 250 - 750 fs after time zero as seen in Figure A.5. In the O 1s spectra, no peak can be assigned to adsorbed atomic or molecular oxygen under the experimental conditions of $3 \cdot 10^{-8}$ mbar O_2 and $3 \cdot 10^{-8}$ mbar CO at 80 K. Physisorbed O_2 was observed below 60 K on anatase (101) with a binding energy of 537.3 eV as a double peak in a triplet state [260]. On the stoichiometric rutile TiO_2(110), molecular oxygen only interacts weakly with the surface and physisorbs at low temperatures below 85 K [53]. When oxygen vacancies are present, O_2 chemisorbs on the surface in a peroxo O_2^{2-} state in the oxygen vacancy itself or in the direct vicinity, on top of a five-fold coordinated Ti (Ti_{5c}) atom. Even at low temperatures below 80 K, adsorbed O_2 can heal an oxygen vacancy, leaving oxygen adatoms on the TiO_2 surface [261]. Due to defects (oxygen vacancies) of 5 %, chemisorption of O_2 is probable on the surface but due to the very low amount, it is below the detection limit in the O 1s spectra.

The DFT calculations were performed by Adrian Domínguez-Castro, Verena Gupta, Adriel Domínguez Garcia and Thomas Frauenheim from the collaborating group at Bremen Center for Computational Materials Science. To explain the experimental observation of ultrafast CO oxidation within 800 fs, we performed first principle TD-DFTB calculations for the adsorption of O_2 and CO on the rutile TiO_2(110) surface. The optimized geometry of CO and O_2 adsorption can be found in Figure A.6 and the Density of states (DOS) of these systems in A.7. Two favorable configurations are found for the coadsorption of CO and O_2. In both configurations, the CO molecule interacts via the carbon atom with Ti_{5c} in agreement with previous reports [53, 71, 262]. The O_2 molecules either adsorb perpendicular or parallel to the surface on top of the neighboring Ti_{5c} site with a calculated adsorption energy of -0.667 eV for the perpendicular and -0.505 eV for the parallel O_2+CO configuration, respectively. The DOS calculations reveal that the presence of adsorbed O_2 molecules is related to the appearance of electronic states in the band

gap of the surface model, which are responsible for a new band at lower energies in the absorption spectrum. This indicates the formation of an O_2-TiO_2 CT complex that is activated by visible/infrared light via a direct electron transfer from the TiO_2 valence band to adsorbed O_2 molecules. Such a charge transfer complex was proposed previously by Wagstaffe *et al.* [34] for the ultrafast CO oxidation on anatase initiated by a 770 nm laser and by Freitag *et al.* [263] for the visible light activity of TiO_2 with adsorbed nitrogen(II) oxide. In this study, we additionally calculated the absorption spectrum of TiO_2 with and without adsorbed O_2 using real-time TD-DFTB implementation. The absorption spectra are shown in Figure 5.4. Stoichiometric TiO_2 has no adsorption bands in the visible light region, but upon O_2 adsorption, new adsorption bands in the visible light region appear due to CT excitations. Via the CT excitation, adsorbed O_2 is reduced to O_2^-, which is the initial step of O_2 dissociation.

5.3 Discussion

In this experiment, the oxidation of CO to CO_2 is observed within the first 800 fs after initiation. After 800 fs CO_2 desorbs and no new CO_2 forms (see Figure 5.2). This indicates that O_2 dissociates on this timescale on TiO_2 as O_2 only physisorbs on stoichiometric TiO_2 at 80 K and does not dissociate. On the other hand, on defective rutile (110) oxygen adatoms were observed in small concentrations at 80 K after O_2 adsorption and healing of an oxygen vacancy which leaves an isolated oxygen adatom [261]. However, this mechanism is not possible for a reaction cycle, as the oxygen vacancy is healed after the O_2 dissociative adsorption.

For CO photooxidation on TiO_2, the activation of oxygen is considered the rate-defining step. This includes charge transfer to oxygen and dissociation of the anion. To generate electron-hole pairs on TiO_2, photons with either an energy larger than the bandgap or, in case of photons with a smaller energy, multi-photon absorption is required to excite electrons from the valence to the conduction band. Multi-photon absorption to match the bandgap of 3 eV for bulk rutile TiO_2 [264] was reported for laser pulses with pulse energies up to 3 µJ and wavelengths of 774, 800, and 813 nm from a chirped-pulse amplified Ti:Sapphire system [265]. The optical laser used in this study fits within those parameters, having a pulse energy of 5-10 µJ and a wavelength of 770 nm. The excited electrons in the conduction band can either recombine, be trapped, or induce an oxidation/reduction pathway, in this case, the reduction of O_2.

Photogenerated electrons in the TiO_2 band structure are generated in less than 100 fs and conduction band electrons are trapped at the surface within 200 fs [266]. The transfer of surface-trapped electrons to oxygen was only observed on a nanosecond timescale in less than 100 ns [251] and is significantly faster than the transfer of conduction band

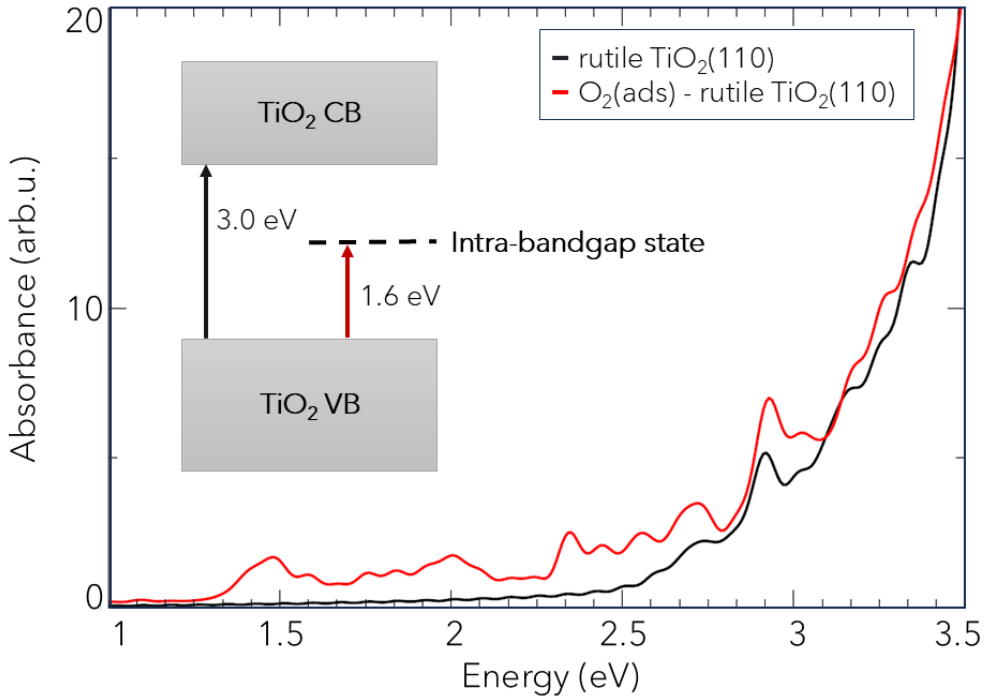

Figure 5.4: DFT calculation of an absorption spectrum of TiO_2 before (black) and after (red) O_2 adsorption. The data was provided by Adrian Domínguez-Castro, Verena Gupta, Adriel Domínguez Garcia and Thomas Frauenheim.

electrons to oxygen in 10-100 µs [267]. In this activation pathway, the electron-driven oxygen activation competes not only with charge carrier recombination but also with the hole-driven desorption of oxygen [268].

Alternatively, based on performed DFT calculations, an O_2-TiO_2 CT complex is probable. Adsorbed oxygen on stoichiometric rutile (110) introduces unoccupied states into its band gap with excitation energies relating to the visible light range as seen in Figure 5.4. The direct excitation of the oxygen molecule may activate oxygen faster than by photogenerated conduction band electrons. As a result, the activated O_2^- dissociates and reacts with CO to CO_2. The activation with a 770 nm laser only requires one photon absorption to excite the O_2-TiO_2 CT complex. The CT complex's excitation probability is lower than band-to-band excitations since the excitation is limited by the number of acceptor states offered by the adsorbed oxygen molecules. But the CT complex excitation is more efficient since the charge is directly trapped in the reduced oxygen molecule and does not compete with recombination. A similar charge transfer complex was proposed for NO on TiO_2 for the visible light for the degradation of NO [263]. The photonic efficiency under UV (bandgap excitation) and visible light (CT complex excitation) are in the same order of magnitude. However, the CT process is one order of magnitude less likely to occur. The CT pathway does not compete with charge carrier recombination and thus increases

the photonic efficiency of the desired reaction.

The O_2-TiO_2 CT is also a possible mechanism for anatase TiO_2(101). In a similar study at FLASH in which the ultrafast CO oxidation on anatase (101) at 60 K was investigated, the CO_2 formation was assigned to the direct activation of oxygen [34] and was observed from 1.2 ps to 2.8 ps after initiation. In contrast, this study on rutile (110) at 80 K reveals that CO_2 is observed already at 0.2 ps after initiation. The temperature difference might influence the diffusion of the adsorbates on the surface, thus enabling a faster reaction between CO and O_2 [269]. In our experiment, measurements at 60 K were not feasible due to rapid water adsorption on rutile (110), which blocked adsorption sites for the reactants. Therefore, we conducted measurements at 80 K instead.

In comparison, CO oxidation was observed in the first few picoseconds after initiation on catalytic metals such as Ru(0001) [96,97], Pt(111) [98] and Pd(111) [99]. Important to note is, that only atomic and no molecular oxygen was adsorbed on these metal surfaces. Furthermore, the oxygen was not dissociated during the reaction process. The role of the optical laser was to excite electrons in the substrate, resulting in an energy transfer to the adsorbate. This causes vibrational motions that induce the reaction between CO and O. Öström *et al.* [97] studied the ultrafast CO oxidation on Ru(0001) with femtosecond X-ray laser pulses and reported the activation of O within 300 fs, of CO in 500 fs, and a formation time for CO_2 of 800 fs. In our experiment, we observe a shorter CO_2 formation time hinting at a different reaction mechanism.

As mentioned above, atomic oxygen on rutile-TiO_2(110) is only observed on reduced rutile at surface oxygen vacancies. Molecular oxygen chemisorbs on top of an oxygen vacancy, heals the vacancy by dissociation, and leaves an O adatom [261].

We argue that atomic oxygen on oxygen vacancies is unlikely to be responsible for the fast CO oxidation. The low amount of 2.5 % oxygen vacancies in the Ti 2p spectra is in disagreement with the maximum of 13 $\pm$ 4 % CO_2. Additionally, this pathway is not sustainable and cannot establish a cycle, as the vacancy would be healed and no longer available as a chemisorption site. The amount of oxygen vacancies indicated by Ti^{3+} does not change during the CO oxidation (see Figure A.8). It also indicates that another CO oxidation mechanism without defect contribution takes place, since the CO oxidation is also observed on the stoichiometric rutile (110) and anatase (101)-TiO_2 surfaces [85]. Oxygen adatoms are observed to be unstable on anatase (101), so the mechanism including complexes of CO and oxygen adatoms is not a possible pathway on anatase [77]. Other CO_2 signals were not detected in the 12 ps delay window, which would indicate another CO oxidation pathway with a different timescale (see Figure A.3). The CO_2 signal therefore implies that oxygen was reduced, dissociated, and reacted with CO to CO_2 within 800 fs.

The surfaces differ in three aspects: in the amount of observed CO_2 compared to CO, the time between initiation and first CO_2 signal detection, and the decay time of the

CO_2 peak. The CO_2 signal on anatase (101) was detected for 1.6 ps with a maximal CO_2 concentration of $\sim$ 25 % relative to the CO signal. After 2.8 ps the formed CO_2 was desorbed. For comparison, on rutile (110) no CO_2 is observed after 1 ps and the maximum relative CO_2 concentration was $\sim$ 13% after 0.4 ps. The higher relative CO_2 concentration aligns with the observation that anatase (101) shows higher photocatalytic activity than rutile (110).

One major argument for the higher photocatalytic activity of anatase is the charge carrier lifetime difference in rutile and anatase which were studied for single-crystals and powders [84, 88, 250, 270, 271]. However, those measurements always detected the concentration of bulk charge carriers and not e^-/h^+ at surface sites for charge transfer to adsorbates. In stoichiometric rutile, charge carrier recombination is more likely and charge carriers are shorter-lived than in stoichiometric anatase. Maity *et al.* [88] found using transient absorption spectroscopy, that bulk charge carriers decaying in $\sim$0.5 ps for stoichiometric and reduced rutile (110) single crystals, whereas in stoichiometric and reduced anatase the lifetime was 32 ps and 24 ps, respectively. The timescale for rutile in that study is similar to the timescale of the CO_2 formation in our study. The longer lifetime of charge carriers in anatase than rutile is in agreement with measurements from Xu *et al.* [84] who observed a direct band gap with faster charge carrier recombination for rutile and an indirect bandgap for anatase with inhibited charge carrier recombination which links the bulk properties of rutile and anatase to its photocatalytic performance. In an indirect bandgap semiconductor, recombination requires a phonon to conserve momentum due to the mismatch between the valence band maximum and conduction band minimum [272] and results in a prolonged lifetime of charge carriers. But the lifetime of surface charge carriers depends highly on surface adsorbates and not only on bulk properties [58]. Adsorbates can not only act as traps for photogenerated charge carriers but also induce band bending, promoting the migration of charge carriers to the bulk. The separation of charges directly influences the charge carrier lifetimes [250]. In this experiment, the surface dynamics are measured on a picosecond timescale, in contrast to the bulk lifetimes of charge carriers of several nanoseconds. The decay of the CO_2 signal within 1 ps can also indicate that the direct excitation of O_2 via the CT complex and not charge carriers from the bulk are responsible for the ultrafast oxidation of CO observed in this study. The reaction time is therefore dependent on the lifetime of the excited oxygen. We cannot exclude a further oxygen activation mechanism mediated by trapped charge carriers from the TiO_2 conduction band on a nanosecond timescale, which is not detected in our study.

It is important to note that, although the surface is not deliberately exposed to water in this experiment, a growing water peak is observed after 5 min at 80 K in the CO/O_2 atmosphere. Since the time-resolved data requires 15 min of each run for sufficient statis-

tics water is present in the time-resolved spectra but in too low amount for a quantitative analysis. On rutile (110) water adsorbs on top of Ti_{5c} [273] and partially dissociates to bridging (OH_{br}) and terminal (OH_t) hydroxyls in the absence of oxygen vacancies and to two OH_{br} by dissociation in an oxygen vacancy [259, 274].

On rutile (110) OH groups can either adsorb on a fivefold coordinated Ti as OH_t, when H adsorbs on bridging oxygen, or on an oxygen vacancy as OH_{br}. The characteristics of these OH groups differ, as OH_t is negatively charged with basic and OH_{br} positively charged with acidic characteristics [275]. These characteristics were also observed in DFT calculations investigating CO adsorption close to OH_t, OH_{br} and on the clean rutile (110) surface [276]. The site close to OH_t shows an increased surface electrophilicity resulting in a closer CO - Ti bond and increased adsorbate-substrate interaction energy compared to the clean surface. The adsorption next to OH_{br} results in a longer CO - Ti bond length and a decreased interaction energy.

Water influences CO oxidation and can promote or inhibit the reaction. In one study [277], the CO oxidation rate under UV light increased until a coverage of up to 1/2 ML of water was reached and decreased for higher coverages. It was proposed that on rutile (110) under UV light in the presence of water H_2O_2 as well as surface peroxo-species such as Ti – O – O – H and Ti – O – O – Ti are formed [278]. The CO oxidation in the presence of water appears to correlate with the amount of peroxide species formed. Several studies [277–281] agree, that water blocks the adsorption sites for CO decreasing CO adsorption and therefore decreasing the CO_2 formation rate. We also observe a decrease in CO adsorption with increasing water adsorption (see Figure 5.3). Water could also influence the activation of oxygen and the charge transfer from TiO_2 to O_2 as the initial step of the CO oxidation. Wagstaffe *et. al.* [92] reported the ultrafast hole transfer from anatase-TiO_2(101) to water within 285 fs as well as the formation of a hydrogen bond between water and the O_{2c} site.

Tilocca *et. al.* [282] investigated the adsorption of O_2 on the hydroxylated rutile (110) surface with molecular dynamics simulations. Physisorbed O_2 can interact with OH-groups without going through a chemisorbed state. The adsorption structures included hydrogen bonds between chemisorbed O_2 and OH, structures resulting from proton transfer as the formation of hydroperoxyls (HO_2), and hydrogen peroxide (H_2O_2), and less stable structures resulting from dissociative O_2 adsorption as OH_t and O_a. Hydroperoxyls HO_2 and bridging hydroxyls OH_t were observed experimentally by Scanning Tunneling Microscopy [283,284], Kelvin Probe Force Microscopy, and Atomic Force Microscopy [285]. Molecularly chemisorbed O_2 next to OH_{br} was not observed. Calculations found an increased O_2 adsorption mediated by adsorbed OH groups due to a charge transfer from OH to TiO_2 [286]. This excess charge is not localized but spreads over the Ti_{5c} atoms. Upon adsorption, the charge is transferred to O_2 thus stabilizing the adsorption. The magnitude

of the charge transfer determines the adsorption strength and ionicity of the interaction. Local Contact Potential Difference measurements suggest experimental evidence for the charge transfer from Ti_{5c} atoms to oxygen O_a [285]. More recent calculations confirmed that O_2 adsorption is favored on rutile (110) in the presence of OH groups [287] and that the energy barrier for the O=O scission, necessary for the CO oxidation, is lowered by proton transfer, which is induced by adsorbed water [288]. The interaction of OH/H_2O with O_2 might thus facilitate the interfacial charge transfer, leading to a enhanced O_2 and CO interaction, and therefore CO_2 formation. We cannot exclude that the faster CO_2 formation on rutile TiO_2(110) compared to anatase TiO_2(101) could be due to the presence of water.

5.4 Conclusion

In conclusion, we investigated the dynamics of the CO oxidation on rutile TiO_2(110) by optical pump, FEL probe X-ray photoemission spectroscopy. In an O_2/CO atmosphere at 80 K, CO adsorbs on the rutile (110) surface and is oxidized to CO_2 within the first 800 ($\pm$200) fs after excitation by the 770 nm laser. We propose that O_2 adsorbs molecularly on the surface and is activated via an O_2-TiO_2-CT complex. Residual water in UHV blocks CO adsorption sites and reduces the CO_2 oxidation but might, in low coverages, facilitate charge transfer. With time-resolved XPS, several oxygen-containing components in the O 1s core level were monitored simultaneously, allowing studying reaction dynamics of co-adsorbed reactants or several products non-destructively in real-time.

While on anatase TiO_2(101) the CO oxidation is observed between 1.2 and 2.8 ps after initiation, the CO_2 signal on rutile is visible between in the first 0.8 ps. Although anatase is the more active photocatalyst compared to rutile the dynamics of the CO oxidation on rutile are observed to be faster. The observation of different reaction dynamics on rutile and anatase is a further step to link the electronic structure of a material to its dynamics and the charge transfer to reactants. Tailoring photocatalytic systems is crucial for developing more efficient materials for green energy production, as water splitting or photovoltaics.

5.5 Methods

5.5.1 Experimental

The time-resolved photoemission data were taken at the plane grating monochromator beamline PG2 [242, 243] of the free-electron laser FLASH [230, 244] located at Deutsches Elektronen-Synchrotron (DESY) in Hamburg, Germany. The fundamental wavelength

of FLASH was 5.79 nm (214 eV) with a pulse energy of 25-40 µJ. To probe the core level of oxygen O 1s the monochromator was tuned to the third harmonic of 1.93 nm (643 eV). The FEL pulses were delivered with a macrobunch repetition rate of 10 Hz with each macrobunch consisting of 400 bunches with a 1 MHz repetition rate. The temporal FWHM of each FEL pulse was <100 fs, though stretched in the monochromator to 150 fs. The optical pump laser with a wavelength of 770 nm (1.6 eV) matches the pulse pattern of the FEL. The maximum single pulse energy of the optical laser was 5-10 µJ with a spot size of approx. 300 µm under normal incidence. The fluence could be calculated to be 7-14 mJ·cm^{-2} under the measurement geometry of 55° sample tilt with respect to the incoming laser beam. To prevent CO desorption the laser fluence was attenuated to 2.2 mJ cm^{-2}. The temporal FWHM of the optical laser pulse was ∼120 fs. A mechanical delay stage set the temporal delay of the optical laser with respect to the FEL beam. The experimental setup used at the beamline was the wide-angle electron spectrometer (WESPE) [234] chamber. WESPE consists of a sample preparation chamber with an ion gun, heating station, and low energy electron diffraction (LEED). The main experimental chamber is equipped with a Themis 1000 high-resolution time of flight spectrometer with a three-dimensional delay line detector (3D-DLD4040-4Q, Surface Concept), beamline connection, and leak valves for dosing gases. The spectra were recorded with a pass energy of 20 eV. The used gases were Ar (purity 99.999%) for sample preparation and CO (purity 99.97%) and O_2 (purity 99.999%). The cryostat in the manipulator, which holds the sample under investigation, allowed cooling with liquid He. The rutile TiO_2(110) single crystal (7 mm x 7 mm x 1 mm) was cleaned under ultra-high vacuum (UHV) conditions with a base pressure of $3 \cdot 10^{-10}$ mbar by repeated cycles of 1 keV Ar^+ ion sputtering and annealing to 650 °C and cooled in $1 \cdot 10^{-6}$ mbar O_2 until a (1 x 1) LEED pattern was obtained (Figure A.10). X-ray photoelectron spectra confirmed the absence of carbon contaminations (Figure A.9). Although the sample was annealed and cooled in oxygen, the Ti 2p core level spectra show 4-6 % of Ti^{3+} as a small shoulder next to the lattice peak of Ti^{4+}, as seen in Figure 5.1c. Ti^{3+} indicates defects in the form of oxygen vacancies [289]. During the CO oxidation, the sample was cooled by liquid He to 80 K and was held in an atmosphere of CO and O_2 with partial pressures of both $3 \cdot 10^{-8}$ mbar. To avoid potential laser-induced damage, the incident pulses were scanned across the sample surface. During data acquisition at 80 K in a gas atmosphere of CO and O_2 each with a partial pressure of $3 \cdot 10^{-8}$ mbar, residual water from the UHV environment adsorbed on the cold sample surface resulting in a growing peak at 534.8 eV, as seen in Figure 5.3. To limit the influence of water on the reaction dynamics, only spectra recorded until 15 min after brief flash-annealing of the surface to 600 K are used to study the dynamics of the CO oxidation. The sample was cleaned by sputtering and annealing in O_2 after two measurement cycles with flash-annealing to obtain a stoichiometric surface.

The binning of the extracted spectra was were 200 fs in temporal domain and 200 mV in energy. In total, the data of the first 10-15 min of 22 runs was used, depending on the amount of adsorbed water. Due to shifts of the FEL energy, the Ti 2p spectra of each run were calibrated by aligning the Ti^{4+} $2p_{3/2}$ to 459.0 eV and the O 1s spectra by calibration the lattice O^{2-} to 530.4 eV [1]. For each run time zero, the temporal overlap of FEL and optical laser was determined by fitting the sidebands of the O 1s lattice peak. The spectra were fitted in CasaXPS with Gaussian/Lorentzian curves on a Shirley or linear background. The Shirley background emulates the inelastic electron scattering of the intensive O 1s lattice peak. Regions with lower counts were fitted with a linear background as the modeling of the inelastic scattering did not improve the fit.

5.5.2 Theroretical

The DFT calulations were performed by Adrian Domínguez-Castro, Verena Gupta, Adriel Domínguez Garcia and Thomas Frauenheim from the collaborating group at Bremen Center for Computational Materials Science. The DFT periodic calculations on the neutral TiO_2 rutile (110) surface were performed with the Vienna ab initio simulation package (VASP) code [290–293] The TiO_2 rutile (110) surface was modeled by a slab model of 40 Ti atoms and 80 O atoms using the following lattice parameters: a = 5.9612 Å, b = 13.0834 Å, and c = 30.0000 Å. For the optimization of the structures with the Perdew-Burke-Ernzerhof (PBE) functional [294], the projecto augmented-wave (PAW) method [295,296] was used and the Brillouin zone was sampled with a (2x2x1) Monkhorst-Pack k-points grid with an energy cutoff of 400 eV. In the systems with O_2 molecule presence, spin polarization calculations are performed to include the triplet nature of the O_2 molecule in the ground state. Van der Waals interactions were included by using the DFT-D3 dispersion corrections with Becke-Johnson damping [297, 298]. All minima were confirmed by frequency calculations. The adsorption energies E_{ads} were calculated by: $E_{\text{ads}} = 1/n\ (E_{\text{complex}} - E_{\text{TiO}_2} - nE_{\text{mol}})$ where: E_{complex}, E_{TiO_2}, E_{mol}, n are the total energy of the molecule-TiO_2 complex formed by molecule-TiO_2 rutile (110) surface, the TiO_2 rutile (110) surface, the molecule and number of molecules, respectively. Within this definition of adsorption energy, a negative value indicates an exothermic process. For the Density of States (DOS) analysis a (4x4x1) k-points grid, PBE functional [294] at DFT level of theory with the semi-empirical nonlocal external potentials (NLEP) was used [299–301]. The absorption spectra of O_2 were calculated using DFTB+ code [302]. The repulsive potential for the Ti-O pair was improved for a better description of the physisorption of O_2 over TiO_2 rutile (110) surface. The set of DFTB parameters *tiorg-0-1* [303] were modified and used. To determine the absorption spectra at the real-time TD-DFTB level, a cluster model was used to simulate the TiO_2 rutile (110) surface. The cluster is formed by $Ti_{21}O_{68}H_{52}$ formula, in which the peripherical O atoms were saturated

with H atoms to keep the cluster neutral. To obtain the absorption spectra, an initial perturbation to the initial ground-state matrix is introduced. This perturbation has the shape of a Dirac delta pulse, and the density matrix evolves in time. Its evolution can be resolved by time integration of the Liouville-von Newmann equation of motion. For this, an initial electric field of 0.001 V/Å was used.

Chapter 6

Results and Discussion of the Photooxidation of Au and Pt-Au on TiO_2

The aim of this project was to study the photocatalytic properties of gold nanoparticles, focusing on the influence of the local surface plasmon resonance of gold nanoparticles on CO photooxidation. First, the growth of Au and Pt-Au nanoparticles is discussed, and then their catalytic activity is probed by CO oxidation.

6.1 Growth of Au and Pt-Au Nanoparticles on Rutile TiO_2(110)

The growth of Au nanoparticles on rutile (110) and the overgrowth with Pt were characterized by XPS, STM and XRR. The results for each method are presented.

Clean Rutile TiO_2(110) Surface

To evaluate the XPS data for the (Pt-)Au/TiO_2, the clean rutile TiO_2 substrate surface is presented first. The O 1s region (Fig. 6.1a) consists of two peaks, one at 530.3 eV assigned to lattice oxygen atoms and one at 531.6 eV assigned to surface bridging oxygen atoms [304]. The Ti 2p core level (Fig. 6.1b) consists of two peaks due to spin-orbit splitting with Ti^{4+} $2p_{1/2}$ at 464.8 eV and Ti^{4+} $2p_{3/2}$ at 459.0 eV [305]. The latter was used as a reference to calibrate the binding energy of the XP spectra. A shoulder on the lower binding energy side is assigned to Ti^{3+}, indicative of defects on the surface such as oxygen vacancies or titanium interstitials. The LEED image in Fig. 6.1 c) shows the pattern of the 1x1 rutile (110) surface, which indicates a smooth, stochiometric surface.

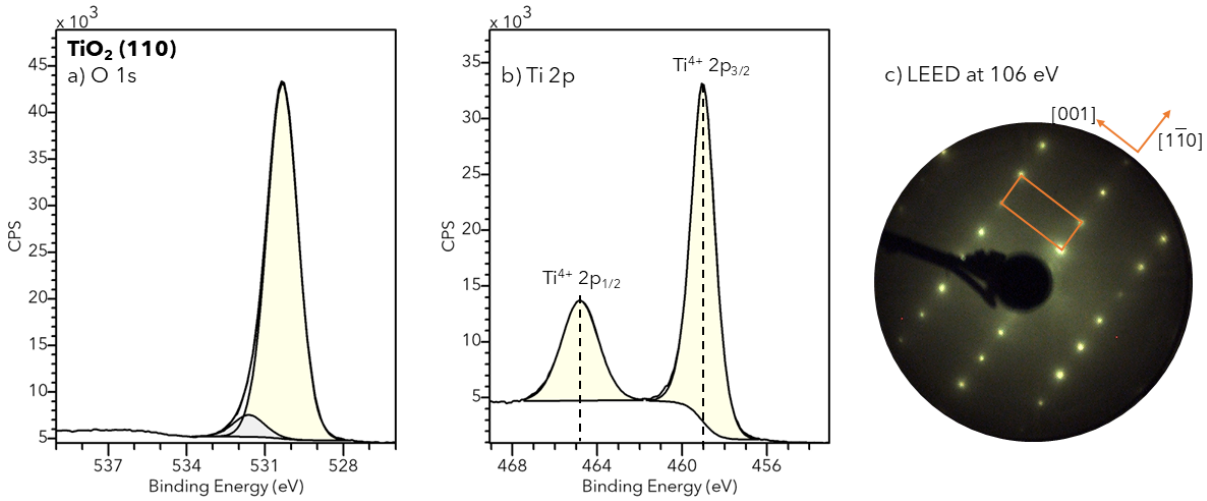

Figure 6.1: XP spectra of stoichiometric TiO_2 (110) of the a) O 1s, b) Ti 2p core level region and c) (1x1) LEED pattern taken at 106 eV.

6.1.1 Au Growth on TiO_2

Nine Au/TiO_2 samples were prepared, numbered chronologically from #1 to #9. The diameter distribution of the Au nanoparticles was determined by 30×30 nm to 50×50 nm STM images using line profiles through each particle. The median diameter is given in brackets in the sample name. The varied growth parameters were the amount of evaporated gold, the sample temperature during evaporation, and the time of post-evaporation annealing, which was always carried out at the same temperature as during evaporation. The aim was to increase the size of the Au nanoparticles to observe plasmonic properties. The samples were further characterized by XPS, XRR, GIXRD, and UV-Vis SDRS (Tab. 6.1). Samples #1 and #6-#9 were used to test the CO oxidation, which is described in Sec. 6.2.

Variation of Growth Parameters

The first Au(2.5 nm)/TiO_2 (#1) sample was grown at room temperature with a gold amount of 0.4 ML, determined by XRR. For sample Au(3 nm)/TiO_2 (#2), the temperature during evaporation was elevated to 250 °C, while for sample Au(3 nm)/TiO_2 (#3) the gold amount increased to grow larger nanoparticles.
For sample Au(4 nm)/TiO_2 (#4), both factors were combined, but the flux during evaporation was unstable from incomplete degassing of the evaporator, resulting in contamination on the surface of the sample. Sample Au/TiO_2 (#5) was only prepared for GIXRD measurements and was not characterized by XPS and STM.
The sample temperature of sample Au(5 nm)/TiO_2 (#6) during evaporation was elevated to 400 °C, and the evaporated amount increased to 3.4 ML. The sample temperature during evaporation was elevated to 500 °C for all subsequent samples to increase the particle

size further. For sample Au(4.5 nm)/TiO_2 (#7), the evaporation was interrupted by one-hour annealing steps so that a sequence of one-hour evaporation, one-hour annealing, one-hour evaporation, and one-hour annealing was carried out. For sample Au(5.5 nm)/TiO_2 (#8) and Au(6 nm)/TiO_2 (#9), the evaporation time was two hours with a subsequent three hours post-annealing step. Before and after deposition of each sample, a LEED image was taken. The image of the nanoparticle-covered surface is blurred compared to the image of the clean substrate. An example is attached in the appendix in Fig. B.2. The preparation parameters for the Au/TiO_2 samples and their characterization are summarized in Tab. 6.1 and B.2.

XPS

The XP spectra for all measured Au/TiO_2 samples are shown in Fig. 6.2. First, some notes on peak fitting, which is required for quantitative analysis of the XPS spectra.
The default symmetric peak shape GL(30) is the product of a Gaussian (70 %) and a Lorentzian (30 %). Ti^{4+} $2p_{3/2}$ is fitted by a GL(50) because it approximates the peak shape more accurately. The core levels of Pt 4f and Au 4f have an asymmetric peak shape and are fitted by a Lorentzian Asymmetric (LA) line shape. The XP spectra of each prepared sample for characterization were taken after cleaning or metal evaporation (including post-annealing) and before any other treatment (such as heating, cooling, dosing gases, or illumination) and were calibrated to Ti $2p_{3/2}$ at 459.0 eV, measured at 296 K [1]. The fitting parameters are given in Tab. B.4 and B.5 in the appendix.

The most interesting information provided by XPS in the Au 4f spectra is the position, FWHM, and peak area relative to the O 1s and Ti 2p peak areas. The peak areas are used to determine the gold amount on the sample with eq. 4.1. The Ti 2p core level spectra contain information on defects, visible in the Ti 2p spectra as Ti^{3+} as a small shoulder at 457.0 eV next to the Ti^{4+} lattice peak. Defects are either Ti interstitials or oxygen vacancies, from which the additional charge of $2-$ is transferred to surrounding Ti atoms. The amount of Au varies from 0.9 ± 0.2 % gold (#1) to 10.9 ± 0.5 % (#8). The values for all samples are listed in Tab. 6.1. The position of the Au $4f_{7/2}$ peak shifts from 84.1 eV (#1) to 83.7 eV (#7-#9) with increasing Au particle size. This shift of Au 4f to lower binding energies with increasing Au particle size is generally observed for Au on TiO_2, called size-effect [306], and can arise from initial and final state effects. Change transfer to the Au nanoparticle affects the initial state of the Au 4f level, thus being observable in XP spectra [307]. The electric environment of the atom affects the final state after photoelectron emission: for larger Au nanoparticles, the local electric environment screens the generated core hole, resulting in a smaller positive shift in binding energy [306,308]. Also, the temperature the nanoparticles were exposed to, affects the peak position: after flash annealing sample Au(2.5 nm)/TiO_2 (#1) to 500 K, the Au $4f_{7/2}$ peak shifts by 0.2 eV to

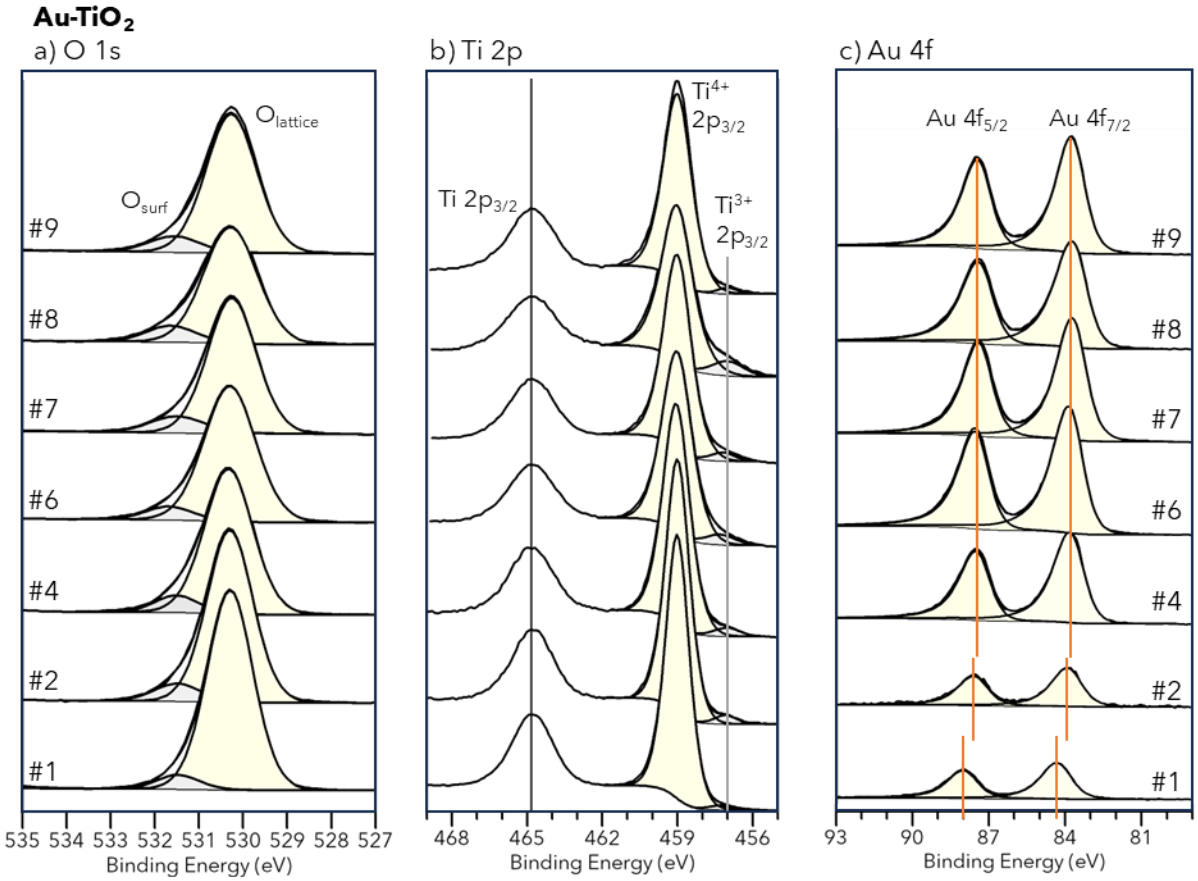

Figure 6.2: XP spectra of a) O 1s, b) Ti 2p and c) Au 4f core level region of samples Au/TiO_2 recorded dierectly after Au deposition.

83.9 eV and narrows from an FWHM of 1.3 eV to 1.2 eV. The narrowing indicates that the Au atoms reorganize by heating, leading to a more ordered electronic structure. The shift might also be partially due to the increase in size upon heating, which has been observed in STM measurements before and after XPS experiments (which included heating).
With increasing Au amount the signal of Ti^{3+} relative to Ti^{4+} increases from 1.4 ± 0.5 % (#1) to 8.4 ± 0.5 % (#8). The increase in Ti^{3+} is observed with increased Au amount but may also be due to the elevated temperature during evaporation or post-annealing, since heating in UHV reduces TiO_2. For example, sample $Au(2.5\ nm)/TiO_2$ (#1) prepared at room temperature shows 1.4 % Ti^{3+} and 0.9 % Au in the XP spectra, whereas sample $Au(3\ nm)/TiO_2$ (#2) prepared at 250 °C shows more defects with 2.8 % Ti^{3+} but similar gold content with 0.8 % Au.
Before evaporation, some rutile crystals were used to test the CO oxidation. XPS characterization revealed a stoichiometric surface with no Ti^{3+} shoulder in the Ti 2p spectrum. Therefore, the defects must have been induced during the Au evaporation process, showing a trend of increasing Ti^{3+} peak with increasing Au amount and temperature during Au evaporation. An exception to this trend is observed for sample $Au(6\ nm)/TiO_2$ (#9)

with 2.3 ± 0.5 % Ti^{3+}. Possible reasons could be deviations in the temperature during evaporation. The temperature during evaporation might have differed without notice, since before this sample was grown, the experimental UHV chamber was opened, and a cable to the heating filament was changed. The sample plate's temperature cannot be measured by an external pyrometer during Au evaporation due to the geometry of the UHV chamber. Another reason could be deviations in the gold amount, which is estimated by the flux monitor and might have been overestimated due to possible degassing during evaporation. On sample Au(6 nm)/TiO_2 (#9), XPS measurement indicated 9 % Au and XRR 2.6 ML Au, which is lower compared to the three previously discussed samples #6-#8, which could be a cause for fewer defects.

STM

STM was measured to determine the Au nanoparticle size distribution. An overview of 50 nm×50 nm is shown in Fig. 6.3 for all samples. The size was analyzed via line profiles over all nanoparticles in a 30 nm×30 nm to 50 nm×50 nm region in the shown images. The shape observed by the line profiles is hemispherical. The minimum, maximum, and median diameters and maximal height are listed in Tab. 6.1. The histograms of measured diameters are in the appendix in Fig.B.5. As Tab. 6.1 shows, the Au amount determined by XPS and the median diameters correlate. The median diameters range from 2.5 nm on the sample with the lowest Au amount (sample #1 with 0.9 % Au) to 6 nm on sample #9 with 9.2 % Au.
Another parameter influencing the diameter of the Au nanoparticles is the temperature of the sample during evaporation. The diameter increases with higher temperature. This effect is visible when comparing sample Au(3 nm)/TiO_2 (#2) before and after annealing at 570 °C. The STM images in Fig. B.3 give a nanoparticle diameter of 1 to 4 nm with

Table 6.1: Overview on Au/TiO_2 samples. The % Au content is in relation to the Ti and O peaks areas.

	XPS	STM Diameter (nm)			Height (nm)	XRR	Evaporation	
Sample	% Au	median	min	max	max	ML Au	T_{sample}	Post-anneal.
#1	0.9	2.5	1.5	4	1	0.4	20 °C	–
#2	0.8	3	1	4	1.3	0.7	250 °C	–
#3	–	4	2	6.5	1.2	3	20 °C	–
#4	4.2	4	2.5	6	1	too rough	250 °C	–
#5	–	–	–	–	–	3.6	400 °C	20 min
#6	10.8	5	2	7	2	3.4	400 °C	10 min
#7	10.3	4.5	2	7.5	2	4.8	500 °C	2 x 1h
#8	10.9	5.5	3.5	8	1.8	5.2	500 °C	3 h
#9	9.2	6	3	12	2	2.6	500 °C	3 h

a median of 3 nm and a maximum height of 1.3 nm for the as-prepared sample. After annealing for one hour at 570 °C, the diameter is 1.5 to 5 nm with a median of 3 nm and a maximum height of 1.5 nm. This confirms that annealing slightly increases the particle diameter.

For sample Au(4 nm)/TiO_2 (#3), bigger gold particles of 30 nm width with a height of up to 3 nm are observed by STM images within a scan range of 1 µm×1 µm. The cropped image of the scan is shown in Fig. B.4.

In the STM measurement of sample Au(4 nm)/TiO_2 (#4), several larger particles with sizes of 12 nm are visible, yet most particles show sizes between 2.5 to 6 nm. The distribution of the nanoparticles is not homogeneous, and the surface appears rough. Gold nanoparticles preferably nucleate at oxygen vacancy sites and step edges [135], so the density of those defects influences the density of particles.

The sample Au(4.5 nm)/TiO_2 (#7) was shortly sputtered after the CO oxidation and before STM measurements, which could lead to a smaller determined nanoparticle diameter.

The measured diameter for sample Au(5.5 nm)/TiO_2 (#8) is larger than all previous samples, which was the result of prolonging the post-annealing time.

The Au nanoparticles diameter of Au(6 nm)/TiO_2 (#9) is even larger than for the sample Au(5.5 nm)/TiO_2 (#8), although the amount of Au determined by XPS and XRR is less. A possible explanation would be the preference for Au nucleation at oxygen vacancy sites, leading to more but smaller Au NPs. The XPS measurement of sample Au(5.5 nm)/TiO_2 (#8) indeed reveals with 8.4 % more defects than sample Au(6 nm)/TiO_2 (#9) with 2.3 % defects. The observed result, that fewer defects result in larger Au NPs, is in agreement with the diffusion rate of Au on stoichiometric rutile (110) being greater than on reduced [309]

Since the tip of the STM is broader than the distance between the nanoparticles, it does not reach the substrate between them, so the height is underestimated. STM is a local technique and only scans a range of a few hundred nm^2, which is not necessarily the same spot as measured by XPS. The scanned area for XPS and STM was chosen in the center of the sample.

UV-Vis Surface Differential Reflectance Spectroscopy (SDRS)

To determine the localized surface plasmon resonance frequency (LSPR), UV-Vis SRDS measurements were performed in reflectance of sample Au(3 nm)/TiO_2 (#2) (Fig.6.4). The reflectance UV-Vis spectra show an enhanced reflection in the 400 - 600 nm regime. This increased reflection can be partially assigned to the local surface plasmon resonance. An additional factor is the reflection of the nanoparticles, as gold scatters more light in the visible range compared to the rutile substrate. Gold has two interband transitions in

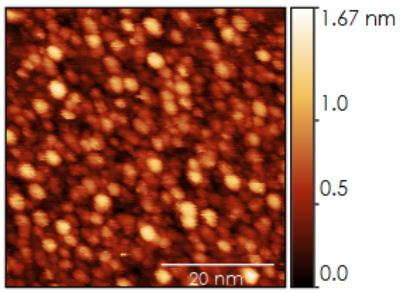

(a) #1: 2.5 nm Au, RT

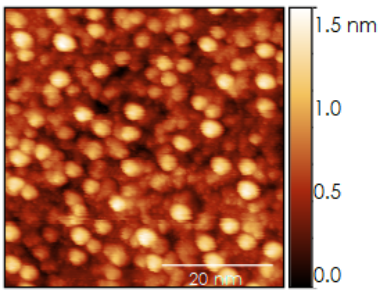

(b) #2: 3 nm Au, 250 °C

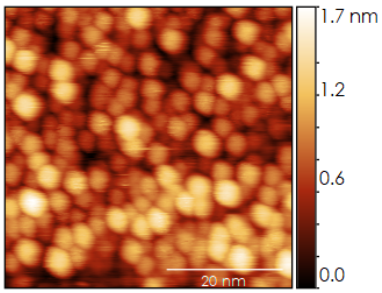

(c) #3: 4 nm Au, RT

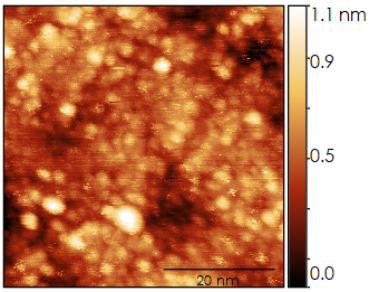

(d) #4: 4 nm Au, 250 °C

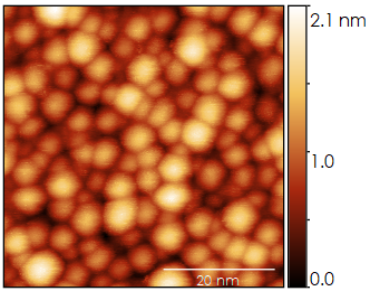

(e) #6: 5 nm Au, 400 °C

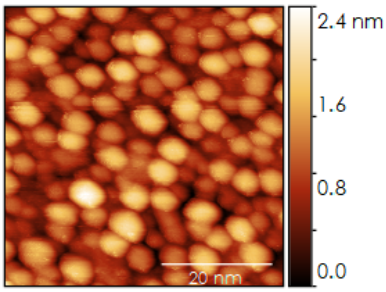

(f) #7: 4.5 Au, 500 °C

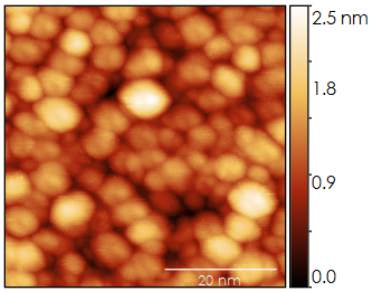

(g) #8: 5.5 nm Au, 500 °C

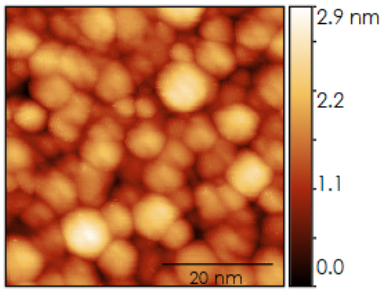

(h) #9: 6 nm Au, 500 °C

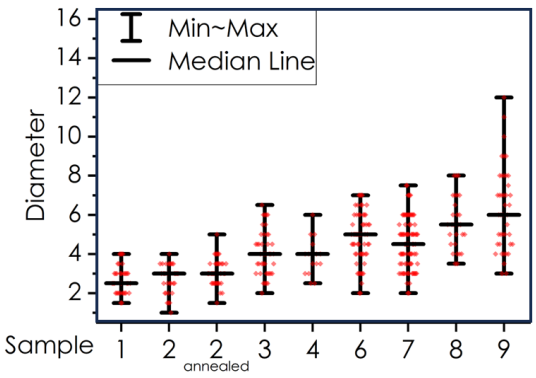

(i) Measured diameter ranges

Figure 6.3: STM images (50×50 nm) of Au on TiO_2(110) and i) diameter measurement results using line profiles through each particle. Each red dot represents one nanoparticle.

the UV-Vis region at 300 nm and 470 nm, which also contribute to the reflectance spectra [310]. A similar spectrum was published by Soldo-Olivier *et al.* [180]. In their study, Au/TiO_2 grown at room temperature had a localized plasmon resonance at 560-620 eV, depending on the treatment of the sample and the amount of gold. Although enhanced absorption would be expected at the LSPR for small nanoparticles, studies on SDRS on Au/TiO_2 by Soldo-Olivier *et al.* [180] and Lazzari *et al.* [311] showed enhanced scattering in the LSPR region, even for small nanoparticles. In their studies, the reflection maximum red shifts with increasing Au diameter, which is an expected behavior for the plasmon resonance of gold.
From the measured data, combined with other experiments [312, 313] studying the plasmonic properties of Au/TiO_2, a 530 nm wavelength was chosen. This wavelength also coincides with the second harmonic of the FLASH laser [314], which would be used as a pump laser in a pump-probe experiment.

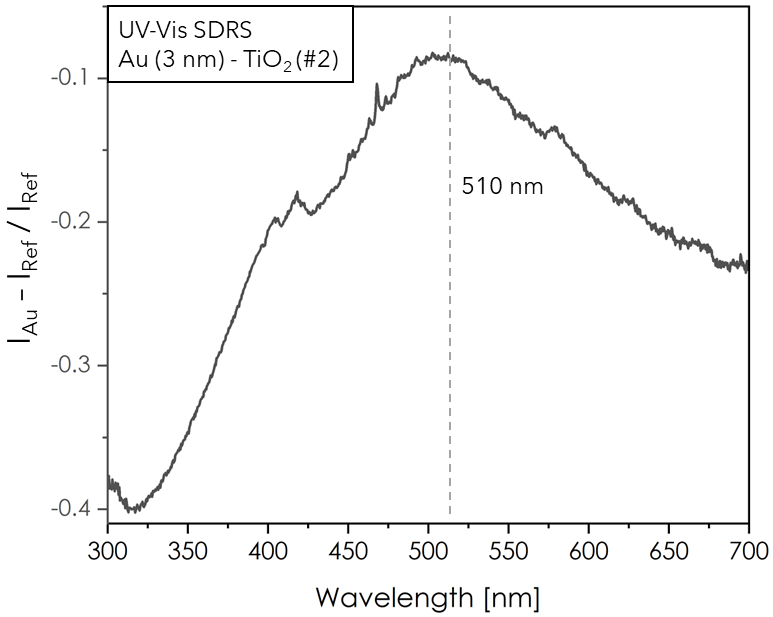

Figure 6.4: UV-Vis SDRS of sample $Au(3\,nm)/TiO_2$ (#2) grown at 250 °C after annealing.

Grazing Incidence X-ray Diffraction

Samples #3 and #5 were studied by Grazing Incidence X-ray diffraction (GIXRD) at the PETRA III beamline P07 to determine the preferred growth orientation of the particles. The samples were measured with a photon energy of 73.7 keV and an incident angle of 0.03°, slightly below the critical angle for TiO_2 at that energy at 0.032°. To protect the 2D detector, the high-intensity spots caused by Bragg reflexes of the substrate rutile (110) are covered with tungsten beamstops attached to the surface of the 2D detector, thus appearing as black circles and squares in the datasets. The spots with the highest intensity

originate from the rutile TiO_2(110) substrate, which are the (110) and (220) reflections at $q_{xy} = 0$ Å^{-1}. Four faint powder rings are visible on the detector image (Fig. 6.5) with no preferred orientation. The first four powder rings match the q values and intensity of Au. The lattice distance can be calculated from q by

$$d\ (\text{Å}) = \frac{2\pi}{q\ (\text{Å}^{-1})}. \tag{6.1}$$

The best visible ring with the smallest q value is assigned to the (111) planes with a lattice distance of 2.35 Å. Very close to this ring is the (200) Bragg reflex from the substrate rutile (110), which contributes to a seemingly higher Au intensity. The other three rings are fainter and are assigned to (200), (220), and (113). No preferred growth orientation is visible.

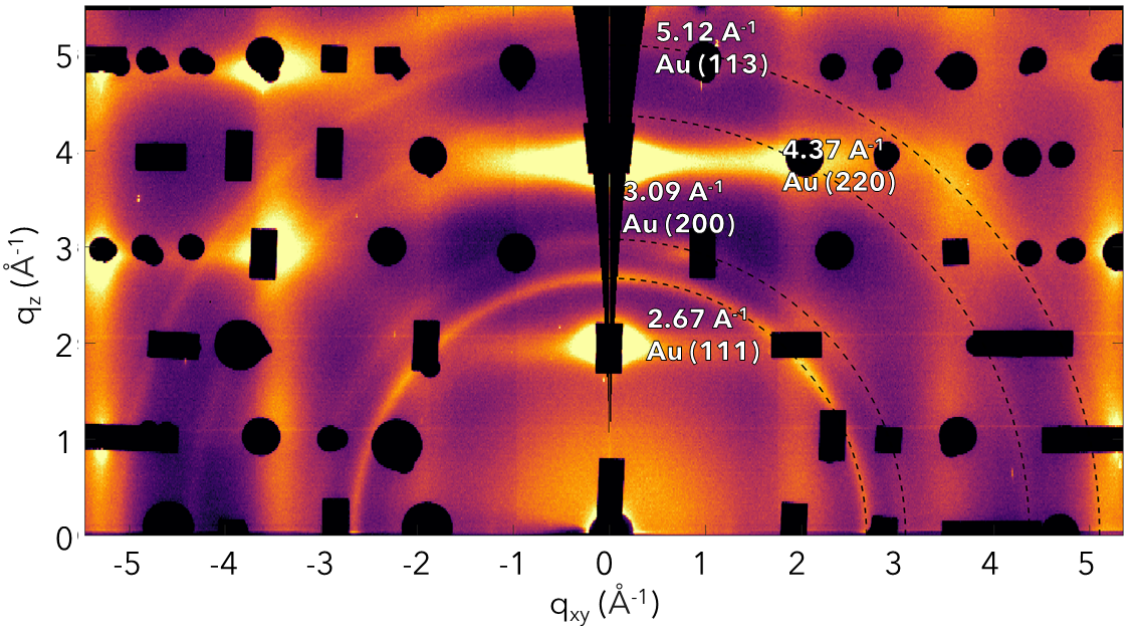

Figure 6.5: GIXRD of sample Au(4 nm)/TiO_2 (#3) binned over a rotation of 16°. No preferred orientation is visible.

Summarizing remarks on growth of Au on TiO_2

The parameters influencing the size of the gold nanoparticles were the amount of evaporated gold on the sample surface, the sample's temperature during evaporation, post-evaporation annealing, and the number of defects. It was shown that a higher amount of evaporated gold leads to large Au nanoparticles.
Although the TiO_2 (110) is prepared to aim for a stoichiometric surface, defects in the form of Ti^{3+} appear after Au evaporation. With increasing NP size and elevated sample temperature during evaporation, a higher amount of defects is observed. Annealing of

TiO_2 in UHV leads to defects [54], so annealing during or after Au evaporation causes defects, such as oxygen vacancies. As defects were also observed on the sample annealed at 250 °C (#2 and #4) and the sample Au(2.5 nm)/TiO_2 (#1) grown at room temperature, the growth of Au itself is found to cause defects.
Defects on TiO_2 are nucleation centers for gold nanoparticles [126] and increase the diffusion barriers of Au atoms on the surface [315]. The sample preparation in this thesis included exposure of TiO_2 at 850 °C to molecular oxygen and during cooling down, resulting in a stoichiometric TiO_2 at the beginning of the evaporation. During the evaporation, the stoichiometric surface is reduced due to the elevated temperature of 400 °C or 500 °C, respectively, but also due to deposited Au.
Samples Au(5.5 nm)/TiO_2 (#8) and Au(6 nm)/TiO_2 (#9) are prepared with a similar protocol but differ in defects, gold amount, and nanoparticle diameter. Sample Au(6 nm)/TiO_2 (#9) shows the larger median and maximum diameter in STM than sample Au(5.5 nm)/TiO_2 (#8), but simultaneously sample #9 has a lower gold amount (2.6 ML Au in XRR, 9.2 % in XPS) and a low amount of defects (2.3 % Ti^{3+} in XPS) compared to sample #8 (with 5.2 ML Au in XRR, 10.9 % Au in XPS and 8.4 % Ti^{3+} in XPS). Sample #9, having fewer defects and larger nanoparticles, shows that nanoparticle diameter and defect amount correlate in this case. The lower amount of Au on #9 could be a cause for fewer defects, but the cause for larger particles, as fewer defects increase the diffusion barrier for the gold atoms [315]. Differences in the CO UV-induced oxidation are also observed and are discussed in section 6.2.3.
For all Au/TiO_2 samples, a so-called particle size effect is observed in the binding energy of the Au 4f core level. The Au 4f binding energy shifts to lower values with increasing Au coverage. The highest binding energy for Au 4f of 84.1 eV is observed on sample Au(2.5 nm)/TiO_2 (#1) with 0.4 ML Au deposited at room temperature while the lowest binding energy of Au 4f is measured on sample Au(5.5 nm)/TiO_2 (#8) with 5.2 ML Au deposited at 500 °C. A shift of 0.3 eV to lower binding energies of the Au 4f core level is also observed after heating #1 to 500 K. The particle size effect can arise from initial and final state effects [306].

6.1.2 Pt-Au Growth on TiO_2

To increase the CO adsorption on the Au nanoparticles, Pt in coverages ranging from 0.25 ML to 2 ML were deposited on top of the Au nanoparticles. The sample preparation and the Au deposition were carried out as described in Section 6.1.1. After gold deposition and post-annealing, the sample was transferred to the UHV chamber MBE I with the Pt evaporator.
In total, five different Pt-Au/TiO_2 samples were grown. The growth parameters are summarized in Tab. 6.2 and B.3. The STM measurements were carried out after CO

oxidation experiments.
The Au deposition for all Pt overgrown samples (#10-#14) was carried out similarly to sample #9 with a nominal layer thickness of 2.5 ML and a sample temperature of 500 °C with three hours post-annealing at the evaporation temperature. On top of the gold nanoparticles, 0.5 ML platinum was deposited with a sample temperature during deposition of 500 °C for sample #10. This resulted in bimetallic nanoparticles fitted by one layer with the same electron density in XRR (Fig.B.7), which indicates that Au and Pt form mixed, alloyed nanoparticles. But to improve CO adsorption, Pt must stay at the surface of the gold nanoparticle. Thus, for samples #11-#14, the sample temperature during evaporation was held at room temperature to achieve an overlayer of Pt. The amount according to the calibration on the evaporator ranges from 0.25 ML (#11,#12) over 1 ML (#13) to 2 ML (#14).
For sample Pt-Au(5.5 nm)/TiO_2 (#11), an overlayer of Pt is achieved as the XRR curve is best approximated by a model of two layers of 4.7 nm and 2.1 nm, which can be interpreted as an Au and a Pt layer, respectively. Similar results are found for the similarly prepared sample Pt-Au(5 nm)/TiO_2 (#12). For samples #11 and #12, it is unclear if Pt is only located on top of the Au or if it is also covering the substrate. Yet the two layers from the XRR fit of the samples #11 to #14 are in contrast to the XRR fit for sample #10, which is approximated by one mixed layer.
For sample Pt-Au(4.5 nm)/TiO_2 (#13), the amount of evaporated Pt was increased from 0.25 ML to 1 ML to increase the CO adsorption at room temperature. The XRR curve is fitted by a two-layer model. The first layer on top of the substrate, Au, has a lower electron density than the second layer, Pt. Using the electron densities for Au and Pt for the bottom and top layer, respectively, the coverage of the top Pt layer exceeds the coverage of the bottom Au layer. This indicates that Pt is predominantly located on top of Au. For sample Pt-Au(6 nm)/TiO_2 (#14), the amount of Au and Pt was increased. XRR curves give 7.2 ML Au and 3.2 ML Pt. The aimed amount of Pt was 2 ML, but slight differences in the sample's position or variances in the sample rotation can lead to a difference in the amount compared to what was aimed for. As all XRR measurements are taken in air after the CO oxidation experiments, diffusion of Au and Pt leads to mixed layers that are not purely Au or Pt, leading to a distorted result.

XPS

The XP spectra of the samples Pt-Au/TiO_2 #10-#14 are displayed in Fig. 6.6. XPS analysis of sample Pt-Au(6 nm)/TiO_2 (#10) directly after evaporation shows 7.7 % Au and 2.7 % Pt. The binding energy for Au $4f_{7/2}$ is 83.7 eV before Pt evaporation and shifts 0.1 eV higher to 83.8 eV after Pt evaporation. The Pt $4f_{7/2}$ is at 71.0 eV.
For all Pt-Au/TiO_2 samples that were overgrown with Pt at RT, the binding energy of Au

Table 6.2: Summary of growth parameters of Pt-Au on rutile TiO_2(110)

	XPS		STM Diameter (nm)			Height	Pt evaporation	
Sample	% Au	% Pt	median	min	max	max	T_{sample}	ML Pt
#10	7.7	2.75	6.5	3.5	16	2	500 °C	0.5
#11	9.0	1.6	5.5	3	8	2.1	20 °C	0.25
#12	10.6	1.6	5	2.5	7.5	2	20 °C	0.25
#13	11.1	6.6	4.5	2	8	1.8	20 °C	1
#14	11.6	12.6	6	2.5	7.5	3	20 °C	2

$4f_{7/2}$ is 83.7 eV, similar to all Au/TiO_2 samples that were grown at 500 °C. The Pt $4f_{7/2}$ peaks shift with increasing Pt coverage from 71.2 eV for 0.25 ML to 80.2 eV for 2 ML, similar to the shift to lower binding energies with increasing Au amount.

On sample Pt-Au(5.5 nm)/TiO_2 (#11), XPS was measured under several exit angles to determine the location of the Pt in reference to the Au atoms. By changing the exit angle from 90°, 60° and 40°, XPS measurements become more surface sensitive due to the altered probing depth. The material on top of the nanoparticles contributes more to the observed intensity in XP spectra due to the IMFP of the photoelectrons. This is known as surface sensibility and is described in section 3.2. When comparing the Au 4f and Pt 4f, the Pt content relative to Au was 15 % at 90°, 16 % at 60°, and 17 % at 40° exit angle. The increase in the relative Pt amount indicates that Pt is located on top of Au. After flash-annealing to 160 °C, the relative Pt amount is 13 % (90°) and 14 % (60°), indicating that Pt diffuses into the Au nanoparticle towards the substrate upon heating.

Pt-Au(5 nm)/TiO_2 (#12) was prepared identically to sample #11. In the XP spectra, the Pt amount relative to Au of sample #12 was 13 % and therefore 2 % lower than on the similarly prepared sample #11. The evaporation is not homogeneous over the whole sample, leading to minor variances in the Pt and Au amounts as determined by XPS. In the XP spectra of sample Pt-Au(4.5 nm)/TiO_2 (#13), the amount of Pt was 6.6 % and increased by a factor of four from 1.6 % on sample #12. Spectra taken at different positions on the sample show a deviation of ±1 % for the Au and ±0.5 % for the Pt fraction. For sample Pt-Au(6 nm)/TiO_2 (#14), the amount of Au is 11.6 % and Pt 12.6 %. Although the nominal evaporated amount of gold was doubled compared to sample #13, the observed % fraction in XPS only increased by ∼1 %. The XPS signal does not scale linearly with the gold amount. The probing depth of XPS is considered three times the inelastic mean free path, from which 95 % of photoelectrons originate, but 63 % originate from the top third of the probing depth. The inelastic mean free path in Au and Pt for a kinetic energy of ∼1400 eV is 1.5 nm. As the gold nanoparticles increase in height and are additionally overgrown by a Pt layer, fewer photoelectrons from gold contribute to the spectra.

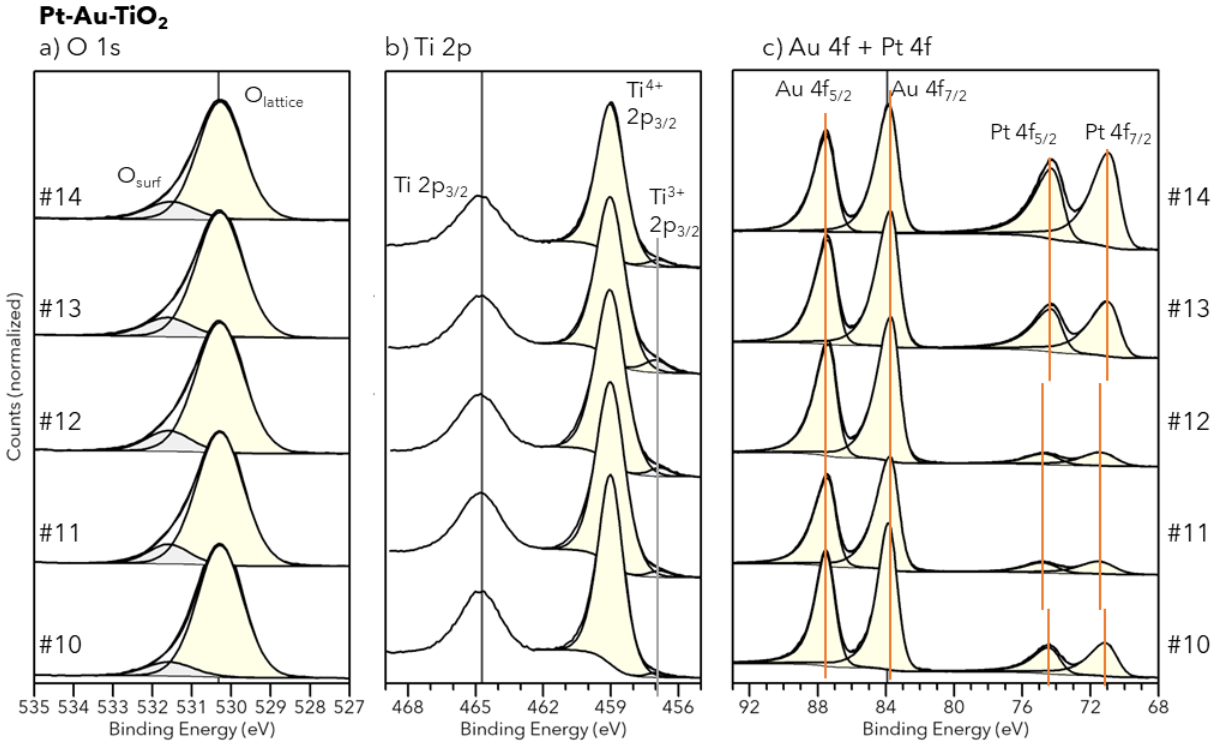

Figure 6.6: XP spectra of a) O 1s, b) Ti 2p, c) Au 4f and Pt 4f core level region of samples Pt-Au/TiO_2 #10-#14 recorded dierectly after Pt deposition. The spectra in a) are normalized on the $O_{lattice}$ peak and b) and c) on the Ti $2p_{3/2}$ peak, indicated by the black line.

STM

To compare the Pt-Au nanoparticles' size distributions, 50×50 nm STM images are displayed in Fig. 6.7. The Pt-Au nanoparticles on sample Pt-Au(6.5 nm)/TiO_2 (#10) differ in size and shape from the other samples. While the Au nanoparticles are round, the Pt overgrowth at 500 °C of sample #10 leads to large, less-defined, and elongated particles with smaller round particles in between. The diameter of the Pt-Au nanoparticles ranges from 3.5 to 16 nm, with a median of 6.5 nm. The smaller nanoparticles have a round shape, whereas the large nanoparticles seem to consist of smaller, agglomerated nanoparticles. Before Pt evaporation, the Au nanoparticles were presumably round, with a maximum size comparable to that of previous samples, approximately 12 nm. Au and Pt can form alloys, but the solubility of Pt in Au is limited to 17 % due to a wide miscibility gap [316]. This might lead to a non-homogeneous distribution of Au and Pt atoms in the nanoparticles. The lower surface free energy of Au energetically favors the segregation of Au at the surface [198]. This was not investigated on this sample, since no measurements with other exit angles were performed.

The STM images of sample Pt-Au(5.5 nm)/TiO_2 (#11) already show that the particle morphology differs from that of the Au particles overgrown with Pt at 500 °C. The Pt-Au

particles overgrown at room temperature look similarly round as the un-overgrown Au particles. The diameter of the Pt-Au nanoparticles ranges from 3 to 8 nm, with a median diameter of 5.5 nm and a maximum height of 2.1 nm. The diameter distribution of the samples overgrown with Pt at room temperature is similar to sample Au/TiO_2 #8.
The increase in the amount of Au and Pt of sample #14 gives rise to the increase in the diameter in STM, ranging from 2.5 to 7.5 nm with a median of 6 nm. Also, the maximum height increases to up to 3 nm. Additionally, the particles appear slightly more triangular, which can be attributed to the formation of facets.

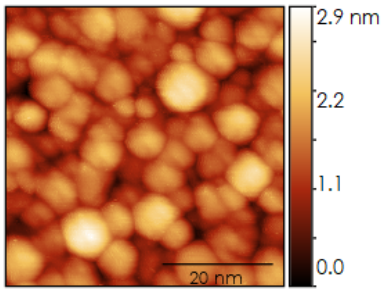

(a) #9 6 nm Au, 500 °C for comparision

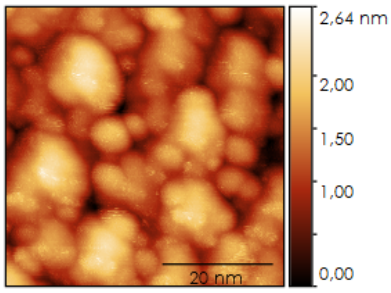

(b) #10 6.5 nm Au + Pt, 500 °C

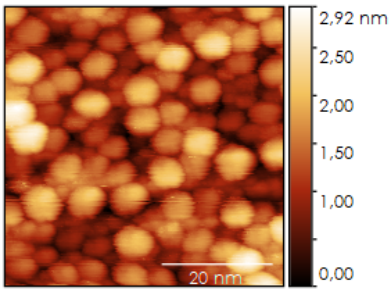

(c) #11 5.5 nm Au 500 °C + Pt RT

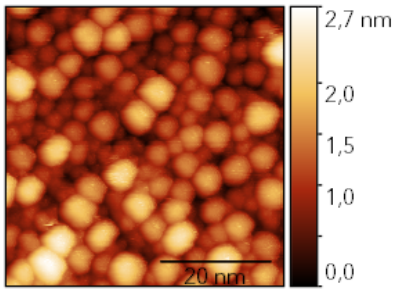

(d) #12 5 nm Au, 500 °C + Pt, RT

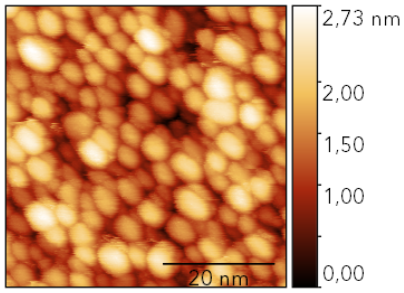

(e) #13 4.5 Au, 500 °C + 1 ML Pt, RT

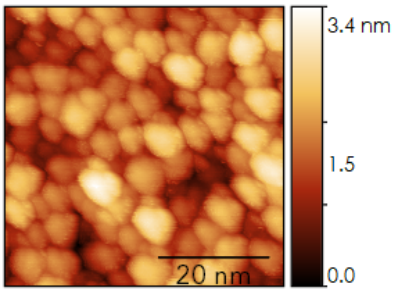

(f) #14 6 Au, 500 °C + 2 ML Pt, RT

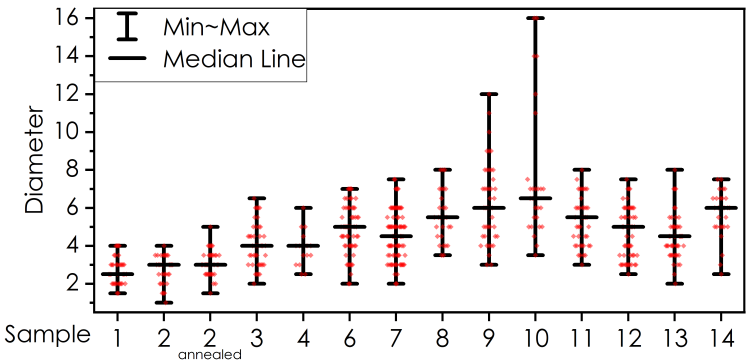

(g) Measured diameter ranges.

Figure 6.7: STM images (50x50 nm) of Pt-Au on TiO_2(110).

Summarizing remarks on the overgrowth of Pt on Au/TiO_2

The varied parameters for the overgrowth of Au nanoparticles on TiO_2 were the amount of Pt and the overgrowth temperature. The temperature during Pt evaporation influences the size and shape of the nanoparticles and the distribution of the Pt on the Au nanoparticles. A temperature of 500 °C during Pt evaporation led to an agglomeration of nanoparticles. The Au and Pt are mixed to some extent as the XRR data is fitted by a single layer. Probably Au and Pt do not form a homogeneous alloy as the solubility of Pt in Au is limited to 17 % due to a wide miscibility gap [316]. In contrast, when Pt is evaporated at room temperature, the Au nanoparticles keep their round shape, and Pt is located on top of Au. Due to the higher surface free energy of Pt, diffusion of Pt into the Au particles is energetically favorable [198], but XRR measurements reveal two layers with different electron densities. Studies by Tenney *et al.* [198] found no Pt on the surface of bimetallic Pt-Au nanoparticles when the fraction of Au was at least 50 %. This is further discussed in the context of the CO oxidation on Pt-Au/TiO_2, where CO is adsorbed on Pt atoms located at the surface.

6.2 (Photo-)Catalytic CO Oxidation on Au and Pt-Au on TiO_2

The CO oxidation was carried out in the XPS chamber under UHV conditions with a base pressure better than $5 \cdot 10^{-10}$ mbar. The sample was cooled with liquid nitrogen (LN2) to 96 ± 2 K. After cooling the samples, they were flash-annealed to 500 K to desorb water and other contaminants that adsorbed during cooling. After 15 min, the samples were cooled to at least 97 K again, and 2-5 L CO was dosed, after which it was exposed to $1{\cdot}10^{-6}$ mbar of O_2. Depending on the experiment, the sample was kept dark or illuminated by UV (365 nm) or visible (530 nm) light. For the CO oxidation *in steps*, XPS scans of the C 1s, Ti 2p, and O 1s core level were acquired after dosing and in 10-20 min steps during the CO oxidation. Measurements were recorded in the dark and under UHV conditions. During the CO oxidation, the X-ray source was turned off.
To reduce the experimental time, samples #7, #8, #9, and #10 were measured *in situ*, meaning the XP spectra were acquired continuously during dosing CO or O_2, so each O 1s and C 1s spectra is an average over a 15-min time slot during the CO oxidation. In prior experiments, no CO oxidation by the XPS source on TiO_2 was observed, so the influence of the X-ray source on the reaction can be neglected.

Fitting CO and CO_2

The signal of adsorbed CO and CO_2 in the C 1s and O 1s regions is two orders of magnitude lower than the signal from the substrate or nanoparticles due to the sub-monolayer adsorption. To identify the exact binding energy of each component, the gases were dosed individually. In the O 1s spectra, CO and CO_2 adsorbed on TiO_2 have a similar binding energy compared to the satellite peak of TiO_2 at 536 eV. During CO oxidation, multiple changes occur in the O 1s spectra in that region. The CO signal decreases, the CO_2 signal increases, but with twice the peak area due to the number of oxygen atoms in the molecule, and additionally, a water peak grows at around 534 eV. First, a background has to be chosen for accurate fitting. For a clean TiO_2 O 1s spectra, a Shirley background with the binding energy boundaries at 534 eV and 527-528 eV is applied. However, under CO oxidation conditions, a water signal appears at 534 eV, leading to a too-high background. For a consistent analysis, the linear background is chosen. The area and position of the satellite feature are adjusted to the linear background, and the area is in fixed relation to the $O_{lattice}$ peak. For the C 1s spectra, the peak intensity is lower than that of the lattice peaks, and the background intensity does not drop; thus, the linear background is an accurate approximation.
The error of the determined CO_2 amount depends on the signal-to-noise ratio. For the catalysis experiment on sample Au(2.5 nm)/TiO_2 (#1), the small nanoparticles allowed

a high CO adsorption. Combined with high counts of the XPS, the C 1s and O 1s spectra clearly show the oxidation of CO to CO_2, due to the high signal-to-noise ratio and were fitted with an error of max. 5 % for the relative CO_2 amount compared to CO. For all other CO oxidation experiments on gold nanoparticles, the O 1s region is primarily used to determine the amount of CO_2 relative to CO. The C 1s region of the experiments on samples #6-#10 exhibits a too-low signal-to-noise ratio for reliable peak fitting. The signal-to-noise ratio of O 1s compared to C 1s for similar scan times is greater since the photoelectric absorption of Al Kα with an energy of 1485.6 eV is 1588 cm^2/g for oxygen atoms and 719 cm^2/g for carbon atoms [317]. All adsorbates in C 1s and O 1s spectra are fitted with a GL(30) peak shape.

6.2.1 CO and CO_2 Adsorption

For an accurate assignment of CO and CO_2 in the C 1s and O 1s region, the adsorption at 97 K was studied on the stoichiometric surface without Au, on small Au NPs with a median diameter of 2.5 nm (#1), and on larger Au nanoparticles with a median diameter of 4.5 nm to 6 nm (#6-#9). On the **stoichiometric rutile (110)** surface, CO adsorbs at 97 K up to a maximum coverage of 0.5 ML with the C-atom on top of the Ti_{5c} atom [73]. In the C 1s spectra(Fig. 6.8), the CO signal consists of two peaks, one at 290.0 ± 0.1 eV and a smaller peak at 292.0 ± 0.3 eV, whose area is 25-30 % of the first peak. These individual contributions may arise from different adsorption sites or geometries. In the O 1s spectra, the CO peak at 536.1 eV is located in close proximity to the lattice oxygen's satellite peak at 536.0 eV, while lattice oxygen itself is centered at 530.3 eV.
CO_2 adsorption at 97 K is, in contrast to CO, not limited to 0.5 ML. When 1 L CO_2 is dosed, it appears in the C 1s region as one peak at 291.4 eV with a small shoulder at 293.1 eV that attributes to 10% of the CO−2 signal (Fig. 6.8). With increasing coverage, the peak shifts by 0.2 eV to 292.6 eV due to multilayer formation. The shoulder remains unchanged. In the O 1s region, the CO_2 peak is located at 535.0 eV and does not shift with increasing coverage.
On **sample Au(2.5 nm)/TiO_2 (#1)**, 2 L of CO were dosed, and then the sample was slowly heated until complete desorption. XPS scans of C 1s were taken every 3 K. This measurement protocol was repeated with CO_2. The C 1s region of the CO signal at 97 K consists of three peaks, shown in Fig. 6.9. Two features are similar to the observation on clean rutile, located at 290.0 eV and 291.9 eV, and are assigned to CO on the rutile substrate. The third component at 291.0 eV is assigned to CO bound to either gold or the Au/TiO_2 interface. Another peak at 293.5-294.0 eV arises from potassium contaminants within the TiO_2 bulk, with the K 2p core level at ∼293 eV. When the sample is heated, the component assigned to CO-Au desorbs between 100 K and 103 K. CO on TiO_2 desorbs between 106 K and 110 K. In the O 1s core-level spectra, adsorbed CO is visible at a

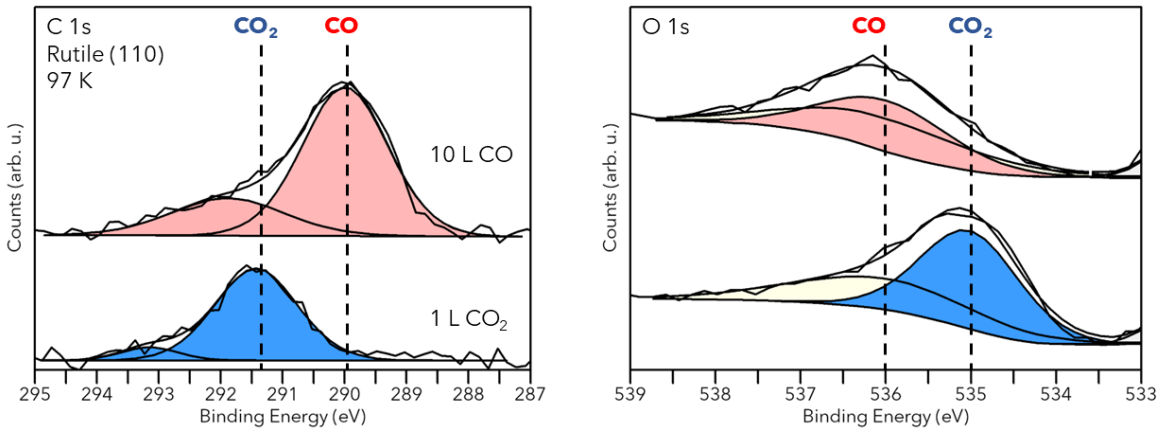

Figure 6.8: C 1s and O 1s XP spectra of CO (red) and CO_2 (blue) adsorption on rutile (110). In C 1s an additional peak for CO and CO_2 is observed. In O 1s the CO and CO_2 peak overlap with the satellite feature.

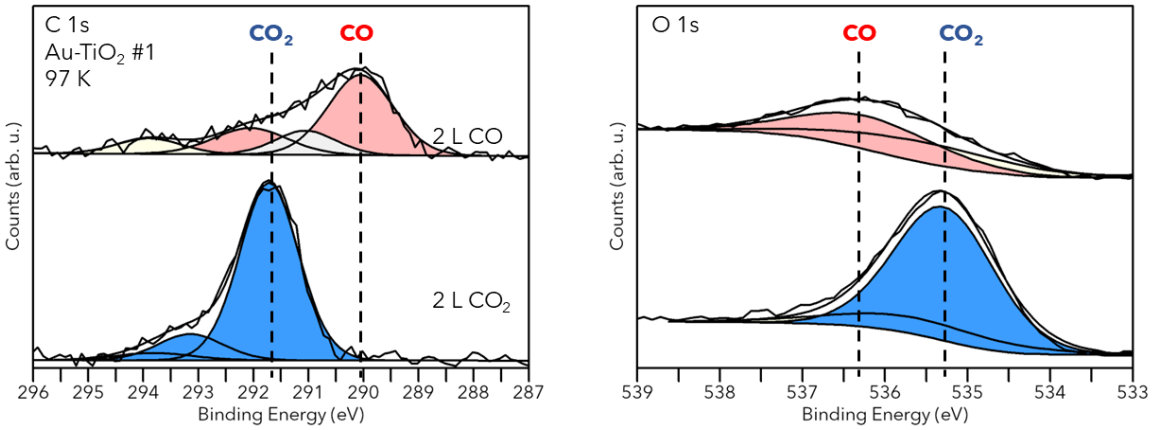

Figure 6.9: C 1s and O 1s XP spectra of CO (red) and CO_2 (blue) adsorption on Au(2.5 nm)/TiO_2 (#1)

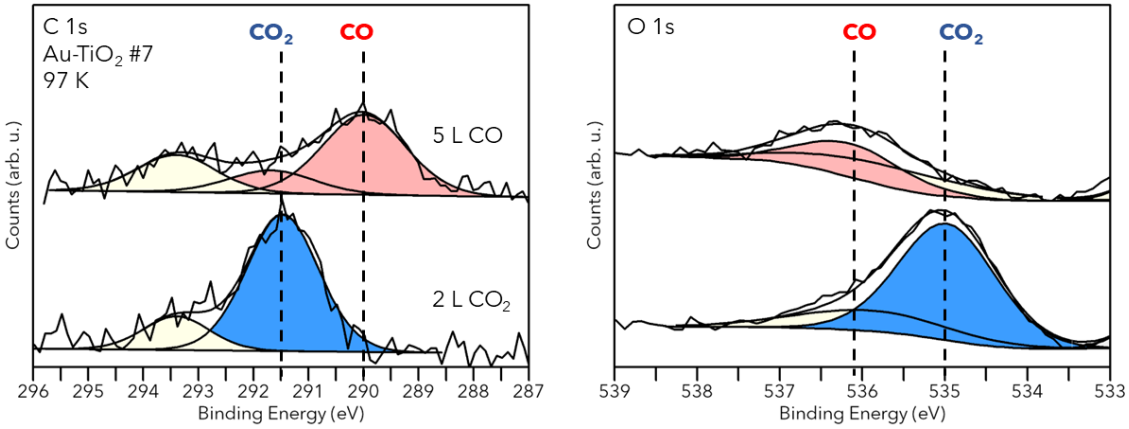

Figure 6.10: C 1s and O 1s XP spectra of CO (red) and CO_2 (blue) adsorption on Au(4.5 nm)/TiO_2 #7.

binding energy of 536.2 eV. After exposure to 2 L CO_2, the C 1s spectra reveal a feature at 291.7 eV with a small shoulder at 293.1 eV, amounting to about 13% of the CO_2 signal. CO_2 desorbs from Au(2.5 nm)/TiO_2 (#1) at 115 K. In the O 1s region, CO_2 is observed at 535.2 eV. To determine the adsorption position of CO on gold, an **Au (111)** single crystal was cleaned, cooled to 97 K, and exposed to CO. No adsorption was observed even in $1{\cdot}10^{-7}$ mbar CO atmosphere. Previous studies also found no CO adsorption on Au (111) at 90 K under UHV conditions [318].
For the **samples with higher Au coverage and larger nanoparticles** (#6-#9) CO adsorbs with 2 peaks similar to clean rutile in the C 1s region at 290.0 eV and 291.7 eV ± 0.2 eV and as one peak in the O 1s region at 536.1 ± 0.1 eV (Fig. 6.10). The results in the C 1s region suggest a lower CO adsorption compared to sample Au(2.5 nm)/TiO_2 (#1) due to the more bulk-like configuration of the larger gold nanoparticles. CO_2 adsorbs at 291.5±0.1 eV in the C 1s and at 535.0 eV in the O 1s core level spectra.

6.2.2 CO Oxidation on Bare Rutile TiO_2(110)

To study the effect of the gold nanoparticles, the UV-induced CO photooxidation on rutile (110) was studied as a reference in two different settings: in steps (alternating measurement and exposure to gases and light) and in situ (measurement during exposure to gases and light). Additionally, the CO oxidation was tested under 530 nm light and without light. In the following, the amount of CO_2 will be indicated relative to the CO amount measured in the same spectra.
The CO oxidation in steps was repeated several times in this study to ensure consistency of results and has also been published by Wagstaffe *et al.* [85]. The oxidation was monitored in the O 1s and C 1s regions. The CO oxidation was observed on the C 1s spectra (Fig. 6.11) measured in steps of 20 minutes. During the XPS measurement, the O_2 valve was closed, so the residual partial pressure was $1 \cdot 10^{-9}$ mbar, and the chamber was shielded from light. During CO oxidation, the X-ray source was turned off when the sample was exposed to O_2 and light. After 120 minutes, the reaction reached the final CO_2 amount with a relative CO_2 amount of 50 %. The relative CO_2 amount for each displayed spectrum can be found in the appendix in Tab. B.7.
This experiment was repeated with 530 nm light instead of UV on different rutile (110) substrates (Fig. 6.13). Under 530 nm light, the oxidation was not changing anymore after 120 min with a final CO_2 amount of 60%. Both oxidation experiments have a low overall CO_2 yield, as rutile is the less active photocatalyst compared to anatase. The visible light activation might be due to new intra-bandgap states induced by adsorbed oxygen. This mechanism is also discussed in Chapter 5 and was observed by a previous study on anatase [34].

In comparison, for the in situ CO oxidation in Fig. 6.12, the C 1s region was measured continuously, while the sample was exposed to light and $1 \cdot 10^{-6}$ mbar O_2. The final relative CO_2 amount was also reached after 120 min but was with 30 % lower than for the experiment measured in steps. This can be explained by the lower desorption of CO, as the total time of the experiment is reduced by saving time by combining XPS measurement and exposure to reaction conditions. With less CO desorption, the final relative CO_2 fraction decreases. A factor also might be water adsorption. Residual water from the UHV chamber adsorbs during the reaction at 97 K and can interact with CO and CO_2. It is reported that water stabilizes CO_2 adsorption [82]. A longer time at low temperatures, which is the case for the step-wise measurement, leads to higher water adsorption, which stabilizes formed CO_2 and prevents desorption, leading to a higher CO_2 amount.

In the C 1s region, CO was fitted with two components. The ratio of those components was constant over the whole CO oxidation, assuming that both adsorbed CO variants are equally likely to be oxidized to CO_2. CO_2 was fitted by one component. In the O 1s spectra, CO and CO_2 were fitted by one component. Additionally, a water feature was fitted at 534.0 ± 0.2 eV. Residual water from the UHV chamber adsorbs steadily on the cold substrate and accumulates over time. With increasing coverage, the peak shifts from 534.2 eV to 533.8 eV. No CO_2 formation was observed after 90 min in O_2 on rutile (110) with 2 L CO (Fig. B.9). Also, after 180 min in UHV under X-ray radiation from the XPS source with 5 L CO preadsorbed, no oxidation was observed.

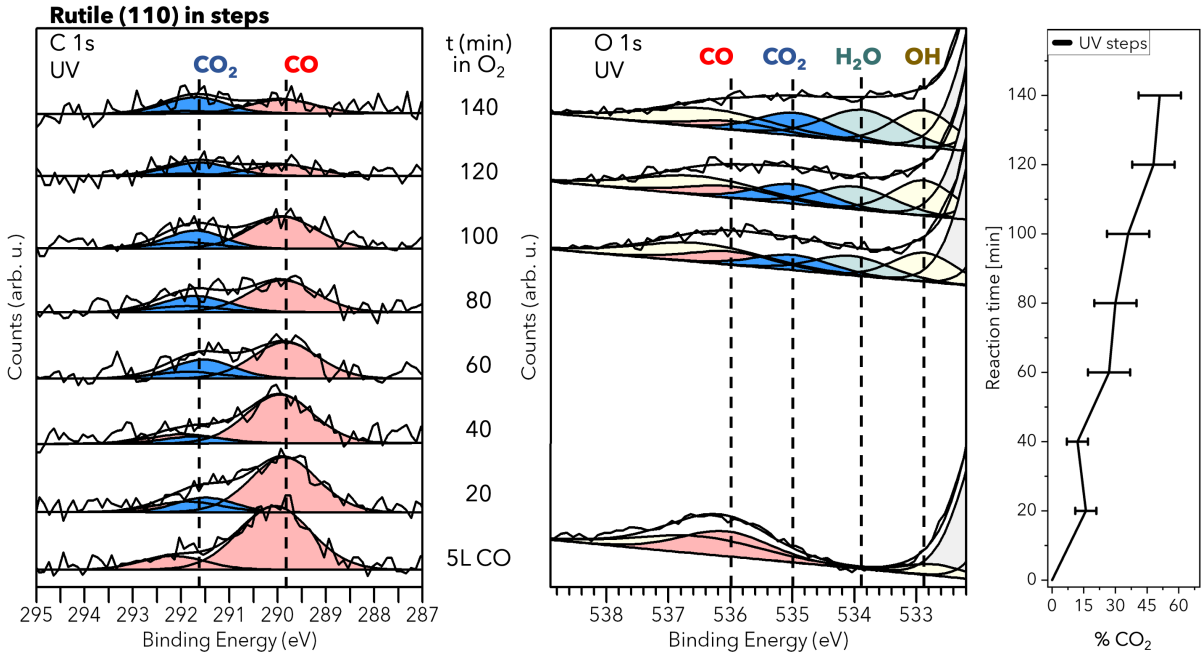

Figure 6.11: UV-induced CO photooxidation on pristine stoichiometric rutile/TiO_2(110) monitored in the C 1s (left) and O 1s (right) core level region by XPS *in 20 min steps.*

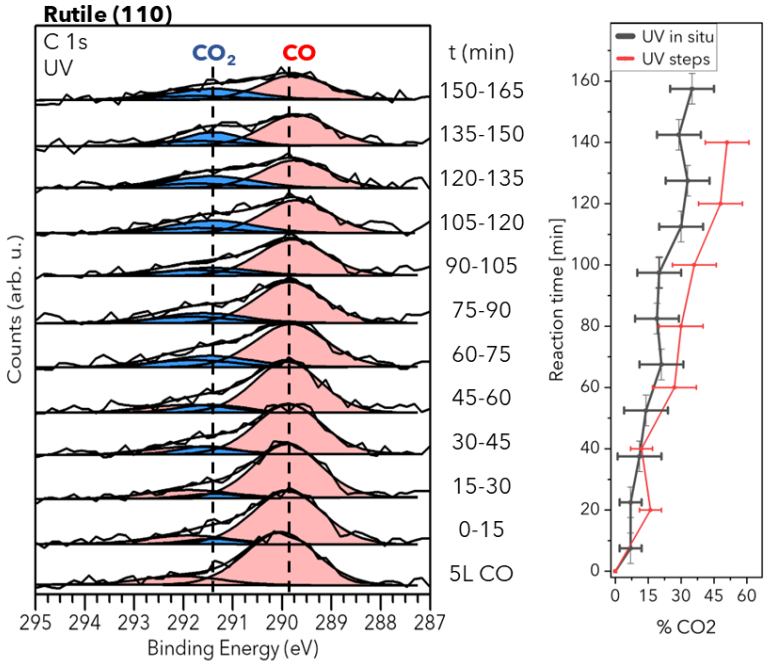

Figure 6.12: UV-induced CO photooxidation on pristine stoichiometric rutile/TiO_2(110) monitored during gas and UV light exposure in the C 1s (left) core level region by XPS *in situ*.

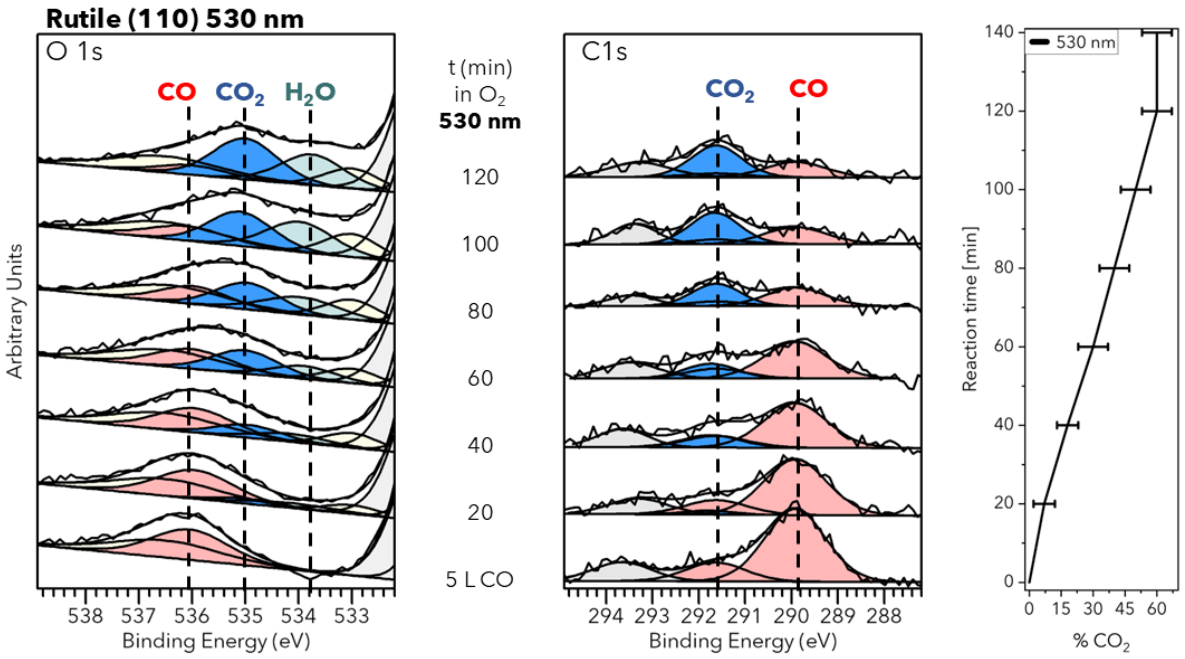

Figure 6.13: 530 nm induced CO photooxidation on pristine stoichiometric rutile/TiO_2(110) monitored in the O 1s (left) and C 1s (right) core level region by XPS in 20 min steps.

6.2.3 CO Oxidation on Au/TiO_2

CO Oxidation on Sample Au(2.5 nm)/TiO_2 (#1)

The CO oxidation at 97 K on sample Au(2.5 nm)/TiO_2 (#1) was monitored in 10 min steps under UV light and without light (Fig. 6.14). The C 1s spectra were fitted by three CO components, for which the area ratio and distance in binding energy were kept constant over the whole oxidation period. The core-level scans of C 1s showed a complete conversion of CO to CO_2 in 40 minutes, regardless of dark conditions or UV light irradiation. The relative final CO_2 amount was 90 %. No desorption of CO and CO_2 during the reaction is observed since the peak area of the spectra does not decrease. Compared to the pure rutile (110) substrate, Au nanoparticles increase the CO adsorption, lower CO desorption, and increase the catalytic performance. Interestingly, UV light does not influence the CO oxidation. Repeated heating of the surface as part of the cooling procedure before each experiment does not decrease the catalytic performance, as indicated by the converted CO during oxidation. The dark CO oxidation was carried out 4 days after the UV-induced CO oxidation, and the substrate was flash-annealed 4 times to 600 K between the CO oxidation experiments. Dark CO oxidation results in the same outcome as UV light. If the repeated flash annealing had decreased the catalytic performance, UV light would have had a similar inhibiting character. This is unlikely since it initiates photocatalysis of the rutile (110) substrate.
The low amount of gold nanoparticles increases the (photo-)catalytic CO oxidation, especially without light, as clean rutile does not convert CO to CO_2 without light. The final CO_2 amount of 90 % is nearly a complete conversion and more than on rutile (110). The relative CO_2 amount for each displayed spectrum is in the appendix in Tab. B.8.

CO Oxidation on Sample Au(5 nm)/TiO_2 (#6)

The CO oxidation at 97 K was performed under UV, 530 nm, and dark in 10-minute steps (Fig. 6.15). The signal of 5 L CO adsorbed at 97 K was lower than on sample Au(2.5 nm)/TiO_2 (#1). This can be partly due to the less intense X-ray source. Secondly, the high amount of gold increases the background contribution in the XP spectra, leading to a worse signal-to-noise ratio. However, the main reason is that the adsorption of CO on gold declines with the increasing size of the nanoparticle. Due to the low signal-to-noise ratio, the O 1s core level was used for analysis, as the CO_2 signal is double in O 1s compared to C 1s scans due to its stoichiometry. The CO oxidation under dark conditions was recorded up to 50 min and reached a relative amount of 50 % CO_2. Under 530 nm and UV light, the CO oxidation was completed after 40 min with a relative CO_2 amount of 50 % and 55 %, respectively. This shows that CO oxidation is slightly promoted by 530 nm or UV light. It is especially clear in the spectra after 10 min in O_2, where a

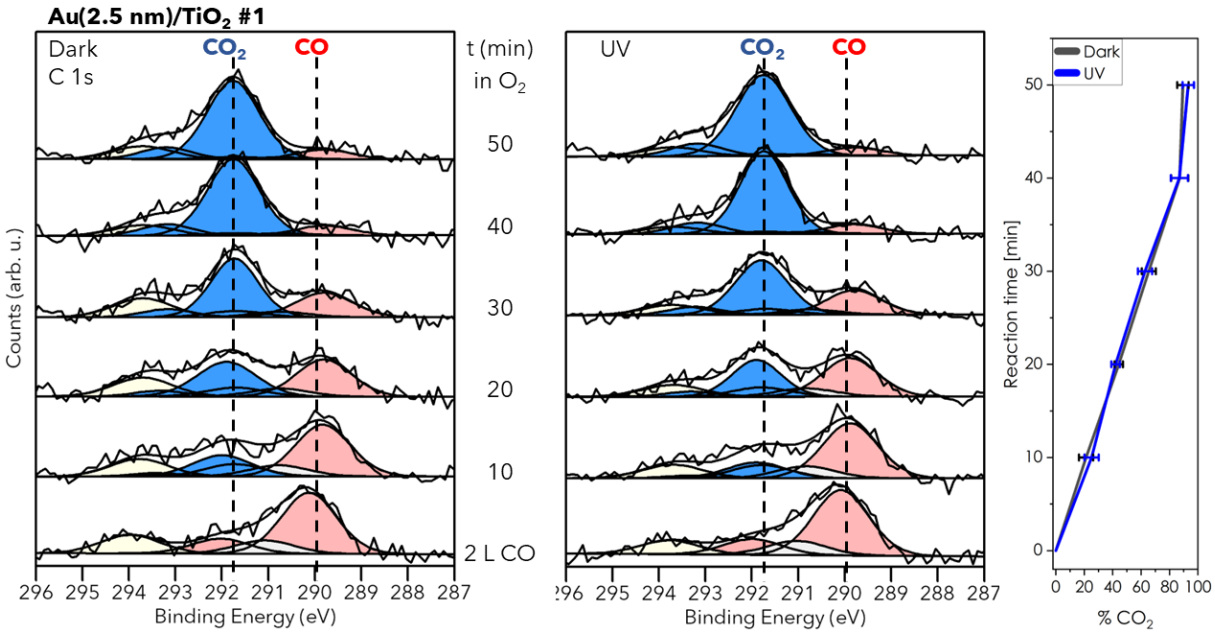

Figure 6.14: C 1s XP spectra of CO oxidation on sample Au(2.5 nm)/TiO_2 (#1).

higher amount of CO_2 for the light-induced CO oxidation reactions is observed. During the oxidation, ∼20 % of CO desorbed. In the O 1s core level region, water adsorbs at 534.2 eV. For each spectrum, the area of CO and CO_2 was confined so as not to extend the area of the initially adsorbed CO measured in the first spectrum. The relative CO_2 amount for each displayed spectrum can be found in the appendix in Tab. B.8.
In comparison to sample Au(2.5 nm)/TiO_2 (#1), sample Au(5 nm)/TiO_2 (#6) differs in the amount of gold deposited during the nanoparticle growth and the sample temperature during evaporation, leading to larger gold nanoparticles. The CO oxidation is less effective on sample Au(5 nm)/TiO_2 (#6) with a relative CO_2 amount of up to 55% and a higher desorption of CO or CO_2. However, a slight influence of light on the catalytic activity was observed. For sample Au(2.5 nm)/TiO_2 (#1), the smaller gold nanoparticles reached a conversion rate of 90 % with nearly no desorption, but no effect of UV light was observed. Compared to stoichiometric rutile (110), the CO oxidation is faster.

CO Oxidation on Sample Au(4.5 nm)/TiO_2 (#7)

The CO oxidation on sample Au(4.5 nm)/TiO_2 (#7) was monitored under dark and 530 nm light conditions in 10-minute steps and under UV light in 15-minute steps (Fig. 6.16). The dark CO oxidation was complete after 50-60 min with a relative CO_2 amount of 35 %, the 530 nm after 60 min with 40 % CO_2, and the CO oxidation under UV light after 90 min with 50 % CO_2. The CO oxidation induced by light has a higher final relative CO_2 amount compared to the dark CO oxidation, but the effect on the rate is insignificant. The relative CO_2 amount for each displayed spectrum can be found in the appendix in

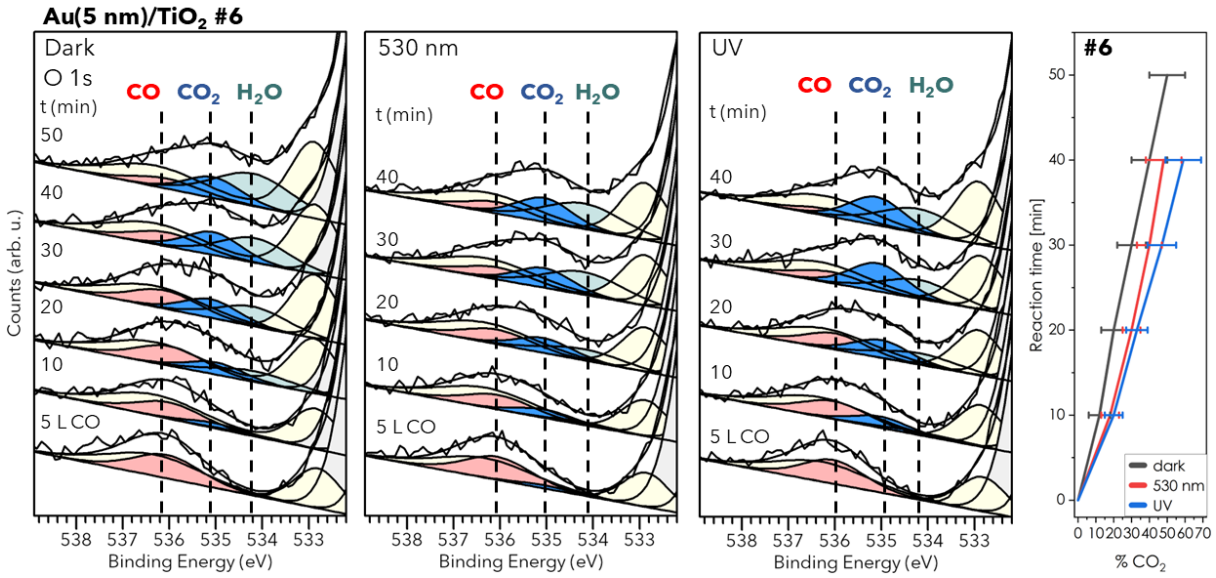

Figure 6.15: O 1s of the CO (red) oxidation to CO_2 (blue) on Au(5 nm)/TiO_2 (#6) under dark, 530 nm and UV light conditions.

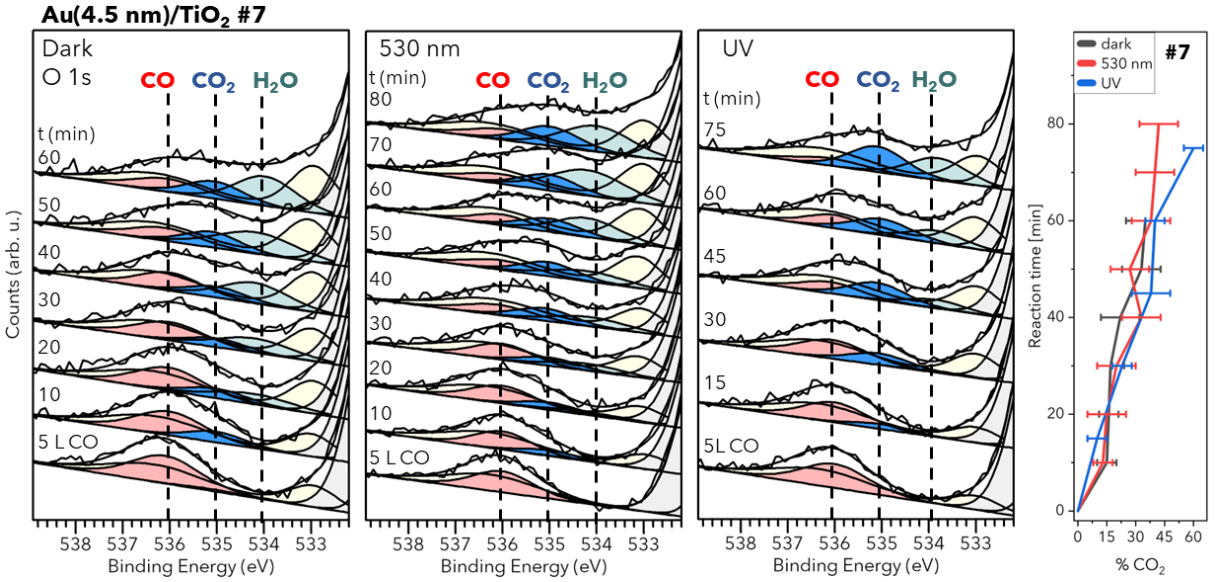

Figure 6.16: O 1s of the CO (red) oxidation to CO_2 (blue) on Au(4.5 nm)/TiO_2 #7 under dark, 530 nm and UV light conditions.

Tab. B.9.

The desorption of CO is estimated to amount to ∼30 % compared to the peak area of adsorbed CO before the oxidation. This is higher than the desorption on sample Au(5 nm)/TiO_2 (#6), but the error bar on this estimation is ∼10 %. The amount of gold measured in XPS was similar, but the sample temperature during evaporation and the annealing time differs, as sample Au(4.5 nm)/TiO_2 (#7) was deposited at 500 °C (400 °C for sample #6) and the post-annealing was two hours in total (10 min for sample #6). CO oxidation is less efficient despite the sizes being comparable, as sample #7

has more bulk-like properties induced by post-annealing. The CO oxidation (under all light conditions tested) is less efficient on sample Au(4.5 nm)/TiO_2 (#7) than on sample Au(5 nm)/TiO_2 (#6) measured by the relative amount of CO_2. The final amount of CO_2 is lower, and more CO/CO_2 desorbs. The oxidation rate under dark, UV, and 530 nm light is similar. Compared to stoichiometric rutile (110), the CO oxidation is faster on sample #7.

CO Oxidation on Sample Au(5.5 nm)/TiO_2 (#8)

For sample Au(5.5 nm)/TiO_2 (#8), the measurement of the CO oxidation was changed to measuring in situ and not in steps. Therefore, the sample was exposed to $1{\cdot}10^{-7}$ mbar CO during the XPS measurement of the C 1s, O 1s, and Ti 2p core level region for 30 min. After completion of the scans, the CO valve was closed, and the sample was exposed to $1{\cdot}10^{-6}$ mbar O_2. Simultaneously, the C 1s, O 1s, and Ti 2p core-level regions were scanned continuously. The CO oxidation was monitored for up to 150 minutes. On this sample, the relative final amount of produced CO_2 is greater for the light-induced CO oxidation (530 nm and UV light) with 50 % than the dark CO oxidation with 30 %, as seen in the O 1s spectra in Fig. 6.17. The relative CO_2 amount for each displayed spectrum can be found in the appendix in Tab. B.10. On this sample, UV and 530 nm light enhanced the CO oxidation. Compared to pristine rutile (110), the final relative CO_2 amount is higher. The dark CO oxidation is probably catalyzed on the smaller nanoparticles. The minimum measured diameter was 3.5 nm, which is close to the catalytically most active size of 2.5-3 nm for Au nanoparticles.

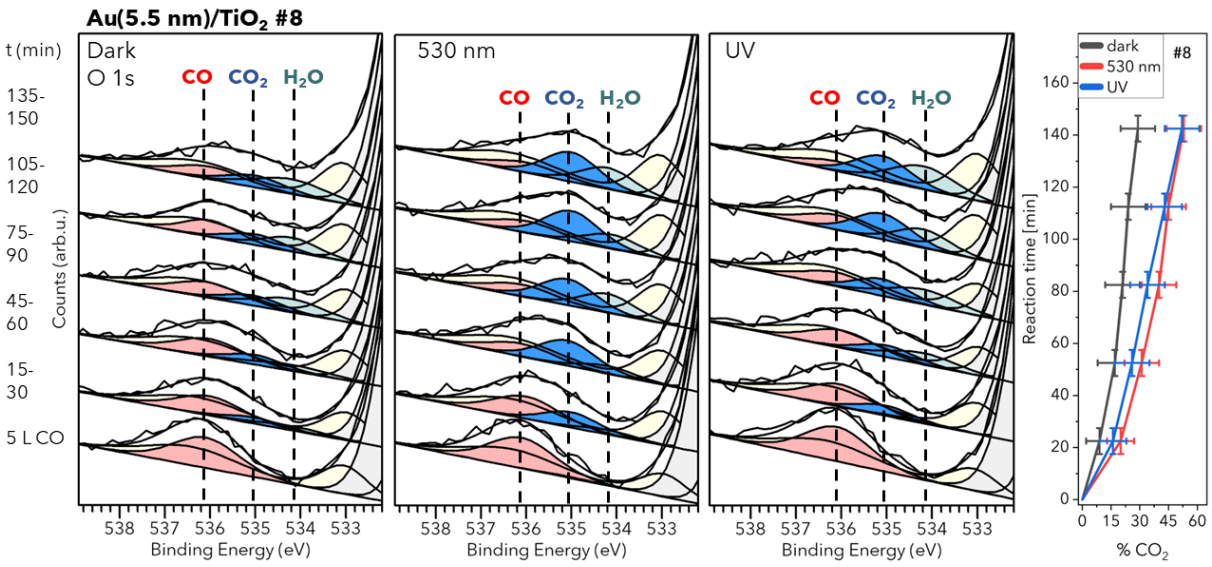

Figure 6.17: O 1s of the CO (red) oxidation to CO_2 (blue) on Au(5 nm)/TiO_2 #8 under dark, 530 nm and UV light conditions.

CO Oxidation on Sample Au(6 nm)/TiO_2 (#9)

Sample Au(6 nm)/TiO_2 (#9) was prepared similarly to sample Au(5.5 nm)/TiO_2 (#8) but differs in the number of defects, observed by the amount of Ti^{3+} in the Ti 2p spectrum in section 6.1.1. The CO oxidation on sample Au(6 nm)/TiO_2 (#9) was investigated under UV light (Fig. 6.18). The relative CO_2 amount for each displayed spectrum can be found in the appendix in Tab. B.10.

The conversion to CO_2 was complete after 200 min with a final relative CO_2 amount of 34%. Thus, the catalytic process is slower and a lower relative CO_2 amount compared to sample Au(5.5 nm)/TiO_2 (#8) is observed. The most obvious difference between samples #8 and #9 is the number of defects, leading to the conclusion that surface defects detected as Ti^{3+} promote UV-induced CO oxidation. However, the size also differs, which is probably connected to the defect amount. The smaller median and maximum diameter measured on sample #8 might contribute to its more efficient CO oxidation compared to sample #9. The CO oxidation on sample #9 has a lower rate than on stoichiometric rutile (110).

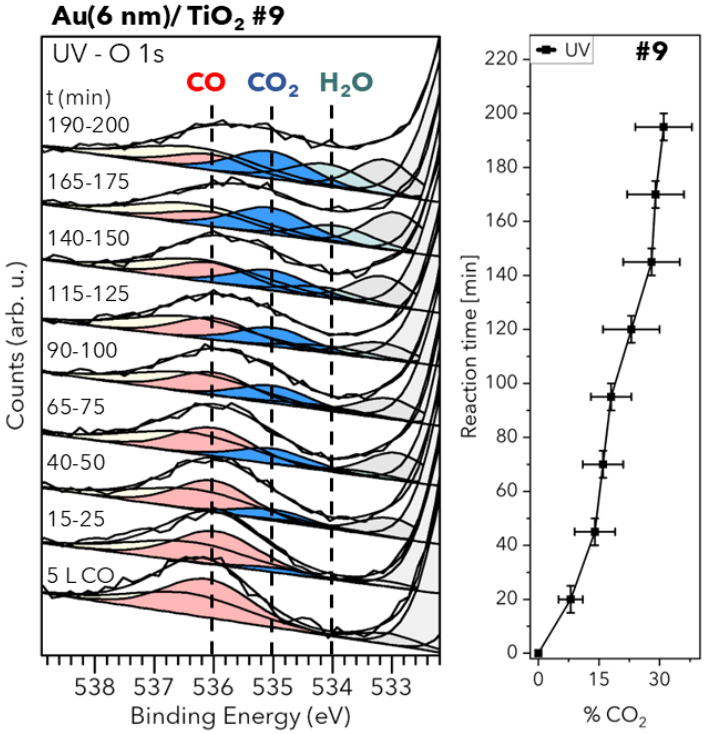

Figure 6.18: O 1s of the CO (red) oxidation to CO_2 (blue) on Au(6 nm)/TiO_2 #9 under UV light.

Table 6.3: Summary of CO oxidation experiments on Au/TiO_2 in XPS.

Sample	CO Oxidation	Steps	Complete After (min)	Final Rel. % CO_2	Result
Rutile	UV	20 min	120	50	
	530 nm		120	60	
	dark		no oxidation	–	
	UV	in situ	130	35	
#1	dark, UV	10 min	40	90	no UV effect
#6	dark	10 min	50	50	faster
	530 nm		40	50	with
	UV		40	60	light
#7	dark	20 min	50	35	similar
	530 nm		60	40	rate
	UV		75	60	
#8	dark	in situ	140	30	higher
	530 nm		140	53	conversion
	UV		140	52	with light
#9	UV		200	35	least efficient

Concluding Remarks on the CO Oxidation Au on TiO_2

The CO oxidation on Au/TiO_2 was carried out on five samples under dark, UV, and 530 nm light. Small Au nanoparticles on TiO_2 (110) with a median size of 2.5 nm showed a 90 % conversion of CO to CO_2 in 40 minutes under dark conditions and UV light. The rate and the relative final CO_2 amount of the CO oxidation exceed the results on pristine rutile (110). The results are in agreement with previous research [25] that small Au nanoparticles on metal oxides are efficient catalysts for CO oxidation, with a peak efficiency at a diameter of 2.5-3 nm and a declining rate with increasing size.

The Au nanoparticle size was increased by increasing the amount of deposited Au and elevating the sample temperature during and after the Au evaporation to study the influence of light on CO oxidation. The increased nanoparticle diameter reduced CO adsorption as the Au nanoparticles became more bulk-like. For the sample Au(5 nm)/TiO_2 (#6) and sample Au(5.5 nm)/TiO_2 (#8), a slight increase in CO oxidation was observed under UV light and 530 nm light. Sample #6 was not post-annealed, whereas sample #8 was post-annealed for three hours. The difference in median size is only 0.5 nm, but the CO oxidation was significantly faster on the not-annealed sample Au(5 nm)/TiO_2 (#6) with 40 min instead of 140 min (#8). The reason can be the difference in catalytic sites: smaller nanoparticles provide more perimeter sites with the substrate compared to larger ones. Another reason could be the decrease in low-coordinated Au atoms and more bulk-like properties due to the elevated temperature and post-annealing of sample #8. Low-coordinated Au atoms are considered catalytically active sites [115, 155]. The

increase in CO oxidation under 530 nm light might be due to the excitation of the LSPR. Interestingly, also on rutile (110), the CO oxidation was observed under 530 nm light, so the mechanism might also occur on Au on rutile(110). As a dark activity is found on both samples, light might induce several CO-oxidation mechanisms.
No light-induced effect was observed for sample Au(4.5 nm)/TiO_2 (#7), which coincides with the smallest median nanoparticle size of the samples grown at elevated temperatures (#6-#9). This emphasizes the high catalytic activity of smaller gold nanoparticles. To control the CO oxidation by light, the amount of small nanoparticles has to be minimized. Sample Au(6 nm)/TiO_2 (#9) was least efficient for the CO oxidation, even compared to stoichiometric rutile (110). It has the largest nanoparticle diameter yet a low defect rate. A low amount of defects might lead to larger nanoparticles, which are less efficient catalysts, while defects also might directly influence the catalytic activity, and in this case, promote the CO oxidation. These findings agree with a study [319] observing a coupling effect of oxygen vacancies with the LSPR of the Au particles, leading to an enhanced catalytic performance. Additionally, on pure rutile (110) surface defects lead to a faster CO oxidation [85].

6.2.4 CO Oxidation on Pt-Au/TiO_2

The CO oxidation was tested on samples #10, #12, and #14. While CO does not adsorb on Au(111), neither at room temperature nor at 97 K (Fig. B.8), it does adsorb on Pt(111) at room temperature. The role of overgrown Pt was not only to increase the CO adsorption but also to enable room temperature adsorption.

CO Adsorption on Pt(111)

To assign CO and CO_2 bound to Pt on the C 1s and O 1s XP spectra, the CO (Fig. 6.19) and CO_2 adsorption on a **Pt(111)** single crystal was studied. The cleaned Pt (111) single crystal was exposed at room temperature (296 K) to 10 L CO. The spectra were recorded for C 1s, O 1s, and Pt 4f. The O 1s core level shows two peaks, one broader at 532.7 eV with a FWHM of 1.7 eV and one at 530.8 eV with a FWHM of 1.1 eV. The ratio of the peak areas is 73:27. The peaks are assigned to different adsorption sites: top and bridge positions [320]. The C 1s spectra consist of one broader asymmetric peak at 286.3 eV with a FWHM of 2.2 eV. The broad peak includes the top and bridge adsorption sites, which have an energy difference of 0.7 eV and are not resolved in this spectrum. The asymmetry is partly due to an unresolved vibrational fine structure [321]. Additionally, adventitious carbon is visible at 283.7 eV. The sample was cleaned the previous day for the overnight cool down to room temperature, leading to adventitious carbon adsorption. In an O_2

atmosphere, no RT CO oxidation was observed since CO blocks all adsorption sites. On Pt, two neighboring adsorption sites are required for dissociative O_2 adsorption. Usually, CO oxidation experiments on Pt are done with preadsorbed O_2 to avoid CO poisoning of the sample.
For the CO_2 adsorption, the sample was reprepared by sputtering and annealing. No CO_2 adsorption was observed at room temperature after exposure to 20 L CO_2.

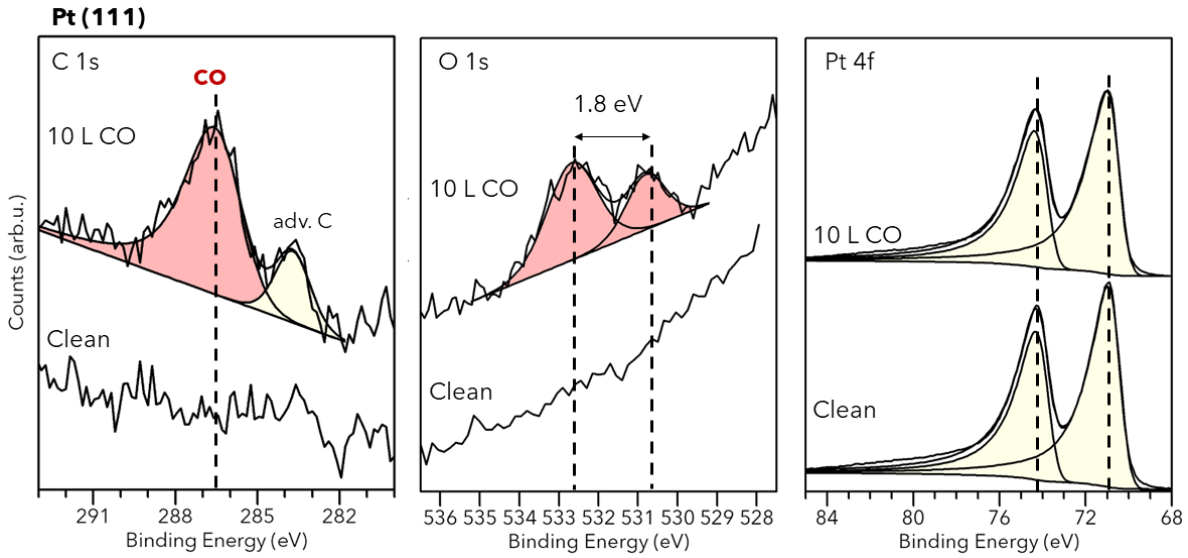

Figure 6.19: XPS data of C 1s, O 1s and Pt 4f of CO adsorption on Pt (111) at RT.

CO Adsorption on Pt-Au/TiO_2

Room temperature CO adsorption on Pt-Au/TiO_2 was tested for three samples with different Pt coverages overgrown at room temperature. On sample Pt-Au(5 nm)/TiO_2 (#12) with a nominal layer thickness of Pt of 0.25 ML, no room-temperature CO adsorption was observed (Fig. 6.20). On the samples Pt-Au(4.5 nm)/TiO_2 (#13) with 1 ML Pt and Pt-Au(6 nm)/TiO_2 (#14) with 2 ML Pt, CO adsorbs at room temperature with a binding energy of 286.7 eV in the C 1s region. In the O 1s region, the binding energy of CO-Pt(111) coincides with the lattice peak of TiO_2, so the C 1s region is used for analysis.

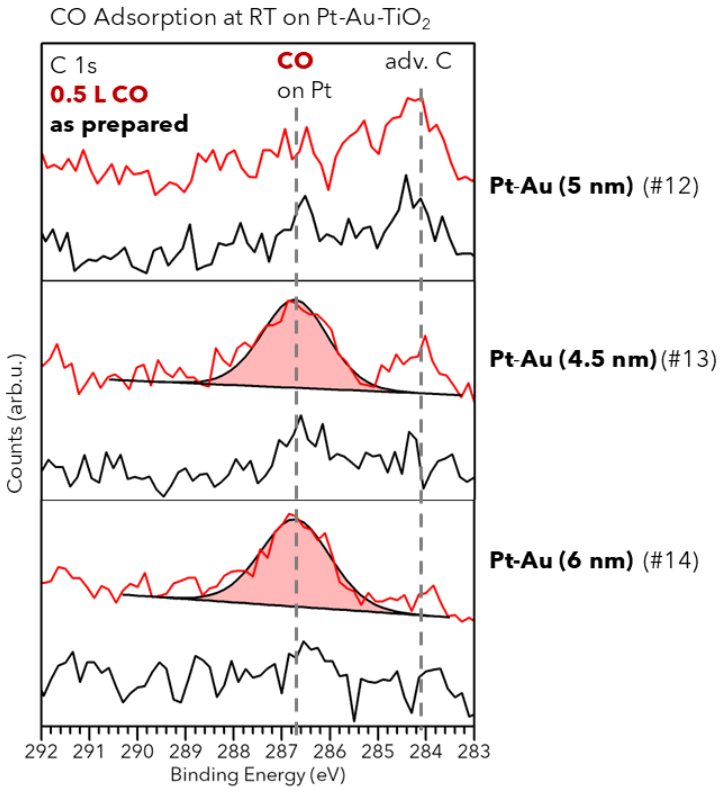

Figure 6.20: CO adsorption on samples Pt-Au/TiO_2 #12-#14.

Low Temperature CO Oxidation

Sample Pt (500 °C)- Au(6.5 nm)/TiO_2 (#10). The room temperature CO adsorption was not tested on this sample, but the CO oxidation at 97 K under dark, 530 nm, and UV light conditions (Fig. 6.21). The relative CO_2 amount for each displayed spectrum can be found in the appendix in Tab. B.11.

The CO adsorption was similar to the Au/TiO_2 samples regarding binding energy and peak shape, and was fitted similarly in C 1s and O 1s. The adsorption behavior indicates that Pt is located either within the subsurface or not in an electronic configuration similar to bulk Pt, for which CO adsorption at 286 eV in the C 1s spectrum would be observed. For the CO oxidation at 97 K, only 22 ± 5% CO_2 relative to CO is observed. No influence of light (UV or 530 nm) on CO oxidation is observed. The CO conversion is less efficient than on pure Au/TiO_2, for which a final CO_2 amount of 50 to 90 % was measured (Tab. 6.3). Pt has a hindering effect on CO oxidation when alloyed with Au. The CO oxidation rate and final relative CO_2 amount are lower than on stoichiometric rutile (110).

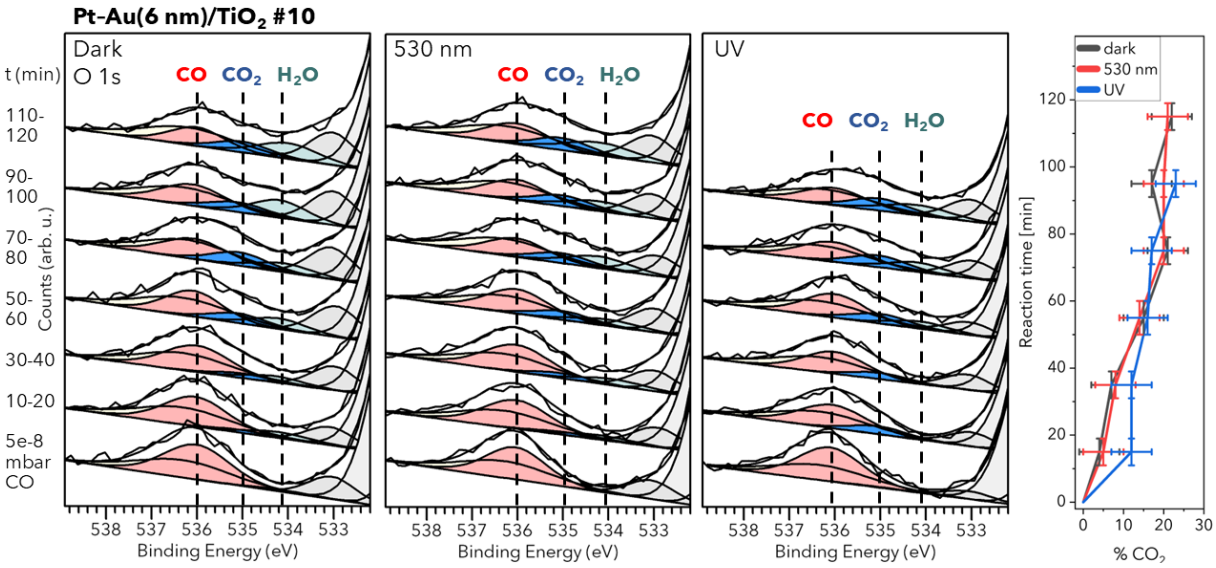

Figure 6.21: O 1s of the CO (red) oxidation to CO_2 (blue) on Pt-Au(6.5 nm)/TiO_2 (#10) under dark, 530 nm and UV light conditions.

Sample Pt-Au(5 nm)/TiO_2 (#12). The CO adsorption on sample Pt-Au(5 nm)/TiO_2 (#12) was not observed at room temperature (Fig. 6.20). 2 L CO were dosed 97 K, resulting in a low amount of adsorbed CO in the C 1s spectrum at 290 eV, assigned to CO on Au/TiO_2. As CO was dosed at room temperature before, adventitious carbon partially covered the sample. The sample was exposed to O_2 without light and scanned after 20, 40, and 60 min (Fig. 6.22). After O_2 exposure, CO_2 at 292 eV was visible in the C 1s spectra, and the contribution of CO at 290 eV decreased. After 40 min, no further increase in CO_2 was observed. The total amount of CO_2 was at least 55 %. The relative CO_2 amount for each displayed spectrum can be found in the appendix in Tab. B.12.
Due to contaminations that are indicated by the yellow peaks in the C 1s spectrum, no further CO oxidation was performed. The CO oxidation is faster and has a higher conversion rate than the low-temperature CO oxidation on rutile (110) and the sample Pt-Au(6 nm)/TiO_2 (#10). Similar to the sample Au(2.5 nm)/TiO_2 (#1), the low coverage and room temperature lead to a fast CO oxidation (both samples within 40 min). Interestingly, on this sample Pt-Au(5 nm)/TiO_2 (#12), the binding energy in the C 1s region corresponds to CO on TiO_2 and not Pt, which is the material that should have the undercoordinated atoms. So, a low amount of Pt on the Au nanoparticle promotes the dark CO oxidation but does not bind CO.

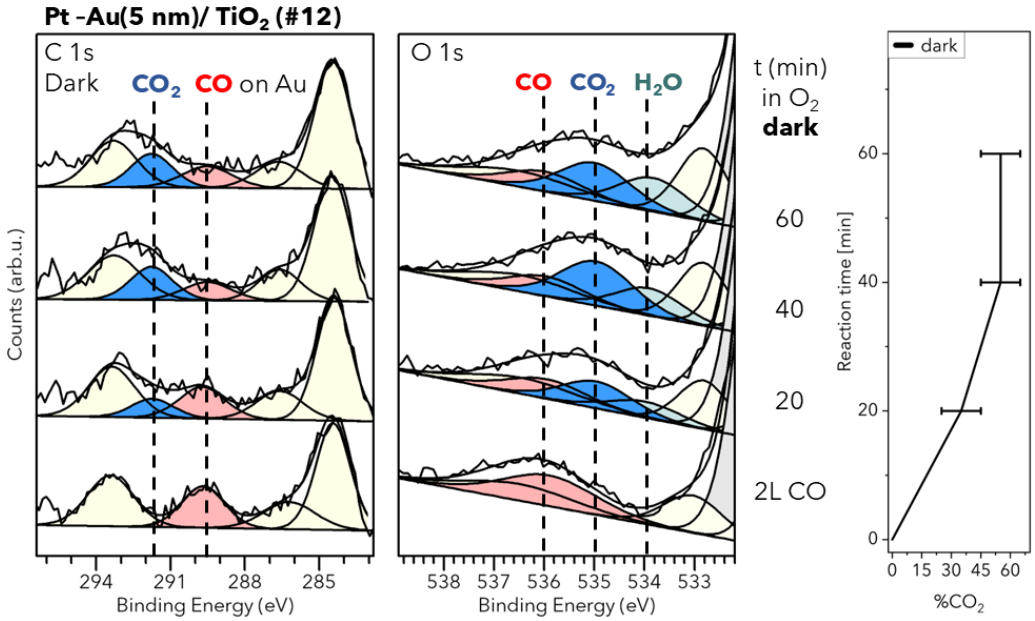

Figure 6.22: Low temperature CO (red) oxidation to CO_2 (blue) on sample Pt-Au(5 nm)/TiO_2 (#12) monitored in the C 1s (left) and O 1s (right) core level region.

Room temperature CO oxidation on Sample Pt-Au(6 nm)/TiO_2 (#14)

Sample Pt-Au(6 nm)/TiO_2 (#14) was prepared with the doubled amount of Au compared to #12 and was overgrown with 2 ML Pt at room temperature. A known problem regarding CO on Pt is that CO can block all adsorption sites at room temperature, which inhibits CO oxidation. For this reason, 0.5 L CO was adsorbed to cover only half of the adsorption sites. The C 1s spectra show a peak at 286.7 eV, matching the binding energy of CO on Pt (111). After exposure to $1 \cdot 10^{-6}$ mbar O_2 for 15 min and 530 nm light, the CO signal disappears due to CO oxidation, as seen in Fig. 6.23. CO_2 is not expected to adsorb on the surface at room temperature on Pt. Therefore, no CO_2 peak in the C 1s spectra is observed. This was repeated without light; the CO signal also disappeared, and no influence of 530 nm light could be monitored in this time frame. This experiment was repeated, but 1 L CO was adsorbed. Under an exposure of $1 \cdot 10^{-7}$ to $1 \cdot 10^{-6}$ mbar O_2 under various light conditions (dark/530 nm/UV), no CO oxidation was observed. This is most likely due to the blockage of adsorption sites by CO. Therefore, no O_2 can adsorb to react with CO. The CO could only be removed by flash annealing the sample in O_2 to 400 K. The CO and the buildup of adventitious carbon were nearly completely removed. But Pt, which acts as an adsorption site for CO, segregates subsurface into the Au nanoparticle and reduces the possible adsorption site for CO at room temperature. This is visible by the reduced CO adsorption after heating to 400 K in O_2.
During the CO oxidation at room temperature in steps, peak shifts were observed in the lattice peak in O 1s, Ti^{4+} $2p_{3/2}$, Au $4f_{7/2}$, and Pt $4f_{7/2}$ core level peaks. The shifts rela-

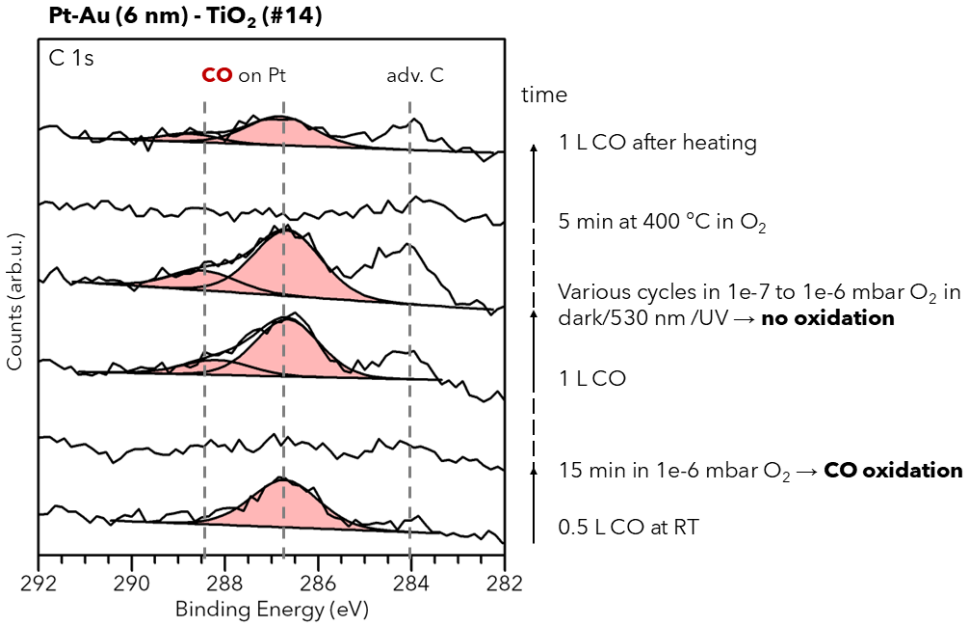

Figure 6.23: CO oxidation on sample Pt-Au(6 nm)/TiO_2 (#14) with 0.5 L CO and 1 L CO at room temperature.

tive to the freshly prepared surface (directly after Pt overgrowth) and the corresponding FWHM of the core level peak are shown in Fig. 6.24. First, the Ti 2p and O 1s core levels are discussed. The shifts of Ti 2p and O 1s of TiO_2 are similar in the different conditions. Most significant is the negative shift to lower binding energies in O_2 atmosphere after <1 L CO is dosed. This shift is due to the upward band bending of TiO_2 induced by O_2 [166] and is reversed after a few hours in UHV. The shift towards lower binding energies is more pronounced after exposure to O_2 at 400 K. The band bending in TiO_2 only occurs if O_2 can adsorb on the surface. After a dosage of 1 L CO, the surface is saturated. The subsequent exposure to O_2 does not induce band bending since CO blocks O_2 adsorption sites. Consequently, no CO oxidation is observed in C 1s, as mentioned above.

The Au $4f_{7/2}$ peak does not shift after exposure to gases, yet it 1) shifts, 2) increases in intensity, and 3) widens after heating to 400 K in O_2. Firstly, a shift of -0.1 eV is observed after heating the sample to 400 K in O_2, and Pt segregates into the Au nanoparticle, resulting in a different electric environment. Secondly, the intensity of Au increases as the Pt atoms on top of the Au nanoparticles migrate into the Au NP. Lastly, the FWHM increases because the electronic environment of the Au atoms becomes more varied when mixed with Pt.

The Pt $4f_{7/2}$ peak shifts to higher binding energies when exposed to CO for the first time and when CO is dosed after 1 night under UHV conditions. In addition to the CO-induced shift, the Pt 4f peak broadens as the bond of Pt to CO shifts the binding energy of the surface Pt atoms. With exposure to O_2, the CO is oxidized, but the Pt peak only shifts

insignificantly and not into its original position, so the electronic structure of Pt stays altered. After 16 h under UHV conditions, the Pt 4f peaks return to their original FWHM, and the position shifts 0.05 eV back to lower binding energies. When exposed to 1 L CO, the same shift to higher binding energies and increased FWHM is observed. After exposure to O_2 of the 1 L covered surface, the Pt 4f peak does not shift but narrows after the first step in O_2. Yet, CO is not oxidized by exposure to O_2 and blocks all adsorption sites. After 16 h in UHV, CO stays on the surface, and the Pt 4f peak does not shift back or narrow as CO stays on the surface.

After heating to 400 K in O_2, the Pt 4f peak shifts by 0.2 eV to lower binding energies due to the desorption of CO and possibly due to electronic changes of Pt. Ti 2p and O 1s shift by 0.25 eV to lower binding energies due to O_2 induced band bending. Au 4f shows a minor shift of 0.1 eV, probably due to mixing with Pt.

In contrast to Au 4f, Ti 2p, and O 1s, the FWHM of Pt 4f decreases upon heating to 400 K in O_2, indicating an increased ordering of Pt. Pt was deposited at room temperature, and the treatment to a higher temperature of 400 K led to a more ordered Pt structure as well as to the segregation of Pt atoms into the Au nanoparticle. The relative measured amounts under a 90° exit angle of Pt and Au change from 52.3 % (Pt) and 47.7 % (Au) to 47.6 % (Pt) and 52.4 % (Au), indicating that Pt segregates into the Au particle.

As a result of fewer Pt atoms at the surface, the CO adsorption is reduced. Comparing the area of the CO peaks in the C 1s spectrum, less than half of the original amount of CO adsorbs at room temperature. The shift of Pt 4f after exposure to CO is with 0.2 eV reduced in comparison to the shift of 0.9 eV observed in Pt 4f after exposure to CO of the untreated sample.

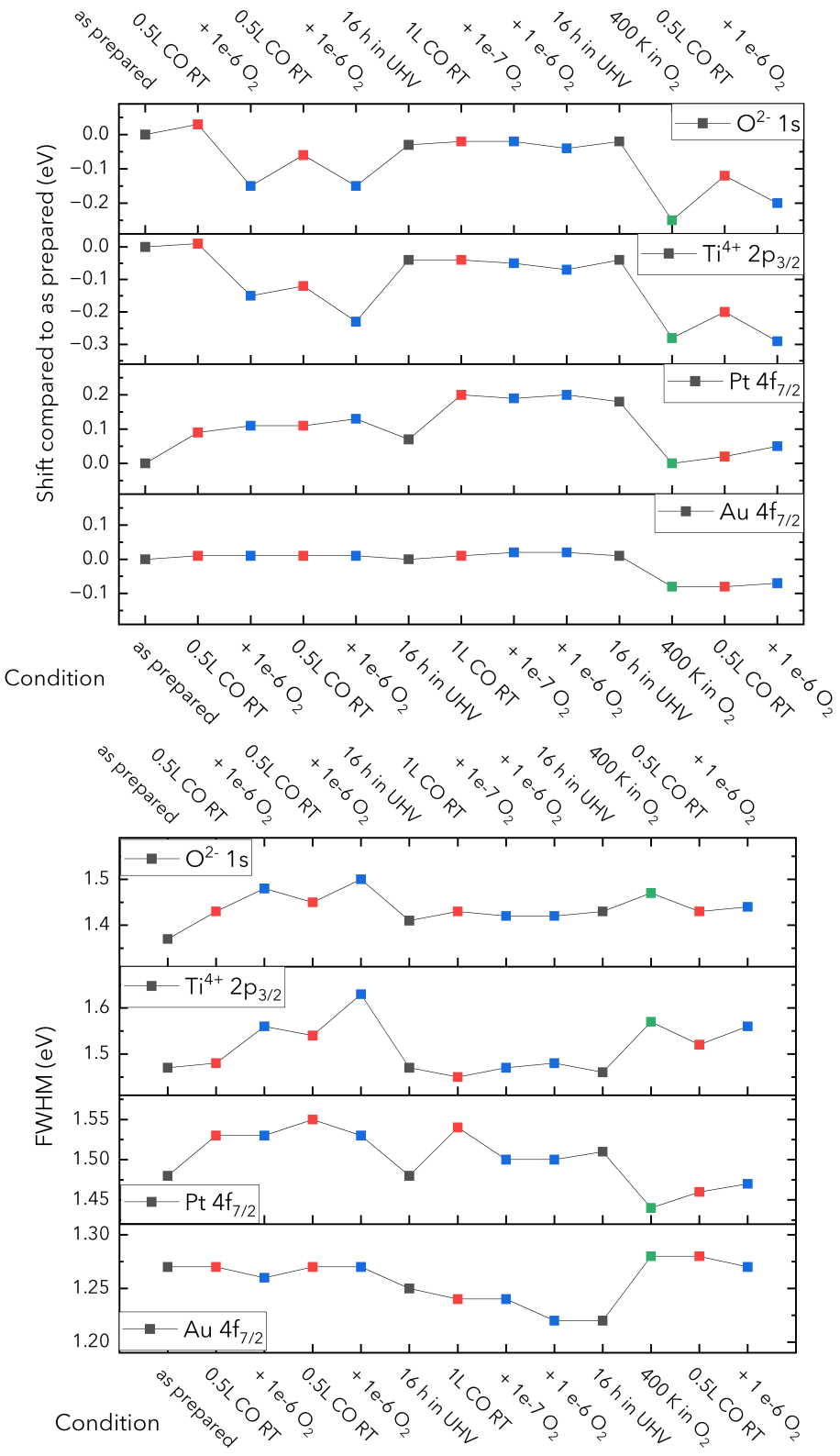

Figure 6.24: Evaluation of peak shifts (top) and FWHM (bottom) observed in XP spectra of O 1s, Ti 2p, Pt 4f and Au 4f regions for Pt-Au/TiO_2 model catalyst. Various conditions indicated on the x-axis are compared to the respective as-prepared sample. Red dots indicate data obtained after CO adsorption, blue after exposure to O_2, green after heating, and black after time under UHV conditions.

Concluding Remarks on the CO Oxidation on Pt-Au/TiO_2

The Pt overgrowth and especially its location mainly influenced the CO oxidation on Pt-Au/TiO_2. The CO oxidation results are summarized in Tab. 6.4. If at least 1 ML Pt was located on top of Au, CO adsorption at room temperature on Pt adsorption sites was possible. If the surface was not saturated with CO, or in this specific case, 0.5 L CO was dosed, CO was oxidized in 1 $\cdot 10^{-6}$ mbar O_2. No CO oxidation was observed at room temperature if the surface was covered with 1 L CO. Upon heating the sample, the Pt atoms diffuse subsurface into the nanoparticles, reducing the surface adsorption sites for CO. Unfortunately, removing CO from the surface requires heating, leading to a decrease in CO adsorption sites. No CO adsorption on Pt, only on Au, was observed at 97 K for alloyed Pt-Au nanoparticles. For the low-temperature CO oxidation on alloyed Pt-Au(6.5 nm)/TiO_2, the final CO_2 amount was 22 $\pm$ 5 % and, therefore, significantly lower compared to all other Au/TiO_2 samples.

In a study by Tenney *et al.* [198] on bimetallic Pt-Au clusters with various compositions, it was found that Au enriches at the surface of the particles. The fraction of Pt at the surface decreases with increasing Au coverage, and at a coverage of at least 50 % Au, no Pt can be detected at the surface. However, they found that CO adsorbs at the bimetallic particles for coverages of 3 ML on 0.25 ML Pt. The CO adsorption on Pt atoms, which fluctuate to the surface, is energetically favorable. The CO oxidation (with preadsorbed O_2) is, on the other hand, only observed for Au coverages below 0.25 ML. So, although CO adsorbs, it cannot be oxidized since no adsorption sites for O_2 are available. Dissociative adsorption, the first step of the CO oxidation on Pt, would need two adsorption sites. The CO oxidation in this thesis had a different protocol than the mentioned study [198] by first adsorbing CO and then exposing the sample to an O_2 atmosphere, which circumvents the requirement of preadsorbed molecular oxygen.

The room temperature CO oxidation was observed on the sample Pt-Au(6 nm)/TiO_2 (#14), overgrown with 2 ML Pt at room temperature. Heating to 400 K influences the amount of CO adsorption, which indicates further segregation of Au to the surface and Pt into the nanoparticle.The reduction in CO adsorption after heating indicates that Pt is present at the surface before heating, providing enough adsorption sites for CO adsorption. If not all adsorption sites are covered by CO, O_2 dissociates and oxidizes the adsorbed CO. Due to their thickness, more Au is present on the surface below the Pt. The XRR electron density profile gives a higher density for the top layer than the bottom layer due to the higher electron density of Pt and a higher coverage. Probably, some Au atoms segregate to the surface of the overlayer.

Table 6.4: Summary of CO oxidation experiments on Pt-Au/TiO_2 in XPS.

Sample	CO Oxidation	Steps	Complete After (min)	Final Rel. % CO_2	Result
Rutile	UV	20 min	120	50	
	530 nm		120	60	
	dark		no oxidation	–	
	UV	in situ	130	35	
Pt-Au #10	dark		115	22	least
	530 nm		75	20	active
	UV		65	20	sample
#12	dark	20 min	40	55	fast oxidation
#14	dark, 530 nm	15 min	<15 min	–	only for <1 L CO

Chapter 7

Summary and Conclusion

This thesis investigated two projects: the dynamics of CO oxidation on rutile TiO_2(110) and the LSPR-induced CO oxidation on Au/TiO_2 and Pt-Au/TiO_2 from a surface science perspective.

At the free-electron laser FLASH in Hamburg, the ultrafast dynamics of CO oxidation on rutile TiO_2(110) were investigated using time-resolved X-ray photoelectron spectroscopy (XPS) in a pump-probe experiment. In an O_2/CO atmosphere at 80 K, CO adsorbs on the rutile (110) surface and is oxidized to CO_2 within the first 800 ($\pm$ 200) fs following excitation by the 770 nm laser pump. Density functional calculations by the collaborating group of Prof. Thomas Frauenheim confirm that molecularly adsorbed O_2 is activated via an O_2-TiO_2 charge transfer (CT) complex. Due to the low temperature of 80 K, residual water in the ultra-high vacuum environment inhibits CO adsorption, thereby reducing CO_2 formation, but it may enhance charge transfer at low coverages. Simultaneously monitoring multiple oxygen-containing species in the O 1s core level enabled real-time, non-destructive tracking of reaction dynamics involving co-adsorbed reactants and intermediates. A comparison with previous studies on anatase [34] TiO_2(101) highlights notable differences in reaction dynamics. While CO oxidation on anatase occurs within 1.2 to 2.8 ps post-excitation, the process on rutile proceeds significantly faster, with CO_2 formation observed within the first 0.8 ps. Although anatase is generally regarded as the more active photocatalyst, rutile exhibits faster CO oxidation dynamics.

Water could play an enhancing role in TiO_2 based photocatalysis and requires further studies.

These findings offer valuable insights into the relationship between a material's electronic structure, surface reaction dynamics, and charge transfer processes. A deeper understanding of ultrafast photocatalytic mechanisms is essential for advancing the design and optimization of sustainable photocatalytic systems for energy-related applications, such as water splitting and photovoltaics. This work contributes to the development of more efficient materials for green energy conversion and environmental remediation by establishing

links between material properties and catalytic performance on femtosecond timescales.
The other project explored the synthesis and catalytic properties of Au and Pt-Au nanoparticles on TiO_2 (110). The nanoparticles were grown via molecular beam epitaxy under UHV conditions on single-crystal stoichiometric rutile TiO_2(110) substrates. Characterization was performed using XPS, STM, LEED, and XRR. The nanoparticle size and size distribution increased with the amount of evaporated material and the substrate temperature during and after evaporation, resulting in Au nanoparticles with diameters ranging from 2 to 12 nm.
The CO oxidation at 95 K of preadsorbed CO under an O_2 atmosphere was monitored via XPS in the C 1s and O 1s core levels. The CO oxidation on 3 nm Au nanoparticles grown at room temperature was fast and efficient, achieving a 90 % conversion into CO_2 within 40 minutes. For larger nanoparticles with median diameters of 4.5 to 6 nm grown at 400-500 °C, CO oxidation was studied under UV illumination, 530 nm excitation (to excite the localized surface plasmon resonance, LSPR), and in the absence of light.
Nanoparticles grown at 400-500 °C (4.5-6 nm) exhibited more bulk-like properties, resulting in reduced CO adsorption compared to pure rutile (110) and small (2.5 nm) Au particles on rutile (110). While CO oxidation on larger Au nanoparticles on TiO_2 was less efficient, some samples demonstrated higher and faster CO to CO_2 conversion under UV or 530 nm light compared to dark conditions. To enhance CO adsorption, Au nanoparticles were overgrown with Pt. A Pt coverage of at least 1 ML enabled CO adsorption at room temperature. However, Pt atoms migrated beneath the Au surface upon heating to 200 °C due to their higher surface free energy, effectively suppressing CO adsorption at room temperature.
The room-temperature CO oxidation on Pt-Au/TiO_2 was studied under an O_2 atmosphere with 0.5 L and 1 L preadsorbed CO. Oxidation was observed for 0.5 L CO under both 530 nm illumination and dark conditions but not for 1 L CO. The complete occupation of adsorption sites at 1 L CO led to self-poisoning of the catalyst, preventing further reaction.
Overall, this work underscores the importance of nanoparticle size, defect density, and Pt surface enrichment in tuning the catalytic efficiency of Au and Pt-Au nanoparticles on TiO_2. The results provide insights into optimizing nanoparticle-based catalysts for CO oxidation and other catalytic reactions.
Lab-based steady-state studies are the first step in studying the dynamics of localized surface plasmon-induced photocatalysis to enhance visible light-induced catalysis. The lab study on Au on rutile (110) combined with the findings on the dynamics of the CO oxidation on rutile was the basis for a follow-up investigation of the dynamics of CO photooxidation on plasmonic Au/TiO_2 at the FEL FLASH.
Further studies assessing the stability of these nanoclusters over prolonged catalytic cy-

cles may offer valuable insights into their long-term viability for industrial applications. Additionally, future research should investigate the dynamic nature of photo-induced metal-support interactions, particularly at ambient pressures. Ambient-pressure XPS is a relatively recent addition to the toolkit of surface science, bridging the gap between atomic-scale precision and real-world complexity. Such experiments are deemed crucial to enable the full potential of this unique catalytic system and should, therefore, be pursued by subsequent projects in this field.

Appendix A

Supporting Information of Dynamics of the CO Photooxidation to CO_2 on Rutile (110)

This is the Supporting Information to the manuscript "Dynamics of CO Photooxidation to CO_2 on Rutile (110)" and was part of the submission to Communications Chemistry in February 2025.

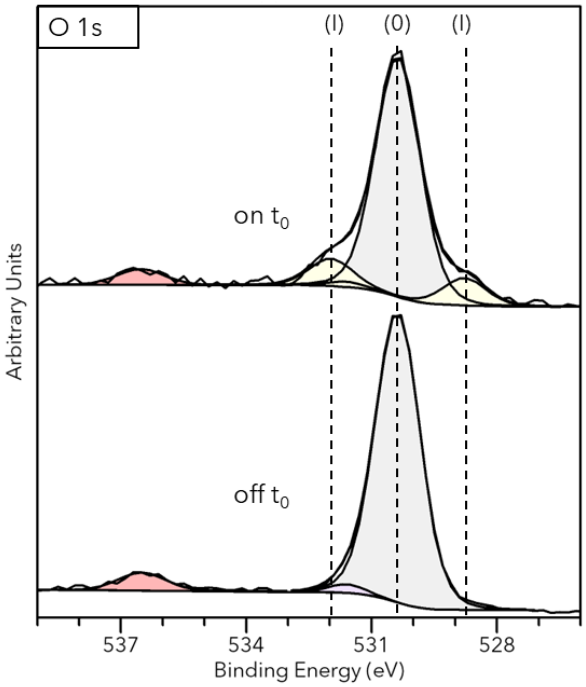

Figure A.1: Formation of first-order sidebands (I) in the O 1s core level of the O^{2-} lattice peak (0) at time zero (top). The temporal binning is 250 fs.

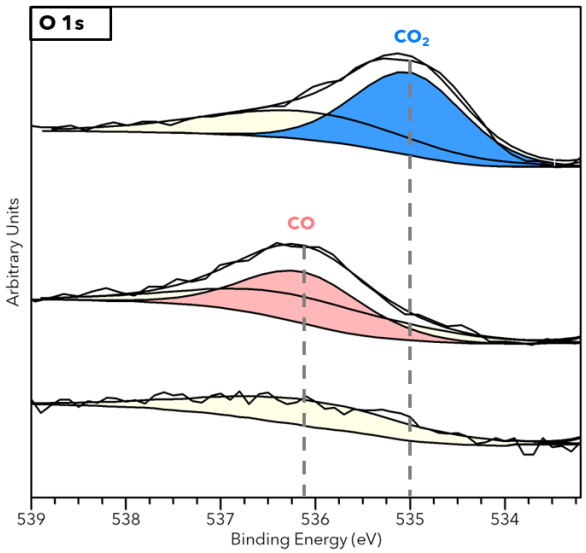

Figure A.2: XP spectra of O 1s core level of the cleaned rutile surface, after CO and after CO_2 adsorption at 98 K. Spectra are recorded with a lab-based Al Kα source (hν_{Mono} = 1486.6 eV, E_p=40 eV) under normal emission. Adsorbed CO (red) shows a component at 536.1 eV and CO_2 (blue) at 535.0 eV on top of the O 1s satellite peak (yellow).

System	E_{ads} (eV)
A) CO adsorption	-0.525
B) O_2 adsorption (perpendicular)	-0.132
C) O_2 adsorption (parallel)	-0.105
D) coadsorption CO and O_2 (perpendicular)	-0.667
E) coadsorption CO and O_2 (parallel)	-0.505

Table A.1: Energetic values obtained by DFT periodic calculations for the adsorption energies in eV per adsorbed molecule in the systems depicted in the FigureA.6 below. Calculation were performed by Adrian Domínguez-Castro, Verena Gupta, Adriel Domínguez Garcia and Thomas Frauenheim.

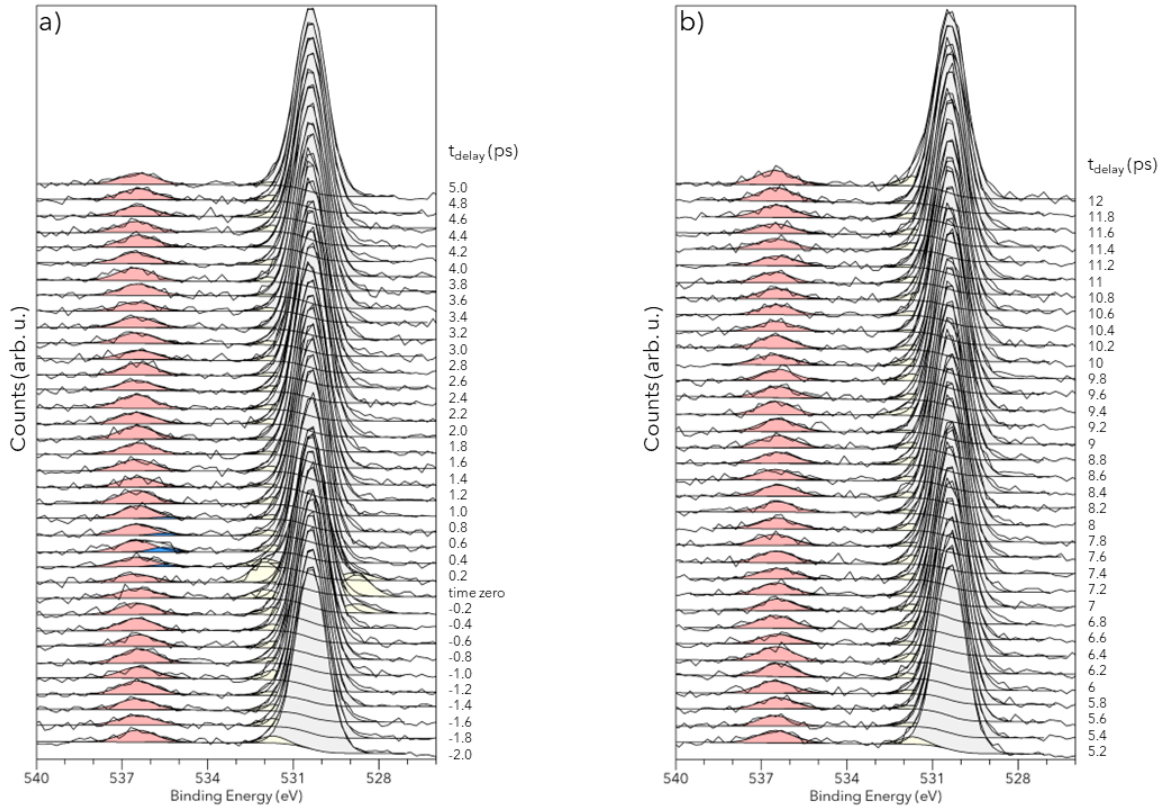

Figure A.3: Time resolved XP spectra of O 1s core level during photooxidation of CO to CO_2 on rutile TiO_2(110) at 80 K binned in 200 fs intervals at the marked time a) from -2 ps to 5 ps and b) from 5.2 to 12 ps. The spectra show no indication of any intermediate species during the CO oxidation with a lifetime longer than 200 fs.

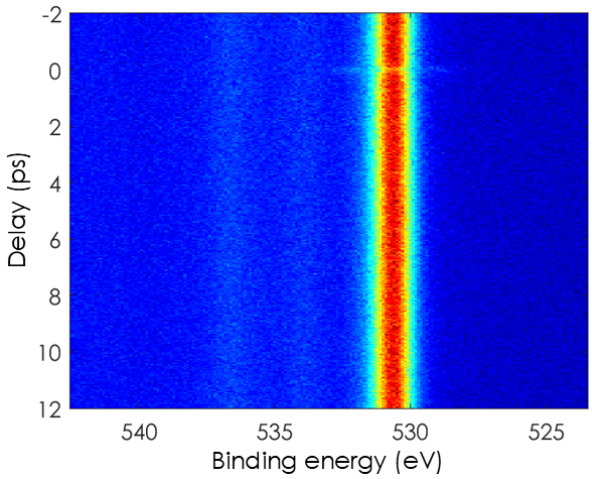

Figure A.4: The time-resolved XP map of the energy region of O 1s core level taken at FLASH. The color scale indicates the intensity of the XP spectra, with the TiO_2 O 1s lattice peak at 530.4 eV. At time zero the intensity of the lattice peak decreases and sidebands appear 1.6 eV ahigher and lower binding energy. The binning size is 0.05 ps for the delay and 0.1 eV for the binding energy.

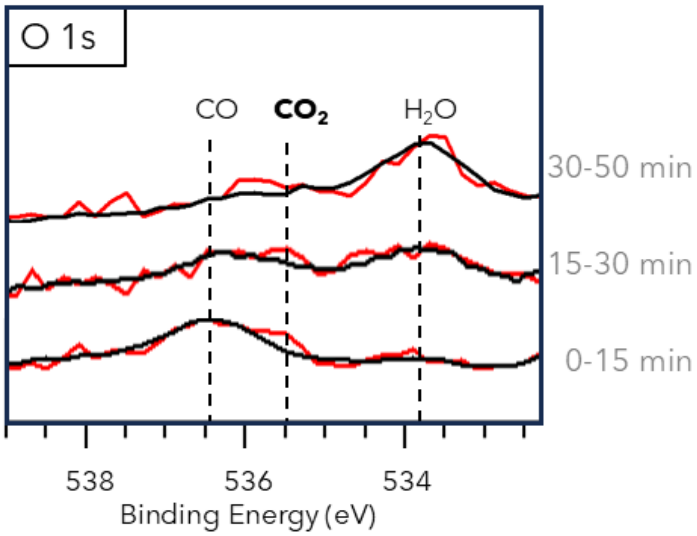

Figure A.5: Average (black) and time-resolved from 0.25 to 0.75 ps after initiation (red) O 1s spectra during CO oxidation binned in 0-15 min, 15-30 min, and 30-50 min after flash-annealing. The CO_2 signal from 0.25 to 0.75 ps is visible in two datasets with different water coverages assigned to the ultrafast oxidation of CO.

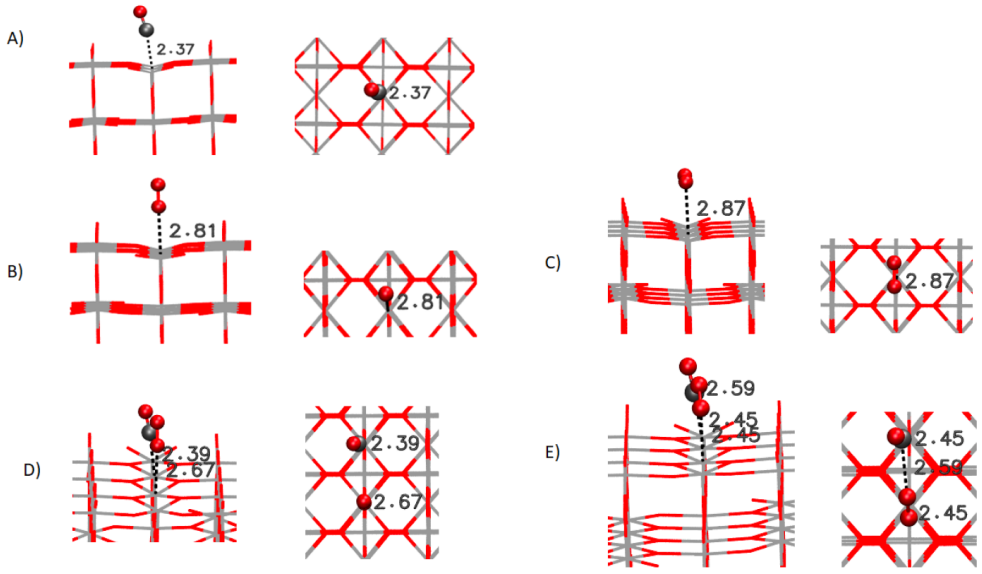

Figure A.6: Snapshots of the optimized geometry obtained (left side view, right top view, respectively) corresponding with: A) CO adsorption; B) O_2 adsorption (perpendicular configuration); C) O_2 adsorption (parallel configuration); D) coadsorption of CO and O_2 (perpendicular configuration); E) coadsorption of CO and O_2 (parallel configuration). Bond lengths are given in Angstrom(Å). The optimized geometries and energetics for CO and O_2 underline the preference of both molecules to interact with the pentacoordinated Ti (Ti_{5c}) atoms, in agreement with previous reports [53, 262]. The chemistry of CO is ruled by the intrinsic properties of the CO molecule with the C atom presenting a negative electronic partial charge based on the Lewis structure, explaining the C atom ending orientation in the interaction with Ti atoms. Two different configurations were considered for the adsorption case of O_2 on TiO_2 rutile (110) surface. The first one with the perpendicular O_2 molecule interacting with an interatomic distance between the Ti_{5c} and the nearest molecular oxygen of 2.81 Å and a binding energy value of -0.132 eV. The second one with the parallel O_2 molecule interacting with an interatomic distance between the Ti_{5c} and the nearest molecular Oxygen of 2.87 Å and a binding energy value of -0.105 eV. Calculation were performed by Adrian Domínguez-Castro, Verena Gupta, Adriel Domínguez Garcia and Thomas Frauenheim.

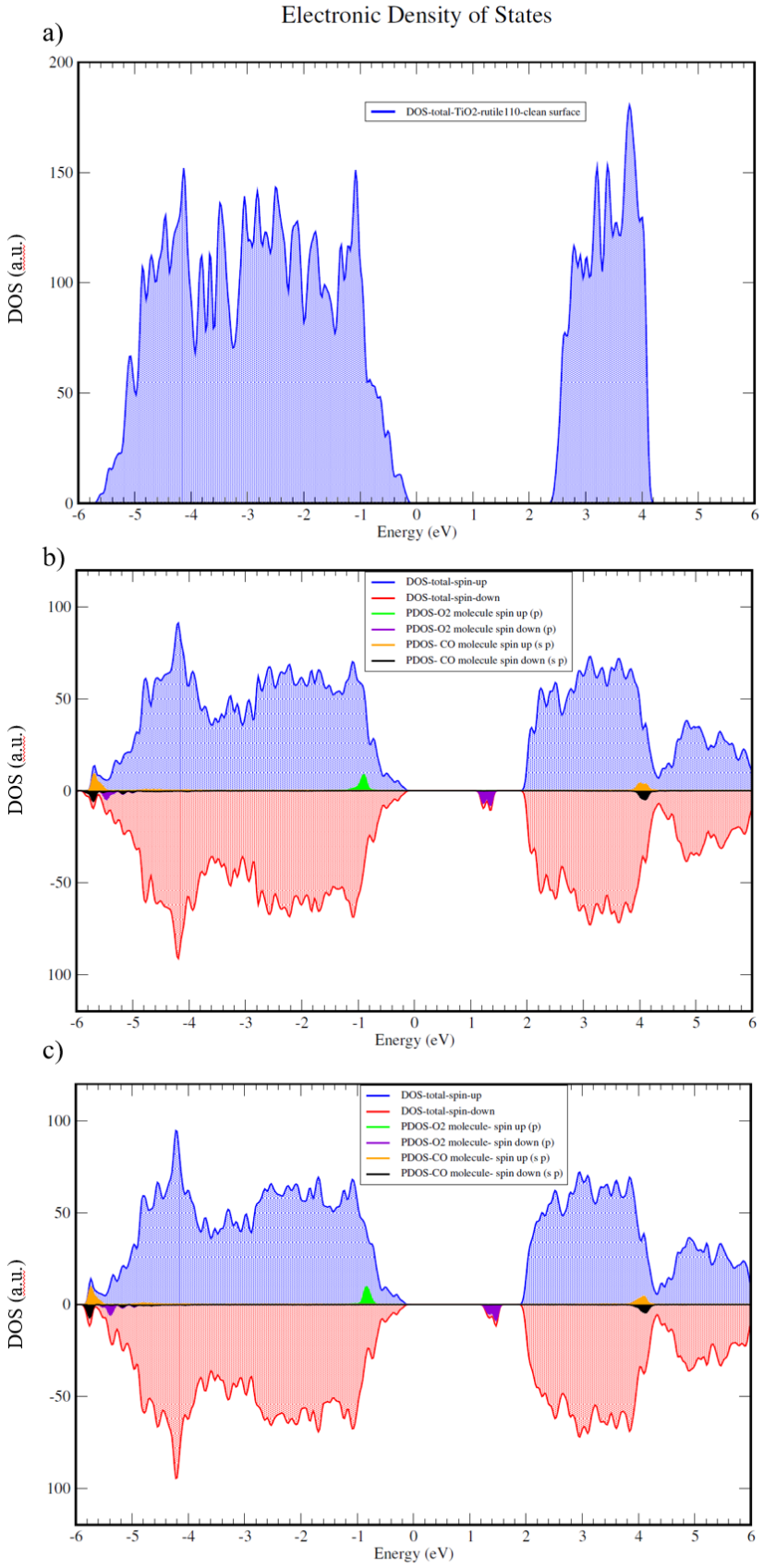
Electronic Density of States
a)
DOS-total-TiO2-rutile110-clean surface
DOS (a.u.)
Energy (eV)
b)
DOS-total-spin-up
DOS-total-spin-down
PDOS-O2 molecule spin up (p)
PDOS-O2 molecule spin down (p)
PDOS- CO molecule spin up (s p)
PDOS- CO molecule spin down (s p)
DOS (a.u.)
Energy (eV)
c)
DOS-total-spin-up
DOS-total-spin-down
PDOS-O2 molecule- spin up (p)
PDOS-O2 molecule- spin down (p)
PDOS-CO molecule- spin up (s p)
PDOS-CO molecule- spin down (s p)
DOS (a.u.)
Energy (eV)

Figure A.7: previous page: Density of states (DOS) of a) the pristine TiO_2 rutile 110 surface, b) the coadsorption of CO and O_2 in parallel configuration and c) the coadsorption of CO and O_2 in perpendicular configuration, using PBE functional at the DFT level of theory with the semi-empirical nonlocal external potentials. Additionally, the projections of the DOS on the adsorbate orbitals are displayed. Calculation were performed by Adrian Domínguez-Castro, Verena Gupta, Adriel Domínguez Garcia and Thomas Frauenheim.

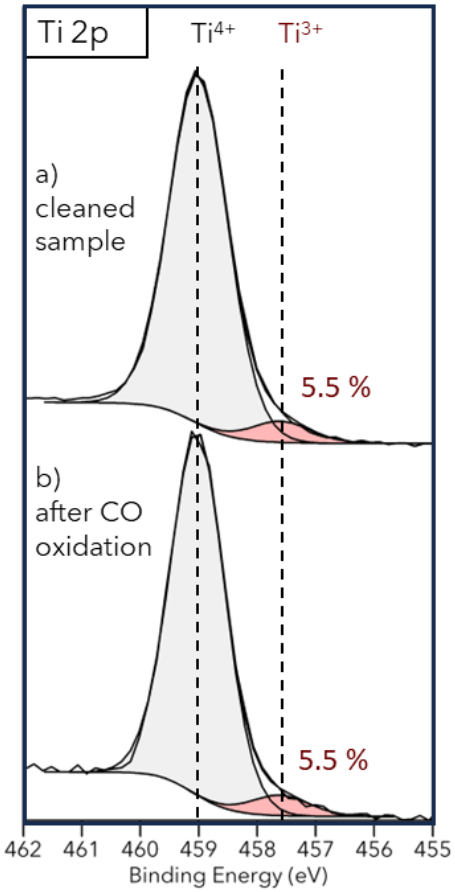

Figure A.8: Ti 2p spectrum a) after cleaning in oxygen at 650 °C before CO oxidation and b) after several cycles of CO oxidation at 80 K. The defect concentration (determined by the Ti^{3+} component) does not change during the CO oxidation

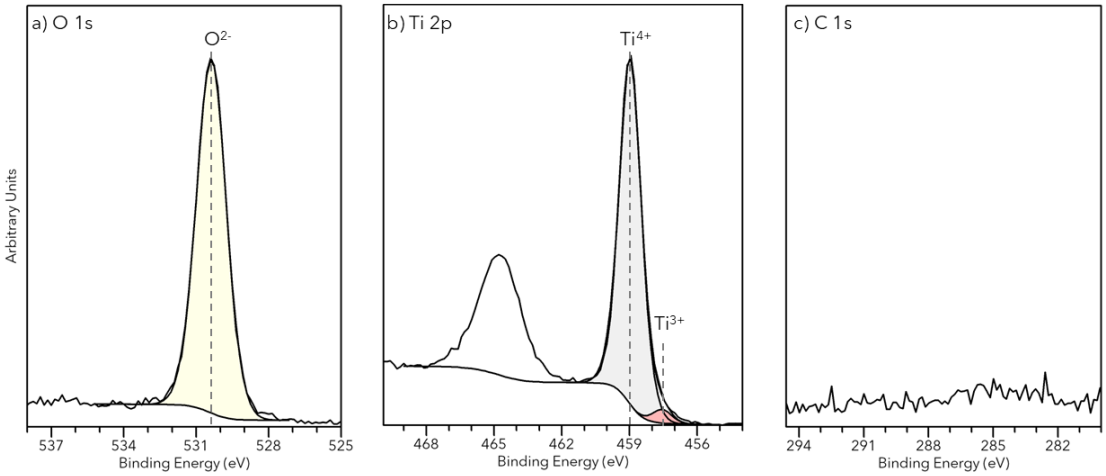

Figure A.9: XP Spectra ($h\nu_{FEL}$ = 643 eV, T = 293 K) of a) O 1s, b) Ti 2p and c) C 1s of the cleaned TiO_2(110) surface. The O 1s spectra show the O^{2-} lattice peak. The Ti 2p spectrum consists of the Ti^{4+} $2p_{3/2}$ at 459 eV and the broader Ti^{4+} $2p_{1/2}$ peak. The Ti^{4+} $2p_{3/2}$ peak exhibits a slight asymmetry on the lower binding energies, which is assigned to a low amount of Ti^{3+} defects. The C 1s spectrum showed no contaminants on the cleaned surface.

Figure A.10: (1x1) LEED pattern of prepared rutile TiO_2(110) surface.

Appendix B

Appendix of Photooxidation of Au and Pt-Au on TiO_2

B.1 Calibration of the Au evaporator

The flux measured during evaporation is proportional to the amount of deposited material d as follows:

$$\text{d (nm)} = \text{evaporation rate } (\tfrac{\text{nm}}{\text{nA}\cdot\text{min}}) \cdot \text{flux (nA)} \cdot \text{evaporation time (min)} \tag{B.1}$$

To determine the evaporation rate of the gold evaporator, gold was deposited on an Al_2O_3 (0001) sample for four hours. The cumulative flux over 4 h was 37548 nA·min with a mean flux of 156 nA. The thickness of the gold layer was determined by fitting the XRR data in FEWLAY (Fig. B.1). XRR is sensitive to the electron density and thickness of a layer. Comparing the fitted electron density with the bulk electron density, the coverage is derived by

$$\text{coverage} = \frac{\text{fitted density}}{\text{bulk density}}. \tag{B.2}$$

The nominal thickness or amount of the deposited material is

$$\text{nominal d (nm)} = \text{thickness} \cdot \text{coverage}. \tag{B.3}$$

The determined rate was

$$\text{evaporation rate} = \frac{0.71 \text{ nm}}{37548 \text{ nA} \cdot \text{min}} = 1.89 \cdot 10^{-5} \ \frac{\text{nm}}{\text{nA} \cdot \text{min}}. \tag{B.4}$$

The amount of gold is also often given in monolayers (ML). In this case, the thickness of one Au ML is the atomic distance in the [111] direction is 2.35 Å [322]. This gives the

$$\text{evaporation rate} = \frac{3.02\ \text{ML}}{37548\ \text{nA} \cdot \text{min}} = 8.05 \cdot 10^{-5}\ \frac{\text{ML}}{\text{nA} \cdot \text{min}}. \tag{B.5}$$

The calibration on Al_2O_3 vastly understimates the nominal thickness fitted on TiO_2 by XRR. This might be due to degassing of the evaporator during evaporation, resulting in an overestimated flux. Due to deviations in the position, the calibration sample might not have been hit correctly.

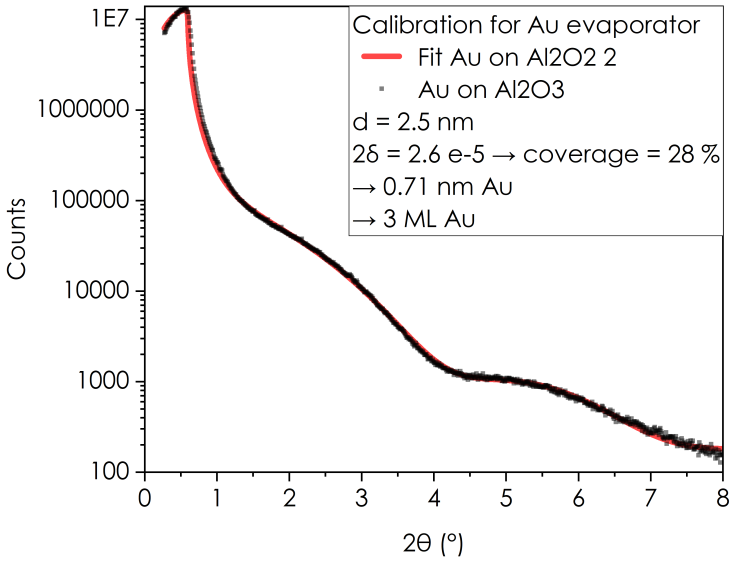

Figure B.1: XRR fit to determine the evaporated amount of Au on Al_2O_3 after 4 h with an average Au flux of 156 nA/min.

B.2 Preparation Parameters

Table B.1: Sample preparation parameters of rutile TiO_2(110) substrates. The size of the substrates was 7 mm×7 mm, and the height is given in the table. The samples were prepared by repeated cycles of sputtering and annealing. The argon pressure during sputtering was always $1 \cdot 10^{-6}$ mbar. If the annealing step included exposure to O_2, the pressure was $1 \cdot 10^{-6}$ mbar and the sample was also cooled down in O_2 to ∼200 °C.

Sample	Height (mm)	Cycles	Sputtering	Annealing
#1	1	5	10 min, U=1 keV	T_{plate}=830 °C, in O_2
#2	1	3	see #1	see #1
#3	1	8	first 3 cycles see #1, then 5 min, U=0.5 keV	first 3 cycles see #1, then T_{plate}=900-950 °C, 20 min, 7th in UHV, all other in O_2
#4	1	5	see #1	T_{plate} = 970 °C, first 2 cycles 20 min in UHV, then last 5-10 min in O_2
#5	0.5	4	see #1	T_{plate} = 980-1030 °C in UHV, last cycle 10min UHV + 15 min in O_2
#6	0.5	7	see #1	T_{plate} = 1030 °C in UHV 30 min, every 3rd cycle 10min UHV + 20 min in O_2
#7	0.5	12	see #1	T_{plate} = 1000-1050 °C, in UHV 15 min, every 3rd cycle 10 min UHV + 10-15 min in O_2
#8	0.5	8	see #1	see #7
#9	0.5	6	see #1	see #7
#10	0.5	8	see #1	see #7
#11	0.5	17	see #1	see #7
#12	0.5	8	see #1	see #7
#13	0.5	9	see #1	see #7
#14	0.5	7	see #1	see #7

Table B.2: Growth parameters of Au on rutile TiO_2(110). The amount of % Au (XPS) is relative to the Ti 2p and O 1s area.

Sample	Au Evaporation	T_{sample}	Post Annealing	ML Au (XRR)	% Au (XPS)	Median d (nm)(STM)
#1	I_{fil}=1.86 A, U=950 V, I_E=17 mA, flux 71 nA, 15 min	20 °C	-	0.4	0.7	2.5
#2	see #1, flux 60 nA	250 °C	-	0.7	0.8	3
#3	see #1, 60 min	20 °C	-	3		4
#4	I_{fil}=2.43 A, U=1900 V, I_E=8.7 mA, flux 50-200 nA, 90 min	250 °C	-	–	4.2	4
#5	I_{fil}=2.41 A, U=1850 V, I_E=8.7 mA, flux 160 nA, 60 min	400 °C	20 min	3.6	–	–
#6	see #5, flux 168 nA, 2 h	400 °C	10 min	3.4	10.8	5
#7	see #5, adjusted U to match flux to 160-170 nA, 2x 1h	500 °C	2 x 1h	4.8	10.3	4.5
#8	see #5, 2h	500 °C	3 h	5.2	10.9	5.5
#9	see #8	500 °C	3 h	2.6	9.2	6

Table B.3: Summary of growth parameters of Pt-Au NP on rutile TiO_2(110). The amount of % Au and Pt (XPS) is relative to the Ti 2p, O 1s, and Pt 4f and Au 4f area, respectively.

				XPS		STM
Sample	Pt	T_{sample}	ML Pt	% Au	% Pt	median d (nm)
#10	I_{fil}=2.77 A, U=980 V, I_E=22.5 mA, flux 11 nA, 19 min	500 °C	0.5	7.7	2.75	6.5
#11	see #10, 9 min	20 °C	0.25	9.0	1.6	5.5
#12	12 nA, 8 min	20 °C	0.25	10.6	1.6	5
#13	12 nA, 32 min	20 °C	1	11.1	6.6	4.5
#14	20 nA, 46 min	20 °C	2	11.6	12.6	6

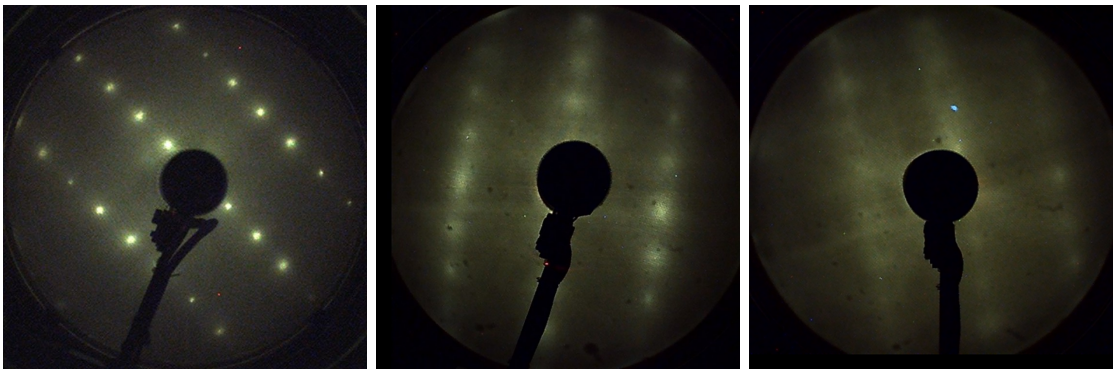

(a) Cleaned Rutile (110) (b) After Au deposition (c) After Pt deposition

Figure B.2: LEED pattern (105 eV) of sample #11 as a) cleaned rutile (110), b) after Au deposition at 500 °C and c) after Pt deposition at RT.

B.3 STM

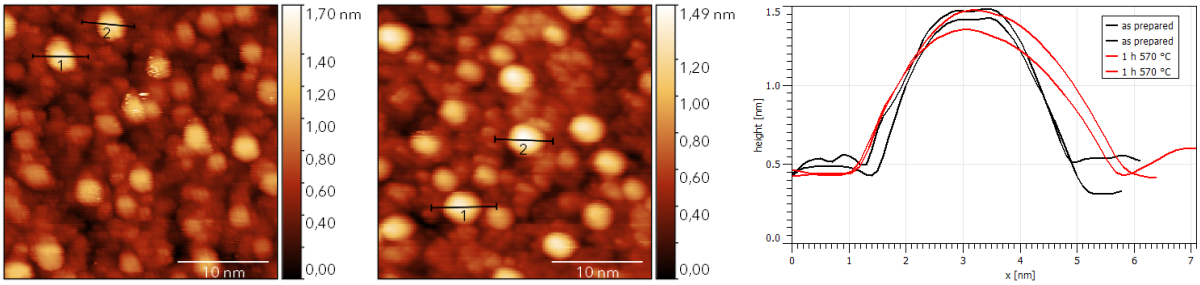

(a) as prepared (b) annealed at 570 °C (c) Line profile

Figure B.3: STM images of the (a) as prepared and (b) annealed to 570 °C sample Au(3 nm)/TiO_2 (#2) and (c) line profiles indicated in (a) and (b).

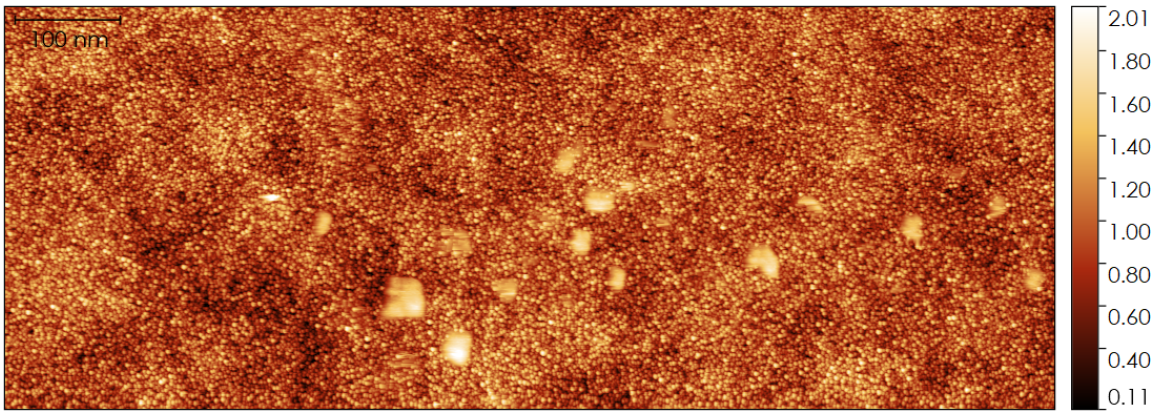

Figure B.4: STM image (1000×380 nm) of Sample Au(4 nm)/TiO_2 (#3).

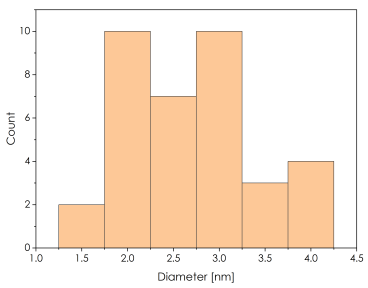

(a) #1 2.5 nm Au, RT

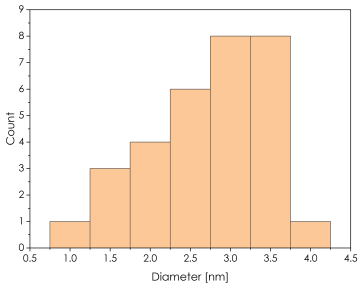

(b) #2: 3 nm Au, 250 °C

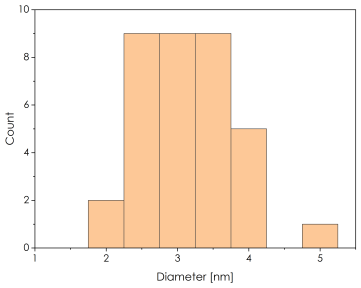

(c) #2: 3 nm Au, annealed

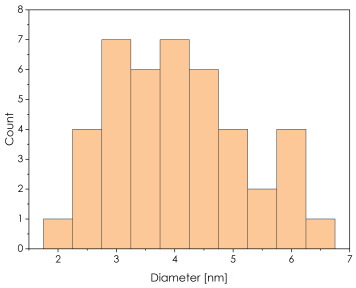

(d) #3: 4 nm Au, RT

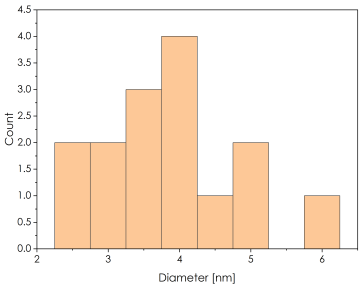

(e) #4: 4 nm Au, 250 °C

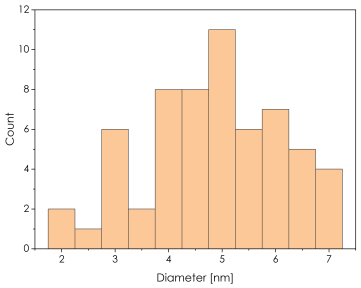

(f) #6: 5 nm Au, 400 °C

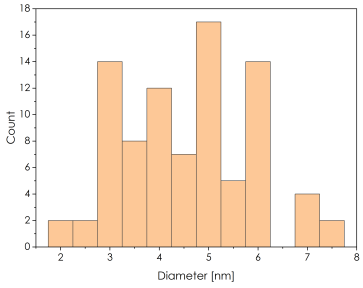

(g) #7: 4.5 Au, 500 °C

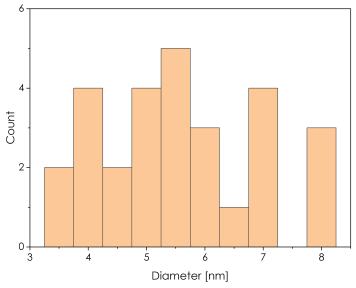

(h) #8: 5.5 nm Au, 500 °C

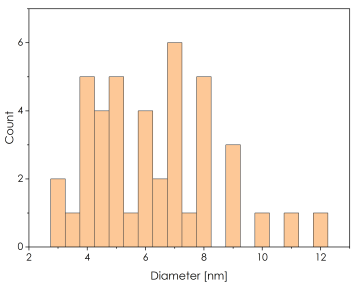

(i) #9: 6 nm Au, 500 °C

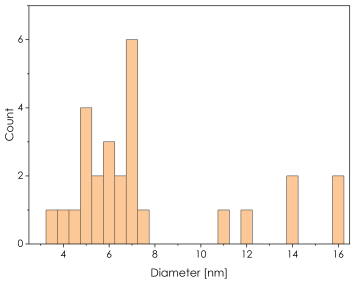

(j) #10: 6.5 nm Au + Pt

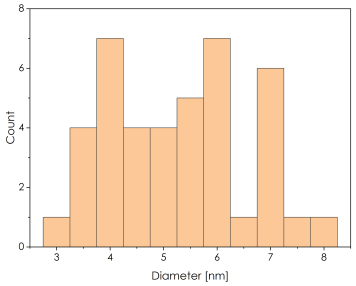

(k) #11: 5.5 nm Au + Pt, RT

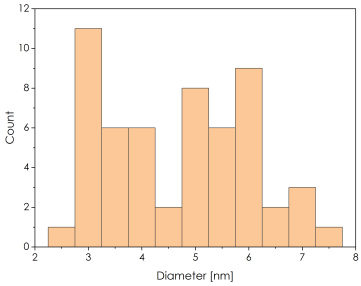

(l) #12: 5 nm Au + Pt, RT

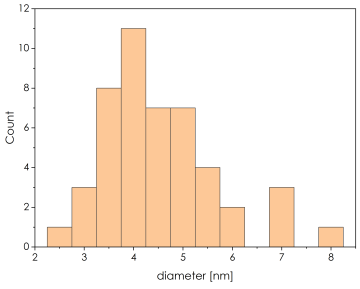

(m) #13: 4.5 nm Au + Pt RT

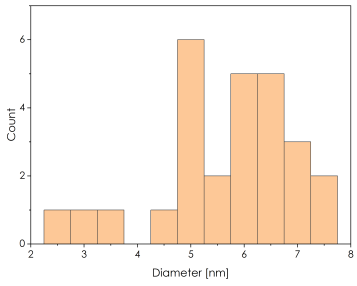

(n) #14: 6 nm Au+Pt

Figure B.5: Histograms of measured diameters by line profiles of Au and Pt-Au NP on $TiO_2(110)$.

B.4 XPS Fitting Parameters

Table B.4: XPS Fitting Parameters of Au 4f and Pt 4f for Au-TiO_2 and Pt-Au-TiO_2 samples. The error is derived from fitting several spectra of each core level.

	Au $4f_{7/2}$					Pt $4f_{7/2}$				
Sample	BE (eV)	FWHM (eV)	amount %	error ±%	Lineshape	BE (eV)	FWHM (eV)	amount %	error ±%	Lineshape
#1	84.1	1.35	0.72	0.3	LA(1.3,2.1,60)					
#1 heated	84.8	1.13			LA(1.3,2.1,60)					
#2	83.91	1.32	0.84	0.3	LA(1.3,2.1,60)					
#4	83.75	1.28	4.22	0.4	LA(1.3,2.8,60)					
#6	83.75	1.2	10.83	0.5	LA(1.3,2.5,60)					
#7	83.72	1.28	10.32	0.5	LA(1.3,2.3,50)					
#7 sputtered	83.7	1.28		0.5	LA(1.3,2.3,50)					
#8	83.71	1.35	10.93	0.5	LA(1.3,2.8,50)					
#9	83.75	1.24	9.26	0.5	LA(1.3,2.3,50)					
#10 only Au	83.73	1.27	7.16	0.5	LA(1.3,2.8,60)					
#10	83.78	1.23	7.66	0.5	LA(1.3,2.8,60)	70.95	1.63	2.75	0.5	LA(1.3,5,50)
#11	83.73	1.2	9	0.5	LA(1.9,5.6,10)	71.23	2.18	1.63	0.5	LA(1.45,6,80)
#12	83.68	1.19	10.65	0.5	LA(1.9,5.6,10)	71.14	2.13	1.6	0.5	LA(1.45,6,80)
#13	83.7	1.18	11.13	1	LA(1.9,5.6,10)	70.86	1.53	6.6	0.5	LA(1.6,7,20)
#14	83.75	1.27	11.58	1	LA(2,5.4,20)	70.82	1.48	12.6	1	LA(1.45,6,25)

Table B.5: XPS Fitting Parameters of Ti 2p and O 1s for Au-TiO_2 and Pt-Au-TiO_2 samples. The error is based on uncertainty from fitting.

Sample	Ti 2p 3/2 BE Ti^{4+} (eV)	FWHM	Ti 2p 3/2 BE Ti^{3+} (eV)	FWHM	% Ti^{3+}	± %	O 1s BE O^{2-} (eV)	FWHM	O 1s BE surface (eV)	FWHM	% O surface
#1	459	1.1	457.07	1	1.4	0.5	530.29	1.2	531.42	1.15	7.6
#1 after heating	459	1.08	457.2	1.03	2.1	0.5	530.28	1.2	531.3	1.27	8.1
#2	459	1.21	457.08	1	2.8	0.5	530.3	1.22	531.5	1.24	9.3
#4	459	1.27	457	1.2	3.4	0.5	530.33	1.28	531.51	1.14	9.5
#6	459	1.29	457.07	1.53	5	1	530.27	1.22	531.44	1.19	11.2
rutile #7	459	1.32	–	–			530.33	1.4	531.62	1.4	–
#7	459	1.31	457	1.24	4	1	530.26	1.31	531.5	1.37	10
#7 sputtered	459	1.35	456.9	1.48	4.5	1	530.27	1.35	531.64	1.32	9.8
rutile #8	459	1.39	–	–			530.38	1.35	531.46	1.34	10.9
#8	458	1.48	457	1.46	8.4	0.5	530.3	1.41	531.64	1.21	11
rutile #9	459	1.46	–	–			530.32	1.48	531.62	1.48	8.5
#9	459	1.34	457	1	2.3	0.5	530.27	1.35	531.57	1.3	10
#10 only Au	459	1.33	457	1	1.4	0.5	530.28	1.34	531.48	1.26	10
#10	459	1.33	457	1	2	0.5	530.28	1.34	531.45	1.3	10
#11	459	1.49	458.8	1.1	2.5	1	530.29	1.41	531.6	1.21	11
#12	459	1.54	456.8	1.08	3	1	530.29	1.43	531.6	1.31	12.2
#13	459	1.51	457	1.26	6	1	530.29	1.4	531.62	1.41	13.2
#14	459	1.47	456.9	1.14	3	0.5	530.28	1.37	531.54	1.2	13.3

B.5 XRR

All samples were characterized by X-ray reflectivity to determine the nominal thickness and coverage of evaporated Au and Pt. The coverage is given by $\delta_{\mathrm{fit}}/\delta_{\mathrm{bulk}}$. The electron density ρ_e is proportional to δ

$$\rho_e = \frac{2\delta\pi}{r_e\lambda^2}$$

with $r_e = 2.818 \cdot 10^{-15}$ m and $\lambda = 1.54$ Å. The data and fits are displayed in Fig. B.6 and the fitting parameters in Tab. B.6. The minimum number of layers needed for an accurate fit was used for fitting. Due to variations in the height of the nanoparticles, two layers of Au with different electron densities were applied to model the less dense top of the higher particles compared to the more dense first layer of smaller and larger particles. For the Pt-Au nanoparticles, two layers of material were fitted, assuming an Au and a Pt layer. However, both layers are more likely a mixture of both materials because Pt sits on top of the hemispherical Au particles and possibly directly on the TiO_2 substrate. The higher density of the top layer, assigned to Pt, of samples #13 and #14 indicates that Pt is predominantly located on top of the Au nanoparticles. For Cu Kα X-rays (1.54 Å), the 2δ values for Au and Pt are $9.43{\cdot}10^{-5}$ and $1.04{\cdot}10^{-4}$, respectively, and differ by 10 %. For the thickness in monolayers (ML), the d-spacing in (111) was used and is 2.36 Å for Au and 2.26 Å for Pt [322].

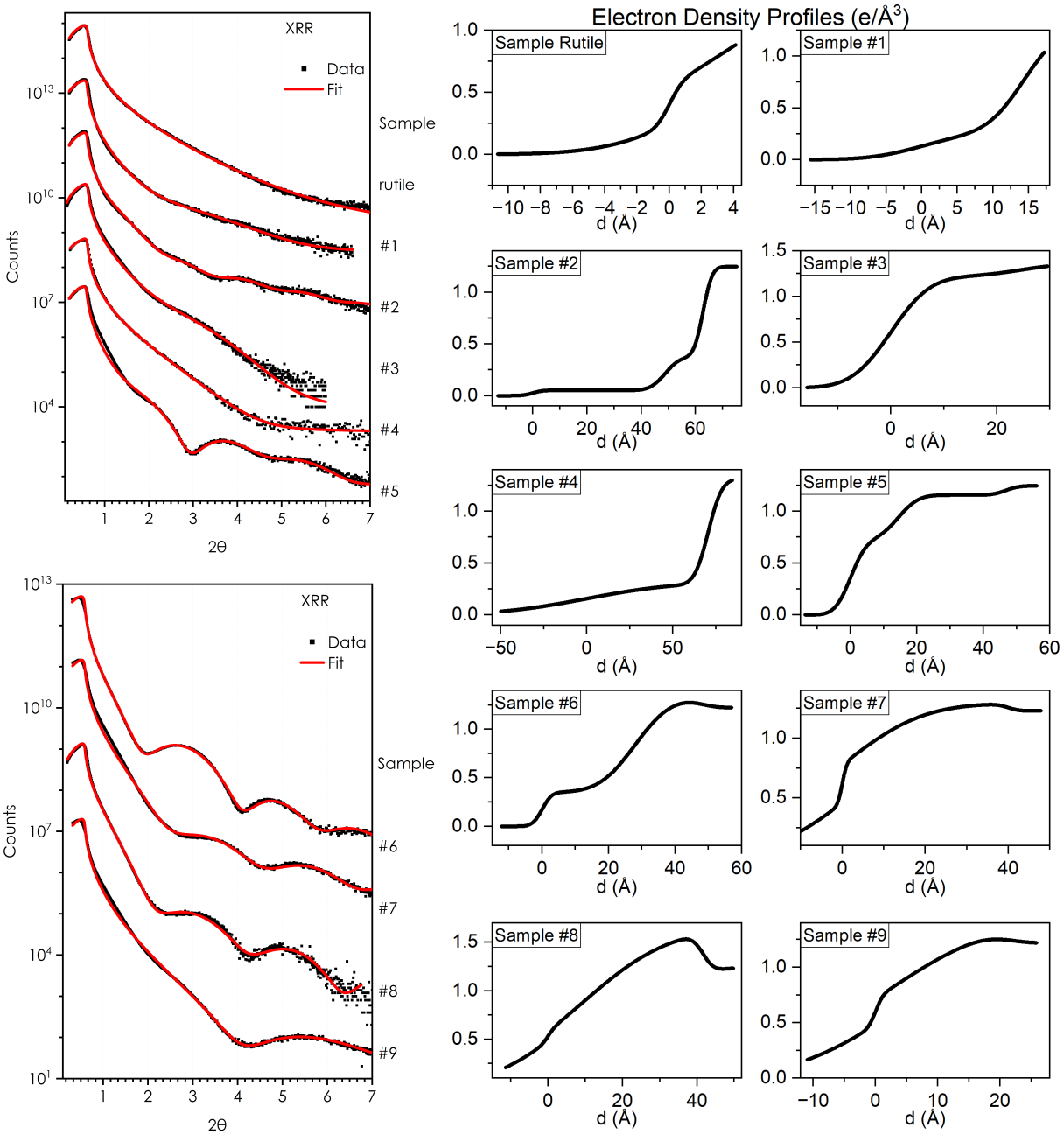

(a) Fitted XRR scans

(b) Electron density profiles

Figure B.6: X-Ray Reflectivity data (black dots) and fit (red line) of UHV-prepared rutile (110) and Au-TiO_2 samples #1 to #9 after CO oxidation. The XRR data fits were used to determine the coverage and amount of evaporated material. Fit parameters used for determining coverage and amounts of deposited material are presented in Table B.6. From the fit results, the electron density profile in 2δ is calculated in FEWLAY. The electron density $\rho_e = 2\delta \cdot \frac{\pi}{r_e \lambda^2}$.

Table B.6: X-Ray Reflectivity Fitting Parameters.

Sample	Layer	d (Å)	sigma(Å)	2δ	2β	Coverage	d_{eff} (nm)	ML
#1	Au	14.4	5.6	6E-6	5.11E-6	0.06	0.08	0.4
	TiO_2	–	4.1	2.7E-5	1.2E-6	–	–	–
#2	Au	48.8	2.9	1E-6	1E-8	0.01	0.06	0.2
	Au	14	4.3	8E-6	6E-7	0.08	0.12	0.5
	TiO_2	–	2.7	2.7E-5	1.2E-6	–	–	–
#3	Au	24.7	5.8	2.6E-5	1E-7	0.28	0.68	2.9
	TiO_2	–	6.4	2.9E-5	1.4E-6	–	–	–
#4	Au	70.6	40	7E-6	1.1E-6	0.07	0.5	2.1
	TiO_2	–	6.2	2.8E-5	1.4E-6	–	–	–
#5	Au	14.4	3.7	1.5E-5	1.31E-6	0.16	0.23	1
	Au	32.4	4.8	2.5E-5	8.2E-7	0.26	0.85	3.6
	TiO_2	–	3.1	2.7E-5	1.4E-6	–	–	–
#6	Au	27.8	2.3	7E-6	2.4E-7	0.08	0.22	0.9
	Au	19.7	8.5	2.8E-5	4.52E-6	0.3	0.59	2.5
	TiO_2	–	4	2.6E-5	1.33E-6	–	–	–
#7	Au	1.7	0.2	7E-6	1E-8	0.07	0.01	0
	Au	39.5	14.5	2.7E-5	2.31E-6	0.29	1.14	4.8
	TiO_2	–	1.5	2.6E-5	1.35E-6	–	–	–
#8	Au	9.1	1.4	2E-6	1.9E-7	0.02	0.02	0.1
	Au	32.4	18.6	3.5E-5	7.6E-7	0.37	1.2	5.1
	TiO_2	–	2.3	2.7E-5	1.35E-6	–	–	–
#9	Au	3	0.9	5E-6	1E-8	0.05	0.02	0.1
	Au	18.6	12.9	3E-5	1.73E-6	0.32	0.59	2.5
	TiO_2	–	3.6	2.7E-5	1.35E-6	–	–	–
#10	Pt	1	1.1	1E-6	1E-8	0.01	0	0
	Au	41.5	8.1	2.6E-5	1.09E-6	0.27	1.13	4.8
	TiO_2	–	2.9	2.7E-5	1.35E-6	–	–	–
#11	Pt	20.7	3.9	1.1E-5	3.2E-7	0.11	0.22	1
	Au	46.7	10.7	3.1E-5	1.54E-6	0.33	1.53	6.5
	TiO_2	–	9.6	2.8E-5	1.35E-6	–	–	–
#12	Pt	15.9	9.4	2.3E-5	1.9E-6	0.22	0.35	1.6
	Au	43.7	3.4	3E-5	2.2E-6	0.32	1.39	5.9
	TiO_2	–	3.5	2.8E-5	1.35E-6	–	–	–
#13	Pt	14.6	6.9	4.7E-5	2.58E-6	0.45	0.66	2.9
	Au	37.6	14.3	3.1E-5	5E-7	0.33	1.23	5.2
	TiO_2	–	4.6	2.8E-5	1.35E-6	–	–	–
#14	Pt	9.8	7.9	6.6E-5	8.71E-6	0.63	0.62	2.7
	Au	50.5	8	3.4E-5	1.18E-6	0.36	1.82	7.8
	TiO_2	–	4.6	2.7E-5	1.35E-6	–	–	–

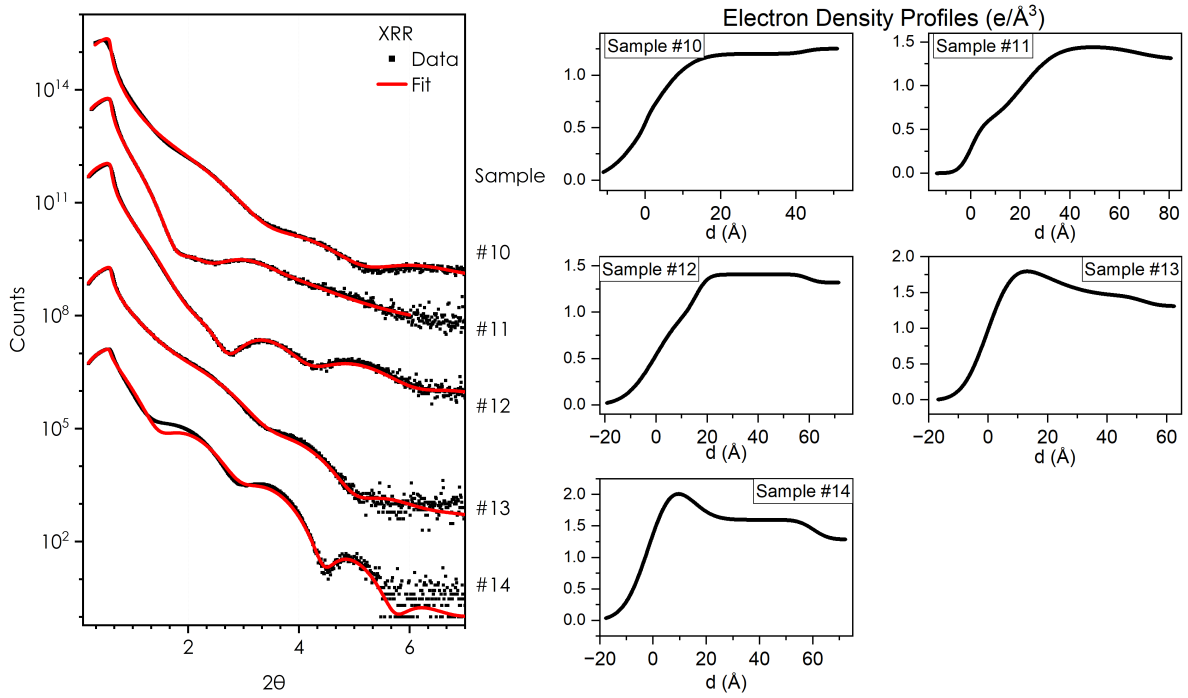

Figure B.7: X-Ray Reflectivity data (black dots) and fit (red line) of Pt-Au-TiO_2 samples #10 to #14 after CO oxidation. The XRR fits were used to determine the coverage and amount of evaporated material. The fit results are presented in Table B.6

B.6 Testing CO and CO_2 Adsorption on Au(111) at 97 K

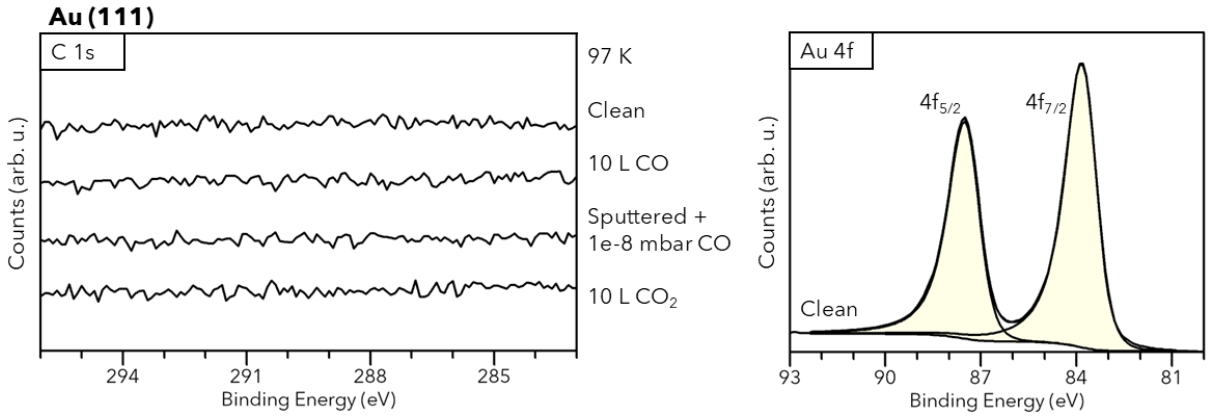

Figure B.8: CO and CO_2 adsorption monitored by XPS in C 1s core level spectrum on Au(111). No adsorption was observed.

B.7 Dark CO Oxidation Test on Rutile (110)

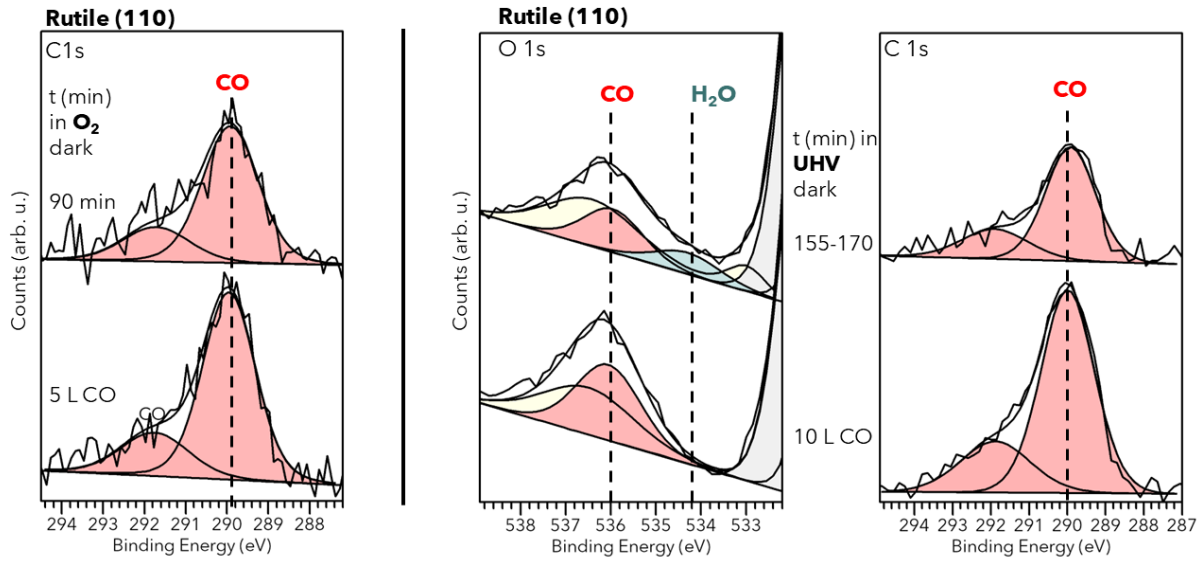

Figure B.9: XP Spectra of CO on stoichiometric rutile (110) in dark conditions under (left) O_2 atmosphere and (right) UHV conditions. No oxidation was observed, but water adsorbs.

Table B.7: Relative CO_2 amount during CO oxidation on stoichiometric rutile (110).

Stoichiomentric rutile (110)							
steps	relative CO_2				in situ	rel. CO_2	
Time	UV		530 nm		Time	UV	
min	%	± %	%	± %	min	%	± %
0	0	0	0	0	0	0	0
20	16	5	7	5	0 - 15	7	5
40	12	5	18	5	15 - 30	7	5
60	27	10	30	7	30 - 45	11	10
80	30	10	40	7	45 - 60	14	10
100	36	10	50	7	60 - 75	21	10
120	48	10	60	7	75 - 90	19	10
140	51	10	60	7	90 - 105	20	10
					105 - 120	30	10
					120 - 135	33	10
					135 - 150	35	10

Table B.8: Relative CO_2 amount during CO oxidation on samples #1 and #6.

	Au(2.5 nm)/TiO_2 #1				Au(5 nm)/TiO_2 #6					
steps	relative CO_2				relative CO_2					
Time	UV		dark		dark		530 nm		UV	
min	%	± %	%	± %	%	± %	%	± %	%	± %
0	0	0	0	0	0		0	0	0	0
10	21	5	25	5	12	6	18	5	20	5
20	44	3	42	3	20	7	30	5	33	6
30	65	5	62	5	30	8	40	7	47	8
40	87	6	86	6	40	10	48	10	59	10
50	89	4	93	4	50	10				

Table B.9: Relative CO_2 amount during CO oxidation on sample #7.

Au(4.5 nm)/TiO_2 #7							
	relative CO_2					rel. CO_2	
Time	dark		530 nm		Time	UV	
min	%	± %	%	± %	min	%	± %
0	0	0	0	0	0	0	0
10	15	5	13	5	15	10	5
20	16	5	15	10	30	23	5
30	17	7	20	10	45	38	10
40	22	10	33	10	60	40	5
50	33	10	27	10	75	60	5
60	35	10	38	10			
70			40	10			

Table B.10: Relative CO_2 amount during CO oxidation on samples #8 and #9.

Au(5 nm)/TiO_2 #8							Au(6 nm)/TiO_2 #9		
in situ	relative CO_2						in situ		
Time	dark		530 nm		UV		Time	UV	
min	%	± %	%	± %	%	± %	min	%	± %
0	0		0		0		0	0	
15 - 30	9	7	20	7	16	7	15 - 25	8	3
45 - 60	17	9	31	9	26	9	40 - 50	14	5
75 - 90	21	9	40	9	34	9	65 - 75	16	5
105 - 120	24	9	45	9	43	9	90 - 100	18	5
135 - 150	29	9	53	9	52	9	115 - 125	23	7
							140 - 150	28	7
							165 - 175	29	7
							190 - 200	31	7

Table B.11: Relative CO_2 amount during CO oxidation on sample #10.

Pt-Au(6 nm)/TiO_2 #10						
in situ	relative CO_2					
Time	dark		530 nm		UV	
min	%	± %	%	± %	%	± %
0	0	0	0	0	0	0
10 - 20	4	5	5	5	12	5
30 - 40	7	5	8	5	12	5
50 - 60	15	5	14	5	16	5
70 - 80	21	5	20	5	17	5
90 - 100	17	5	20	5	23	5
110 - 120	22	5	21	5		

Table B.12: Relative CO_2 amount during CO oxidation on sample #12.

Pt-Au(5 nm)/TiO_2		
steps	relative CO_2	
Time	dark	
min	%	± %
0	0	
20	35	10
40	55	10
60	55	10

List of Figures

List of Tables

List of Abbrevations

AO Atomic Orbital

arb.u. arbitrary units

CB Conduction Band

DFT Density Functional Theory

DLD Delay Line Detector

DESY Deutsches Elektronen-Synchrotron

DFT Density Functional Theory

FEL Free-Electron Laser

FWHM Full Width Half Haximum

GIXRD Grazing Incidence X-Ray Diffraction

L Langmuir

LCAO Linear Combination of Atomic Orbitals

LEED Low Energy Electron Diffraction

LSPR Localized Surface Plasmon Resonance

MBE Molecular Beam Epitaxy

MCP Microchannel Plate

ML Mono Layer

MO Molecular Orbitals

NP Nanoparticle

pDOS projected Density of States

RAIRS Reflection Absorption Infrared Spectroscopy

RT Room Temperature

SDRS Surface Differential Reflectance Spectroscopy

STM Scanning Tunneling Microscopy

TOF Time-of-Flight

UHV Ultra High Vacuum

UPS Ultraviolet Phtotelectron Spectrocopy

UV Ultraviolett

VB Valence Band

VIS Visible

XRD X-Ray Diffraction

XRR X-Ray Reflectivity

XPS X-Ray Photoelectron Spectrocopy

List of Publications

[I] **Dynamics of the CO Photooxidation to CO_2 on Rutile (110)**
Helena Gleißnner, Michael Wagstaffe, Lukas Wenthaus, Adrian Domínguez-Castro, Verena Gupta, Simon Chung, Steffen Palutke, Siarhei Dziarzhytski, Dmytro Kutnyakhov, Michael Heber, Günter Brenner, Harald Redlin, Federico Pressacco, Adriel Domínguez Garcia, Thomas Frauenheim, Heshmat Noei, Andreas Stierle; *submitted to Communications Chemistry*, **2025**.

[II] **Photoinduced Dynamics at the Water/TiO_2(101) Interface**
Michael Wagstaffe, Adrian Dominguez-Castro, Lukas Wenthaus, Steffen Palutke, Dmytro Kutnyakhov, Michael Heber, Federico Pressacco, Siarhei Dziarzhytski, Helena Gleißner, Verena Kristin Gupta, Harald Redlin, Adriel Dominguez, Thomas Frauenheim, Angel Rubio, Andreas Stierle, and Heshmat Noei; *Phys. Rev. Lett. 130*, 108001, **2023**.

Bibliography

[1] U. Diebold. The surface science of titanium dioxide. *Surf. Sci. Rep.*, 48(5-8):53–229 (**2003**). doi:10.1016/S0167-5729(02)00100-0.

[2] L. Burgio and R. J. H. Clark. Comparative pigment analysis of six modern Egyptian papyri and an authentic one of the 13th century BC by Raman microscopy and other techniques. *J. Raman Spectrosc.*, 31(5):395–401 (**2000**). doi:10.1002/1097-4555(200005)31:5<395::AID-JRS527>3.0.CO;2-E.

[3] K. Nakata and A. Fujishima. TiO_2 photocatalysis: Design and applications. *J. Photochem. Photobiol. C Photochem. Rev.*, 13(3):169–189 (**2012**). doi:10.1016/j.jphotochemrev.2012.06.001.

[4] A. Fujishima, T. N. Rao and D. A. Tryk. Titanium dioxide photocatalysis. *J. Photochem. Photobiol. C Photochem. Rev.*, 1(1):1–21 (**2000**). doi:10.1016/S1389-5567(00)00002-2.

[5] A. Fujishima, X. Zhang and D. A. Tryk. TiO_2 photocatalysis and related surface phenomena. *Surf. Sci. Rep.*, 63(12):515–582 (**2008**). doi:10.1016/j.surfrep.2008.10.001.

[6] A. Fujishima and K. Honda. Electrochemical Photolysis of Water at a Semiconductor Electrode. *Nature*, 238(5358):37–38 (**1972**). doi:10.1038/238037a0.

[7] M. Ismael. Latest progress on the key operating parameters affecting the photocatalytic activity of TiO_2-based photocatalysts for hydrogen fuel production: A comprehensive review. *Fuel*, 303(May):121207 (**2021**). doi:10.1016/j.fuel.2021.121207.

[8] J. Carbajo, A. Bahamonde and M. Faraldos. Photocatalyst performance in wastewater treatment applications: Towards the role of TiO_2 properties. *Mol. Catal.*, 434:167–174 (**2017**). doi:10.1016/j.mcat.2017.03.018.

[9] J. Ying, B. Zhou and J. Xiao. Pore structure and chloride diffusivity of recycled aggregate concrete with nano-SiO_2 and nano-TiO_2. *Constr. Build. Mater.*, 150:49–55 (**2017**). doi:10.1016/j.conbuildmat.2017.05.168.

[10] A. Šuligoj *et al.* TiO_2-SiO_2 films from organic-free colloidal TiO_2 anatase nanoparticles as photocatalyst for removal of volatile organic compounds from indoor air. *Appl. Catal. B Environ.*, 184:119–131 (**2016**). doi:10.1016/j.apcatb.2015.11.007.

[11] S. Linic *et al.* Photochemical transformations on plasmonic metal nanoparticles. *Nat. Mater.*, 14(6):567–576 (**2015**). doi:10.1038/nmat4281.

[12] B. Boro *et al.* Nano-structured TiO_2/ZnO nanocomposite for dye-sensitized solar cells application: A review. *Renew. Sustain. Energy Rev.*, 81(May 2017):2264–2270 (**2018**). doi:10.1016/j.rser.2017.06.035.

[13] B. Çalışkan and E. Şayan. Review on TiO_2 nanotubes in dye-sensitized solar cells: electrochemical anodization and hydrothermal method. *J. Solid State Electrochem.* (**2025**). doi:10.1007/s10008-024-06168-y.

[14] L. E. Oi *et al.* Recent advances of titanium dioxide (TiO_2) for green organic synthesis. *RSC Adv.*, 6(110):108741–108754 (**2016**). doi:10.1039/c6ra22894a.

[15] K. Hashimoto, H. Irie and A. Fujishima. TiO_2 Photocatalysis: A Historical Overview and Future Prospects. *Jpn. J. Appl. Phys.*, 44(12R):8269 (**2005**). doi:10.1143/JJAP.44.8269.

[16] TiO_2 coated Centre Pompidou in Metz in France. https://www.taiyo-europe.com/projekte/project/centre-pompidou-metz/ date accessed: 21.10.2019.

[17] M. Janczarek *et al.* Progress of functionalized TiO_2-based nanomaterials in the construction industry: A comprehensive review. *Chem. Eng. J.*, 430(August 2021) (**2022**). doi:10.1016/j.cej.2021.132062.

[18] R. Ciriminna *et al.* Industrial Applications of Gold Catalysis. *Angew. Chemie - Int. Ed.*, 55(46):14210–14217 (**2016**). doi:10.1002/anie.201604656.

[19] F. Gao and D. W. Goodman. Pd–Au bimetallic catalysts: Understanding alloy effects from planar models and (supported) nanoparticles. *Chem. Soc. Rev.*, 41(24):8009–8020 (**2012**). doi:10.1039/c2cs35160a.

[20] Z. Zha and P. Deshlahra. Mechanistic Framework and Effects of High Coverage in Vinyl Acetate Synthesis. *ACS Catal.*, 11(3):1841–1857 (**2021**). doi:10.1021/acscatal.0c03673.

[21] P. Johnston, N. Carthey and G. J. Hutchings. Discovery, Development, and Commercialization of Gold Catalysts for Acetylene Hydrochlorination. *J. Am. Chem. Soc.*, 137(46):14548–14557 (**2015**). doi:10.1021/jacs.5b07752.

[22] G. J. Hutchings. Vapor phase hydrochlorination of acetylene: Correlation of catalytic activity of supported metal chloride catalysts. *J. Catal.*, 96(1):292–295 (**1985**). doi:10.1016/0021-9517(85)90383-5.

[23] G. J. Hutchings. Catalysis using gold containing materials. *J. Catal.*, 432(January):115392 (**2024**). doi:10.1016/j.jcat.2024.115392.

[24] K. Suzuki *et al.* Aerobic oxidative esterification of aldehydes with alcohols by gold-nickel oxide nanoparticle catalysts with a core-shell structure. *ACS Catal.*, 3(8):1845–1849 (**2013**). doi:10.1021/cs4004084.

[25] M. Haruta *et al.* Novel Gold Catalysts for the Oxidation of Carbon Monoxide at a Temperature far Below 0 °C. *Chem. Lett.*, 16(2):405–408 (**1987**). doi:10.1246/cl.1987.405.

[26] S. S. Punde and B. J. Tatarchuk. CO removal at ambient conditions: Catalyst screening and impact of operating conditions. *Sep. Purif. Technol.*, 183:43–53 (**2017**). doi:10.1016/j.seppur.2017.03.007.

[27] X. Zhang *et al.* Plasmonic photocatalysis. *Reports Prog. Phys.*, 76(4):046401 (**2013**). doi:10.1088/0034-4885/76/4/046401.

[28] D. A. Panayotov and J. R. Morris. Surface chemistry of Au/TiO_2: Thermally and photolytically activated reactions. *Surf. Sci. Rep.*, 71(1):77–271 (**2016**). doi:10.1016/j.surfrep.2016.01.002.

[29] Y. Shiraishi *et al.* Quantum tunneling injection of hot electrons in Au/TiO_2 plasmonic photocatalysts. *Nanoscale*, 9(24):8349–8361 (**2017**). doi:10.1039/c7nr02310c.

[30] N. S. Mueller *et al.* Surface-Enhanced Raman Scattering and Surface-Enhanced Infrared Absorption by Plasmon Polaritons in Three-Dimensional Nanoparticle Supercrystals. *ACS Nano*, 15(3):5523–5533 (**2021**). doi:10.1021/acsnano.1c00352.

[31] H. J. Freund *et al.* CO oxidation as a prototypical reaction for heterogeneous processes. *Angew. Chemie - Int. Ed.*, 50(43):10064–10094 (**2011**). doi:10.1002/anie.201101378.

[32] A. Nilsson *et al.* Catalysis in real time using X-ray lasers. *Chem. Phys. Lett.*, 675:145–173 (**2017**). doi:10.1016/j.cplett.2017.02.018.

[33] S. Neppl *et al.* Nanoscale Confinement of Photo-Injected Electrons at Hybrid Interfaces. *J. Phys. Chem. Lett.*, 12(49):11951–11959 (**2021**). doi:10.1021/acs.jpclett.1c02648.

[34] M. Wagstaffe *et al.* Ultrafast Real-Time Dynamics of CO Oxidation over an Oxide Photocatalyst. *ACS Catal.*, 10(22):13650–13658 (**2020**). doi:10.1021/acscatal.0c04098.

[35] D. A. H. Hanaor and C. C. Sorrell. Review of the anatase to rutile phase transformation. *J. Mater. Sci.*, 46(4):855–874 (**2011**). doi:10.1007/s10853-010-5113-0.

[36] P. Torres and R. Rurali. Thermal Conductivity of Rutile and Anatase TiO_2 from First-Principles. *J. Phys. Chem. C*, 123(51):30851–30855 (**2019**). doi:10.1021/acs.jpcc.9b09299.

[37] R. Gross and A. Marx. *Festkörperphysik*. OLDENBOURG WISSENSCHAFTSVERLAG (**2014**). ISBN 978-3-11-035869-8. doi:10.1524/9783110358704.

[38] P. A. Cox. *The Electronic Structure and Chemistry of Solids*. Oxford University Press (**1987**).

[39] H. Ibach and H. Lüth. Semiconductors. In *Solid-State Phys.*, pp. 419–515. Springer Berlin Heidelberg, Berlin, Heidelberg (**2009**). doi:10.1007/978-3-540-93804-0_12.

[40] C. Boukouvala, J. Daniel and E. Ringe. Approaches to modelling the shape of nanocrystals. *Nano Converg.*, 8(1) (**2021**). doi:10.1186/s40580-021-00275-6.

[41] M. Ramamoorthy, D. Vanderbilt and R. D. King-Smith. First-principles calculations of the energetics of stoichiometric TiO_2 surfaces. *Phys. Rev. B*, 49(23):16721–16727 (**1994**). doi:10.1103/PhysRevB.49.16721.

[42] M. Lazzeri, A. Vittadini and A. Selloni. Structure and energetics of stoichiometric TiO_2 anatase surfaces. *Phys. Rev. B - Condens. Matter Mater. Phys.*, 63(15):1554091–1554099 (**2001**). doi:10.1103/PhysRevB.63.155409.

[43] M. A. Henderson. A surface perspective on self-diffusion in rutile TiO_2. *Surf. Sci.*, 419(2-3):174–187 (**1999**). doi:10.1016/S0039-6028(98)00778-X.

[44] M. Li, W. Hebenstreit and U. Diebold. Oxygen-induced restructuring of the rutile $TiO_2(110)(1\times1)$ surface. *Surf. Sci.*, 414(1-2):L951–L956 (**1998**). doi:10.1016/S0039-6028(98)00549-4.

[45] Q. Guo *et al.* Elementary photocatalytic chemistry on TiO_2 surfaces. *Chem. Soc. Rev.*, 45(13):3701–3730 (**2016**). doi:10.1039/C5CS00448A.

[46] L. Jing *et al.* Effects of surface oxygen vacancies on photophysical and photochemical processes of Zn-doped TiO_2 nanoparticles and their relationships. *J. Phys. Chem. B*, 110(36):17860–17865 (**2006**). doi:10.1021/jp063148z.

[47] I. Nakamura *et al.* Role of oxygen vacancy in the plasma-treated TiO_2 photocatalyst with visible light activity for NO removal. *J. Mol. Catal. A Chem.*, 161(1-2):205–212 (**2000**). doi:10.1016/S1381-1169(00)00362-9.

[48] H. Li, Y. Guo and J. Robertson. Calculation of TiO_2 Surface and Subsurface Oxygen Vacancy by the Screened Exchange Functional. *J. Phys. Chem. C*, 119(32):18160–18166 (**2015**). doi:10.1021/acs.jpcc.5b02430.

[49] H. Cheng and A. Selloni. Surface and subsurface oxygen vacancies in anatase TiO_2 and differences with rutile. *Phys. Rev. B*, 79(9):2–5 (**2009**). doi:10.1103/physrevb.79.092101.

[50] Y. He *et al.* Evidence for the Predominance of Subsurface Defects on Reduced Anatase TiO_2. *Phys. Rev. Lett.*, 102(10):106105 (**2009**). doi:10.1103/PhysRevLett.102.106105.

[51] J. Yan *et al.* Understanding the effect of surface/bulk defects on the photocatalytic activity of TiO_2: anatase versus rutile. *Phys. Chem. Chem. Phys.*, 15(26):10978–10988 (**2013**). doi:10.1039/c3cp50927c.

[52] N. G. Petrik and G. A. Kimmel. Photoinduced dissociation of O_2 on rutile TiO_2(110). *J. Phys. Chem. Lett.*, 1(12):1758–1762 (**2010**). doi:10.1021/jz100513e.

[53] Z. Dohnálek *et al.* Physisorption of N_2, O_2, and CO on fully oxidized TiO_2 (110). *J. Phys. Chem. B*, 110(12):6229–6235 (**2006**). doi:10.1021/jp0564905.

[54] M. Li *et al.* The Influence of the Bulk Reduction State on the Surface Structure and Morphology of Rutile TiO_2(110) Single Crystals. *J. Phys. Chem. B*, 104(20):4944–4950 (**2000**). doi:10.1021/jp9943272.

[55] J. Cai *et al.* Light-Driven Sustainable Hydrogen Production Utilizing TiO_2 Nanostructures: A Review. *Small Methods*, 3(1):1800184 (**2019**). doi:10.1002/smtd.201800184.

[56] Y. Nosaka and A. Y. Nosaka. Generation and Detection of Reactive Oxygen Species in Photocatalysis. *Chem. Rev.*, 117(17):11302–11336 (**2017**). doi:10.1021/acs.chemrev.7b00161.

[57] M. Ye *et al.* Synthesis of Black TiO_x Nanoparticles by Mg Reduction of TiO_2 Nanocrystals and their Application for Solar Water Evaporation. *Adv. Energy Mater.*, 7(4) (**2017**). doi:10.1002/aenm.201601811.

[58] J. Schneider *et al.* Understanding TiO_2 Photocatalysis: Mechanisms and Materials. *Chem. Rev.*, 114(19):9919–9986 (**2014**). doi:10.1021/cr5001892.

[59] M. Batzill, E. H. Morales and U. Diebold. Influence of nitrogen doping on the defect formation and surface properties of TiO_2 rutile and anatase. *Phys. Rev. Lett.*, 96(2):1–4 (**2006**). doi:10.1103/PhysRevLett.96.026103.

[60] C. Han *et al.* Innovative visible light-activated sulfur doped TiO_2 films for water treatment. *Appl. Catal. B Environ.*, 107(1-2):77–87 (**2011**). doi:10.1016/j.apcatb.2011.06.039.

[61] C. Di Valentin and G. Pacchioni. Trends in non-metal doping of anatase TiO_2: B, C, N and F. *Catal. Today*, 206:12–18 (**2013**). doi:10.1016/j.cattod.2011.11.030.

[62] C.-y. Wang, D. W. Bahnemann and J. K. Dohrmann. A novel preparation of iron-doped TiO_2 nanoparticles with enhanced photocatalytic activity. *Chem. Commun.*, (16):1539–1540 (**2000**). doi:10.1039/b002988m.

[63] W. Zhou *et al.* Preparation and properties of vanadium-doped TiO2 photocatalysts. *J. Phys. D. Appl. Phys.*, 43(3) (**2010**). doi:10.1088/0022-3727/43/3/035301.

[64] N. S. Peighambardoust *et al.* Band-gap narrowing and electrochemical properties in N-doped and reduced anodic TiO2 nanotube arrays. *Electrochim. Acta*, 270:245–255 (**2018**). doi:10.1016/j.electacta.2018.03.091.

[65] S. Chen, C. Li and Z. Hou. A novel in situ synthesis of TiO2/CdS heterojunction for improving photoelectrochemical water splitting. *Int. J. Hydrogen Energy*, 44(47):25473–25485 (**2019**). doi:10.1016/j.ijhydene.2019.08.049.

[66] L. G. Devi and R. Kavitha. A review on plasmonic metal-TiO_2 composite for generation, trapping, storing and dynamic vectorial transfer of photogenerated electrons across the Schottky junction in a photocatalytic system. *Appl. Surf. Sci.*, 360:601–622 (**2016**). doi:10.1016/j.apsusc.2015.11.016.

[67] M. A. Garcia. Surface plasmons in metallic nanoparticles: fundamentals and applications. *J. Phys. D. Appl. Phys.*, 45(38):389501 (**2012**). doi:10.1088/0022-3727/45/38/389501.

[68] V. Subramanian, E. E. Wolf and P. V. Kamat. Catalysis with TiO_2/Gold Nanocomposites. Effect of Metal Particle Size on the Fermi Level Equilibration. *J. Am. Chem. Soc.*, 126(15):4943–4950 (**2004**). doi:10.1021/ja0315199.

[69] S. T. Kochuveedu, Y. H. Jang and D. H. Kim. A study on the mechanism for the interaction of light with noble metal-metal oxide semiconductor nanostructures for various photophysical applications. *Chem. Soc. Rev.*, 42(21):8467–8493 (**2013**). doi:10.1039/c3cs60043b.

[70] A. L. Linsebigler, G. Lu and J. T. Yates. Photocatalysis on TiO_2 Surfaces: Principles, Mechanisms, and Selected Results. *Chem. Rev.*, 95(3):735–758 (**1995**). doi: 10.1021/cr00035a013.

[71] D. C. Sorescu and J. T. Yates. Adsorption of CO on the TiO_2(110) surface: A theoretical study. *J. Phys. Chem. B*, 102(23):4556–4565 (**1998**). doi:10.1021/jp9801626.

[72] N. G. Petrik *et al.* Chemical reactivity of reduced TiO_2(110): the dominant role of surface defects in oxygen chemisorption. *J. Phys. Chem. C*, 113(28):12407–12411 (**2009**). doi:10.1021/jp901989x.

[73] M. Kunat *et al.* Formation of weakly bound, ordered adlayers of CO on rutile TiO_2(110): A combined experimental and theoretical study. *J. Chem. Phys.*, 130(14) (**2009**). doi:10.1063/1.3098318.

[74] M. Xu *et al.* The surface science approach for understanding reactions on oxide powders: The importance of IR spectroscopy. *Angew. Chemie - Int. Ed.*, 51(19):4731–4734 (**2012**). doi:10.1002/anie.201200585.

[75] M. Xu *et al.* UHV-FTIRS studies on molecular competitive adsorption: ^{12}CO, ^{13}CO and CO_2 on reduced TiO_2(110) surfaces. *Phys. Chem. Chem. Phys.*, 16(43):23711–23715 (**2014**). doi:10.1039/c4cp03158j.

[76] M. A. Henderson and I. Lyubinetsky. Molecular-Level Insights into Photocatalysis from Scanning Probe Microscopy Studies on TiO_2 (110). *Chem. Rev.*, 113(6):4428–4455 (**2013**). doi:10.1021/cr300315m.

[77] M. Setvin *et al.* Identification of adsorbed molecules via STM tip manipulation: CO, H_2O, and O_2 on TiO_2 anatase (101). *Phys. Chem. Chem. Phys.*, 16(39):21524–21530 (**2014**). doi:10.1039/c4cp03212h.

[78] M. Setvin *et al.* A Multitechnique Study of CO Adsorption on the TiO_2 Anatase (101) Surface. *J. Phys. Chem. C*, 119(36):21044–21052 (**2015**). doi:10.1021/acs.jpcc.5b07999.

[79] M. Reticcioli *et al.* Interplay between Adsorbates and Polarons: CO on Rutile TiO_2(110). *Phys. Rev. Lett.*, 122(1):1–6 (**2019**). doi:10.1103/PhysRevLett.122.016805.

[80] T. L. Thompson, O. Diwald and J. T. Yates. CO_2 as a Probe for Monitoring the Surface Defects on TiO_2 (110) Temperature-Programmed Desorption. *J. Phys. Chem. B*, 107(42):11700–11704 (**2003**). doi:10.1021/jp030430m.

[81] D. C. Sorescu, W. A. Al-Saidi and K. D. Jordan. CO_2 adsorption on TiO_2(101) anatase: A dispersion-corrected density functional theory study. *J. Chem. Phys.*, 135(12) (**2011**). doi:10.1063/1.3638181.

[82] D. C. Sorescu *et al.* Coadsorption properties of CO_2 and H_2O on TiO_2 rutile (110): A dispersion-corrected DFT study. *J. Chem. Phys.*, 137(7):074704 (**2012**). doi:10.1063/1.4739088.

[83] C. Rohmann *et al.* Direct monitoring of photo-induced reactions on well-defined metal oxide surfaces using vibrational spectroscopy. *Chem. Phys. Lett.*, 460(1-3):10–12 (**2008**). doi:10.1016/j.cplett.2008.05.056.

[84] M. Xu *et al.* Photocatalytic Activity of Bulk TiO_2 Anatase and Rutile Single Crystals Using Infrared Absorption Spectroscopy. *Phys. Rev. Lett.*, 106(13):138302 (**2011**). doi:10.1103/PhysRevLett.106.138302.

[85] M. Wagstaffe, H. Noei and A. Stierle. Elucidating the Defect-Induced Changes in the Photocatalytic Activity of TiO_2. *J. Phys. Chem. C*, 124(23):12539–12547 (**2020**). doi:10.1021/acs.jpcc.0c02809.

[86] M. Anpo *et al.* Quantum chemical and $^{18}O_2$ tracer studies of the activation of oxygen in photocatalytic oxidation reactions. *J. Phys. Chem.*, 88(12):2572–2575 (**1984**). doi:10.1021/j150656a029.

[87] Z. Zhang and J. T. Yates. Band Bending in Semiconductors: Chemical and Physical Consequences at Surfaces and Interfaces. *Chem. Rev.*, 112(10):5520–5551 (**2012**). doi:10.1021/cr3000626.

[88] P. Maity *et al.* Study of the Bulk Charge Carrier Dynamics in Anatase and Rutile TiO_2 Single Crystals by Femtosecond Time-Resolved Spectroscopy. *J. Phys. Chem. C*, 122(16):8925–8932 (**2018**). doi:10.1021/acs.jpcc.8b00256.

[89] R. G. W. Norrish and G. Porter. Chemical Reactions Produced by Very High Light Intensities. *Nature*, 164(4172):658–658 (**1949**). doi:10.1038/164658a0.

[90] A. H. Zewail. Femtochemistry: Atomic-Scale Dynamics of the Chemical Bond. *J. Phys. Chem. A*, 104(24):5660–5694 (**2000**). doi:10.1021/jp001460h.

[91] M. Fushitani. Applications of pump-probe spectroscopy. *Annu. Reports Prog. Chem. - Sect. C*, 104:272–297 (**2008**). doi:10.1039/b703983m.

[92] M. Wagstaffe *et al.* Photoinduced Dynamics at the Water/TiO_2(101) Interface. *Phys. Rev. Lett.*, 130(10):108001 (**2023**). doi:10.1103/PhysRevLett.130.108001.

[93] Z. B. Ma *et al.* Kinetics and dynamics of photocatalyzed dissociation of ethanol on TiO_2(110). *Chinese J. Chem. Phys.*, 26(1):1–7 (**2013**). doi:10.1063/1674-0068/26/01/1-7.

[94] A. R. Muraca *et al.* Ultrafast dynamics of acetone photooxidation on TiO_2(110). *J. Chem. Phys.*, 151(16):161103 (**2019**). doi:10.1063/1.5122269.

[95] S. H. Park *et al.* Direct and real-time observation of hole transport dynamics in anatase TiO_2 using X-ray free-electron laser. *Nat. Commun.*, 13(1):2531 (**2022**). doi:10.1038/s41467-022-30336-1.

[96] M. Bonn *et al.* Phonon- Versus Electron-Mediated Desorption and Oxidation of CO on Ru(0001). *Science*, 285(5430):1042–1045 (**1999**). doi:10.1126/science.285.5430.1042.

[97] H. Öström *et al.* Probing the transition state region in catalytic CO oxidation on Ru. *Science*, 347(6225):978–982 (**2015**). doi:10.1126/science.1261747.

[98] T.-H. Her *et al.* Surface femtochemistry of $CO/O_2/Pt(111)$: The importance of nonthermalized substrate electrons. *J. Chem. Phys.*, 108(20):8595–8598 (**1998**). doi:10.1063/1.476289.

[99] P. Szymanski, A. L. Harris and N. Camillone. Efficient subpicosecond photoinduced surface chemistry: The ultrafast photooxidation of CO on palladium. *J. Phys. Chem. C*, 112(40):15802–15808 (**2008**). doi:10.1021/jp8044737.

[100] K. L. Kostov, H. Rauscher and D. Menzel. Adsorption of CO on oxygen-covered Ru(001). *Surf. Sci.*, 278(1-2):62–86 (**1992**). doi:10.1016/0039-6028(92)90584-S.

[101] B. Hammer and J. K. Norskov. Why gold is the noblest of all the metals. *Nature*, 376(6537):238–240 (**1995**). doi:10.1038/376238a0.

[102] G. C. Bond and D. T. Thompson. Gold-catalysed oxidation of carbon monoxide. *Gold Bull.*, 33(2):41–50 (**2000**). doi:10.1007/BF03216579.

[103] O. Schmidt. Beiträge zur Kenntnis der katalytischen Hydrierung organischer Substanzen. *Zeitschrift für Phys. Chemie*, 118U(1):193–239 (**1925**). doi:10.1515/zpch-1925-11818.

[104] M. Haruta *et al.* Gold catalysts prepared by coprecipitation for low-temperature oxidation of hydrogen and of carbon monoxide. *J. Catal.*, 115(2):301–309 (**1989**). doi:10.1016/0021-9517(89)90034-1.

[105] T. Ishida *et al.* Importance of Size and Contact Structure of Gold Nanoparticles for the Genesis of Unique Catalytic Processes. *Chem. Rev.*, 120(2):464–525 (**2020**). doi:10.1021/acs.chemrev.9b00551.

[106] I. X. Green *et al.* Low-temperature catalytic H2 oxidation over Au nanoparticle/TiO2 dual perimeter sites. *Angew. Chemie - Int. Ed.*, 50(43):10186–10189 (**2011**). doi:10.1002/anie.201101612.

[107] J. A. Rodriguez *et al.* The activation of gold and the water-gas shift reaction: Insights from studies with model catalysts. *Acc. Chem. Res.*, 47(3):773–782 (**2014**). doi:10.1021/ar400182c.

[108] N. W. Cant and W. K. Hall. Catalytic oxidation. IV. Ethylene and propylene oxidation over gold. *J. Phys. Chem.*, 75(19):2914–2921 (**1971**). doi:10.1021/j100688a007.

[109] J. Chen *et al.* A comparative study of size effects in the au-catalyzed oxidative and non-oxidative dehydrogenation of benzyl alcohol. *Chem. - An Asian J.*, 9(8):2187–2196 (**2014**). doi:10.1002/asia.201402238.

[110] M. McEntee *et al.* Selective catalytic oxidative-dehydrogenation of carboxylic acids - Acrylate and Crotonate Formation at the Au/TiO_2 Interface. *J. Am. Chem. Soc.*, 136(13):5116–5120 (**2014**). doi:10.1021/ja500928h.

[111] Y. Guan and E. J. Hensen. Ethanol dehydrogenation by gold catalysts: The effect of the gold particle size and the presence of oxygen. *Appl. Catal. A Gen.*, 361(1-2):49–56 (**2009**). doi:10.1016/j.apcata.2009.03.033.

[112] A. Marikutsa *et al.* Comparison of Au-functionalized semiconductor metal oxides in sensitivity to VOC. *Sensors Actuators, B Chem.*, 326(July 2020):128980 (**2021**). doi:10.1016/j.snb.2020.128980.

[113] P. Dumas, R. Tobin and P. Richards. Study of adsorption states and interactions of CO on evaporated noble metal surfaces by infrared absorption spectroscopy. *Surf. Sci.*, 171(3):579–599 (**1986**). doi:10.1016/0039-6028(86)91061-7.

[114] J. Kim, E. Samano and B. E. Koel. CO adsorption and reaction on clean and oxygen-covered Au(211) surfaces. *J. Phys. Chem. B*, 110(35):17512–17517 (**2006**). doi:10.1021/jp061685d.

[115] T. Jiang *et al.* Trends in CO oxidation rates for metal nanoparticles and close-packed, stepped, and kinked surfaces. *J. Phys. Chem. C*, 113(24):10548–10553 (**2009**). doi:10.1021/jp811185g.

[116] A. Hussain *et al.* Two gold surfaces and a cluster with remarkable reactivity for CO oxidation, a density functional theory study. *Top. Catal.*, 54(5-7):415–423 (**2011**). doi:10.1007/s11244-011-9672-3.

[117] H. Poppa. Nucleation, Growth, and TEM Analysis of Metal Particles and Clusters Deposited in UHV. *Catal. Rev.*, 35(3):359–398 (**1993**). doi:10.1080/01614949308013911.

[118] S. D. Lin, M. Bollinger and M. A. Vannice. Low temperature CO oxidation over Au/TiO_2 and Au/SiO_2 catalysts. *Catal. Letters*, 17(3-4):245–262 (**1993**). doi:10.1007/BF00766147.

[119] S. Arrii *et al.* Oxidation of CO on Gold Supported Catalysts Prepared by Laser Vaporization: Direct Evidence of Support Contribution. *J. Am. Chem. Soc.*, 126(4):1199–1205 (**2004**). doi:10.1021/ja036352y.

[120] M. M. Schubert *et al.* CO oxidation over supported gold catalysts -"Inert" and "active" support materials and their role for the oxygen supply during reaction. *J. Catal.*, 197(1):113–122 (**2001**). doi:10.1006/jcat.2000.3069.

[121] T. Bligaard and J. Nørskov. Heterogeneous Catalysis. In *Chem. Bond. Surfaces Interfaces*, pp. 255–321. Elsevier (**2008**). doi:10.1016/B978-044452837-7.50005-8.

[122] M. Haruta. When Gold Is Not Noble: Catalysis by Nanoparticles. *Chem. Rec.*, 3(2):75–87 (**2003**). doi:10.1002/tcr.10053.

[123] B. Yoon *et al.* Charging Effects on Bonding and Catalyzed Oxidation of CO on Au_8 Clusters on MgO. *Science*, 307(5708):403–407 (**2005**). doi:10.1126/science.1104168.

[124] T. Minato *et al.* Investigation of the electronic interaction between $TiO_2(110)$ surfaces and Au clusters by PES and STM. *Surf. Sci.*, 566-568(1-3 PART 2):1012–1017 (**2004**). doi:10.1016/j.susc.2004.06.047.

[125] L. M. Molina, M. D. Rasmussen and B. Hammer. Adsorption of O_2 and oxidation of CO at Au nanoparticles supported by $TiO_2(110)$. *J. Chem. Phys.*, 120(16):7673–7680 (**2004**). doi:10.1063/1.1687337.

[126] M. Chen and D. W. Goodman. Catalytically active gold on ordered titania supports. *Chem. Soc. Rev.*, 37(9):1860 (**2008**). doi:10.1039/b707318f.

[127] J. C. Fierro-Gonzalez and B. C. Gates. Catalysis by gold dispersed on supports: the importance of cationic gold. *Chem. Soc. Rev.*, 37(9):2127 (**2008**). doi:10.1039/b707944n.

[128] J. Guzman and B. C. Gates. Catalysis by Supported Gold: Correlation between Catalytic Activity for CO Oxidation and Oxidation States of Gold. *J. Am. Chem. Soc.*, 126(9):2672–2673 (**2004**). doi:10.1021/ja039426e.

[129] L. Fu *et al.* Direct Evidence of Oxidized Gold on Supported Gold Catalysts. *J. Phys. Chem. B*, 109(9):3704–3706 (**2005**). doi:10.1021/jp045117e.

[130] S. Laursen and S. Linic. Oxidation catalysis by oxide-supported Au nanostructures: The role of supports and the effect of external conditions. *Phys. Rev. Lett.*, 97(2):1–4 (**2006**). doi:10.1103/PhysRevLett.97.026101.

[131] G. R. Bamwenda *et al.* The influence of the preparation methods on the catalytic activity of platinum and gold supported on TiO_2 for CO oxidation. *Catal. Letters*, 44(1-2):83–87 (**1997**). doi:10.1023/a:1018925008633.

[132] X. Lai and D. W. Goodman. Structure-reactivity correlations for oxide-supported metal catalysts: New perspectives from STM. *J. Mol. Catal. A Chem.*, 162(1-2):33–50 (**2000**). doi:10.1016/S1381-1169(00)00320-4.

[133] S. Parker *et al.* Island growth kinetics during the vapor deposition of gold onto TiO_2(110). *Surf. Sci.*, 441(1):10–20 (**1999**). doi:10.1016/S0039-6028(99)00753-0.

[134] A. K. Santra *et al.* Growth of Au on TiO_2 (110) on a Cluster-by-Cluster Basis. *Jpn. J. Appl. Phys.*, 42(Part 1, No. 7B):4795–4798 (**2003**). doi:10.1143/JJAP.42.4795.

[135] J. Gong. Structure and surface chemistry of gold-based model catalysts. *Chem. Rev.*, 112(5):2987–3054 (**2012**). doi:10.1021/cr200041p.

[136] R. P. Galhenage *et al.* Understanding the nucleation and growth of metals on TiO_2: Co compared to Au, Ni, and Pt. *J. Phys. Chem. C*, 117(14):7191–7201 (**2013**). doi:10.1021/jp401283k.

[137] F. Cosandey and T. E. Madey. Growth, Morphology, Interfacial Effects and Catalytic Properties of Au on TiO_2. *Surf. Rev. Lett.*, 08(01n02):73–93 (**2001**). doi:10.1142/S0218625X01000884.

[138] G. Wulff. XXV. Zur Frage der Geschwindigkeit des Wachsthums und der Auflösung der Krystallflächen. *Zeitschrift für Krist. - Cryst. Mater.*, 34(1-6):449–530 (**1901**). doi:10.1524/zkri.1901.34.1.449.

[139] H. Galinski *et al.* Agglomeration of Pt thin films on dielectric substrates. *Phys. Rev. B - Condens. Matter Mater. Phys.*, 82(23):1–11 (**2010**). doi:10.1103/PhysRevB.82.235415.

[140] R. Meyer *et al.* Surface chemistry of catalysis by gold. *Gold Bull.*, 37(1-2):72–124 (**2004**). doi:10.1007/BF03215519.

[141] S. C. Parker and C. T. Campbell. Reactivity and sintering kinetics of $Au/TiO_2(110)$ model catalysts: Particle size effects. *Top. Catal.*, 44(1-2):3–13 (**2007**). doi:10.1007/s11244-007-0274-z.

[142] L. Zhang, R. Persaud and T. E. Madey. Ultrathin metal films on a metal oxide surface: Growth of Au on TiO_2 (110). *Phys. Rev. B*, 56(16):10549–10557 (**1997**). doi:10.1103/PhysRevB.56.10549.

[143] J. R. Kitchin, M. A. Barteau and J. G. Chen. A comparison of gold and molybdenum nanoparticles on $TiO_2(110)$ 1×2 reconstructed single crystal surfaces. *Surf. Sci.*, 526(3):323–331 (**2003**). doi:10.1016/S0039-6028(02)02679-1.

[144] C. Mitchell *et al.* Direct observation of behaviour of Au nanoclusters on $TiO_2(110)$ at elevated temperatures. *Surf. Sci.*, 490(1-2):196–210 (**2001**). doi:10.1016/S0039-6028(01)01333-4.

[145] F. Pesty, H.-P. Steinrück and T. E. Madey. Thermal stability of Pt films on $TiO_2(110)$: evidence for encapsulation. *Surf. Sci.*, 339(1-2):83–95 (**1995**). doi:10.1016/0039-6028(95)00605-2.

[146] I. Laoufi *et al.* Size and catalytic activity of supported gold nanoparticles: An in operando study during CO oxidation. *J. Phys. Chem. C*, 115(11):4673–4679 (**2011**). doi:10.1021/jp1110554.

[147] M. C. Saint-Lager *et al.* Catalytic properties of supported gold nanoparticles: New insights into the size-activity relationship gained from in operando measurements. *Faraday Discuss.*, 152:253–265 (**2011**). doi:10.1039/c1fd00028d.

[148] F. Cosandey. Epitaxy, interfacial energy and atomic structure of Au/TiO_2 interfaces. *Philos. Mag.*, 93(10-12):1197–1218 (**2013**). doi:10.1080/14786435.2013.770178.

[149] A. Grirrane, A. Corma and H. García. Gold-Catalyzed Synthesis of Aromatic Azo Compounds from Anilines and Nitroaromatics. *Science*, 322(5908):1661–1664 (**2008**). doi:10.1126/science.1166401.

[150] L. Aschwanden *et al.* Development of a new generation of gold catalysts for amine oxidation. *ChemCatChem*, 2(6):666–673 (**2010**). doi:10.1002/cctc.201000092.

[151] A. Corma, P. Serna and H. García. Gold catalysts open a new general chemoselective route to synthesize oximes by hydrogenation of α,β-unsaturated nitrocompounds with H_2. *J. Am. Chem. Soc.*, 129(20):6358–6359 (**2007**). doi:10.1021/ja0704131.

[152] P. E. Strizhak. ChemInform Abstract: Nanosize Effects in Heterogeneous Catalysis. *ChemInform*, 44(27):1–19 (**2013**). doi:10.1002/chin.201327226.

[153] M. Valden and D. W. Goodman. Structure-Activity Correlations for Au Nanoclusters Supported on TiO_2. *Isr. J. Chem.*, 38(4):285–292 (**1998**). doi:10.1002/ijch.199800034.

[154] A. Visikovskiy *et al.* Electronic d-band properties of gold nanoclusters grown on amorphous carbon. *Phys. Rev. B - Condens. Matter Mater. Phys.*, 83(16):1–9 (**2011**). doi:10.1103/PhysRevB.83.165428.

[155] T. V. Janssens *et al.* Insights into the reactivity of supported Au nanoparticles: Combining theory and experiments. *Top. Catal.*, 44(1-2):15–26 (**2007**). doi:10.1007/s11244-007-0335-3.

[156] B. Hammer and J. K. Nørskov. Theoretical surface science and catalysis—calculations and concepts. *Adv. Catal.*, 45(C):71–129 (**2000**). doi:10.1016/S0360-0564(02)45013-4.

[157] M. Haruta. Catalysis of gold nanoparticles deposited. *Cattech*, 6(3):61–73 (**2002**).

[158] I. N. Remediakis, N. Lopez and J. K. Nørskov. CO oxidation on rutile-supported Au nanoparticles. *Angew. Chemie - Int. Ed.*, 44(12):1824–1826 (**2005**). doi:10.1002/anie.200461699.

[159] I. X. Green *et al.* Spectroscopic observation of dual catalytic sites during oxidation of CO on a Au/TiO_2 catalyst. *Science*, 333(6043):736–739 (**2011**). doi:10.1126/science.1207272.

[160] W.-K. Chen *et al.* Adsorption and dissociation of methanol on Au(1 1 1) surface: A first-principles periodic density functional study. *J. Mol. Struct. THEOCHEM*, 770(1-3):87–91 (**2006**). doi:10.1016/j.theochem.2006.05.040.

[161] A. S. Wörz *et al.* Charging of Au atoms on TiO_2 thin films from CO vibrational spectroscopy and DFT calculations. *J. Phys. Chem. B*, 109(39):18418–18426 (**2005**). doi:10.1021/jp054093o.

[162] Z. Zhao *et al.* $Au/TiO_2/Ru(0001)$ model catalysts and their interaction with CO. *Surf. Sci.*, 600(22):4992–5003 (**2006**). doi:10.1016/j.susc.2006.08.022.

[163] D. C. Meier and D. W. Goodman. The Influence of Metal Cluster Size on Adsorption Energies: CO Adsorbed on Au Clusters Supported on TiO_2. *J. Am. Chem. Soc.*, 126(6):1892–1899 (**2004**). doi:10.1021/ja030359y.

[164] V. A. Bondzie, S. C. Parker and C. T. Campbell. The kinetics of CO oxidation by adsorbed oxygen on well-defined gold particles on TiO_2(110). *Catal. Letters*, 63(3):143–151 (**1999**). doi:10.1023/A:101901290393.

[165] K. Dumbuya *et al.* Evidence for an active oxygen species on Au/TiO_2(110) model catalysts during investigation with in situ X-ray photoelectron spectroscopy. *Catal. Today*, 181(1):20–25 (**2012**). doi:10.1016/j.cattod.2011.09.035.

[166] S. Porsgaard *et al.* Charge state of gold nanoparticles supported on titania under oxygen pressure. *Angew. Chemie - Int. Ed.*, 50(10):2266–2269 (**2011**). doi:10.1002/anie.201005377.

[167] T. Wu, W. E. Kaden and S. L. Anderson. Water on rutile TiO_2(110) and Au/TiO_2(110): Effects on Au mobility and the isotope exchange reaction. *J. Phys. Chem. C*, 112(24):9006–9015 (**2008**). doi:10.1021/jp800521q.

[168] M. Daté *et al.* Vital role of moisture in the catalytic activity of supported gold nanoparticles. *Angew. Chemie - Int. Ed.*, 43(16):2129–2132 (**2004**). doi:10.1002/anie.200453796.

[169] T. Yan *et al.* The Effect of Adsorbed Water in CO Oxidation on Au/TiO_2(110). *J. Phys. Chem. C*, 115(5):2057–2065 (**2011**). doi:10.1021/jp109295u.

[170] T. Fujitani and I. Nakamura. Mechanism and active sites of the oxidation of CO over Au/TiO_2. *Angew. Chemie - Int. Ed.*, 50(43):10144–10147 (**2011**). doi:10.1002/anie.201104694.

[171] M. Haruta. Size- and support-dependency in the catalysis of gold. *Catal. Today*, 36(1):153–166 (**1997**). doi:10.1016/S0920-5861(96)00208-8.

[172] Y. G. Wang *et al.* CO Oxidation on Au/TiO_2: Condition-Dependent Active Sites and Mechanistic Pathways. *J. Am. Chem. Soc.*, 138(33):10467–10476 (**2016**). doi:10.1021/jacs.6b04187.

[173] D. Widmann *et al.* How temperature affects the mechanism of CO oxidation on Au/TiO_2: A combined EPR and TAP reactor study of the reactive removal of TiO_2 surface lattice oxygen in Au/TiO2 by CO. *ACS Catal.*, 6(8):5005–5011 (**2016**). doi:10.1021/acscatal.6b01219.

[174] I. X. Green *et al.* Low-temperature catalytic H_2 oxidation over Au nanoparticle/TiO_2 dual perimeter sites. *Angew. Chemie - Int. Ed.*, 50(43):10186–10189 (**2011**). doi:10.1002/anie.201101612.

[175] I. X. Green *et al.* Insights into Catalytic Oxidation at the Au/TiO_2 Dual Perimeter Sites. *Acc. Chem. Res.*, 47(3):805–815 (**2014**). doi:10.1021/ar400196f.

[176] R. T. Tung. The physics and chemistry of the Schottky barrier height. *Appl. Phys. Rev.*, 1(1) (**2014**). doi:10.1063/1.4858400.

[177] Y. Maeda *et al.* Local barrier height of Au nanoparticles on a TiO_2(110)-(1×2) surface. *Appl. Surf. Sci.*, 222(1-4):409–414 (**2004**). doi:10.1016/j.apsusc.2003.09.007.

[178] M. A. Garcia. Surface plasmons in metallic nanoparticles: fundamentals and applications. *J. Phys. D. Appl. Phys.*, 44(28):283001 (**2011**). doi:10.1088/0022-3727/44/28/283001.

[179] K. M. Mayer and J. H. Hafner. Localized surface plasmon resonance sensors. *Chem. Rev.*, 111(6):3828–3857 (**2011**). doi:10.1021/cr100313v.

[180] Y. Soldo-Olivier *et al.* Localized surface plasmon resonance of Au/TiO_2 (110): substrate and size influence from in situ optical and structural investigation. *Nanoscale Adv.*, 2(6):2448–2461 (**2020**). doi:10.1039/D0NA00165A.

[181] E. Cottancin *et al.* Optical properties of noble metal clusters as a function of the size: Comparison between experiments and a semi-quantal theory. *Theor. Chem. Acc.*, 116(4-5):514–523 (**2006**). doi:10.1007/s00214-006-0089-1.

[182] C. Sönnichsen *et al.* Drastic reduction of plasmon damping in gold nanorods. *Phys. Rev. Lett.*, 88(7):774021–774024 (**2002**). doi:10.1103/PhysRevLett.88.077402.

[183] Z. Liu *et al.* Plasmon Resonant Enhancement of Photocatalytic Water Splitting Under Visible Illumination. *Nano Lett.*, 11(3):1111–1116 (**2011**). doi:10.1021/nl104005n.

[184] S. Mukherjee *et al.* Hot Electrons Do the Impossible: Plasmon-Induced Dissociation of H 2 on Au. *Nano Lett.*, 13(1):240–247 (**2013**). doi:10.1021/nl303940z.

[185] S. K. Cushing *et al.* Transfer from Metal to Semiconductor. *J. Am. Chem. Soc.*, 134:15033–15041 (**2012**).

[186] M. Hu and G. V. Hartland. Heat dissipation for au particles in aqueous solution: Relaxation time versus size. *J. Phys. Chem. B*, 106(28):7029–7033 (**2002**). doi:10.1021/jp020581CCC:22.00.

[187] J. B. Park, S. F. Conner and D. A. Chen. Bimetallic Pt-Au Clusters on TiO_2 (110): Growth, Surface Composition, and Metal-Support Interactions. *J. Phys. Chem. C*, 112(14):5490–5500 (**2008**). doi:10.1021/jp076027n.

[188] S. A. Tenney *et al.* Characterization of Pt-Au and Ni-Au clusters on TiO_2(110). *Top. Catal.*, 54(1-4):42–55 (**2011**). doi:10.1007/s11244-011-9646-5.

[189] S. Krick Calderón *et al.* CO oxidation on Pt(111) at near ambient pressures. *J. Chem. Phys.*, 144(4) (**2016**). doi:10.1063/1.4940318.

[190] D. C. Skelton *et al.* Oxidation of CO on Gold-Covered Pt(335). *J. Phys. Chem. B*, 103(6):964–971 (**1999**). doi:10.1021/jp983670o.

[191] P. A. Thiel *et al.* The interaction of CO and Pt(100). II. Energetic and kinetic parameters. *J. Chem. Phys.*, 78(12):7448–7458 (**1982**). doi:10.1063/1.444735.

[192] T. Gritsch *et al.* Mechanism of the CO-induced 1×2→1×1 structural transformation of Pt(110). *Phys. Rev. Lett.*, 63(10):1086–1089 (**1989**). doi:10.1103/PhysRevLett.63.1086.

[193] C. T. Campbell *et al.* A molecular beam study of the catalytic oxidation of CO on a Pt(111) surface. *J. Chem. Phys.*, 73(11):5862–5873 (**1980**). doi:10.1063/1.440029.

[194] A. C. Luntz, J. Grimblot and D. E. Fowler. Sequential precursors in dissociative chemisorption: O_2 on Pt(111). *Phys. Rev. B*, 39(17):12903–12906 (**1989**). doi:10.1103/PhysRevB.39.12903.

[195] T. Zambelli *et al.* Complex pathways in dissociative adsorption of oxygen on platinum. *Nature*, 390(6659):495–497 (**1997**). doi:10.1038/37329.

[196] B. Shan *et al.* CO-coverage-dependent oxygen dissociation on Pt(111) surface. *J. Phys. Chem. C*, 113(2):710–715 (**2009**). doi:10.1021/jp808763h.

[197] J. L. Gland and E. B. Kollin. Carbon monoxide oxidation on the Pt(111) surface: Temperature programmed reaction of coadsorbed atomic oxygen and carbon monoxide. *J. Chem. Phys.*, 78(2):963–974 (**1982**). doi:10.1063/1.444801.

[198] S. A. Tenney *et al.* Adsorbate-induced changes in the surface composition of bimetallic clusters: Pt-Au on TiO_2(110). *J. Phys. Chem. C*, 114(49):21652–21663 (**2010**). doi:10.1021/jp108939h.

[199] K. Jousten (Editor). *Wutz Handbuch Vakuumtechnik*. Vieweg+Teubner Verlag, Wiesbaden (**2004**). ISBN 978-3-322-96972-9. doi:10.1007/978-3-322-96971-2.

[200] H. Lüth. *Surfaces and Interfaces of Solid Materials*. Springer Berlin Heidelberg, Berlin, Heidelberg (**1995**). ISBN 978-3-540-58576-3. doi:10.1007/978-3-662-03132-2.

[201] H. Hertz. Ueber einen Einfluss des ultravioletten Lichtes auf die electrische Entladung. *Ann. der Phys. und Chemie*, 267(8):983–1000 (**1887**). doi:10.1002/andp.18872670827.

[202] A. Einstein. Über einen die Erzeugung und Verwandlung des Lichtes betreffenden heuristischen Gesichtspunkt. *Ann. Phys.*, 322(6):132–148 (**1905**). doi:10.1002/andp.19053220607.

[203] G. Greczynski *et al.* X-ray photoelectron spectroscopy of thin films. *Nat. Rev. Methods Prim.*, 3(1):1–19 (**2023**). doi:10.1038/s43586-023-00225-y.

[204] D. Briggs and J. T. Grant. *Surface analysis by Auger and X-ray photoelectron spectroscopy*. SurfaceSpectra (**2012**).

[205] G. C. Smith. *Surface Analysis by Electron Spectroscopy*. Springer US, Boston, MA (**1994**). ISBN 978-1-4899-0969-5. doi:10.1007/978-1-4899-0967-1.

[206] Neal Fairley. *CasaXPS Manual 2.3.15 Rev 1.2*. Casa Software Ltd (**2009**).

[207] D. A. Shirley. High-resolution x-ray photoemission spectrum of the valence bands of gold. *Phys. Rev. B*, 5(12):4709–4714 (**1972**). doi:10.1103/PhysRevB.5.4709.

[208] G. H. Major *et al.* Guide to XPS data analysis: Applying appropriate constraints to synthetic peaks in XPS peak fitting. *J. Vac. Sci. Technol. A*, 40(6) (**2022**). doi:10.1116/6.0001975.

[209] C. Powell and A. Jablonski. *NIST Electron Inelastic-Mean-Free-Path Database*. Version 1.2. National Institute of Standards and Technology, Gaithersburg, MD (**2010**).

[210] S. Hüfner. *Photoelectron Spectroscopy*. Advanced Texts in Physics. Springer Berlin Heidelberg, Berlin, Heidelberg (**2003**). ISBN 978-3-642-07520-9. doi:10.1007/978-3-662-09280-4.

[211] M. P. Seah and W. A. Dench. Quantitative Electron Spectroscopy of Surfaces : A Standard Data base for Electron Inelastic Free Paths in Solids. *Surf. Interface Anal.*, 1 (**1979**).

[212] SPECS User Manual. *Focus 500 - X-Ray Monochromator*. 2.0 ed. (**2011**).

[213] SPECS User manual. *Delay Line Detector 3D-DLD4040-150*. 2.1 ed. (**2012**).

[214] G. Binnig and H. Rohrer. Scanning tunneling microscopy. *Surf. Sci.*, 126(1-3):236–244 (**1983**).

[215] H. Lüth. *Solid Surfaces, Interfaces and Thin Films*. Graduate Texts in Physics. Springer Berlin Heidelberg, Berlin, Heidelberg (**2010**). ISBN 978-3-642-13591-0. doi:10.1007/978-3-642-13592-7.

[216] P. K. Hansma and J. Tersoff. Scanning tunneling microscopy. *J. Appl. Phys.*, 61(2) (**1987**). doi:10.1063/1.338189.

[217] A. Wang and T. Y. Chien. Perspectives of cross-sectional scanning tunneling microscopy and spectroscopy for complex oxide physics. *Phys. Lett. Sect. A Gen. At. Solid State Phys.*, 382(11):739–748 (**2018**). doi:10.1016/j.physleta.2018.01.016.

[218] M. Henzler and W. Göpel. *Oberflächenphysik des Festkörpers*. Teubner Studienbücher Physik. Vieweg+Teubner Verlag, Wiesbaden (**1994**). ISBN 978-3-519-13047-5. doi:10.1007/978-3-322-84875-8.

[219] J. Als-Nielsen and D. McMorrow. *Elements of Modern X-ray Physics*. John Wiley & Sons, Inc., Hoboken, NJ, USA (**2011**). ISBN 9781119998365. doi:10.1002/9781119998365.

[220] L. G. Parratt. Surface studies of solids by total reflection of x-rays. *Phys. Rev.*, 95(2):359–369 (**1954**). doi:10.1103/PhysRev.95.359.

[221] L. Névot and P. Croce. Caractérisation des surfaces par réflexion rasante de rayons X. Application à l'étude du polissage de quelques verres silicates. *Rev. Phys. Appliquée*, 15(3):761–779 (**1980**). doi:10.1051/rphysap:01980001503076100.

[222] Andreas Stierle. Fewlay - a software for fitting x-ray reflectivity curves. Information about the software can be obtained from A. Stierle: andreas. stierle@desy.de.

[223] L. De Broglie. *Recherches sur la théorie des Quanta*. Theses, Migration - université en cours d'affectation (**1924**).

[224] G. P. Thomson and A. Reid. Diffraction of Cathode Rays by a Thin Film. *Nature*, 119(3007):890–890 (**1927**). doi:10.1038/119890a0.

[225] A. Stierle and E. Vlieg. Surface-Sensitive X-Ray Diffraction Methods. In *Mod. Diffr. Methods*, pp. 221–257. Wiley (**2012**). doi:10.1002/9783527649884.ch8.

[226] C. Pellegrini. The history of X-ray free-electron lasers. *Eur. Phys. J. H*, 37(5):659–708 (**2012**). doi:10.1140/epjh/e2012-20064-5.

[227] P. Willmott. *An Introduction to Synchrotron Radiation*. Wiley (**2019**). ISBN 9781119280392. doi:10.1002/9781119280453.

[228] E. J. Jaeschke *et al.* (Editors). *Synchrotron Light Sources and Free-Electron Lasers*. Springer International Publishing, Cham (**2020**). ISBN 978-3-030-23200-9. doi:10.1007/978-3-030-23201-6.

[229] Z. Huang and K. J. Kim. Review of x-ray free-electron laser theory. *Phys. Rev. Spec. Top. - Accel. Beams*, 10(3):1–26 (**2007**). doi:10.1103/PhysRevSTAB.10.034801.

[230] W. Ackermann *et al.* Operation of a free-electron laser from the extreme ultraviolet to the water window. *Nat. Photonics*, 1(6):336–342 (**2007**). doi:10.1038/nphoton.2007.76.

[231] E. Allaria *et al.* Two-stage seeded soft-X-ray free-electron laser. *Nat. Photonics*, 7(11):913–918 (**2013**). doi:10.1038/nphoton.2013.277.

[232] B. W. Mcneil and N. R. Thompson. X-ray free-electron lasers. *Nat. Photonics*, 4(12):814–821 (**2010**). doi:10.1038/nphoton.2010.239.

[233] H. Redlin *et al.* The FLASH pump–probe laser system: Setup, characterization and optical beamlines. *Nucl. Instruments Methods Phys. Res. Sect. A Accel. Spectrometers, Detect. Assoc. Equip.*, 635(1):S88–S93 (**2011**). doi:10.1016/j.nima.2010.09.159.

[234] L. Wenthaus. *Laser-Assisted Photoemission from Solids with Free Electron Lasers*. Ph.D. thesis, Universität Hamburg (**2018**).

[235] L. Wenthaus *et al.* Insights into the laser-assisted photoelectric effect from solid-state surfaces. *Phys. Rev. B*, 110(23):235406 (**2024**). doi:10.1103/PhysRevB.110.235406.

[236] A. Stierle *et al.* DESY NanoLab. *J. large-scale Res. Facil. JLSRF*, 2:A76 (**2016**). doi:10.17815/jlsrf-2-140.

[237] Omicron Nanotechnology / Focus. *Instruction Manual UHV Evaporator EFM 2/3/3s/4*. 3.9 ed. (**2008**).

[238] N. Fairley *et al.* Systematic and collaborative approach to problem solving using X-ray photoelectron spectroscopy. *Appl. Surf. Sci. Adv.*, 5 (**2021**). doi:10.1016/j.apsadv.2021.100112.

[239] D. Nečas and P. Klapetek. Gwyddion: an open-source software for SPM data analysis. *Open Phys.*, 10(1):181–188 (**2012**). doi:10.2478/s11534-011-0096-2.

[240] U. Diebold *et al.* The relationship between bulk and surface properties of rutile TiO_2(110). *Surf. Rev. Lett.*, 7(5-6):613–617 (**2000**). doi:10.1016/S0218-625X(00)00052-X.

[241] N. Schell *et al.* The high energy materials science beamline (HEMS) at PETRA III. *Mater. Sci. Forum*, 772:57–61 (**2014**). doi:10.4028/www.scientific.net/MSF.772.57.

[242] M. Martins *et al.* Monochromator beamline for FLASH. *Rev. Sci. Instrum.*, 77(11) (**2006**). doi:10.1063/1.2364148.

[243] N. Gerasimova, S. Dziarzhytski and J. Feldhaus. The monochromator beamline at FLASH: performance, capabilities and upgrade plans. *J. Mod. Opt.*, 58(16):1480–1485 (**2011**). doi:10.1080/09500340.2011.588344.

[244] S. Toleikis. The FLASH facility current status in 2018 and future upgrade plans. *AIP Conf. Proc.*, 2054(January):1–7 (**2019**). doi:10.1063/1.5084578.

[245] B. O'Regan and M. Grätzel. A low-cost, high-efficiency solar cell based on dye-sensitized colloidal TiO_2 films. *Nature*, 353(6346):737–740 (**1991**). doi:10.1038/353737a0.

[246] M. Kohantorabi *et al.* Adsorption and Inactivation of SARS-CoV-2 on the Surface of Anatase TiO_2(101). *ACS Appl. Mater. Interfaces*, 15(6):8770–8782 (**2023**). doi:10.1021/acsami.2c22078.

[247] J. Prakash, J. Cho and Y. K. Mishra. Photocatalytic TiO_2 nanomaterials as potential antimicrobial and antiviral agents: Scope against blocking the SARS-COV-2 spread. *Micro Nano Eng.*, 14:100100 (**2022**). doi:10.1016/j.mne.2021.100100.

[248] M. Basante-Romo, J. O. Gutiérrez-M and R. Camargo-Amado. Non-toxic doses of modified titanium dioxide nanoparticles (m-TiO2NPs) in albino CFW mice. *Heliyon*, 7(3) (**2021**). doi:10.1016/j.heliyon.2021.e06514.

[249] A. Kudo and Y. Miseki. Heterogeneous photocatalyst materials for water splitting. *Chem. Soc. Rev.*, 38(1):253–278 (**2008**). doi:10.1039/B800489G.

[250] K. Ozawa *et al.* Electron-hole recombination time at TiO_2 single-crystal surfaces: Influence of surface band bending. *J. Phys. Chem. Lett.*, 5(11):1953–1957 (**2014**). doi:10.1021/jz500770c.

[251] T. Yoshihara *et al.* Identification of Reactive Species in Photoexcited Nanocrystalline TiO_2 Films by Wide-Wavelength-Range (400-2500 nm) Transient Absorption Spectroscopy. *J. Phys. Chem. B*, 108(12):3817–3823 (**2004**). doi:10.1021/jp031305d.

[252] A. Yamakata, T. A. Ishibashi and H. Onishi. Water- and oxygen-induced decay kinetics of photogenerated electrons in TiO_2 and Pt/TiO_2: A time-resolved infrared absorption study. *J. Phys. Chem. B*, 105(30):7258–7262 (**2001**). doi:10.1021/jp010802w.

[253] H. Zhao, Q. Zhang and Y. X. Weng. Deep surface trap filling by photoinduced carriers and interparticle electron transport observed in TiO_2 nanocrystalline film with time-resolved visible and mid-IR transient spectroscopies. *J. Phys. Chem. C*, 111(9):3762–3769 (**2007**). doi:10.1021/jp0645566.

[254] A. Yamakata, T.-a. A. Ishibashi and H. Onishi. Electron- and Hole-Capture Reactions on Pt/TiO_2 Photocatalyst Exposed to Methanol Vapor Studied with Time-Resolved Infrared Absorption Spectroscopy. *J. Phys. Chem. B*, 106(35):9122–9125 (**2002**). doi:10.1021/jp025993x.

[255] A. Pietzsch *et al.* Towards time resolved core level photoelectron spectroscopy with femtosecond x-ray free-electron lasers. *New J. Phys.*, 10 (**2008**). doi:10.1088/1367-2630/10/3/033004.

[256] A. G. Thomas *et al.* Comparison of the electronic structure of anatase and rutile TiO_2 single-crystal surfaces using resonant photoemission and x-ray absorption spectroscopy. *Phys. Rev. B*, 75(3):035105 (**2007**). doi:10.1103/PhysRevB.75.035105.

[257] W. H. McMaster *et al.* Compilation of X-Ray Cross Sections. Tech. rep., California Univ., Livermore. Lawrence Radiation Lab. (**1969**).

[258] W. H. Baur and A. A. Khan. Rutile-type compounds. IV. SiO_2, GeO_2 and a comparison with other rutile-type structures. *Acta Crystallogr. Sect. B Struct. Crystallogr. Cryst. Chem.*, 27(11):2133–2139 (**1971**). doi:10.1107/S0567740871005466.

[259] L. E. Walle *et al.* Experimental evidence for mixed dissociative and molecular adsorption of water on a rutile TiO_2 (110) surface without oxygen vacancies. *Phys. Rev. B - Condens. Matter Mater. Phys.*, 80(23):1–5 (**2009**). doi:10.1103/PhysRevB.80.235436.

[260] M. Setvin *et al.* Electron transfer between anatase TiO_2 and an O_2 molecule directly observed by atomic force microscopy. *Proc. Natl. Acad. Sci.*, 114(13):E2556–E2562 (**2017**). doi:10.1073/pnas.1618723114.

[261] I. Sokolović *et al.* Resolving the adsorption of molecular O_2 on the rutile $TiO_2(110)$ surface by noncontact atomic force microscopy. *Proc. Natl. Acad. Sci. U. S. A.*, 117(26):14827–14837 (**2020**). doi:10.1073/pnas.1922452117.

[262] A. Linsebigler, G. Lu and J. T. Yates. CO chemisorption on $TiO_2(110)$: Oxygen vacancy site influence on CO adsorption. *J. Chem. Phys.*, 103(21):9438–9443 (**1995**). doi:10.1063/1.470005.

[263] J. Freitag *et al.* Nitrogen(II) oxide charge transfer complexes on TiO_2: A new source for visible-light activity. *J. Phys. Chem. C*, 119(9):4488–4501 (**2015**). doi: 10.1021/jp5108069.

[264] L. Kavan *et al.* Electrochemical and photoelectrochemical investigation of single-crystal anatase. *J. Am. Chem. Soc.*, 118(28):6716–6723 (**1996**). doi:10.1021/ja954172l.

[265] C. C. Evans *et al.* Mixed two- and three-photon absorption in bulk rutile (TiO_2) around 800 nm. *Opt. Express*, 20(3):3118 (**2012**). doi:10.1364/OE.20.003118.

[266] Y. Tamaki *et al.* Femtosecond visible-to-IR spectroscopy of TiO_2 nanocrystalline films: Elucidation of the electron mobility before deep trapping. *J. Phys. Chem. C*, 113(27):11741–11746 (**2009**). doi:10.1021/jp901833j.

[267] A. M. Peiró *et al.* Photochemical reduction of oxygen adsorbed to nanocrystalline TiO_2 films: A transient absorption and oxygen scavenging study of different TiO_2 preparations. *J. Phys. Chem. B*, 110(46):23255–23263 (**2006**). doi: 10.1021/jp064591c.

[268] Z. Zhang and J. T. Yates. Direct observation of surface-mediated electron-hole pair recombination in TiO_2(110). *J. Phys. Chem. C*, 114(7):3098–3101 (**2010**). doi: 10.1021/jp910404e.

[269] J. Lee *et al.* Interaction of CO with Oxygen Adatoms on TiO_2 (110). *J. Phys. Chem. C*, 115(10):4163–4167 (**2011**). doi:10.1021/jp1112697.

[270] Y. Yamada and Y. Kanemitsu. Determination of electron and hole lifetimes of rutile and anatase TiO_2 single crystals. *Appl. Phys. Lett.*, 101(13):133907 (**2012**). doi:10.1063/1.4754831.

[271] Y. Zhang *et al.* State-Selective Dynamics of TiO_2 Charge-Carrier Trapping and Recombination. *J. Phys. Chem. Lett.*, 10(17):5265–5270 (**2019**). doi:10.1021/acs.jpclett.9b02153.

[272] J. Zhang *et al.* New understanding of the difference of photocatalytic activity among anatase, rutile and brookite TiO_2. *Phys. Chem. Chem. Phys.*, 16(38):20382–20386 (**2014**). doi:10.1039/c4cp02201g.

[273] N. G. Petrik and G. A. Kimmel. Reaction Kinetics of Water Molecules with Oxygen Vacancies on Rutile TiO_2(110). *J. Phys. Chem. C*, 119(40):23059–23067 (**2015**). doi:10.1021/acs.jpcc.5b07526.

[274] D. A. Duncan, F. Allegretti and D. P. Woodruff. Water does partially dissociate on the perfect TiO_2(110) surface: A quantitative structure determination. *Phys. Rev. B - Condens. Matter Mater. Phys.*, 86(4):1–4 (**2012**). doi:10.1103/PhysRevB.86.045411.

[275] M. Miyazaki, Y. Sugawara and Y. J. Li. Charge Behavior of Terminal Hydroxyl on Rutile TiO_2(110). *Langmuir*, 37(35):10588–10593 (**2021**). doi:10.1021/acs.langmuir.1c01845.

[276] J. Scaranto and S. Giorgianni. Influence of the OH groups of hydroxylated rutile (110) surface on the Lewis acidity: an investigation of CO adsorption by quantum-mechanical simulations. *Mol. Phys.*, 106(21):2425–2430 (**2008**). doi:10.1080/00268970802506114.

[277] D. V. Barsukov, A. N. Pershin and I. R. Subbotina. Increase of CO photocatalytic oxidation rate over anatase TiO_2 particles by adsorbed water at moderate coverages: The role of peroxide species. *J. Photochem. Photobiol. A Chem.*, 324:175–183 (**2016**). doi:10.1016/j.jphotochem.2016.03.021.

[278] D. V. Barsukov and I. R. Subbotina. Effect of surface hydration on the photocatalytic activity of oxide catalysts in the CO oxidation. *Russ. Chem. Bull.*, 67(2):243–251 (**2018**). doi:10.1007/s11172-018-2065-z.

[279] H. Einaga, S. Futamura and T. Ibusuki. Complete oxidation of benzene in gas phase by platinized titania photocatalysts. *Environ. Sci. Technol.*, 35(9):1880–1884 (**2001**). doi:10.1021/es001690+.

[280] H. Einaga *et al.* Generation of active sites for CO photooxidation on TiO_2 by platinum deposition. *J. Phys. Chem. B*, 107(35):9290–9297 (**2003**). doi:10.1021/jp0343638.

[281] C. Youssef *et al.* Effect of Oxygen and Water in the CO Photocatalytic Oxidation with TiO_2. *Adv. Mater. Res.*, 324:149–152 (**2011**). doi:10.4028/www.scientific.net/AMR.324.149.

[282] A. Tilocca, C. Di Valentin and A. Selloni. O_2 Interaction and Reactivity on a Model Hydroxylated Rutile(110) Surface. *J. Phys. Chem. B*, 109(44):20963–20967 (**2005**). doi:10.1021/jp0544181.

[283] Y. Du *et al.* Imaging consecutive steps of O_2 reaction with hydroxylated TiO_2(110): Identification of HO_2 and terminal OH intermediates. *J. Phys. Chem. C*, 113(2):666–671 (**2009**). doi:10.1021/jp807030n.

[284] Z. Zhang *et al.* Water as a catalyst: Imaging reactions of O_2 with partially and fully hydroxylated TiO_2(110) surfaces. *J. Phys. Chem. C*, 113(5):1908–1916 (**2009**). doi:10.1021/jp809001x.

[285] E. Arima *et al.* KPFM/AFM imaging on TiO_2 (110) surface in O_2 gas. *Nanotechnology*, 29(10):105504 (**2018**). doi:10.1088/1361-6528/aaa62c.

[286] L. M. Liu *et al.* Identifying an O_2 supply pathway in CO oxidation on Au/TiO_2(110): A density functional theory study on the intrinsic role of water. *J. Am. Chem. Soc.*, 128(12):4017–4022 (**2006**). doi:10.1021/ja056801p.

[287] Á. Ganyecz, P. D. Mezei and M. Kállay. Oxygen reduction reaction on TiO_2 rutile (110) surface in the presence of bridging hydroxyl groups. *Comput. Theor. Chem.*, 1168(August):112607 (**2019**). doi:10.1016/j.comptc.2019.112607.

[288] H. Tian *et al.* Intrinsic Role of Excess Electrons in Surface Reactions on Rutile TiO_2 (110): Using Water and Oxygen as Probes. *J. Phys. Chem. C*, 122(15):8270–8276 (**2018**). doi:10.1021/acs.jpcc.7b12451.

[289] M. J. Jackman, A. G. Thomas and C. Muryn. Photoelectron Spectroscopy Study of Stoichiometric and Reduced Anatase TiO_2 (101) Surfaces: The Effect of Subsurface Defects on Water Adsorption at Near-Ambient Pressures. *J. Phys. Chem. C*, 119(24):13682–13690 (**2015**). doi:10.1021/acs.jpcc.5b02732.

[290] G. Kresse and J. Hafner. Ab initio molecular dynamics for liquid metals. *Phys. Rev. B*, 47(1):558–561 (**1993**). doi:10.1103/PhysRevB.47.558.

[291] G. Kresse and J. Hafner. Ab initio molecular-dynamics simulation of the liquid-metalamorphous- semiconductor transition in germanium. *Phys. Rev. B*, 49(20):14251–14269 (**1994**). doi:10.1103/PhysRevB.49.14251.

[292] G. Kresse and J. Furthmüller. Efficiency of ab-initio total energy calculations for metals and semiconductors using a plane-wave basis set. *Comput. Mater. Sci.*, 6(1):15–50 (**1996**). doi:10.1016/0927-0256(96)00008-0.

[293] G. Kresse and J. Furthmüller. Efficient iterative schemes for ab initio total-energy calculations using a plane-wave basis set. *Phys. Rev. B - Condens. Matter Mater. Phys.*, 54(16):11169–11186 (**1996**). doi:10.1103/PhysRevB.54.11169.

[294] J. P. Perdew, M. Ernzerhof and K. Burke. Rationale for mixing exact exchange with density functional approximations. *J. Chem. Phys.*, 105(22):9982–9985 (**1996**). doi:10.1063/1.472933.

[295] P. E. Blöchl. Projector augmented-wave method. *Phys. Rev. B*, 50(24):17953–17979 (**1994**). doi:10.1103/PhysRevB.50.17953.

[296] G. Kresse and D. Joubert. From ultrasoft pseudopotentials to the projector augmented-wave method. *Phys. Rev. B*, 59(3):1758–1775 (**1999**). doi:10.1103/PhysRevB.59.1758.

[297] S. Grimme *et al.* A consistent and accurate ab initio parametrization of density functional dispersion correction (DFT-D) for the 94 elements H-Pu. *J. Chem. Phys.*, 132(15) (**2010**). doi:10.1063/1.3382344.

[298] S. Grimme, S. Ehrlich and L. Goerigk. Effect of the damping function in dispersion corrected density functional theory. *J. Comput. Chem.*, 32(7):1456–1465 (**2011**). doi:10.1002/jcc.21759.

[299] M. Farzalipour Tabriz *et al.* Application of the Lany-Zunger polaron correction for calculating surface charge trapping. *J. Phys. Condens. Matter*, 29(39) (**2017**). doi:10.1088/1361-648X/aa7ebd.

[300] S. Lany, H. Raebiger and A. Zunger. Magnetic interactions of Cr-Cr and Co-Co impurity pairs in ZnO within a band-gap corrected density functional approach. *Phys. Rev. B - Condens. Matter Mater. Phys.*, 77(24):9–12 (**2008**). doi:10.1103/PhysRevB.77.241201.

[301] S. Lany. Semiconducting transition metal oxides. *J. Phys. Condens. Matter*, 27(28) (**2015**). doi:10.1088/0953-8984/27/28/283203.

[302] B. Aradi, B. Hourahine and T. Frauenheim. DFTB+, a sparse matrix-based implementation of the DFTB method. *J. Phys. Chem. A*, 111(26):5678–5684 (**2007**). doi:10.1021/jp070186p.

[303] G. Dolgonos *et al.* An improved self-consistent-charge density-functional tight-binding (SCC-DFTB) set of parameters for simulation of bulk and molecular systems involving titanium. *J. Chem. Theory Comput.*, 6(1):266–278 (**2010**). doi:10.1021/ct900422c.

[304] H. Perron *et al.* Combined investigation of water sorption on TiO_2 rutile (110) single crystal face: XPS vs. periodic DFT. *Surf. Sci.*, 601(2):518–527 (**2007**). doi:10.1016/j.susc.2006.10.015.

[305] U. Diebold and T. E. Madey. TiO_2 by XPS. *Surf. Sci. Spectra*, 4(3):227–231 (**1996**). doi:10.1116/1.1247794.

[306] A. Mellor *et al.* Photoemission core level binding energies from multiple sized nanoparticles on the same support: TiO_2(110)/Au. *J. Chem. Phys.*, 152(2) (**2020**). doi:10.1063/1.5135760.

[307] J. Radnik, C. Mohr and P. Claus. On the origin of binding energy shifts of core levels of supported gold nanoparticles and dependence of pretreatment and material synthesis. *Phys. Chem. Chem. Phys.*, 5(1):172–177 (**2003**). doi:10.1039/b207290d.

[308] Z. Jiang *et al.* Direct XPS Evidence for Charge Transfer from a Reduced Rutile TiO_2 (110) Surface to Au Clusters. *J. Phys. Chem. C*, 111(33):12434–12439 (**2007**). doi:10.1021/jp073446b.

[309] M. Iachella, T. Le Bahers and D. Loffreda. Diffusion Kinetics of Gold and Copper Atoms on Pristine and Reduced Rutile TiO_2 (110) Surfaces. *J. Phys. Chem. C*, 122(7):3824–3837 (**2018**). doi:10.1021/acs.jpcc.7b08183.

[310] P. G. Etchegoin, E. C. Le Ru and M. Meyer. An analytic model for the optical properties of gold. *J. Chem. Phys.*, 125(16) (**2006**). doi:10.1063/1.2360270.

[311] R. Lazzari *et al.* Model-free unraveling of supported nanoparticles plasmon resonance modes. *J. Phys. Chem. C*, 118(13):7032–7048 (**2014**). doi:10.1021/jp500675h.

[312] M. Borgwardt *et al.* Photoinduced Charge Carrier Dynamics and Electron Injection Efficiencies in Au Nanoparticle-Sensitized TiO_2 Determined with Picosecond Time-Resolved X-ray Photoelectron Spectroscopy. *J. Phys. Chem. Lett.*, 11(14):5476–5481 (**2020**). doi:10.1021/acs.jpclett.0c00825.

[313] S. H. Park *et al.* In-situ and wavelength-dependent photocatalytic strain evolution of a single Au nanoparticle on a TiO_2 film. *Nat. Commun.*, 15(1):5416 (**2024**). doi:10.1038/s41467-024-49862-1.

[314] M. Seidel *et al.* Ultrafast MHz-Rate Burst-Mode Pump–Probe Laser for the FLASH FEL Facility Based on Nonlinear Compression of ps-Level Pulses from an Yb-Amplifier Chain. *Laser Photonics Rev.*, 16(3):1–10 (**2022**). doi:10.1002/lpor.202100268.

[315] D. Matthey *et al.* Enhanced Bonding of Gold Nanoparticles on Oxidized TiO_2 (110). *Science*, 315(5819):1692–1696 (**2007**). doi:10.1126/science.1135752.

[316] G. C. Bond. The electronic structure of platinum-gold alloy particles: Better catalysts for selective oxidations. *Platin. Met. Rev.*, 51(2):63–68 (**2007**). doi:10.1595/147106707X187353.

[317] M.J. Berger *et al.* NIST Standard Reference Database 8 (XGAM) (**2010**). doi: 10.18434/T48G6X.

[318] C. Weststrate *et al.* CO adsorption on Au(310) and Au(321): 6-Fold coordinated gold atoms. *Surf. Sci.*, 603(13):2152–2157 (**2009**). doi:10.1016/j.susc.2009.04.026.

[319] L. Lin *et al.* Coupling Effect of Au Nanoparticles with the Oxygen Vacancies of TiO_{2-x} for Enhanced Charge Transfer. *J. Phys. Chem. C*, 124(43):23823–23831 (**2020**). doi:10.1021/acs.jpcc.0c09011.

[320] R. Toyoshima *et al.* A high-pressure-induced dense CO overlayer on a Pt(111) surface: a chemical analysis using in situ near ambient pressure XPS. *Phys. Chem. Chem. Phys.*, 16(43):23564–23567 (**2014**). doi:10.1039/C4CP04318A.

[321] M. Kinne *et al.* Kinetic parameters of CO adsorbed on Pt(111) studied by in situ high resolution x-ray photoelectron spectroscopy. *J. Chem. Phys.*, 117(23):10852–10859 (**2002**). doi:10.1063/1.1522405.

[322] D. Zagorac *et al.* Recent developments in the Inorganic Crystal Structure Database: theoretical crystal structure data and related features. *J. Appl. Crystallogr.*, 52(5):918–925 (**2019**). doi:10.1107/S160057671900997X.

Acknowledgments

It takes a village to raise a child and also to write a doctoral thesis. Every discussion and conversation contributed to this thesis.
First of all, I want to acknowledge Prof. Dr. Andreas Stierle and Dr. Heshmat Noei for giving me the opportunity to research this topic, as well as their supervision and helpful advice during the past years.
Thanks to PD Dr. Michael Martins for serving as the second examiner of my thesis.
I want to acknowledge the Christiane Nüsslein-Volhard Foundation for the financial support for mothers in academia.
I also thank the Cluster of Excellence 'CUI: Advanced Imaging of Matter' and its equal opportunity office for providing funding for the past years.
Thank you to all collaborators from FLASH: Dr. Lukas Wenthaus, Dr. Steffen Palutke, Dr. Siarhei Dziarzhytski, Dr. Dmytro Kutnyakhov, Dr. Michael Heber, Dr. Günter Brenner, Dr. Harald Redlin and Dr. Federico Pressacco who made the beamtime possible. Special shout out to Lukas for his support for the data analysis.
Thanks to Matthias Schwartzkopf for fruitful debates about Gold Nanoparticles.
I also want to thank Arno Jeromin for the SEM images of my hard-to-measure samples.
Thanks to Dennis Renner for quickly and reliably solving technical problems in the UHV lab.
Thanks to all current and former colleagues from the DESY NanoLab, especially Jan-Christian Schober, Dr. Michael Wagstaffe, Dr. Mona Kohantorabi, Dr. Marcus Creuzburg, Dr. Simon Chung, Alexander Meinhardt, Miguel Blanco, Silvan Dolling, Luisa Wartner, and Joris Fuchs. I enjoyed working with you every day!
I especially want to acknowledge Lydia Bachmann. Thank you for proofreading my thesis, all our discussions, coffee breaks, and time together in the lab.
To my parents, Anke and Michael, my brother Jonathan, my in-law family, and my friends, thank you for being my village. Your support and looking after my children helped a lot.

Most importantly, I wish to thank my dear husband, Robert, and my two beloved children, Jarno and Jaris, for their endless love, understanding, and encouragement.